Microstructure and mechanical properties of high strength cast aluminium alloys

Kerry, S.

Award date:
1987

Awarding institution:
University of Bath

MICROSTRUCTURE AND MECHANICAL PROPERTIES OF HIGH STRENGTH CAST ALUMINIUM ALLOYS

Submitted by S. Kerry, B.Eng., M.Eng.,
for the degree of PhD of the
University of Bath
1987

ProQuest LLC
789 East Eisenhower Parkway
P.O. Box 1346
Ann Arbor, MI 48106-1346

SUMMARY

The microstructure and properties developed upon ageing a series of cast aluminium 4.8% copper alloys containing different amounts of magnesium and silver have been investigated.

Ageing at either 140°C or at 170°C produced a tensile strength well in excess of 400 MPa for alloys containing approximately 0.6 wt% of both magnesium and silver, but rather less in an alloy containing a reduced concentratioon (0.23 wt%) of magnesium.

Precipitation in the stronger materials occurred almost entirely on {111} planes of the aluminium lattice, but in the alloy containing less magnesium precipitates were formed on {100} as well as {111} planes.

The {111}-type precipitate has been identified as having a hexagonal crystal structure with a = 0.496 nm, and $^{c}/_{a}$ = 1.414, and it is considered to be an equilibrium phase. Its orientation relationship is given by [0001] parallel to <111> in the aluminium lattice and $<10\bar{1}0>$ parallel to <110>. This alignment results in close registry between the respective structures. A small addition of zinc ($\simeq$ 1.13 wt%) reduces the size of the precipitate but does not change its crystal structure. Precipitation on {100} lattice planes is associated with the formation of the θ' phase.

Quantitative TEM measurements of precipitate sizes and populations have been carried out. The data indicate firstly that precipitate growth is a diffusion-controlled rather than an interface-controlled process. Secondly, it is shown that the precipitation-hardening mechanism which operates as the peak hardness is reached upon ageing is associated with the shear of precipitates by dislocations. As the precipitates coarsen after longer ageing times, the dislocation bowing mechanism comes into operation and the strength of the alloy decreases.

Mechanical tests carried out in a sea water environment showed that the strength of all alloys was degraded. Extensive intergranular attack occurred and corrosion products containing the elements oxygen, sulphur and chlorine were formed. The zinc addition has a beneficial effect on the stress-corrosion resistance of these alloys.

CONTENTS

Page No

SUMMARY

CONTENTS

1 INTRODUCTION

1.1	General Background	1
1.1.1	Aluminium	1
1.1.2	Aluminium alloys	1
1.1.2.1	Wrought aluminium alloys	2
1.1.2.2	Cast aluminium alloys	3
1.2	Principles of Precipitation Hardening	4
1.2.1	Ageing treatment	4
1.2.2	Metastable phases	5
1.3	Nucleation and Growth of Precipitates	8
1.3.1	Homogeneous nucleation	8
1.3.2	Heterogeneous nucleation	10
1.3.3	Growth of precipitates	12
1.3.3.1	Interface-controlled growth	13
1.3.3.2	Diffusion-controlled growth	14
1.3.3.3	Growth dependent upon both diffusion and interface processes	15
1.3.3.4	Overall transformation kinetics	15
1.3.3.5	Particle coarsening (Ostwald ripening)	16
1.4	Strengthening Methods in Alloy Systems	19
1.4.1	Solid solution hardening	19
1.4.2	Dislocation cutting of precipitates	20
1.4.3	Dislocation bowing around precipitates	22
1.4.4	Other proposed strengthening mechanisms	23
1.4.5	The variation of yield stress with ageing time	24
1.5	The Aluminium-Copper Binary System	25
1.5.1	Precipitation hardening behaviour	25
1.5.2	Microstructure	26
1.5.3	Effect of additional elements on microstructure and precipitation-hardening behaviour of Al-Cu alloys	28
1.5.3.1	Effect of trace elements (<0.1 at %)	29
1.5.3.2	Effect of minor additions (<1 at %)	30
1.6	The Al-Cu-Mg Ternary System	31
1.7	The Al-Cu-Mg-Ag System	34
1.8	Stress-Corrosion Cracking (SCC) in Aluminium Alloys	37
1.8.1	Stress-corrosion cracking	37
1.8.2	SCC in aluminium alloys	38
1.8.3	Mechanisms ofSCC in aluminium alloys	40
1.9	Scope of the Present Investigation	42
2	EXPERIMENTAL DETAILS	44
2.1	Materials	44
2.2	Heat Treatment	44

			Page No
	2.3	Optical Microscopy	44
	2.4	Hardness Testing	45
	2.5	Electron Microscopy and Analysis	45
	2.5.1	Scanning electron microscopy (SEM)	45
	2.5.2	Electron-probe microanalysis (EPMA)	46
	2.5.3	Transmission electron microscopy (TEM)	47
	2.5.3.1	Precipitation studies	48
	2.5.3.2	Pricipitation density determination	50
	2.6	Mechanical Testing	51
	2.6.1	Tensile testing	51
	2.6.2	Environmental testing	52
3	RESULTS		53
	3.1	As-Cast Materials	53
	3.2	Solution Treated Materials	53
	3.3	Ageing Characterisitcs	54
	3.3.1	Ageing response	54
	3.3.1.1	Ageing at 140°C	54
	3.3.1.2	Ageing at 170°C	54
	3.3.2	Structure and orientation relationship of precipitates	54
	3.3.3	Calibration curve for foil thickness determination	60
	3.3.4	Nucleation and growth of precipitates	61
	3.3.4.1	Alloy A5	61
	3.3.4.2	Alloy A4	63
	3.3.4.3	Alloy A3	64
	3.4	Tensile Test Data	65
	3.5	Environmental Test Data	66
	3.5.1	Mechanical tests	66
	3.5.2	Fractography	66
	3.5.2.1	Alloy A5	66
	3.5.2.2	Alloy A3	67
	3.5.2.3	Alloy A4	68
4	DISCUSSION		69
	4.1	As-Cast and Solution Treated Materials	69
	4.2	Response to Ageing	70
	4.3	Crystal Structure of the {111}-Type Precipitate	71
	4.4	Precipitate Morphologies	75
	4.5	Nucleation and Growth of Precipitates	76
	4.5.1	Nucleation	76
	4.5.2	Growth of precipitates	79
	4.6	Strengthening Mechanisms	81
	4.7	Environmental Behaviour	85
5	CONCLUSIONS		88

	Page No
SUGGESTIONS FOR FUTURE WORK	90
REFERENCES	91
APPENDIX 1	98
APPENDIX 2	99
ACKNOWLEDGEMENTS	104

CHAPTER 1

INTRODUCTION

1.1 General Background

1.1.1 Aluminium

In its pure form aluminium has properties which make it an attractive material for a wide variety of uses. It has, for example, a low specific gravity, a high resistance to corrosion, excellent electrical and thermal conductivities and can be easily formed.

For many years aluminium has been the accepted metal used in the manufacture of saucepans, frying pans, kettles and similar domestic articles. In the building and allied trades the metal is used extensively because of its light weight, resistance to atmospheric corrosion and the ease with which various visual effects can be obtained. Also, aluminium is being increasingly used in the packaging industry where its absence of toxicity, its ductility, impermeability to moisture and other vapours, and opacity make it an attractive material for use as cigarette foil ranging to beer barrels. In the electrical industry, aluminium is replacing copper in many of the traditional applications on account of its excellent electrical conductivity, its light weight and its cheapness to produce compared with copper. The range of applications of the metal is, however, considerably extended when used as an alloy.

1.1.2 Aluminium alloys

Aluminium is a soft metal which, in its pure form, does not respond well to attempts to improve its mechanical properties by mechanical and/or heat treatment procedures. However, by alloying the aluminium with certain elements it is possible to increase the strength considerably by inducing a "precipitation-hardening" reaction in the material (see section 1.2). More importantly, if the low specific gravity of the alloy can still be retained, very high strength: weight ratios can be achieved. This is particularly important in aerospace applications.

Many metals will alloy with aluminium, although comparatively few have sufficient solid solubility to serve as major alloying additions. Table 1.1 gives the solid solubilities of various

Table 1.1

Solubility of Elements in Aluminium

(from I J Polmear, Light Alloys, Arnold Ltd 1981)

Element	Temperature (°C)	Maximum Solid Solubility	
		(wt%)	(at %)
Cadmium	649	0.40	0.09
Copper	548	5.65	2.40
Chromium	661	0.77	0.40
Iron	655	0.05	0.025
Lithium	600	4.20	16.3
Magnesium	450	17.40	18.5
Manganese	658	1.82	0.90
Nickel	640	0.04	0.02
Silicon	577	1.65	1.59
Silver	566	55.6	13.8
Titanium	665	~1.3	~0.74
Zinc	443	70	28.8
Zirconium	660.5	0.28	0.08

silver?

elements in aluminium and only zinc, magnesium, copper and silicon are dissolved to any appreciable extent. Nevertheless, many elements which have solubilities below 1 atomic % may still confer important benefits; for example, chromium, manganese and zirconium may be added to control grain structure[1].

Each class of alloy behaves differently, with composition and structure dictating the fabrication characteristics and subsequent properties which can be developed. Aluminium alloys are, therefore, classified, as in the International Alloy Designation System (IADS) for wrought products, although many countries still retain their own classification system.

1.1.2.1 Wrought aluminium alloys

The IADS numbering system consists of four digits, the first relating to the major alloying element, see Figure 1.1 (for example, the 2000 series have copper as the major alloying addition, the 7000 series zinc). The remaining numbers refer to the different commercial variations of the binary system. The way in which the alloy was produced is also included in the classification. For example, an aluminium-zinc alloy which has been solution treated, cold worked then artifically aged would be designated 7075-T7. Hence, any alloy can be classified by the major alloying addition (first digit of number), the basic heat treatment condition (letter) and any secondary treatment used to influence the properties of the alloy (last digit(s)).

Approximately 80% of all aluminium alloy products are used in the wrought condition. Wrought alloys can be further divided into non-heat treatable and heat treatable groups. Strength in non-heat treatable alloys is achieved mainly by cold working, usually during the fabrication process itself. They comprise the various grades of aluminium as well as alloys with manganese and/or magnesium as the major additions, these elements offering some measure of dispersion hardening (Al-Mn) and/or solid solution hardening (Al-Mg). Examples of some non-heat treatable alloys and their applications are given in Table 1.2.

Wrought alloys that respond to strengthening by heat treatment are the series 2xxx (Al-Cu, Al-Cu-Mg), 6xxx (Al-Mg-Si) and 7xxx (Al-Zn-Mg, Al-Zn-Mg-Cu), see Table 1.3. Typical properties and applications are listed in Table 1.4. Wrought alloys can be further divided into two groups: those that have medium strength and are

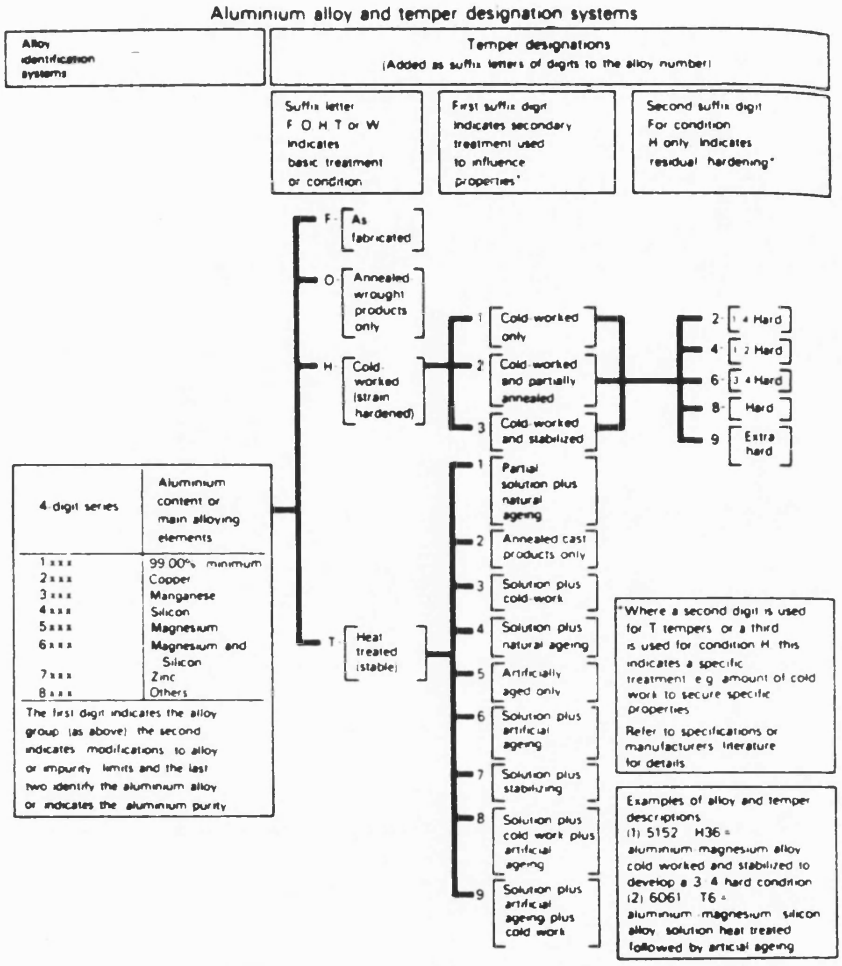

Figure 1.1 The IADS aluminium alloy designation system for wrought alloys (from Polmear [1]).

Table 1.2

Compositions, Mechanical Properties of Selected Non-Heat Treatable Wrought Aluminium Alloys

(Aluminium is balance) All in wt%

IADS Designation	Si	Fe	Cu	Mn	Mg	Zn	Cr	Ti	Temper	Tensile Strength MPa	Elongation %	Typical Applications
1100	1.0 Si + Fe		0.05-0.2	0.05		0.10			0 H18	90 165	35 5	Sheet, plate, tube wire
1199	0.006	0.006	0.006	0.002	0.006	0.006		0.002	0 H18	45 115	50 5	Electrical and electronic foil
3003	0.6	0.7	0.05-0.2	1.0-1.5		0.10			0 H18	110 200	30 4	Sheet, plate, cooking utensils
5005	0.3	0.7	0.2	0.2	0.5-1.1	0.25	0.10		0 H18	125 200	30 4	High strength foil, electrical conductor wire
5083	0.4	0.40	0.1	0.4-1.0	4.0-4.9	0.25	0.05-0.25	0.15	0 H343	290 360	22 8	Special purpose sheet plate etc for such as marine hulls and superstructures
8001	0.17	0.45-0.7	0.15			0.05 + 1.3 Ni			0 H18	110 200	30 4	Sheet, tubing for water cooled nuclear reactors

O = Annealed H18 = Cold worked, fully hard

Table 1.3

Compositions of Selected Heat Treatable Wrought Aluminium Alloys

(All compositions in wt% with balance aluminium)

IADS Designation	Si	Fe	Cu	Mn	Mg	Zn	Cr	Ti	Other
2011	0.4	0.7	5.0-6.0			0.30			0.2-0.6 Bi 0.2-0.6 Pb
2014	0.5-1.2	0.7	3.9-5.0	0.4-1.2	0.20-0.8	0.25	0.10	0.15	0.2 Zr + Ti
2024	0.50	0.50	3.8-4.9	0.30-0.9	1.2-1.8	0.25	0.10	0.15	0.2 Zr + Ti
2124	0.20	0.30	3.8-4.9	0.30-0.9	1.2-1.8	0.25	0.10	0.15	0.2 Zr + Ti
6063	0.20-0.6	0.35	0.1	0.1	0.45-0.9	0.10	0.10	0.10	
6351	0.7-1.3	0.5	0.1	0.4-0.8	0.4-0.8	0.2		0.2	
7010	0.1	0.15	1.5-2.0	0.30	2.2-2.7	5.7-6.7	0.05		0.11-0.17 Zr
7075	0.4	0.5	1.2-2.0	0.30	2.1-2.9	5.1-6.1	0.18-0.28	0.20	0.25 Zr + Ti
7178	0.4	0.5	1.6-2.4	0.30	2.4-3.1	6.3-7.3	0.18-0.35	0.20	
7079	0.3	0.4	0.4-0.8	0.1-0.3	2.9-3.7	3.8-4.8	0.10-0.25	0.10	

Table 1.4

Properties and Applications of Selected Heat Treatable WRought Aluminium Alloys

IADS Designation	Temper	Tensile Strength (MPa)	Elongation (%)	Typical Applications
2014	T6	480	13	Aircraft structures
2024	T6	470	20	Aircraft structures and sheet
6063	T6	240	12	Architectural extrusions, pipes
7075	T6	570	11	High strength aircraft structures
7079	T6	540	14	Aircraft forgings

T6 = Solution treated + artificially aged

readily weldable (Al-Mg-Si and Al-Zn-Mg) and those that have high strength but are not easily welded (Al-Cu, Al-Cu-Mg and Al-Zn-Mg-Cu).

1.1.2.2 Cast aluminium alloys

The special advantages of using aluminium alloys for castings are (apart from light weight) the relatively low melting temperatures, negligible solubility for all gases except hydrogen, and the good quality surface that is usually achieved with the final product. Although high fluidity is displayed by most alloys, the shrinkage of between 3.5 to 8.5% that occurs during solidification is a major problem which means that allowances have to be made in mould design in order to achieve dimensional accuracy. Other problems which must be minimised include hot tearing or cracking, residual stresses and shrinkage porosity.

In all areas except creep, cast alloys generally have mechanical properties that are inferior to wrought products. Also, the properties of cast products tend to be much more variable throughout a given component. In view of the demand for greater assurance in meeting specified mechanical properties a process known as "premium quality" casting has been introduced. This represents a major advance in foundry technology and consistencies in mechanical properties which were previously thought unattainable have been achieved through control of such factors as melting and pouring parameters, impurity levels, grain size and, in the case of sand casting, the use of metal chills to increase solidification rates. Although "premium quality" castings are more expensive to produce than those made by standard methods, such as sand casting and gravity die casting, they may yet be cost-effective if they can replace wrought components.

No internationally accepted system of nomenclature has been adopted for cast aluminium alloys although the Aluminium Association of the United States has recently introduced a system similar to that adopted for wrought alloys. This is detailed in Figure 1.2. For pure aluminium castings the second two digits indicate the minimum percentage of aluminium; the last digit, to the right of the decimal point, indicates product form, with 0 and 1 being used to denote castings and ingot respectively.

	Current designation	Former designation
Aluminium, 99.00% or greater	1xx.x	
Aluminium alloys grouped by major alloying elements:		
Copper	2xx.x	1xx
Silicon with added copper and/or magnesium	3xx.x	3xx
Silicon	4xx.x	1 to 99
Magnesium	5xx.x	2xx
Zinc	7xx.x	6xx
Tin	8xx.x	7xx
Other element	9xx.x	
Unused series	6xx.x	

Figure 1.2 The US alloy designation system for cast alloys (from Polmear [1]).

The 2xx.x to 9xx.x alloys are different in that the second two digits serve to identify the different aluminium alloys in the group, whilst the last digit again indicates product form. The same temper designations used for wrought products are used to identify subsequent heat treatment of castings. Some widely used cast aluminium alloys and their compositions are listed in Table 1.5. Of these only the 2xx.x and 7xx.x series are amenable to post-casting heat treatments to improve properties, although some Al-Mg alloys, eg Al-10wt%Mg, do respond to heat treatment.

As with wrought alloys, the more important high-strength cast alloys are those which respond to heat treatment. Strength is increased via precipitation hardening.

1.2 Principles of Precipitation Hardening

1.2.1 Ageing treatment

The phenomenon of precipitation hardening was discovered by A.Wilm in 1906. Wilm was searching for an aluminium alloy which could be hardened by quenching from an elevated temperature in a similar manner to steel. In one alloy, containing copper and magnesium (later known as 'Duralumin'), it was noticed that the hardness of the quenched alloy increased with time at room temperature[2] . The reasons for this phenomenon remained unknown to Wilm, but Merica et al[3] demonstrated, in 1919, that the solid solubility of copper in aluminium decreased with decreasing temperature. It was proposed that age- or precipitation-hardening had arisen due to the following effect; at high temperatures the alloy existed in a homogeneous solid solution. After "solution heat-treatment" and rapidly cooling to room temperature by quenching into water or other media, the separation of the θ-phase was considered to be suppressed, and an unstable supersaturated solid solution produced. Merica et al suggested that hardening resulted from precipitation of the second phase when the quenched alloy is "aged" for a sufficient time, and that the precipitate was in the form of a fine "submicroscopic dispersion".

Since these pioneering days, many other alloys have been identified as potential precipitation hardening systems. The type of phase diagram most commonly associated with such alloys, is shown in Figure 1.3. A suitable alloy composition, x, exists as a single phase solid solution, α, at an elevated temperature and contains a second phase, β, at

Table 1.5

Compositions and Properties of Selected Cast Aluminium Alloys

(balance aluminium; all compositions in wt%)

Aluminium Association Number	Si	Fe	Cu	Mn	Mg	Cr	Ni	Zn	Ti	Other	Temper	Tensile Strength (MPa)	Elongation (%)
201.0	0.10	0.15	4.0–5.2	0.2–0.5	0.15–0.55				0.15–0.35	Ag 0.4–1.0	T6	415	5.0
213.0	1.0–3.0	1.2	6.0–8.0	0.6	0.10		0.35	2.5	0.25		T6	295	2.0
319.0	5.5–6.5	1.0	3.0–4.0	0.5	0.10		0.35	1.0	0.25		T61	260	0.5
360.0	9.0–10.0	2.0	0.6	0.35	0.4–0.6		0.50	0.50			T6	255	—
413.0	11.0–13.0	2.0	1.0	0.35	0.10		0.50	0.50			F1	265	2.0
520.0	0.25	0.3	0.25	0.15	9.5–10.6			0.15	0.25		T1	320	15.0
707.0	0.20	0.6	0.2	0.4–0.6	1.4–1.8	0.2–0.4		4.0–4.5	0.25		T1	255	4.0

T6 = Solution plus artificially aged
T61 = Solution plus artificially aged plus other treatment
F1 = As-Fabricated
T1 = Partial solution treated plus natural ageing

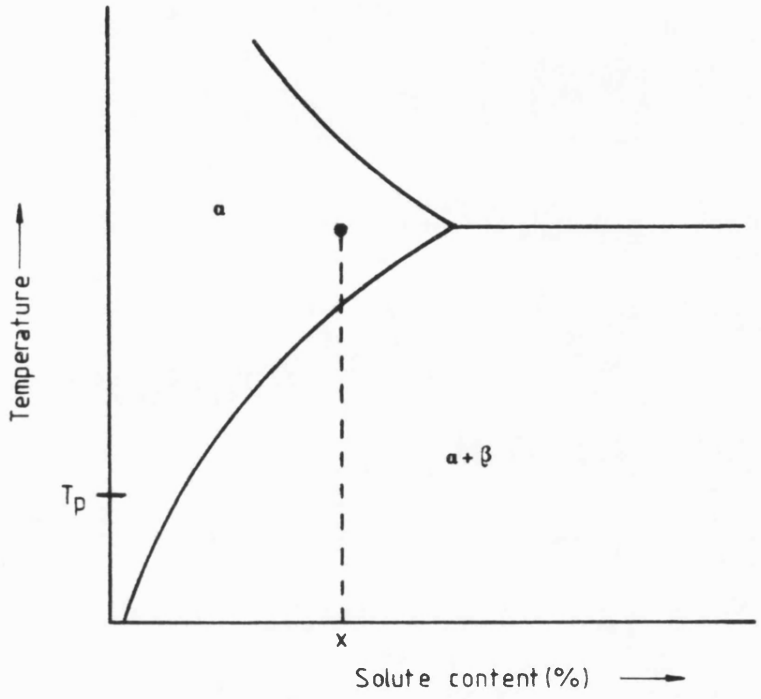

Figure 1.3 Schematic representation of the type of phase diagram generally required for precipitation hardening.

room temperature. On slow cooling the β-phase tends to be precipitated as fairly large agglomerates, mainly at grain boundaries. Hence, in order to precipitate a fine dispersion, the alloy is first quenched from the high temperature single-phase region. The alloy is now in the solution treated condition, and consists of a supersaturated solid solution of the α phase. Hardening is produced in the alloy by allowing the solute(s) to form a very fine dispersion of β-phase which then forms numerous obstacles to dislocation movement. "Ageing" of the alloy is usually carried out at (or slightly above) room temperature or, if the precipitation reaction then occurs too slowly at this temperature, by "tempering" the alloy at some slightly higher temperature (eg T_p in Figure 1.3).

In summary then, a typical precipitation-ageing treatment consists of:

(i) solution treatment at a relatively high temperature within a single phase region to dissolve the alloying elements.

(ii) rapid cooling or quenching to obtain a supersaturated solid solution (ssss) of these elements.

(iii) controlled decomposition of the SSSS to form a finely dispersed precipitate, usually by ageing for suitable times at one or more intermediate temperatures. It should be pointed out that the decomposition of a SSSS is usually a complex process which may involve several stages. Typically, solute-rich zones and metastable phases may be formed before the equilibrium phase is completely produced. With regard to the properties of an aged alloy, the size and shape of the precipitate particles, their nature (ie whether they are hard or soft), and the type of interface between a precipitate and its matrix will clearly have a great influence on its mechanical behaviour.

1.2.2 Metastable phases

The change in free energy, ΔG, on formation of a phase, β, from the supersaturated phase, α, may be represented by the expression:

$$\Delta G = - V\Delta G_V + A\gamma + V\varepsilon \qquad (1.1)$$

where ΔG_V is the volume free energy, V is the volume of the β phase, γ is the interfacial energy between β and α, A is the interfacial area and ε is the strain energy induced in the lattice of α by the formation of β. For a transition phase, β', ΔG_V is less negative and therefore

the most obvious means through which such a phase can achieve a rate of nucleation competitive with the equilibrium phase, β, is to have a smaller value of γ, the net interfacial free energy. Therefore, transition or metastable phases can only form if they achieve exceptionally good lattice matching with the matrix.

In many technologically important systems, a transition phase forms which is completely coherent with the matrix. A coherent interface arises when the two crystals match perfectly at the interface plane so that the two lattices are continuous across the interface, Figure 1.4a. This can only be achieved if, disregarding chemical species, the interfacial plane has the same atomic configuration in both phases, which requires the two crystals to be oriented relative to each other in a special way. However, it is possible to retain a coherent interface if this distance is not identical by straining one, or both, of the two lattices, as illustrated in Figure 1.4b. Such lattice distortions are known as coherency strains[4]. Such interfaces have very low interfacial energies.

As ageing continues, these coherent particles grow in size and tend to induce more strain in the matrix, thus increasing the strain energy term, ε, in equation (1.1) and reducing the effective driving force for the transformation. Therefore, a further transition phase may be formed which has a semi-coherent interface with the matrix. A semi-coherent interface may be defined as one in which the regions of misfit have the characteristics of dislocations lying in the interface, Figure 1.5. The disregistry between the two interfaces is periodically taken up by "misfit" dislocations. The disregistry, or misfit, δ, between the two lattices is defined by:

$$\delta = \frac{a_\beta - a_\alpha}{a_\alpha} \qquad (1.2)$$

where a_α and a_β are the lattice parameters of unstressed α and β respectively. Such an interface has a higher interfacial energy than a coherent interface but the associated strain energy is much less, and therefore its formation may be preferred to continued growth of the coherent phase.

Alternatively, a precipitate with an incoherent interface may be preferred. An incoherent interface is defined as having a very different atomic configuration in the two adjoining phases such that

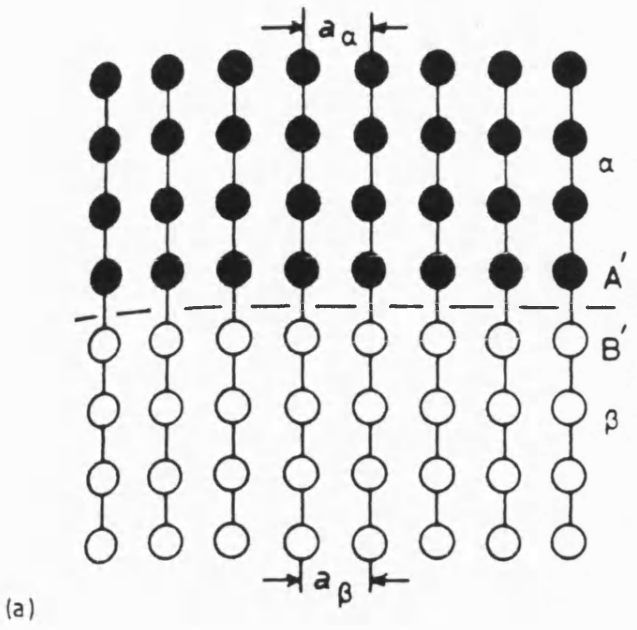

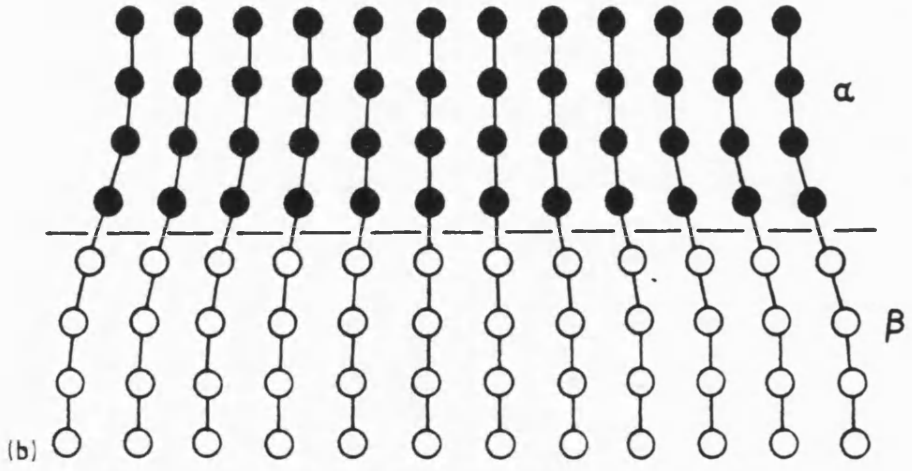

Figure 1.4 Atomic arrangement at coherent interfaces (schematic); (a) strain-free interface , (b) slight mismatch in adjoining lattices .

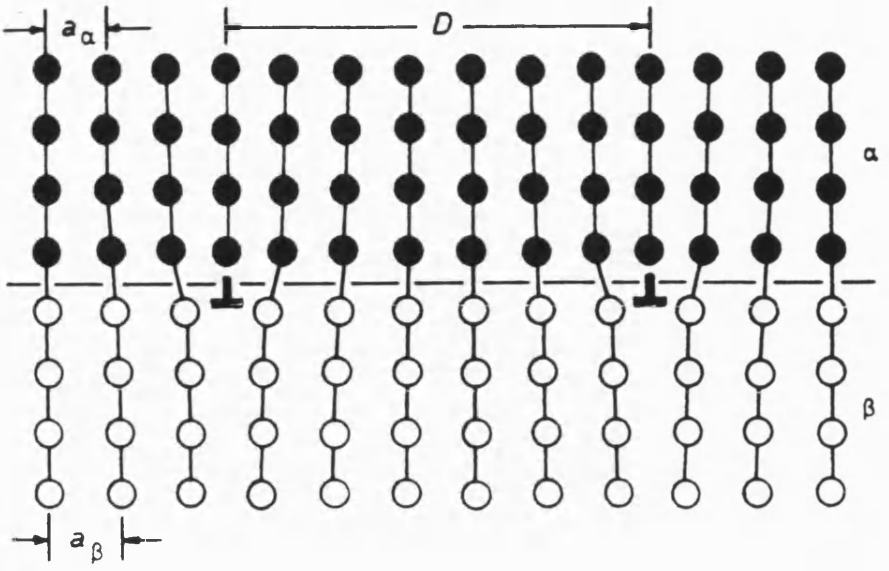

Figure 1.5 A semi-coherent interface.

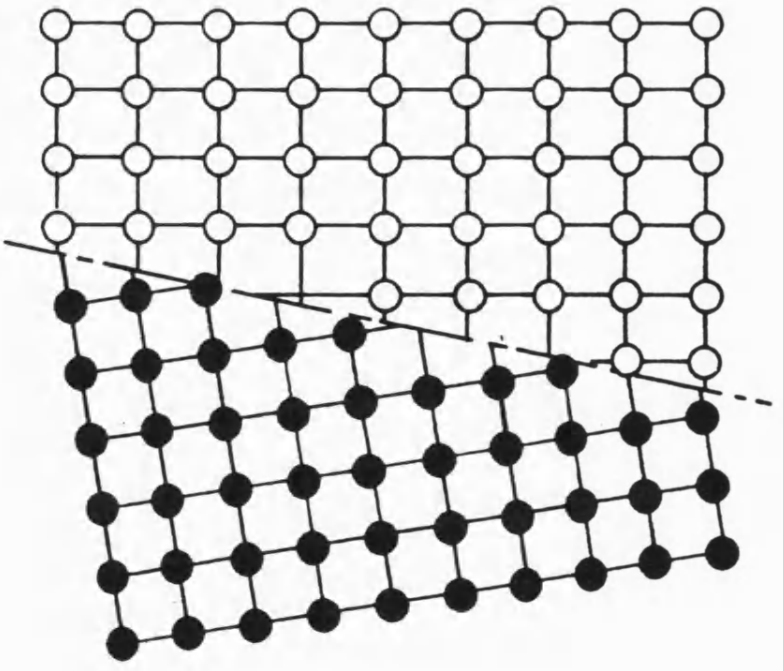

Figure 1.6 An incoherent interface.

there is no possibility of good matching across the interface. The pattern of atoms may be very different in the two phases or, if it is similar, the interatomic distances may differ by more than 25%[4]. An incoherent interface is illustrated in Figure 1.6. Generally, such interfaces result when two randomly-oriented crystals are joined across the interface. However, they may also exist between two crystals with an orientation relationship if the interface has a different structure in the two crystals. An incoherent interface generally has a higher interfacial energy than either a coherent or semi-coherent interface. However, incoherency is the situation where the strain energy is a minimum, and continued ageing will usually result in complete transformation to an incoherent phase. Such a phase is known as the equilibrium phase.

Thus, it is possible to represent a typical ageing sequence by:

SSSS → GP zones → intermediate precipitate → equilibrium precipitate

The zones which form are essentially solute-rich clusters contained within the solvent lattice, and are now termed Guinier-Preston (GP) zones after independent observations of solute clustering in aluminium-copper alloys by Guinier[5] and Preston[6]. These GP zones are ordered and may be only one or two atom planes in thickness. They retain the structure of the matrix and are coherent with it, although they usually produce appreciable elastic strains within the matrix. As these zones form the alloy usually becomes harder, chiefly as a result of the presence of coherency strains.

The intermediate precipitate is normally much larger in size than a GP zone and is only partly coherent with the lattice planes of the matrix. It has a definite composition and crystal structure which may differ only slightly from those of the equilibrium precipitate.

The final equilibrium phase forms at relatively high ageing temperatures and/or long times at lower ageing temperatures. Its formation involves complete loss of coherency with the parent lattice and, because it is coarsely dispersed, little hardening results from its formation. The maximum precipitation hardening effect usually occurs when there is a critical dispersion and/or intermediate precipitate present.

1.3 Nucleation and Growth of Precipitates

The precipitation-ageing process may be considered as occurring in three stages:

(i) nucleation of the new phase,

(ii) growth of the precipitates,

(iii) coarsening of the precipitate without change in its volume fraction.

In the early stages of decomposition, nuclei are randomly formed, some of which begin to grow due to local movement of solute atoms and reach a critical size. The nucleation stage is important in that it generally determines the shape and habit plane of the final precipitate. The formation of nuclei may be divided into homogeneous and heterogeneous nucleation.

1.3.1 Homogeneous nucleation

Homogeneous nucleation in solids occurs without benefit of pre-existing heterogeneities, such as dislocations, stacking faults etc. The classical thermodynamical treatment of Volmer and Weber[7] and Becker and Döring[8], although concerned with vapour to liquid and vapour to solid transformations, may be applied to nucleation in solids as follows.

Consider the homogeneous nucleation of an embryo of a phase β from the supersaturated phase α. The change in free energy, ΔG, is related to the sum of changes in volume free energy, ΔG_V, and the interfacial energy, γ, required to form the new surface (See section 1.2.2). When a new phase is formed in the solid there will be strain induced in the lattice of the parent phase. Thus, a strain energy term, ε, must be introduced, and since the creation of a volume, V, of β will cause a change in the volume free energy, the overall equation for the change in free energy becomes:

$$\Delta G = - V\Delta G_V + A\gamma + V\varepsilon \qquad (1.1)$$

where V is the volume of β and A is the interfacial area. Ignoring the variation of γ with interface orientation and assuming the nucleus is spherical, equation 1.1 becomes:

$$\Delta G = - \frac{4}{3} \pi r^3 (\Delta G_V - \varepsilon) + 4\pi r^2 \gamma \qquad (1.3)$$

The variation of ΔG as a function of r is shown in Figure 1.7. Similar curves would be obtained for any nucleus shape as a function of its size[4]. It should be noted that the effect of the strain energy term is to reduce the effective driving force of the transformation. Differentiation of equation 1.3 can give information on the critical free energy for nucleation, ΔG^*, and the critical radius for continued growth of an embryo, viz (spherical nuclei)

$$r^* = \frac{2\gamma}{(\Delta G_V - \varepsilon)} \tag{1.4}$$

and

$$\Delta G^* = \frac{16\pi\gamma^3}{3(\Delta G_V - \varepsilon)^2} \tag{1.5}$$

For $r < r^*$ the system can lower its free energy by dissolution of the β phase, whereas when $r > r^*$ the free energy is reduced if the nuclei grow. Unstable solid particles with $r < r^*$ are known as clusters or embryos while stable particles with $r > r^*$ are referred to as nuclei.

A steady-state nucleation rate, N_V, may be defined as the number of stable nuclei produced in unit time in unit volume of untransformed solid. According to Martin and Doherty[9]:

$$N_V \propto \exp(-\Delta G^*/kT) \tag{1.6}$$

The rate at which individual nuclei grow will be dependent also on the frequency with which atoms adjacent to the nucleus can join, and this is proportional to $\exp(-\Delta G_D/kT)$, where ΔG_D is the free energy of activation for diffusion. A simplified expression for the rate of nucleation of a precipitate is:[9]

$$N_V = K \exp \frac{-\{[Z\gamma^3/(\Delta G_V - \varepsilon)^2] + \Delta G_D\}}{kT} \tag{1.7}$$

where Z is a geometrical factor and K another constant.

One of the few equilibrium systems which decompose by homogeneous nucleation is that of copper-cobalt alloys. Servi and Turnbull[10] have studied the precipitation of the fcc cobalt from the fcc copper-cobalt alloys and found quantitative agreement between theory and experiment.

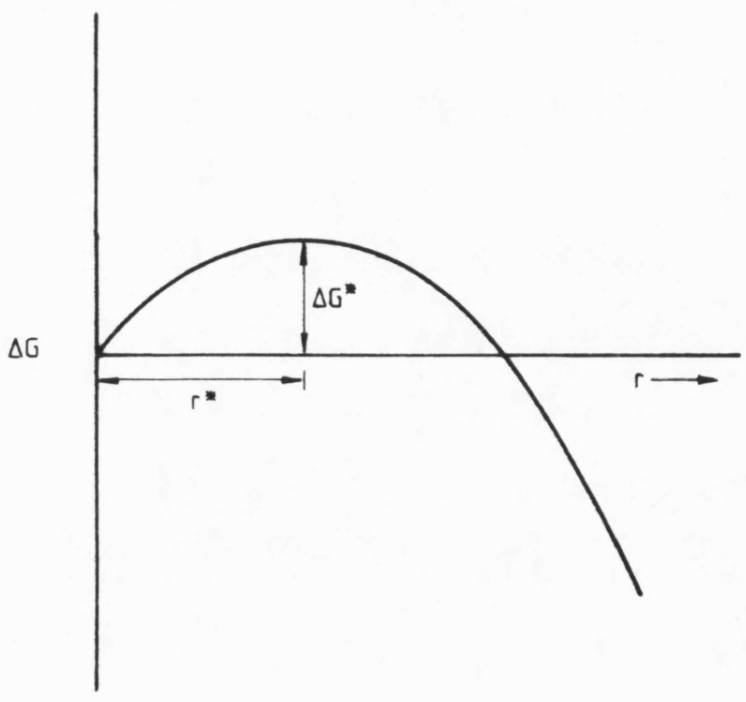

Figure 1.7 The variation of ΔG with radius, r, for a homogeneous nucleus.

1.3.2 Heterogeneous Nucleation

Heterogeneous nucleation is technologically more important in that nucleation in solids, as in liquids, is almost always heterogeneous. Structural defects such as dislocations or grain boundaries represent lattice regions of higher than average free energy[9] and when a nucleus forms there this energy is available to drive the reaction. Other suitable nucleation sites are stacking faults, inclusions and surfaces.

If the creation of a nucleus results in the destruction of a defect, the free energy released, ΔG_d, will reduce the activation energy barrier. The overall equation for the free energy change associated with nucleation at heterogeneities is then:

$$\Delta G_{het} = - V(\Delta G_V - \varepsilon) + A\gamma - \Delta G_d \qquad (1.8)$$

where ΔG_V, ε, and γ have the same meanings as in equation (1.1).

Considering the case of nucleation on a dislocation, in a supersaturated alloy the activation energy for precipitation is smaller at a dislocation since the lattice misfit of the precipitate can be partly or wholly accommodated by the dislocation. Cahn[11] has treated this problem for a cylindrical incoherent precipitate lying along a dislocation by assuming that the effect of nucleation on a dislocation is to reverse the value of the strain energy term, ε, in equation (1.8). The result is shown schematically in Figure 1.8 for different degrees of supersaturation (A < B). The minimum in curve A corresponds to a dislocation surrounded by a Cottrell atmosphere, and this state has been called a "preformed nucleus" by Dehlinger[12]. At higher supersaturations (curve B) there is no nucleation barrier to a diffusionless phase transformation, but if the reaction involves compositional changes, the rate of precipitation will be governed only by diffusion. Cahn also showed that, where a nucleation barrier still exists, the ratio of the activation energy, Q, for dislocation aided to homogeneous nucleation varies such that (for an edge dislocation):

$$\frac{Q_{dislocation}}{Q_{homogeneous}} = f\left(\frac{Gb^2.\Delta G_V}{2\pi^2\gamma^2(1-\nu)}\right) \qquad (1.9)$$

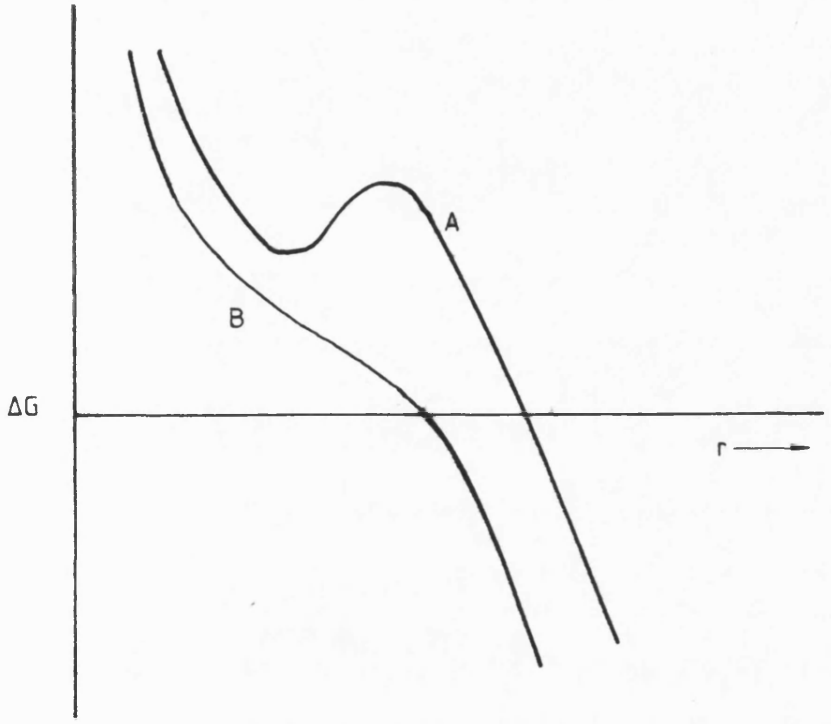

Figure 1.8 Schematic variation of ΔG with radius, r, for heterogeneous nucleation on a dislocation. (from Kelly and Nicholson[15].)

where b is the Burgers vector of the dislocation, γ is the surface energy of the precipitate-matrix interface and ν is Poisson's ratio. This is plotted in Figure 1.9, where α represents the right hand side of equation (1.9). This plot indicates that precipitation on dislocations becomes more important with increasing Burgers vector of the dislocation and with increasing supersaturation (ie larger ΔG_V). When $\alpha = 1$, $Q_{dislocation}$ becomes zero and there is no nucleation barrier to precipitation on dislocations.

Some of the predictions of Cahn's theory have been verified experimentally; for example, precipitation on dislocations increases with alloy content in Al-Zn-Mg alloys[13]. However, the Cahn model is too simplified to account for the observations that precipitation on dislocations is greater at higher ageing temperatures and lower supersaturations[13,14]. The reason is that the growth of precipitates must be considered as well as their nucleation. At low supersaturations, precipitates nucleated on dislocations grow rapidly drawing solute from adjacent regions before homogeneous nucleation starts. Therefore, precipitates on dislocations will be larger than the matrix precipitates and will surrounded by precipitate-free zones. At high supersaturations, nucleation on dislocations may be even more favourable, but homogeneous nucleation is now so copious that there is no chance for heterogeneously nucleated precipitates to grow larger than average. Kelly and Nicholson[15] therefore suggested that the influence of dislocations is greatest at moderate supersaturations.

Cahn's theory assumes that precipitates are always of the same type but this is frequently not the case in alloys where there is a sequence of precipitates. Dislocations do not appear to aid nucleation of coherent precipitates[15] and, typically, the microstructure, in such alloys consists of GP zones in the matrix and an intermediate precipitate on the dislocations. In such a case the precipitates on dislocations will tend to grow at the expense of the matrix precipitates.

Nucleation on stacking faults may also be of importance in precipitation hardening systems. Suzuki[16] has pointed out that the equilibrium concentration of solute at a stacking fault is different from that in the matrix due to the change in crystal structure. Solute segregation at a stacking fault can lead to precipitation if the crystal structure of the fault is similar to the structure of the precipitate.

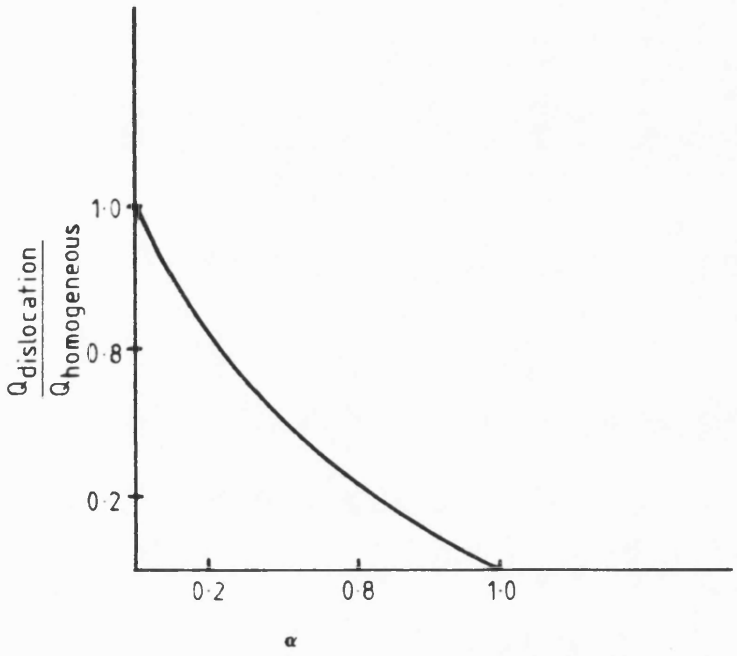

Figure 1.9 Variation in the ratio of activation energies for heterogeneous and homogeneous nucleation of a precipitate as a function of the parameter α

On the other hand a new precipitate structure may be stable at a stacking fault although it cannot be nucleated in the matrix. Heidenreich[17], working on deformed Pb-Ag alloys, was the first to observe precipitation on stacking faults. In these alloys the equilibrium precipitate is fcc, but x-ray diffraction was used to shown an anomolous cph phase was formed when the deformed material was aged. Heidenreich suggested that the thin layer of cph structure present at narrow stacking faults in the fcc Pb matrix was the nucleation site for the hexagonal precipitate. Nucleation at stacking faults has also been observed in Al-Ag alloys[18].

1.3.3 Growth of precipitates

Whether precipitation occurs by homogeneous or heterogeneous nucleation, continued "ageing" results in the growth of the precipitates. The successful critical nuclei are those with the smallest nucleation barrier, as described earlier. In the absence of strain energy effects the precipitate shape satisfying this criterion is that which minimizes the total interfacial energy, γ. Thus, nuclei will usually be bounded by a combination of coherent or semi-coherent facets and smoothly curved interfaces[4]. The growth of precipitates will depend on many factors, but in systems such as precipitation hardening alloys growth is dependent on diffusion of solute to the precipitate for continued growth. The subject of phase transformations in metal systems, including diffusional growth processes, has been reviewed by Christian[19] and is covered in many standard test books (see, for example, Burke[20]).

There is consensus that analysis of growth rates is a complex problem, the usual practice being to assume that the rate of growth is determined by one or possibly two factors. The diffusional growth of a phase in a two-component system, such as the growth of precipitates from supersaturated solid solutions, is considered to be the result of transfer of atoms across an interface and the redistribution of the solute since the growing phase usually has a different composition from the parent phase. The rate of growth in such cases depends upon the rate at which atoms are brought to, or removed from, the interface by diffusion and the rate at which they cross the interface. Thus, we may consider these two limiting cases, ie growth limited by diffusion and growth limited by the interface reaction.

1.3.3.1 Interface-controlled growth

The interface reaction controls the process during the early stages of growth since there is a limited area of interface and the distance over which diffusion is necessary tends to zero. Burke[20] has considered this case where the diffusion of the solute is very much faster than transfer of atoms across the interface. He assumed that the composition of the solution remained uniform throughout and derived the following growth rate equation for interface-controlled growth:

$$\dot{R}(t) = \frac{\Psi_o}{(C_\beta - C_E)} [(C_I - C_E)(1-y)] \qquad (1.10)$$

where Ψ_o is a constant, C_β is the solute concentration in the precipitate, C_E is the solute concentration in the solution in equilibrium with the precipitate, C_I is the initial concentration in the solution, and y is the fraction of solute actually precipitated at time,t. Equation 1.10 predicts that the rate of growth decreases continuously during precipitation. At small times when $(1-y) \approx 1$ the rate of growth is constant whilst at later stages the growth rate decreases. The complete solution of equation 1.10, however, can only be derived in terms of the overall kinetics of nucleation and growth.

Growth in systems where there is good atomic fit between the matrix and precipitate is now considered to proceed by a ledge mechanism. For example, consider the growth of a plate-like precipitate, Figure 1.10(a). Aaronson and co-workers[21,22] have suggested that the good-fit interface is much less mobile than the rim, so that the precipitate thickens more slowly than by diffusion control. The less-mobile interface is shown in Figure 1.10(a). The thickening of this plate-like precipitate is then a process of lateral movement of linear ledges of constant spacing, λ, and height, h, Figure 1.10(b). The half-thickness of the plate should increase at a rate given by $v = \frac{uh}{\lambda}$, where u is the rate of lateral migration[4]. Laird and Aaronson[23], in studies on the thickening of γ-phase plates in an Al-Ag alloy aged at 400°C, Figure 1.11, indicate that the nucleation of ledges is the rate-controlling factor since the thickening rate is not constant. Similarly, the fact that there is no perceptible increase in thickness except when ledges pass is strong evidence for the immobility of semicoherent interfaces. Measurements on

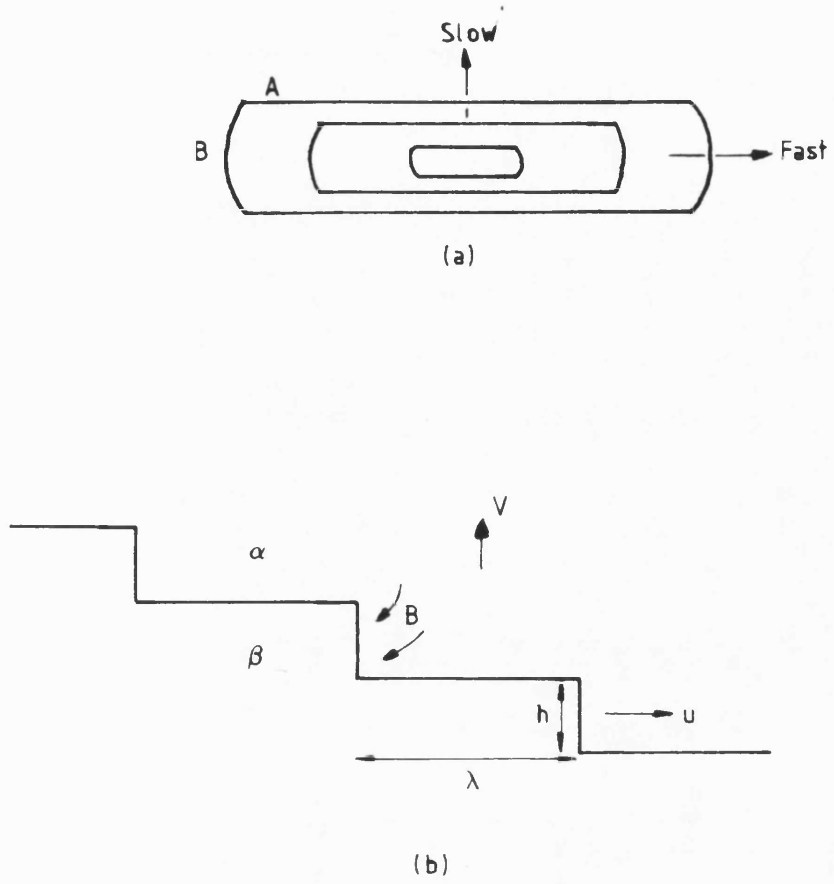

Figure 1.10 Growth of a plate-like precipitate
(a) semi-coherent (slow) and incoherent (fast) interfaces.

(b) thickening by the ledge mechanism.

[from Porter and Easterling [4]]

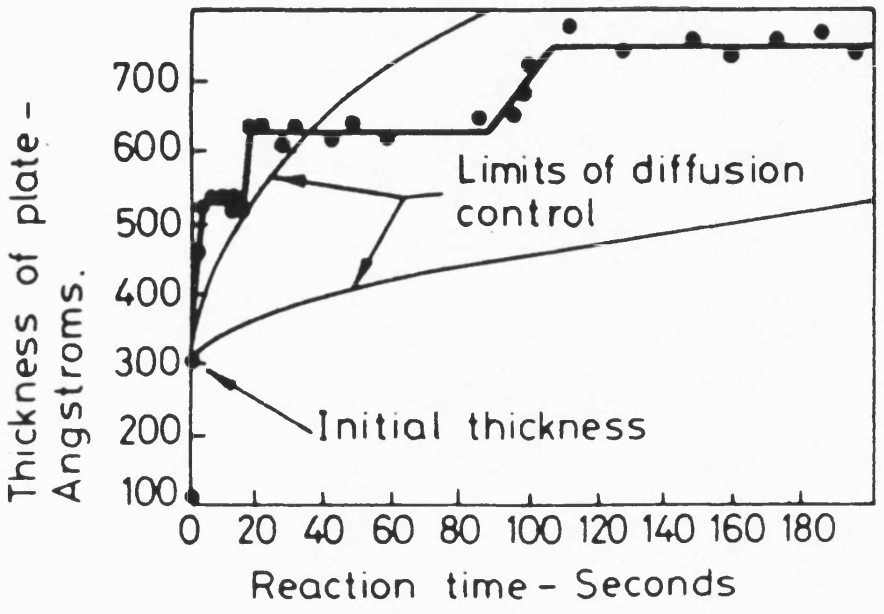

Figure 1.11 Thickening of γ plates in an Al-Ag alloy (from Laird and Aaronson [23]).

precipitates in other systems suggest that even within the same system the thickness/time relationship can vary greatly from plate to plate[4].

1.3.3.2 Diffusion-controlled growth

As particle size increases diffusion-controlled growth becomes more important since the diffusional flux gets progressively slower due to solute removal reducing the concentration gradient (the driving force for diffusion), whilst the flux across the interface increases due to the increase in area.

Burke[20] has considered the diffusion-controlled growth of an isolated spherical particle, radius R and solute concentration C_β, growing in an infinitely large, homogeneous supersaturated solid solution of initial composition C_I. He assumed that the rate of removal of atoms from the solution at the interface was very much faster than the rate at which atoms arrived at the interface. Thus the concentration in solution at the interface was maintained at the equilibrium value C_E, which was regarded as independent of precipitate size. These concentration conditions are shown schematically in Figure 1.12. The growth rate equation for such conditions is given by:

$$R\frac{dR}{dt} = D\left(\frac{C(t)-C_E}{C_\beta-C_E}\right) \qquad (1.11)$$

where C(t) is the concentration of time,t. However, in general precipitation occurs at a number of particles each of which draws solute from the solution. This competition leads to a continuous decrease in the matrix composition from C_I and thus the rate of growth of each particle also decreases. Zener and Wert[24] have considered this aspect and arrive at an equation for the rate of growth for one set of competing particles such that:

$$R\frac{dR}{dt} = D\left(\frac{C_I-C_E}{C_\beta-C_E}\right)(1-y) \qquad (1.12)$$

where $(1-y) = \left(\frac{C(t)-C_E}{C_I-C_E}\right)$. This equation can only be solved when y is known as a function of time. At small time $(1-y) \cong 1$ and R^2 is proportional to time and the volume to $t^{3/2}$. Ham[25] has fully justified this treatment for low supersaturations.

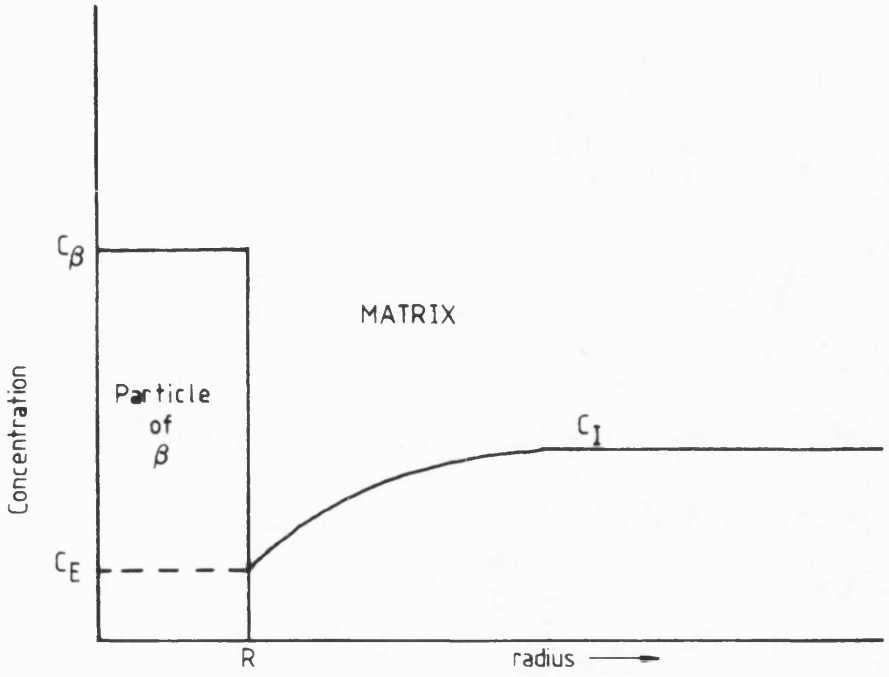

Figure 1.12 Concentration of solute in and around a growing particle under diffusion-controlled conditions. (from Burke[20])

For heavily supersaturated solutions, Zener[26] has suggested that solute depletion is confined to a comparatively thin shell surrounding the growing particles and assumed that concentration gradient can be regarded as linear. The rate of growth under such conditions is given by:

$$R\frac{dR}{dt} = D \cdot \frac{(C_I - C_E)}{\dfrac{[2^{\frac{1}{3}}(C_\beta - \frac{1}{2}C_E - \frac{1}{2}C_I)^{\frac{1}{3}} - 1]}{(C_I - C_E)^{\frac{1}{3}}}} \cdot \frac{1}{(C_\beta - C_E)} \qquad (1.13)$$

1.3.33 Growth dependent upon both diffusion and interface processes

When diffusion and the interface reaction are of comparable rates, the concentration of solute in solution at the interface is maintained at a value between C_E and the average value in the solution c(t). The actual value represents a balance between the rate at which atoms arrive at the interface and the rate at which they are removed.

For an array of particles, the growth rate is:

$$\frac{dR}{dt} = \frac{\Psi_o D(C_I - C_E)}{(\Psi_o . R + D)(C_\beta - C_E)} \cdot (1-y) \qquad (1.14)$$

which can be solved only if y is known as a function of time. During the early stages of a reaction, when y is small, depletion of the matrix is negligible and (1-t) is also negligible. Therefore, when R is small the radius is approximately proportional to t, ie the growth is interface-controlled. At large sizes the growth law is characteristic of diffusion limited growth since the squared term dominates.

1.3.34 Overall transformation kinetics

The progress of an isothermal phase transformation can be conveniently represented by plotting the fraction transformed (f) as a function of time and temperature, ie in a TTT diagram as shown in Figure 1.13(a). For example, for a transformation of the type α-β, f is the volume fraction of precipitate, β, at any time, Figure 1.13(b).

Many factors contribute to variation of f(t,T) such as the nucleation rate, the growth rate, the density and distribution of nucleation sites, and the impingement of adjacent transformed volumes. For example, the effect of continuing nucleation is to increase the

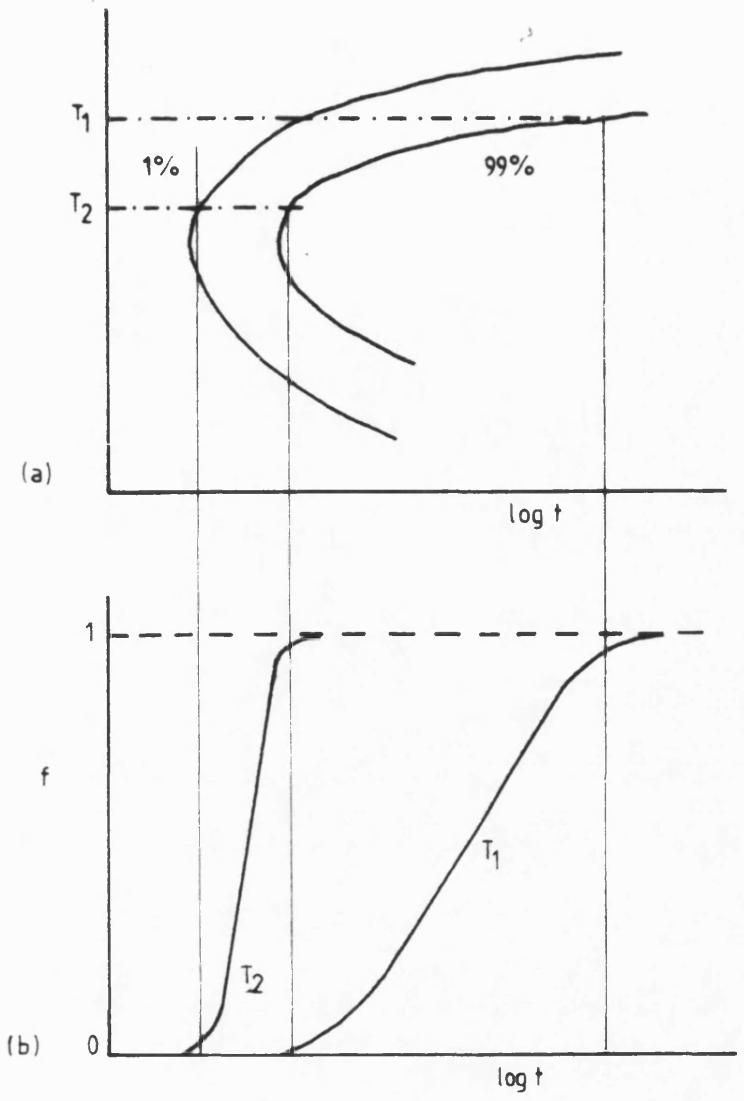

Figure 1.13 Schematic representation of the percentage transformation versus time for different transformation temperatures ($T_2 > T_1$).
(a) TTT diagram
(b) Volume fraction, f, versus time

slope of the sigmoidal rate curve, Figure 1.13(b), by an amount which depends on the form of the variation of the nucleation rate, I, with time, t[27]. In general, depending on the assumptions made regarding nucleation a variety of equations can be obtained of the form:

$$f = 1 - \exp(-kt^n) \qquad (1.15)$$

This is known as an Avrami equation where the numerical exponent, n, can vary from $\sim$ 1 to 4. Provided there is no change in the nucleation mechanism, n is independent of temperature whilst k depends on the nucleation and growth rates and is, therefore, very sensitive to temperature.

1.3.3.5 Particle coarsening (Ostwald ripening)

The microstructure of two-phase alloys is always unstable if the total interfacial energy is not at a minimum. Therefore, a high density of small precipitates will tend to develop into a lower density of larger particles with a lower total interfacial energy.

In any precipitation-hardened specimen there will be a range of particle sizes due to differences in the time of nucleation and rate of growth. Consider the case of two adjacent spherical precipitates with different diameters, Figure 1.14(a). The solute concentration in the matrix adjacent to a particle will increase as the radius of curvature decreases, according to the Gibbs-Thomson effect[9]. This is illustrated in Figure 1.14(b), a schematic free energy diagram. Constructing common tangents to the matrix curve shows that the solubility of the small particles $C_{\alpha(S)}$ is larger than that of larger particles. In a system containing mixed sizes, concentration gradients exist in the matrix which promotes diffusion of solute from regions around small particles to those adjacent to large particles onto which it is precipitated. The removal of solute from the solution near to small particles causes the latter to dissolve.

Greenwood[28] has reviewed the theory of particle coarsening and the extent to which they can be substantiated by experimental results. The variation of particle growth rate with radius, r, in this review is given by:

$$\frac{dr}{dt} = \frac{2DS\gamma\Omega}{kTr} \cdot \left(\frac{1}{\bar{r}} - \frac{1}{r}\right) \qquad (1.16)$$

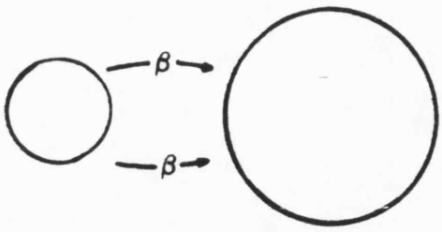

(a)

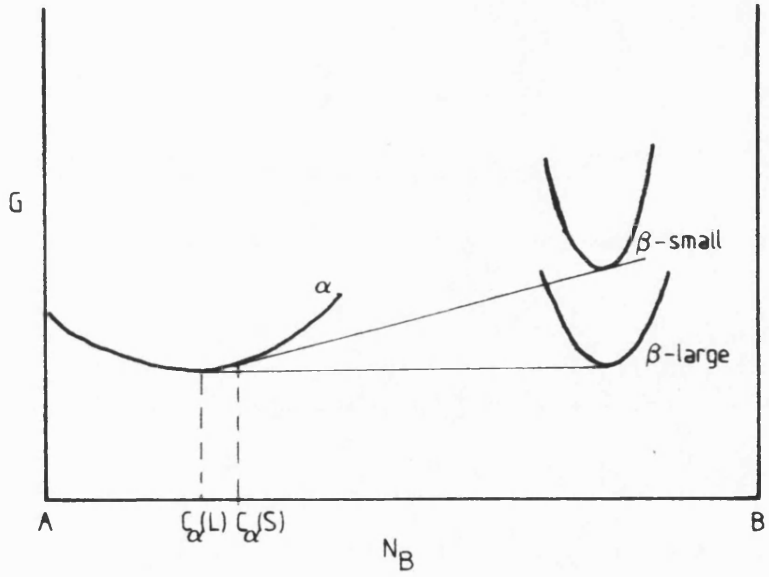

(b)

Figure 1.14 Schematic illustration of particle coarsening
(a) movement of solute, β
(b) solute concentration in α increases as the radius of curvature of particle decreases.

where D is the solute diffusion coefficient, S is the solubility of a particle of infinite radius, Ω is the atomic volume of the particle, γ is the interfacial energy and k is Boltzmann's constant. This variation is shown pictorially in Figure 1.15 for two values of r. Particles of radius equal to the mean radius, $\bar{r}$, are at that instant of time neither growing nor dissolving. Particles of radius $< \bar{r}$ are dissolving at increasing rates with decreasing value of r. All particles of radius $> \bar{r}$ are growing but the graph shows a maximum value for the growth rate that corresponds to the particle which is twice the mean radius. Precipitates $> 2\bar{r}$ will grow slowly and will tend to be caught up by the particles whose radius $r \approx 2\bar{r}$. The consequence of this is that no particles larger than $2\bar{r}$ would be expected after some precipitate coarsening has occurred.

Lifshitz and Slyozov[29] and, independently, Wagner[30] have studied the complicated problem of diffusion-controlled coarsening. For an initially narrow Gaussian distribution of precipitate sizes a steady-distribution of sizes was found when the size distribution was plotted as a function of the reduced radius $(r/\bar{r})$. This had a cut-off at $r/\bar{r} = 1.5$.

The coarsening rate when this steady-state distribution has been achieved, ie for times that are long, is given by:

$$\bar{r}^3 = \frac{8DS\gamma\Omega t}{9kT} \qquad (1.17)$$

A similar situation is apparent for interface-controlled growth/coarsening, and Greenwood[28] gave an approximate relationship between mean particle radius and time under such conditions:

$$\bar{r}^2 = \frac{64CS\gamma\Omega t}{81kT} \qquad (1.18)$$

where C is a constant.

Experimental confirmation of the Lifshitz-Wagner theory of particle coarsening has been reviewed by Greenwood[28]. The most detailed information available is on the coarsening of Ni_3Al (γ') precipitates in the Ni-Al system[32,33]. The results confirmed that growth of γ' follows a cube law relationship, ie diffusion of solute is the limiting process, and that there was a quasi-stationary particle size distribution and a marked cut-off in the distribution curve. Although the cut-off tended to be a larger value than the predicted $1.5\bar{r}$, Greenwood[28] concluded that the form of the curve was roughly similar to that given by the Lifshitz-Wagner theory. Similarly, growth of manganese precipitates in a

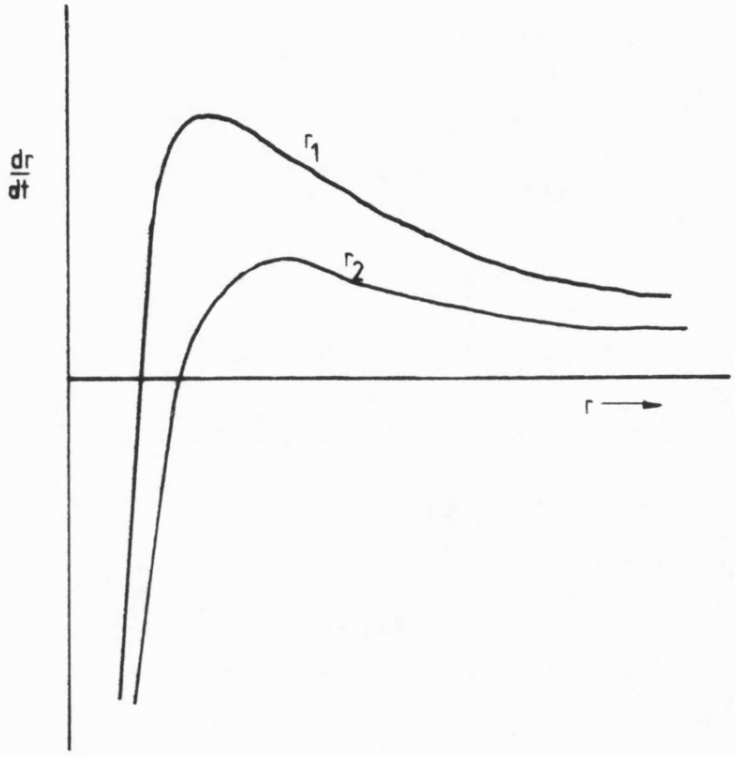

Figure 1.15 Schematic illustration of the variation in growth rate with mean particle radius, $\bar{r}$, for two values of $\bar{r}$ ($r_2 > r_1$)

magnesium-manganese alloy have also been shown[33] to follow a cube law relationship, although again, statistical analysis of size distributions indicated a cut-off $>1.5\bar{r}$. Other systems investigated include Fe_3Si precipitates in α-iron[34,35] and θ" and θ' platelet precipitates in the Al-Cu (-Cd) system[36]. In both cases the power law expected for diffusion-controlled coarsening was observed. For the Al-Cu system, Boyd and Nicholson[36] found, however, that the distribution of precipitates did not fit the Lifshitz-Wagner theory at all, maximum values of $r/\bar{r}$ being about 2.8 for θ' and 2.0 for θ" rather than the expected value of ~ 1.5. However, it must be pointed out that the coarsening rate for these precipitates was much faster than the predictions by the theory[9].

With regard to interface-controlled growth, only two cases have so far been reported. Schwarz and Ralph[37] have studied the coarsening of the very fine precipitates of V_4C_3, a few nanometers in size, which form on the moving phase boundary between α- and γ-iron. Using field ion microscopy they found an r^2 relationship, in good agreement with the interface-controlled kinetic theory. Similarly, Youle et al[38] observed the r^2 kinetics of interface control for the coarsening of fine gold precipitates in an iron-gold alloy quenched and aged in the conventional way. Again, field ion microscopy was used on the small precipitates (1-40 nm).

According to Martin and Doherty[9] the results indicating diffusion control, ie no interfacial barrier to growth, conflicted with the hypothesis put forward by Aaronson[21,22] to account for the morphologies of non-spherical Widmanstätten precipitates. Aaronson suggested that coherent or semi-coherent interfaces were less mobile than incoherent ones so that the rates of migration varied for different parts of the precipitate-matrix interface, particularly if they have different crystal structures as in α-Fe/γ-Fe. Interestingly, the review by Greenwood[27] noted that precipitates of various shapes which were coherent, partially coherent or incoherent, all indicated that r^3 was proportional to coarsening time, in accord with diffusion-controlled growth. Nicholson[39] first pointed out this conflict between coarsening results and Aaronson's hypothesis and suggested that Widmanstätten structures may be related via interfacial energy to the equilibrium shapes.

Two general conclusions from this work may, however, be made. Firstly, the theories have been in general very successful and secondly,

the rate-controlling step has been identified as the diffusion of solute through the lattice for the majority of systems investigated. Hence it should be possible to design precipitate microstructures which are relatively resistant to coarsening by adopting low values of interfacial energy, solubility and diffusion coefficient.

1.4 Strengthening methods in alloy systems

As mentioned previously, the strengthening associated with many aluminium alloy systems is due to a fine dispersion of particles, either formed in the ingot manufacture, as in the non-heat treatable alloys, or formed at a later stage by solution treating and then "ageing" at a lower temperature to create a fine dispersion of precipitates. The different proposed strengthening mechanisms will be reviewed here.

1.4.1 Solid solution hardening

The introduction of solute atoms into solid-solution in the solvent-atom lattice invariably produces an alloy which is stronger than the pure metal. Whether the solute occupies interstitial or substitutional sites in the solvent, the yield stress and the level of the stress-strain curve is usually raised as a whole, Figure 1.16. Solute atoms fall into two broad categories[40] with respect to their relative strengthening effect. Generally, interstitial atoms have a relative strengthening effect per unit concentration of about three times their shear modulus, whilst for substitutional atoms the effect is $\sim G/10$.

As yet no unified theory exists for solid solution hardening, although various factors have been studied in certain systems. The most important factors affecting solution strengthening are:

(a) Elastic distortion of the lattice due to the different size of solute and solvent atoms. A size factor parameter, ε_a, is given by

$$\varepsilon_a = \frac{1}{\underline{a}} \left(\frac{da}{dc}\right)$$

where $\underline{a}$ is the interatomic spacing of the alloy and c is the atomic concentration of the solute.

(b) Relative modulus factor: $\varepsilon'_G = \varepsilon_G/(1 - \varepsilon_G/2)$ where $\varepsilon_G = \frac{1}{G}\left(\frac{dG}{dc}\right)$ and G is the shear modulus of the alloy. Fleischer[41] has shown that the rate of change of shear stress with atomic

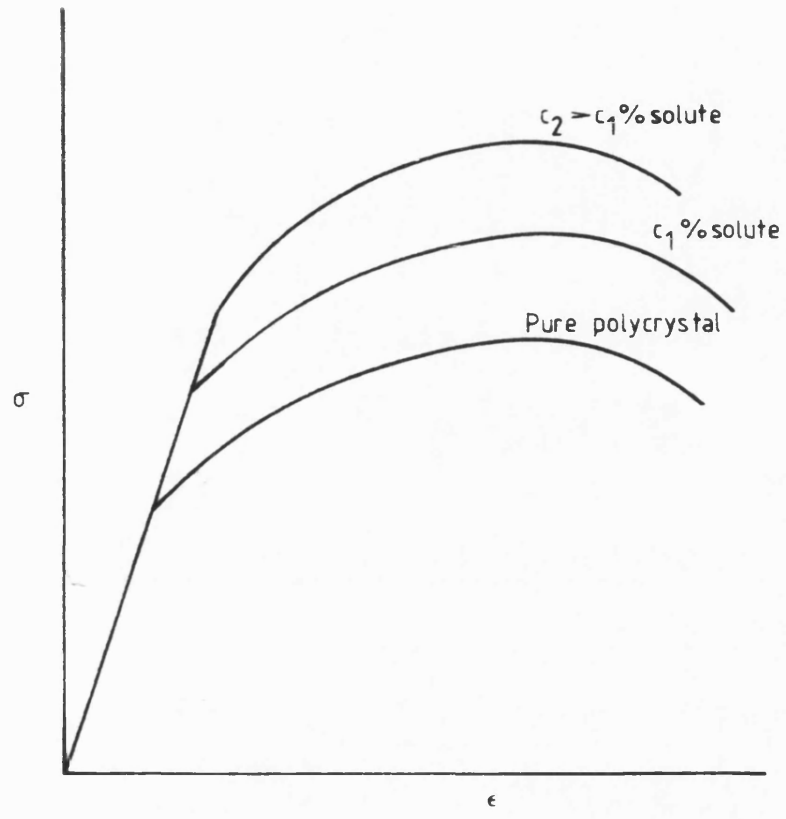

Figure 1.16 Effect of solute alloy additions on the stress - strain curve (schematic)

concentration of solute plots linearly against $\varepsilon'_G - 3\varepsilon_a$ for a large number of dilute solid solutions of copper.

(c) Chemical interaction (Suzuki interaction). The dissociation of dislocations in close packed crystals into partial dislocations affects the periodic arrangement of the lattice. In a fcc crystal the faulted regions have cph stacking. Suzuki[42] observed that there will be an interaction between the extended dislocation and the solute atoms since the change in free energy with solute concentration will not be the same in the matrix and the faulted regions.

These and other factors can contribute to the resistance to dislocation motion. In a random solid solution there will be no net force on the dislocation provided that the dislocation remains straight[43] since the algebraic sum of all interaction energies will tend to zero. Mott and Nabarro[43] pointed out, however, that the dislocation lines are generally not straight but flexible so that the entire line can take up lower energy positions by bending around regions of high interaction energy. These two cases are illustrated in Figure 1.17. For dilute solid solutions the yield stress according to the Mott and Nabarro theory is given by:

$$\tau \approx 2G\varepsilon C \qquad (1.19)$$

where G is the shear modulus of the matrix, ε is the misfit parameter and C is the atomic concentration of solute. A more rigorous analysis reveals that the flow stress, τ can be expressed as:

$$\tau = 2.5G\varepsilon^{4/3}C \qquad (1.20)$$

However, according to Dieter[44] equation (1.20) predicts values for the flow stress which are too large, although many studies have shown that the flow stress is linear with solute concentration for very dilute solutions. Nowadays, equation (1.19) is generally used for evaluation of the yield stress of a solid solution.

1.4.2 Dislocation cutting of precipitates

The theories of yield stress due to particle shear generally assume that the precipitates are either coherent or semi-coherent with the matrix. The work done by the applied stress in forcing the dislocations through the precipitate may then govern the flow stress. Kelly and Fine[45] have suggested that this is the case in Al-Cu and

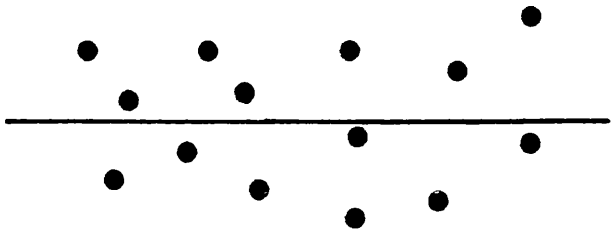

(a)

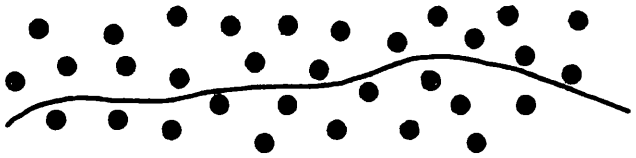

(b)

Figure 1.17 Dislocation lines in a random solid solution
(a) straight.
(b) flexible.

Al-Ag alloys containing GP zones where they found that yield stress in these alloys was insufficient to enable dislocations to expand between the particles (see section 1.4.3). A schematic illustration of particle shear is shown in Figure 1.18.

According to Kelly and Fine[45] the yield stress, τ, of an alloy containing GP zones is given by:

$$\tau = \frac{\gamma f^{\frac{1}{2}}}{b} \qquad (1.21)$$

where f is the volume fraction of precipitate and γ is the energy required to shear the precipitate a distance b (the Burger's vector). This theory predicts that an increase in either f or γ should increase the yield, and has been used to explain the maximum strength developed in Al-Cu alloys[45].

Kelly and Nicholson[15] showed that a type of "chemical hardening" would arise when a dislocation shears through a particle, creating a step of width, b, on either side of the particle. Since this process increases the surface area of the particle, work must be done to shear the particle. The strengthening increment due to this work was given by:

$$\Delta\tau = \frac{2\sqrt{6}}{\pi} \cdot \frac{f\gamma_s}{r} \qquad (1.22)$$

where γ_s is the energy of the particle-matrix interface and r is the radius of the precipitate. Kelly and Nicholson also pointed out that many fine second-phase particles are intermetallic compounds which have ordered structures, and when shearing occurred a new interface will be produced within the particle. They suggested that the <u>extra</u> increment in hardening is given by:

$$\Delta\tau = \frac{2f\gamma_p}{b} \qquad (1.23)$$

where γ_p is the energy for disordering the particle structure. If both principles apply then the strengthening increment is given by:

$$\Delta\tau = \frac{2f\gamma_p}{b} + \frac{2\sqrt{6}}{\pi} \frac{f\gamma_s}{r} \qquad (1.24)$$

However, Kelly and Nicholson also pointed out that if γ_p is much greater than γ_s then the flow stress will be independent of particle size and hence only equation (1.23) will apply, which is independent of particle shape. Similarly, if the particles are not ordered internally

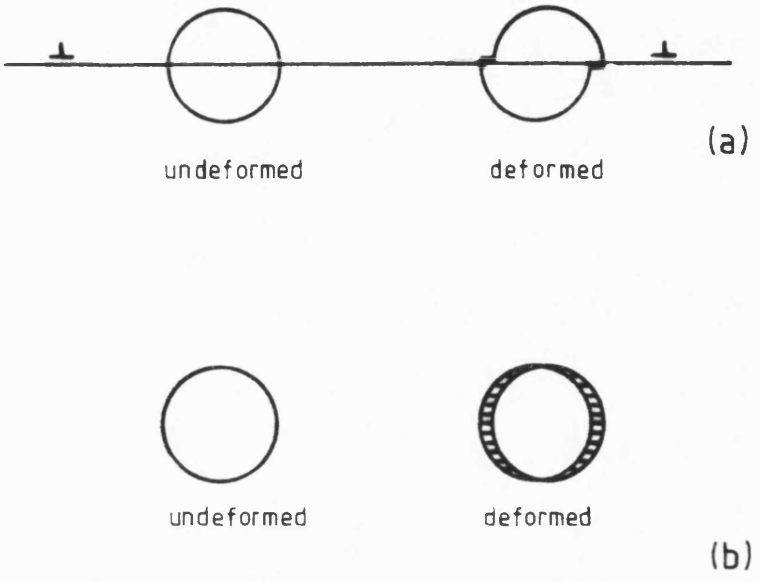

Figure 1.18 Dislocation cutting of a precipitate;
(a) view in the slip plane normal to the Burgers vector of the dislocation,
(b) view normal to the slip plane.
[from Kelly and Nicholson[15]]

then γ_p is zero and only equation (1.22) applies. They concluded that these estimates can only be used if the particle radius is large compared with the Burger's vector of the dislocation.

Kelly and Nicholson[15] have provided an alternative estimate of the stress necessary to move the dislocations through the particles; by equating the work done on the crystal by the applied stress with the work done in creating a new interface as the dislocation cuts a precipitate they found that, for spherical precipitates:

$$\tau = \frac{\gamma f^{\frac{1}{2}}}{\alpha b} \qquad (1.25)$$

where f is volume fraction of precipitate, b is the Burger's vector and α is a constant ≈ 1.1. The term γ, however, includes both the energy of the additional precipitate-matrix interface produced and the energy of the dislocations produced at the interface. Similarly, if the particle is internally ordered it includes, in addition, the energy of the interface produced inside the precipitate due to the change in chemical species of the nearest neighbours of atoms above and below the slip plane.

1.4.3 Dislocation bowing around precipitates

Eventually, a stage may be reached during ageing the precipitate structure where the dislocations find ways of moving around the particles. For the case of overaged incoherent precipitates, Orowan[46] proposed the mechanism illustrated in Figure 1.19. The yield stress is determined by the shear stress required to bow a dislocation line between two particles separated by a distance λ. At stage II in Figure 1.19 the dislocation line is beginning to bend, and at stage III it has reached the critical curvature. The dislocation can then move forward without further decreasing its radius of curvature. The stress required to force the dislocation between the obstacles is given by:

$$\tau_o = \frac{Gb}{\lambda} \qquad (1.26)$$

where G is the shear modulus of the matrix and b is the Burger's vector of the dislocation. Since the segments of dislocation that meet on either side of the particle are of opposite sign, they can annihilate each other over part of their length, leaving a dislocation loop around each particle (stage IV). The original dislocation is then free to move on (stage V).

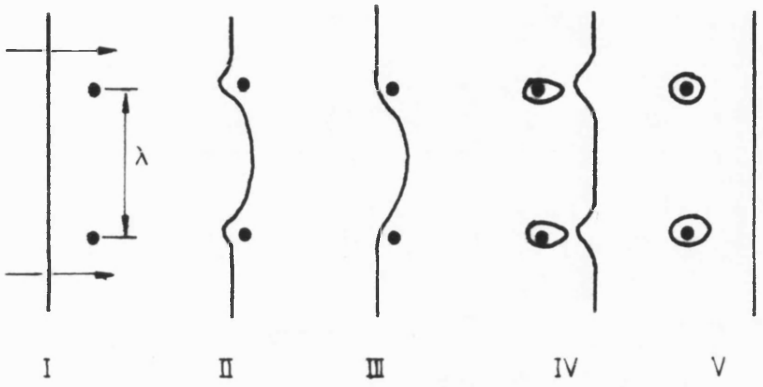

Figure 1.19 Schematic illustration of the Orowan process of dislocation bowing between particles.

The basic Orowan equation (eg 1.26) has been modified by introducing more refined estimates of the dislocation line tension[15], by using the planar spacing γ_p, for the mean free path[47], and by adding a correction for the interaction between dislocation segments on either side of the particle[48]. These have led to a number of versions based on equation (1.26), of which the most common is the Orowan-Ashby equation[49].

$$\Delta\tau = \frac{0.13Gb}{\gamma} \ln \frac{r}{b} \qquad (1.27)$$

where r is the radius of the particles.

1.4.4 Other proposed strengthening mechanisms

Although the theories of dislocation cutting of a precipitate and dislocation bowing between precipitates have been observed in many systems, other strengthening mechanisms have been proposed.

Mott and Nabarro[50] recognized that the strain field resulting from the mismatch between a particle and the matrix would be a source of strengthening, the increment in strengthening, $\Delta\tau$, being given by:

$$\Delta\tau \approx 2G\varepsilon f \qquad (1.28)$$

where f is the volume fraction of precipitate and ε is the measure of the strain field produced. Gerold and Haberkorn[51] have given a more sophisticated estimate of the strengthening due to coherency strains, such that

$$\Delta\tau = \frac{6G(rf)^{\frac{1}{2}}}{b} \varepsilon^{3/2} \qquad (1.29)$$

where r is the radius of the precipitates.

Stacking-fault strengthening has also been considered whereby the energy of an extended dislocation is decreased if the energy of the stacking-fault formed between its component partial dislocations is reduced. Hirsch and Kelly[52] have suggested that such an effect may influence the yield stress of an alloy containing coherent precipitates of lower stacking-fault energy than the matrix. Under such conditions the dislocation will be attracted to the particle and therefore the dislocation must be dragged out of the particles with a local stress given approximately by[9]:

$$\Delta\tau' \approx \frac{\Delta\gamma}{b} \qquad (1.30)$$

where $\Delta\gamma = \gamma_{Sfm} - \gamma_{Sfp}$, and γ_{Sfm} and γ_{Sfp} are the stacking-fault energies of the matrix and precipitate respectively. According to Martin[9], this leads to a variation of τ with r, the radius such that:

$$\tau \alpha r^{\frac{1}{2}} g^{\frac{1}{2}} \qquad (1.31)$$

Modulus hardening is another proposed mechanism. Here the energy of a dislocation is considered as a function of the shear modulus of the lattice in which the strain field of the dislocation exists. Therefore, a change in energy will be associated with a dislocation interacting with a particle whose Shear Modulus differs from that of the matrix. Kelly[53] quotes a complex equation for τ due to Knowles and Kelly, but essentially the variation τ with r is given by equation (1.31).

Ansell and Lenel[54] have developed a theory of yielding in dispersion - hardened alloys based upon the idea that particles must be fractured in order to cause gross plastic yielding, the fracture being produced by stress concentrations due to dislocation pile-ups at the particles. The shear stress needed to cause either shear or fracture of the dispersed phase particle is in general proportional to a shear modulus, G', of the particle, and is taken as G'/C, where C is a constant of proportionality approximately equal to 30. Ansell and Lenel predicted that the yield stress of a dispersion-hardened material should obey the relationship:

$$\tau = \tau_M + \frac{G'}{4C} \frac{f^{\frac{1}{3}}}{(0.82 - f^{\frac{1}{3}})} \qquad (1.32)$$

where τ_M is the yield stress of the matrix without a dispersion and f is volume fraction of the dispersed phase.

1.4.5 The variation of yield stress with ageing time

In conclusion, it must be noted that although two main types of hardening mechanism have been described - that involving alloys containing small coherent particles (say $\leq$15 nm in diameter) and that concerning larger non-coherent particles well separated from each other - an alloy is likely to exhibit intermediate behaviour as its microstructure changes during ageing.

Kelly and Nicholson[15] have summarised the change of yield stress with ageing time for a quenched alloy, and this is illustrated schematically in Figure 1.20. In the early stages of ageing (full curve in Figure 1.20), dislocations are forced through the particles, and the work done depends on many factors, such as coherency stresses around the precipitate etc. The dotted curve represents the situation when Orowan bowing becomes operative, ie when dislocations can be forced between the particles; now a further increase in inter-particle spacing (due to particle coarsening as the alloy is over-aged) leads to a decrease in strength since the yield stress is inversely proportional to the spacing. However, as Martin[55] has suggested, when an alloy is heat-treated by a precipitation process to maximum hardness at ordinary temperatures, the particle-cutting mechanism is controlling yield strength.

1.5 The aluminium-copper binary system

The aluminium-copper binary system includes some of the most widely studied of all precipitation hardening alloys and much data have been published concerning the characterisation of microstructures in relation to their properties. This work will be reviewed in the following sections.

1.5.1 Precipitation hardening behaviour

As mentioned in section 1.2, the basic requirement for an alloy to respond to age-hardening treatments is a decrease in solid solubility of one, or more, of the alloying elements with decrease in temperature, as shown in the binary phase diagram, Figure 1.21. As regards the alloying element copper, its maximum solid solubility in aluminium is 5.65 wt% at 548°C, decreasing to less than 0.02 wt% at room temperature. Thus, if an alloy containing up to $\sim$ 5 wt% copper is solution treated within the single phase region (α) and quenched, then ageing of an intermediate temperature (say, 20-400°C) will cause precipitates to form with an attendant increase in alloy strength. Ageing temperatures for commercial aluminium-copper alloys range from 100 to 200°C.

Typical hardening curves for aluminium-copper alloys are illustrated in Figure 1.22. Figure 1.22, taken from the work of Gayler and Parkhouse[56] shows the effect of an increase in ageing temperatures on the form of the hardening curve. In all cases a two-stage hardening curve was observed, with peak hardness decreasing as ageing temperature was increased. A single hardening peak would be expected if

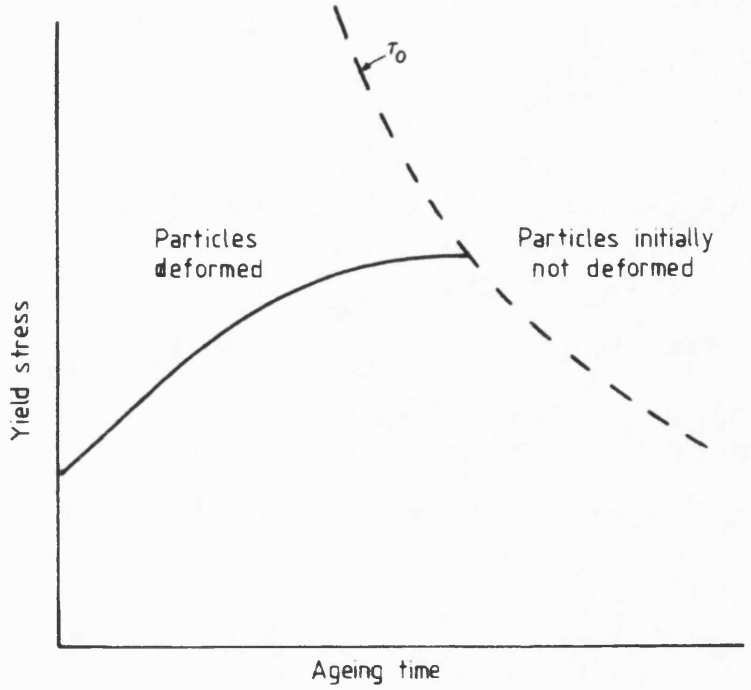

Figure 1.20 Variation of yield stress with ageing time for a typical age-hardening alloy (from Kelly and Nicholson[15])

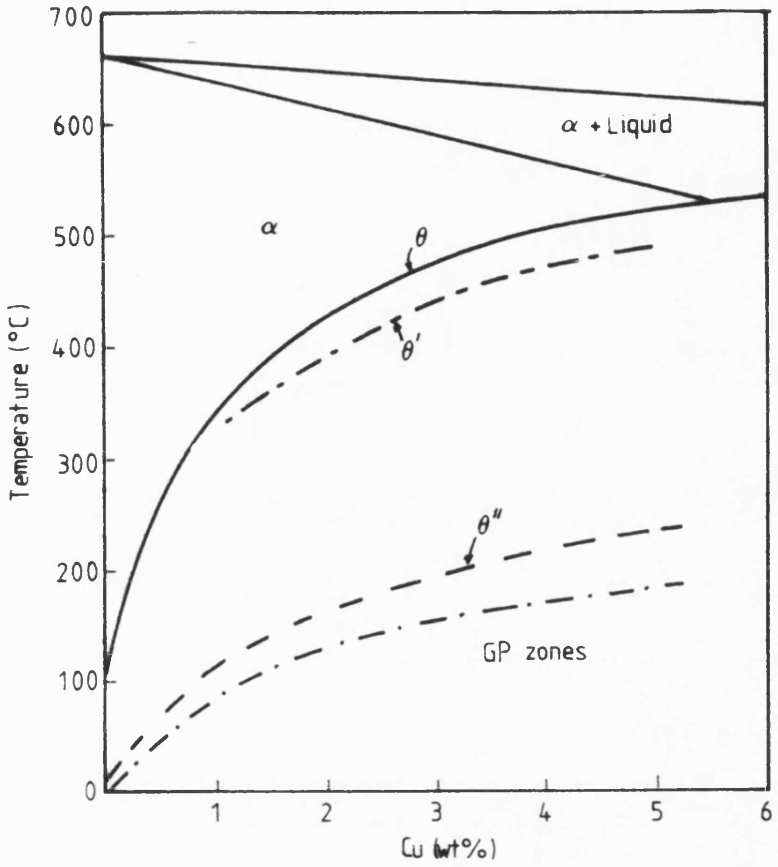

Figure 1.21 Al-Cu phase diagram showing the metastable GP zone, θ'', and θ' solvuses (from Lorimer[68])

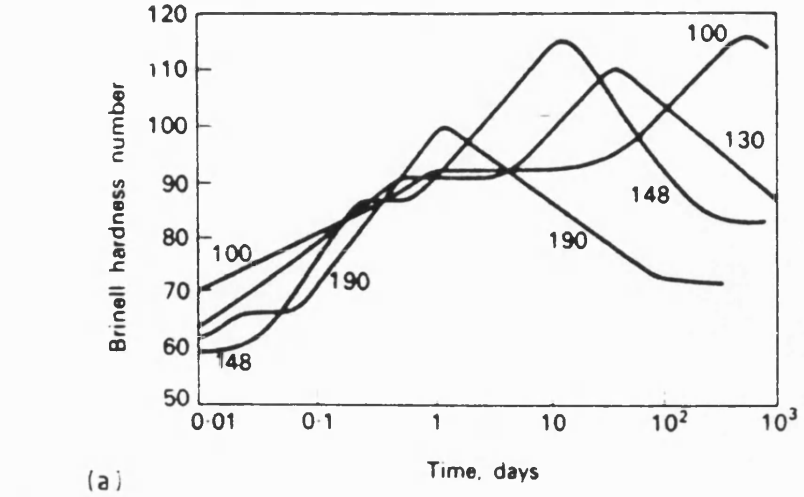

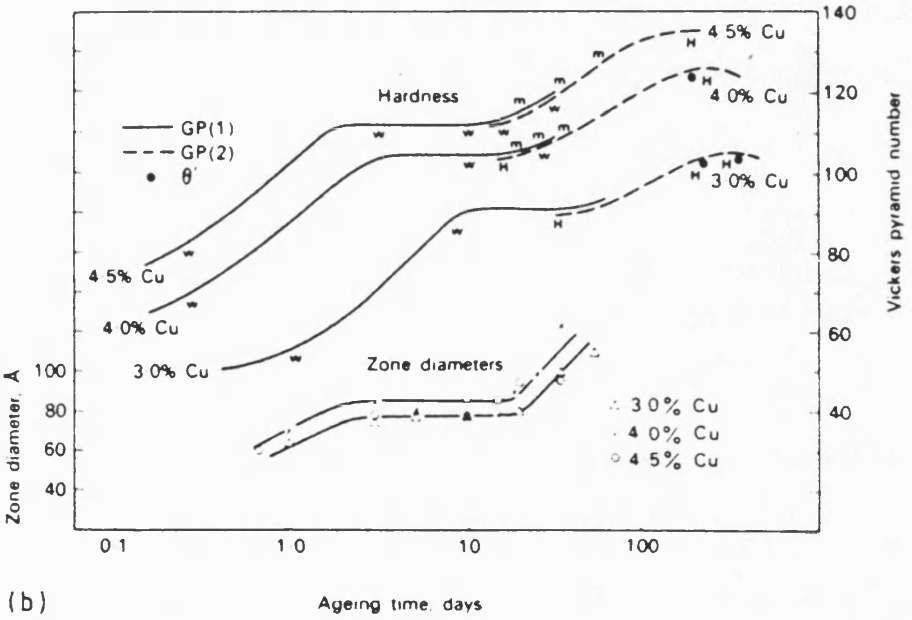

Figure 1.22 Effect of temperature and solute content on precipitation hardening behaviour in binary Al-Cu alloys; (a) Effect of ageing temperature (from Gayler and Parkhouse [56]) , (b) effect of increasing Cu content (After Silcock et al [57]).

precipitation took place by simple nucleation and growth of an equilibrium phase from solid solution but such changes are found only at low supersaturations and high ageing temperatures[55]. At higher supersaturations and lower ageing temperatures an alloy may show two or more age-hardening peaks. Silcock, Heal and Hardy[57] found this to be the case for differing degrees of supersaturation, Figure 1.22(b). An Al-2 wt% Cu alloy showed a single hardness peak because of the low supersaturation of solute, whereas alloys containing $\sim$ 4.0 wt% copper exhibited two-stage hardening curves, with a plateau region between the two "peaks". The hardness begins to fall with increase in ageing time because the precipitates are coarsening and the average interparticle spacing is increasing accordingly.

1.5.2 Microstructure

Extensive microstructural studies have been made on the Al-Cu binary system, using both X-ray and electron diffraction, and it is now established that precipitation hardening of such alloys involves the formation of a number of intermediate, or metastable, precipitates prior to the formation of the equilibrium phase, θ ($CuAl_2$). This sequence may be expressed in the form:

$$\text{GP zones} \rightarrow \theta'' \rightarrow \theta' \rightarrow \theta\ (CuAl_2)$$

The GP zones, so called after independent observations of solute clustering in aluminium-copper alloys by Guinier[5] and Preston[6], are essentially copper-rich clusters in the aluminium lattice. They are fully coherent with the matrix and therefore have a very low interfacial energy. They form on {100} aluminium matrix planes as discs since this is a condition in which they can minimize their strain energy by forming perpendicular to the elastically soft <100> directions in the face-centred cubic matrix. Gerold[58] developed the arguments of Guinier[5] and Preston[6] and proposed that the GP zones consisted of a single disc of copper atoms, Figure 1.23. Nicholson and Nutting[59] have observed GP zones in an Al-1.7 wt% Cu aged at low temperatures and found them to be $\sim$ 0.3-0.6 nm wide with diameters up to $\sim$ 8 nm, in a good agreement with the X-ray results of Guinier[60,61] and Gerold[58].

As ageing continues the phase θ'' forms as fully coherent platelike precipitates on $\{001\}_{Al}$ lattice planes with the following orientation relationship:

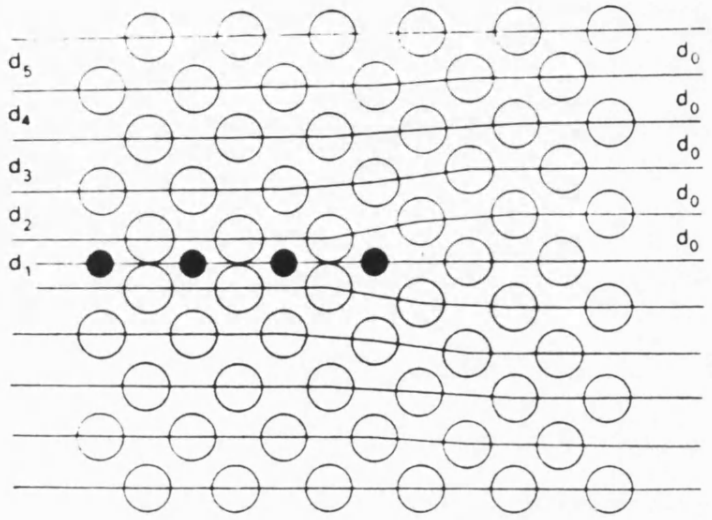

Figure 1.23 Structure of a GP zone according to Gerold [58].

$$(001)_{\theta''} \| (001)_{Al}$$

$$[001]_{\theta''} \| [100]_{Al}$$

The θ" phase has a face-centred tetragonal structure with a = b = 0.404 nm and c = 0.768 nm and the atomic arrangement is shown in Figure 1.24(a). It was first detected by Guinier[60] and called GP(2) zones by Silcock et al[57] but Nicholson et al[15] suggested the symbol θ" would be more appropriate since the phase has a definite crystal structure, not a simple perturbation of the matrix structure, as in the case of GP zones. Hardy[62] observed two-stage hardening behaviour in Al-3.5/4.5 wt% Cu alloys aged at 110°C and 130°C, a result consistent with the sequential formation of two distinct phases. Yoshida et al[63] have reported that weak-beam images of θ" were qualitatively similar to those obtained from GP zones but that they were consistently wider. This supports the model of Gerold[58] for θ": two layers of copper atoms separated by three layers of aluminium atoms. θ" is homogeneously distributed, and direct quenching experiments[64] have indicated that GP zones play a role in its nucleation. θ" precipitates are detectable by virtue of the coherency-strain fields caused by the misfit with the aluminium perpendicular to the θ" platelets. The distortion of the matrix lattice near a coherent θ" precipitate is illustrated in Figure 1.24(b), the dotted line indicates the approximate extent of the strain field[15]. As the peak hardness is approached the microstructure of Al-Cu alloys consists of a high density of θ" precipitates with strain fields stretching from one precipitate to another.

Further ageing results in the formation of the θ' phase, which is tetragonal (a = b = 0.404 nm, c = 0.58 nm), has an approximate composition of $CuAl_2$ and the same orientation relationship with the matrix as θ". The atomic arrangement is shown in Figure 1.25(a). Initially θ' was thought to nucleate on θ" but Thomas and Nutting[65] showed that helical dislocations in the quenched alloy act as preferential nucleation sites for θ' precipitates. Nicholson[66,67] used electron microscopy to study the actual nucleation process and found that only certain θ' orientations are present in each array of precipitates at these helical dislocations, confirming earlier suggestions[14,68]. The initial dispersion of θ' is highly heterogeneous and reflects the dislocation distribution in the as-quenched alloys. According to Lorimer[69] as ageing proceeds bands of θ' form on the initial lines of precipitates that nucleated on dislocations and these bands expand as

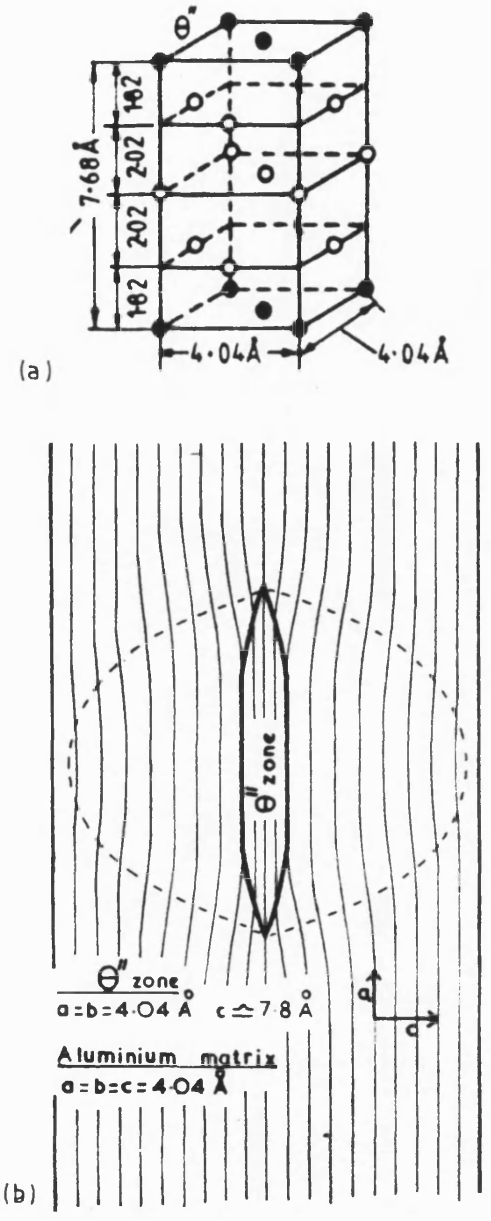

Figure 1.24 (a) Atomic arrangement in θ"(○=Al ,●=Cu).
(b) Distortion of the aluminium lattice due to θ"(from Kelly and Nicholson [15]).

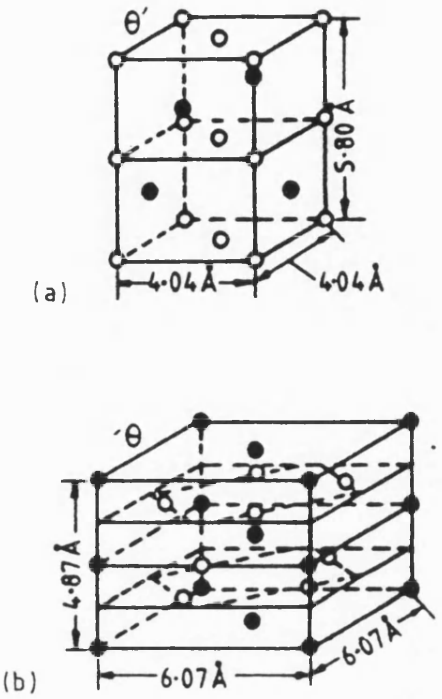

Figure 1.25 (a) Atomic structure in a θ′ precipitate,
(b) Atomic structure in a θ precipitate .
(o = Al, ● = Cu)

ageing progresses until a moderately uniform distribution of θ' has formed throughout a grain. This process is independent of the presence of GP zones or θ'. For typical ageing conditions, Cahn[11] has calculated that dislocation nucleation is 10^{78} faster than homogeneous nucleation.

The equilibrium phase, θ, is body-centred tetragonal with a = 0.6066 nm and c = 0.4874 nm, see Figure 1.25(b). It has the approximate composition $CuAl_2$ and is incoherent with the aluminium matrix. Nucleation of θ takes place heterogeneously at either θ'/matrix interfaces[4], or at grain boundaries[70].

It should be noted that the full structural sequence of GP zones and transition precipitates will be observed only when the alloy is aged at a temperature below the GP zone solvus (see Figure 1.2). For example, if ageing is carried out at a temperature above the θ" solvus but below the θ' solvus, the first precipitate formed will be θ', heterogeneously nucleated on dislocations. If ageing is carried out above the θ' solvus, the only possible precipitate is θ which nucleates and grows at grain boundaries. Also, if an alloy containing GP zones is heated above the GP zones solvus the zones will dissolve, an effect known as reversion.

1.5.3 Effect of additional elements on microstructure and precipitation-hardening behaviour of Al-Cu alloys

It is well known that small additions of elements may modify the nucleation of precipitates and significantly effect the structure and properties of age-hardening alloys. Mechanisms by which trace additions may modify precipitate nucleation have been reviewed by Polmear[71]. Changes in nucleation can arise for a number of reasons including:

(a) preferential interaction with vacancies which reduces the rate of nucleation of GP zones;

(b) raising the GP zone solvus which alters the temperature ranges over which phases are stable;

(c) stimulating the nucleation of an existing precipitate by reducing the interfacial energy between precipitate and matrix;

(d) promoting the formation of a different precipitate.

Although trace element effects have been widely studied only limited progress has been made in establishing rules governing their behaviour. In some cases the trace element effect appears unique to a

particular alloy system whereas in others the same trace element may stimulate further precipitate nucleation in several systems.

With regard to the Al-Cu binary system, the effect of trace elements (0.01 to 0.1 at%) is reviewed and this is followed by a discussion of the effects of minor alloying additions (up to 1 at%).

1.5.3.1 Effect of trace elements (<0.1 at%)

The effect of the presence of trace elements in aluminium alloys has been extensively studied by Hardy and co-workers[72-74] from which it was concluded[73] that the so-called normal precipitation sequence in an alloy may be crucially dependent on trace elements at the impurity level.

Additions of cadmium, indium, tin, magnesium and silver reduce, or inhibit, GP zone formation[71]. Indeed, minor additions of cadmium, tin or indium almost completely suppress the GP zone in the ageing sequence. Silcock[75] and Kimura and Hasiguti[76] suggest that the trace elements might trap excess vacancies and thereby reduce the rate of zone formation since GP zone formation depends on vacancy-aided diffusion of copper atoms. They tested the theory by measuring the resistivity change after an Al-1 at%Cu-0.006 at%Sn alloy, finding that it was much slower than for the pure binary alloy. They concluded, therefore, that the majority of vacancies were bound to tin atoms leading to a reduced rate of diffusion of copper atoms to form GP zones.

Trace element additions also increase the nucleation rate of θ' in Al-Cu alloys. Silcock, Heal and Hardy[77] have investigated the effect of indium addition to an Al-Cu alloy using X-ray diffraction. They confirmed that the formation of GP zones and θ" were virtually suppressed and found that the precipitation of θ' was accompanied by the appearance of some anomolous diffraction effects which were not related to the θ' or aluminium diffraction spots. The diffraction effects were attributed to a new interface structure formed between θ' and the matrix structures by the absorption of trace elements. Cadmium and tin show similar effects. The consequence of these trace element additions is the dense precipitation of θ' and significantly higher strength properties compared to the binary Al-Cu alloys[78]. Silver, on the other hand, has little or no effect on θ' precipitation.

Combinations of elements may also modify θ' precipitation. Brook and Hatt[79] showed that joint additions of magnesium plus silicon

and, more particularly, magnesium plus germanium slow down the rate of coarsening of θ' on prolonged ageing.

1.5.3.2 Effect of minor additions (<1 at%)

Many binary alloys contain, either adventitiously or by design, a small quantity (eg 0.5 - 1.0 wt%) for a third element. This element may be precipitated as coarse particles of an intermetallic compound insoluble at the homogenization temperature, in which case it will have little effect on the precipitation properties of the alloys. Alternatively, minor additions of elements may change the precipitation sequence by altering the solubility of the principal alloying element or by promoting the formation of some precipitate specific to the ternary alloy.

A number of investigations have been made on the effect of minor additions to the Al-Cu system. Fink et al[90] considered additions of up to 1 wt% of the elements silicon, manganese, iron and magnesium to Al-4 wt%Cu alloys. They found that up to 0.5 wt% of silicon had little effect on the age-hardening behaviour, confirming measurements made by Fraenkl[81] and Gayler[82]. Similarly, up to 0.5 wt% manganese had little effect, but amounts greater than this reduced the extent of ageing. All additions of iron were found to decrease the age-hardening potential of the binary alloy. This is, perhaps, not surprising since iron and copper form a compound with aluminium, Cu_2AlFe_7, which is insoluble at the solution treatment temperatures used for homogenisation of aluminium alloys[83]. It must be pointed out that these early investigations were somewhat hampered by the lack of electron microscopy for a detailed structural analysis into the causes and effects of such minor elemental additions.

Mondolfo[84] quoted several references which all suggested that additions of up to 1 wt% zinc had no appreciable effect on the age-hardening behaviour of Al-Cu binary alloys. However, Arkharov and Magat[84] suggested that zinc may retard ageing in the early stage, although tending to accelerate the breakdown of the Al-Cu solid solution in later stages.

Reported effects of silver additions are similar to those for zinc. Modest improvements in properties were observed when small amounts of silver are added, although corrosion resistance was lowered[84]. The phases θ" and θ' formed on ageing with the same

orientation relationship between the matrix and precipitates as quoted for the binary alloy[86,87]. Khatonova and Zakharova[85] suggested that the rate of formation of GP zones and θ" was slower, with smaller and more numerous zones than in the binary alloy. However, it must be noted that their alloy contained 7 wt% silver and competitive precipitation might have been playing an important role since they also observed spherical GP zones and disc-shaped γ' precipitates on {111} aluminium matrix planes, as found in the binary Al-Ag system[15].

With the exception of iron, which forms a compound with copper which is insoluble at solution treatment temperatures, small additions of elements such as Si, Mn, Zn and Ag are generally reported as having little effect on the precipitation hardening behaviour of Al-Cu binary alloys. The effects of small additions of magnesium will be reviewed in the following sections.

1.6 The Al-Cu-Mg ternary system

The effect of different amounts of magnesium (up to 4 wt%) to Al-Cu alloys have been extensively studied since the first discovery of precipitation hardening by Wilm in 1906[2]. Such alloys have wide industrial uses and are known as the "Duralumin" family of alloys.

Early studies by Archer[88], Petrov[89], Fink et al[80] and Gayler[90] all agreed that additions of magnesium to an Al-Cu binary alloy increase the rate of ageing and also increase the degree of hardening, compared with the binary alloy. However, these workers disagreed on the role of magnesium. Archer[89] suggested that additions of magnesium expand the aluminium-rich solid solution, thereby allowing faster diffusion and hence more rapid precipitation of $CuAl_2$. Petrov[89] proposed that when magnesium is present in al Al-Cu alloy, a complex compound $Al_5Cu_2Mg_2$ precipitates during room temperature ageing. Fink et al[80] believed that precipitation of the β' phase (present in Al-Mg binary alloys) was the cause of increased hardening. More recently Entwistle et al[91] have shown that small additions (<0.05 at%) of magnesium have little effect on the precipitation hardening behaviour, whilst concentrations of magnesium above 0.1 at% accelerate the hardness increase observed on ageing.

It is now established[84] that in alloys with a ratio of Cu:Mg greater 8:1 (wt%) the main hardening agent is the precipitation of $CuAl_2$, ie the ageing sequence follows that for the Al-Cu binary system. For Cu:Mg ratios in the range 8:1 to 4:1 both $CuAl_2$ and $CuMgAl_2$ type precipitates are produced upon ageing. For ratios greater than 4:1 the hardening is due entirely to precipitation of the phase $CuMgAl_2$[84].

A section of the ternary Al-Cu-Mg phase diagram at 460°C and 190°C according to Polmear[1] is shown in Figure 1.26. Alloys with Cu:Mg ratios greater than 4:1 generally lie within the α-s pseudo-binary portion of the phase diagram at 190°C. The S phase was shown by Perlitz and Westgren[92] to have the composition Al_2CuMg and to face-centred orthorhombic ('C' face centre) with a = 0.400 nm, b = 0.023 nm and c = 0.714 nm. On ageing supersaturated solutions of these alloys the sequence of precipitates is similar to that for the binary alloy, ie

$$SSSS \rightarrow GP(B) \text{ zones} \rightarrow S' \rightarrow S\ (Al_2CuMg)$$

Silcock[93] has suggested that the GP zones are probably copper-rich and based on the intermetallic compound $Mg_2Al_5Cu_5$. X-ray diffraction data indicated that these zones could be approximately indexed as a face-centred tetragonal cell with a = b = 0.55 nm and c = 0.404 nm. Silcock suggested that the zones are needle-shaped of length 4-8 nm and diameter 1-2 nm. However, Gerold and Haberkorn[94] considered that the structure consisted of small spherical zones (∿ 1-2 nm diameter) containing ordered Mg and Cu planes parallel to {100} aluminium lattice planes.

Continued ageing results in the formation of the S' phase, which is orthorhombic with a = 0.404 nm, b = 0.925 nm and c = 0.718 nm. Silcock[93] and Bagaryatskiĭ[95] have shown that the orientation relationship of S' with the aluminium matrix is:

$$[100]_{S'} \parallel [100]_{Al}, [010]_{S'} \parallel [021]_{Al}, [001]_{S'} \parallel [01\bar{2}]_{Al}$$

The S' precipitates grow as laths on {210} aluminium matrix planes, with growth in <100> directions[96], and are semi-coherent. They nucleate heterogeneously upon dislocation loops and helices formed during the quench[97], and as they grow in size, small lattice strains are produced in the matrix[96].

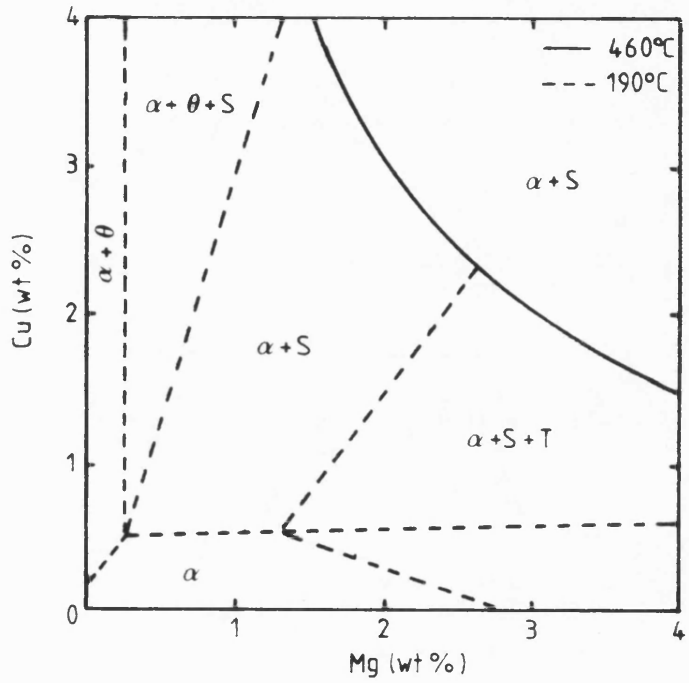

Figure 1.26 Section of the Al-Cu-Mg phase diagram at 460°C and 190°C (from Polmear[1]).

Polmear[1] has noted that S probably transforms from the S' phase. According to Bagaryatskiĭ[95] the peak hardness in such alloys is associated with the S' phase and the over-ageing effect with loss of coherency, probably resulting from the formation of the S phase.

Hardy[98] has reviewed work prior to 1954 on alloys with intermediate Cu:Mg ratios, ie 8:1 to 4:1. His results agreed with previous work in showing that an increase in magnesium content increased both the rate of ageing and the extent of hardening. Silcock[93] used X-ray diffraction to study the microstructure of the alloys investigated by Hardy[98]. For alloys with a 2.2:1 ratio she found that the precipitation sequence followed that described above, ie GP(B) zones → S' → S. In contrast, alloys with a Cu:Mg ratio of 7:1 the structures were a mixture of the sequence produced in binary Al-Cu alloys (ie θ" → θ' etc) and that in the pseudo-binary Al-S alloys. It was also found that the formation of GP zones and θ" occurred at a much faster rate than in binary Al-Cu alloys.

Vietz and Polmear[99] have studied a range of Al-2.5 wt%Cu alloys with additions of magnesium up to 2 wt%. They found that the two-stage hardening curves reported previously (for example, see Hardy[98]) were observed in the whole range of compositions. They noted also that increasing the magnesium content from 0.5 to 2 wt% increased the response to age-hardening. The greater hardening effect was attributed to an increased solid-solution hardening component and the net hardening due to GP(B) zone formation.

There are several reports concerning the effect of small additions of a fourth element on the ageing kinetics of Al-Cu-Mg alloys. Wilson and Forsyth[100] have shown that the addition of 1 wt% Ni or 1 wt% Fe to an Al-2.5Cu-1.2Mg alloy (wt%) reduce the age-hardening response due, it was proposed, to the formation of insoluble phases with copper which prevented the copper from entering into the precipitation reaction. Silcock[93] investigated an addition of 0.05 wt% indium to an Al-3.3Cu-0.58Mg alloy (wt%) and found that the rate of formation of GP zones to be much less than for the ternary alloy. After ageing for eleven days at 130°C, this alloy had about half the quantity of GP zones and about twice the amount of θ' phase when compared to the indium-free alloy. Silcock concluded that the effect of indium was much less in the ternary alloy compared with the equivalent binary alloy.

Small additions of Zr, Cr, Mn, Cd and Ag to an Al-1.9Cu-1.7Mg alloy (at%) have been studied by Baba[87]. He concluded that additions of 0.1 at%Cr, Zr or Mn retarded the clustering of solute atoms and then reduced the extent of age-hardening. When aged in the range 150-200°C, 0.1 at% of Cd or Ag was found to decrease the rate of clustering, ie zone formation, but it increased the age-hardening response. Baba suggested that this may be due to the participation of Ag or Cd atoms in GP zones consisting of Cu and Mg atoms.

1.7 The Al-Cu-Mg-Ag system

Work in the early 1960s by Polmear[101] had shown that additions of ∿ 0.1 at% silver may modify the ageing behaviour of several commercial alloys based on the Al-Cu-Mg system. For example, silver additions (∿ 0.5 wt%) to alloys AA2024 (Al-4.4%Cu - 1.5%Mg - 0.7%Mn) and RR58 (Al-2.2%Cu - 1.5%Mg - 1%Fe - 1%Ni) were found to accelerate the age-hardening response and also increase the strength in both alloys. Similar effects were observed for silver additions to Al-Mg and Al-Zn-Mg alloys[102-104]. However, Polmear[101] found that 0.5 wt% silver had little effect on the commercial alloy L65(Al-4.3%Cu - 0.8%Mg - 0.7%Si - 0.8%Mn and concluded that the Mg-Cu ratio must exceed a certain value before silver exerted any effect.

Subsequent studies were concerned with characterising the age-hardening microstructures. Vietz and Polmear[99] studied the effects of silver on a range of Al-Cu-Mg alloys and noted three equilibrium precipitates:

(i) θ ($CuAl_2$), which occurs in the binary Al-Cu system and has a tetragonal structure (see section 1.6).

(ii) S (Al_2CuMg), which has an orthorhombic structure (see section 1.7).

(iii) T (Al_6CuMg_4) which is isomorphous with the phase $(Al,Zn)_{49}$ Mg_{32} in the Al-Zn-Mg system and has a complex cubic structure[105,106].

These phases are shown on a section of the Al-Cu-Mg phase diagram in Figure 1.26 (section 1.6). For the silver containing alloys, Vietz and Polmear found that the effect of silver on the two-stage hardening curves observed depended upon the Mg:Cu ratio. For example, with alloys based on 2.5 wt% copper, the effects of silver

appeared to be confined mainly to the first or zone-forming stage of ageing if the Mg:Cu ratio was high and to the second stage if the ratio was low.

For two alloys, Al-2.5%Cu - 1.5%Mg and Al-1.5%Cu - 4%Mg, silver was found to promote the homogeneous nucleation of a T-phase structure which predominated at the peak hardness stage, instead of the usual S' precipitate. However, on prolonged ageing at 200°C the microstructure reverted to that of the equivalent silver-free alloy, but the process was slow. Auld et al[107] used X-ray diffraction to determine the structure of the T-phase produced upon ageing an Al-2.5%Cu - 1.5%Mg - 0.5 wt% Ag alloy, but found that the reflections were too diffuse to allow distinction between the compound Al_6CuMg_4 or the T-phase equilibrium precipitate found in an Al-5%Mg - 0.5%Ag alloy, Al_6AgMg_4[108]. More recently Sen and West[110] have found that plastic deformation prior to ageing eliminated the formation of this T-phase in an Al-3.2wt%Cu - 1.5wt%Mg - 0.5wt%Ag alloy.

In recent years work on silver additions has concentrated on alloys with higher Cu:Mg ratios. Auld and Vietz[109] found that an addition of 0.5wt% silver to an Al-2.5%Cu - 0.5%Mg alloy resulted in the formation of thin hexagonal-shaped platelets lying on {111} planes of the aluminium lattice. Electron and X-ray diffraction patterns were interpreted as showing that the precipitate had a hexagonal unit cell with a = 0.496 nm and c = 0.848 nm, and an orientation relationship with the aluminium lattice such that:

$$[0001]_{ppt} \parallel [111]_{Al} \text{ and } [10\bar{1}0]_{ppt} \parallel [1\bar{1}0]_{Al}$$

Large aspect ratios (>100) were observed for this new precipitate and it was suggested that coherency existed between precipitate and matrix, thus allowing plates to grow to large diameters. Indeed, Auld and Vietz found that the new precipitate was stable even after ageing for three days at 350°C, leading to the suggestion that the new precipitate may well be an equilibrium precipitate. Auld[111] later confirmed the lattice parameters but preferred to call the structure monoclinic with a = b = 0.496 nm and γ = 120°, with six-fold symmetry causing the diffraction patterns to be pseudo-hexagonal.

In the early 1970s castings made from Al-Cu-Mg-Ag alloys were introduced on a commercial basis due to the fact that high tensile

properties could be achieved - greater than previously observed in cast aluminium alloys. In fact these alloys, US alloy 201 (or K-01)[112] and French alloy Avior[113], showed properties comparable with those normally expected from high-strength wrought alloys. Each new alloy had a basic composition close to Al-4.7%Cu - 0.27%Mg - 0.7%Ag (wt%) with Avior having an additional 1.3% zinc. In the T6 temper (20h at 155°C)[112] castings of alloy 201 are quoted as giving guaranteed properties of 345MPa yield strength and 415MPa tensile strength, together with a minimum elongation of 5%. Moreover, values as high as 480MPa yield strength and 550MPa tensile strength with 10% elongation have been recorded. It is not surprising, therefore, that such alloys are being considered as replacements for forgings in applications in which they are cost effective.

Taylor et al[114] have studied the effect of an addition of 0.7 wt% silver to an Al-4.7%Cu - 0.27%Mg alloy as well as the effect of adding 0.5 wt% cadmium. Silver was found to increase the rate and extent of hardening compared with the ternary alloy. The two-stage hardening curve normally associated with the ternary alloy was replaced by single-stage hardening in the temperature range 130-230°C. Cadmium had a similar effect but to a lesser extent. Microstructural examination of the three alloys revealed that, for the ternary and cadmium-containing alloys, the only precipitates present were θ' and S when aged to peak-hardness at 170°C and 230°C. However, for the silver-containing alloy, precipitates were observed on both {100} and {111} aluminium lattice planes. The precipitates were in the form of platelets, with thicknesses in the range 2-4 nm and diameters up to 400 nm when aged to peak hardness at 170°C. The phase formed on {111} planes were believed to be a monoclinic form of θ (after Auld[111]), and it was suggested that nucleation of this phase may be controlled through prior formation of the compound Mg_3Ag on the {111} matrix planes.

Chester and Polmear[115] examined the microstructures of several Al-Cu-Mg alloys, with and without silver additions. For the ternary alloys the results confirmed earlier work on the ternary system (see section 1.6), ie at low (0.1 wt%) magnesium contents precipitation followed that observed in binary Al-Cu alloys. Increasing the magnesium level to >0.3 wt% resulted in the formation of the S' phase

sequence, with more S' present as the magnesium content was increased. In all silver-containing alloys precipitation of "monoclinic θ" was observed, the amount depending on composition. For example, an Al-4%Cu - 0.1%Mg - 0.4wt%Ag(wt%) alloy consisted of θ' and sparsely distributed monoclinic θ at peak hardness, whilst an Al-4%Cu - 0.8%Mg - 0.4%Ag alloy consisted of S' and monoclinic θ. An interesting result was observed for an alloy containing 1.5 wt% Mg and 0.4 wt% Ag where precipitation of S' and monoclinic θ was accompanied by formation of the T-phase. In subsequent work Chester and Polmear[116,117] designated the monoclinic phase Ω, to distinguish it from the θ-precipitates observed in binary Al-Cu alloys.

In the next section, the susceptibility of aluminium alloys to stress-corrosion cracking is discussed.

1.8 Stress-corrosion cracking (SCC) in aluminium alloys

1.8.1 Stress-corrosion cracking

Stress-corrosion cracking (SCC) defines the phenomenon of brittle fracture in alloys, normally considered ductile, when exposed to the simultaneous action of surface tensile stress and a corrosive environment, neither of which would separately cause major damage. Indeed, the level of stress needed for crack initiation and growth can be well below the yield stress whilst the corrosive environments can be very mild, as with water vapour at room temperature. Only specific combinations of alloy and chemical environment lead to SCC, but over 80 combinations of alloys and corrosive environments have been reported as causing this type of failure[118]. Many are of common occurrence such as mild steel in NaOH, austenitic stainless steel in salt water, copper alloys in NH_3, and aluminium alloys in sea water.

The fracture mechanics approach is now widely used in the analysis of SCC where fracture is assumed to be influenced by the flaw size, c. Hence, by using pre-cracked specimens of known flaw or crack length, use can be made of the equation for the stress intensity factor, K, such that:

$$K = Y\sigma c^{\frac{1}{2}} \qquad 1.33$$

where σ is the applied stress and Y is a constant. The critical stress intensity or fracture toughness in air is given by:

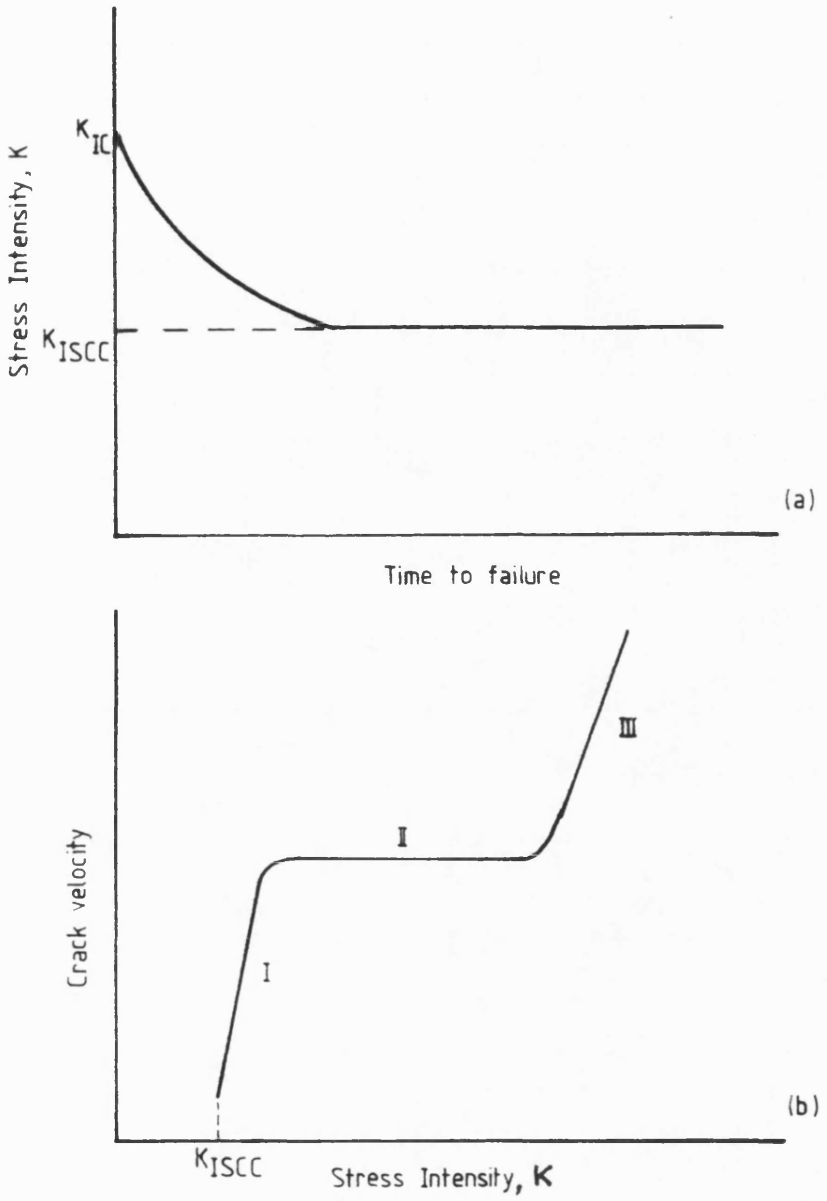

Figure 1.27 Different ways of representing SCC data;
(a)stress intensity vs. time to failure,
(b)crack velocity vs. stress intensity.

$$K_{IC} = Y\sigma_f C^{\frac{1}{2}} \qquad 1.34$$

where σ_f is the failure stress in air. Thus, if a series of specimens is tested in a corrosive environment at various stress intensity levels it is possible to produce a 'curve' similar to that shown in Figure 1.27a. The threshold value of stress intensity is designated K_{ISCC}, and below this level no stress-corrosion cracking would occur. If the initial value of K is above K_{ISCC} then the existing cracks will grow. Thus, the stress intensity increases with time until fracture occurs when K equals the fracture toughness K_{IC}. For safe design in a component containing flaws the greatest initial value of K must be less than K_{ISCC}. In general, the value of K_{ISCC} decreases with an increase in yield strength. This type of data can be presented in another form, as illustrated in Figure 1.27b, where the crack velocity is plotted against stress intensity. Figure 1.27b is a schematic representation of the expected plot. Three distinct regions are apparent. In region I, where the stress intensity is relatively low, the crack velocity is strongly stress dependent. At intermediate stress intensities, region II, the crack velocity is independent of the applied stress intensity and a plateau is observed. At relatively high stress intensities, region III, the crack velocity may again be stress dependent.

The measurement of the stress corrosion crack growth rate as a function of the applied stress intensity is now being used more widely to assess:

(i) the effect of stress on stress corrosion crack growth;

(ii) the effect of environment on stress crack growth;

(iii) alloy performance with respect to resistance to SCC;

(iv) the remaining useful service life of structures where SCC cracks have initiated.

1.8.2 SSC in aluminium alloys

A number of reviews on SCC in aluminium alloys have been published in recent years[119-122]. The general conclusion was that aluminium alloys can fail by cracking along grain boundaries when simultaneously exposed to specific environments, such as water vapour and aqueous solutions, and stresses of sufficient magnitude. The major problem of SCC involves alloys which have been developed for

medium and high strength applications by employing variations in composition, cold work and heat treatment[119,120].

Alloy composition and heat treatment strongly effect the susceptibility of aluminium alloys to SCC. Variations in alloy composition and heat treatment can effect not only the stress dependence of the crack velocity (mechanical variables) but also the dependence of crack growth on the physical and chemical properties of the environment (environmental variables). The majority of alloys found to be susceptible to SCC are the medium- and high-strength wrought materials where precipitation hardening plays an important role in developing strength.

In general, supersaturated solid solutions of aluminium in the as-quenched condition are found to be relatively resistant to SCC, although Spiedel[120] points out that no systematic work has been carried out to substantiate this view. Precipitation at ambient or higher temperatures can cause a severe increase in susceptibility in many aluminium alloys, and maximum susceptibility is often observed before the peak strength is reached. Further ageing beyond peak-hardness (overageing) may, however, substantially increase the resistance to SCC. This is illustrated schematically in Figure 1.28. It would appear that by sacrificing yield strength by overageing some increase in resistance to SCC may be achieved, and this principle is still used today in the development of high-strength, stress-corrosion resistant alloys.

SCC in the presence of liquid metals has been observed with pure aluminium and all aluminium base alloys. In aqueous solutions SCC occurs on a more restricted scale and has been observed in aluminium alloys of the following systems: Al-Ag, Al-Cu, Al-Cu-Mg, Al-Mg, Al-Mg-Zn, Al-Zn, Al-Zn-Mg-Cu and Al-Mg-Si. It should be noted that these data refer to wrought alloys, and whilst SCC is not common in castings it is found occasionally[123]. In general the following rules appear to be valid:

(i) Pure aluminium is not susceptible to SCC.

(ii) For a given alloy system, an increase in the solute content of alloying additions increases susceptibility to SCC.

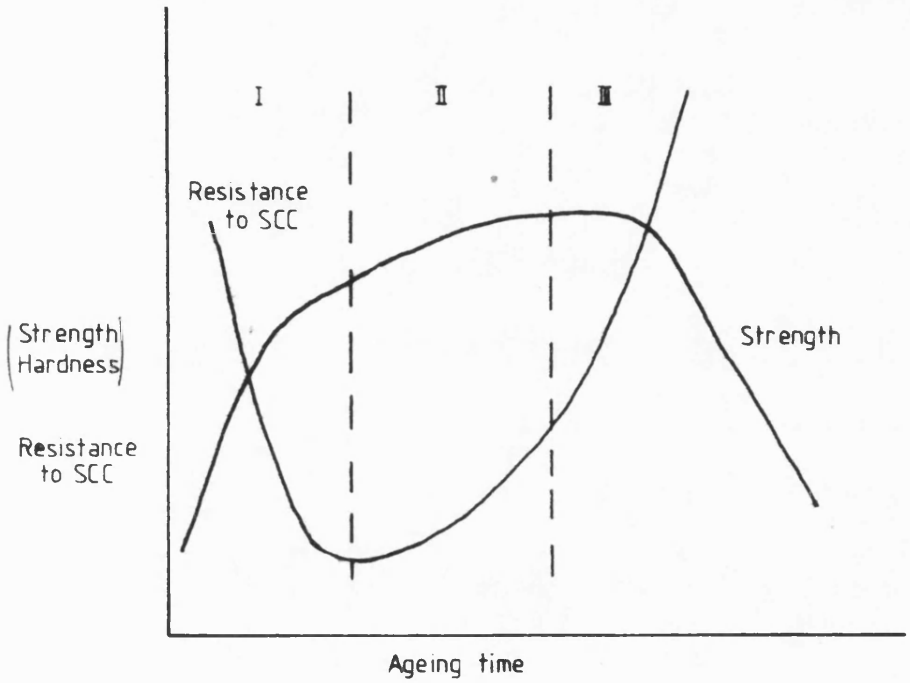

Figure 1.28 Variation of strength and stress-corrosion resistance during ageing of precipitation hardening aluminium alloys (schematic) after Spiedel[120].

(iii) In ternary and higher-order alloy systems listed above, SCC resistance is influenced by the ratios as well as the sum of the amounts of alloying additions[124].

(iv) Small additions of Cr, Mn, Zr, Ti, V, Ni and Li can reduce the susceptibility of wrought products made from high purity binary, ternary and quaternary alloys[124,125].

(v) Alloy composition alone is insufficient to determine the SCC resistance of aluminium alloys. Rather, as Spiedel[122] suggests, it is the sum of the influences of composition, processing, heat treatment and environments which determine the SCC resistance.

This last point is important when it comes to discussing the mechanisms of SCC in aluminium alloys.

1.8.3 Mechanisms of SCC in aluminium alloys

As a result of the considerable effort which has been directed towards understanding the mechanism of SCC in aluminium alloys, the following microstructural features appear to be important:

(a) Precipitate-free zones (PFZ) adjacent to grain boundaries. In a corrosive medium it is considered that either the PFZ or the grain boundaries will be anodic with respect to the grain centres. Moreover, strain is likely to be concentrated in these regions because they are relatively soft. Three contradictory schools of thought have, however, developed regarding PFZs and SCC which state:

(i) Reducing the PFZ width will increase resistance to SCC[126].

(ii) Reducing the PFZ width will decrease resistance to SCC[127].

(iii) PFZ width is of little or no importance to SCC resistance[123,128].

Sedriks et al[127] believe that PFZs are important because preferential deformation in the softer PFZ leads to preferential dissolution in this region and thus to intercrystalline SCC in several aluminium alloys.

(b) Nature of the matrix precipitate. Here it is proposed that SCC is influenced by the type of interaction between dislocations and the precipitates that cause hardening[123,133-5]. Maximum susceptibility to cracking occurs when GP zones are present[1]. In this condition, deformation tends to be concentrated in discrete slip bands, stress being generated where these bands impinge upon grain boundaries which can contribute to intercrystalline cracking under stress-corrosion conditions. It is thought that resistance to SCC in high strength aluminium alloys is reduced by precipitates that are sheared by plastic deformation whilst particles bypassed by moving dislocations are thought to result in improved SCC resistance[136]. According to this hypothesis, overaging reduces susceptibility because the volume fraction of particles that can be sheared decreases.

(c) Dispersion of precipitate particles in grain boundaries. In the 7000 series alloys a correlation has been found[131,137] between SCC behaviour and the amount of grain boundary coverage by η particles. Increased area coverage, which occurs as particle size spacing increase, has been associated with a decrease in susceptibility to SCC.

An important experimental problem, however, is that the character of matrix precipitates, of grain boundary precipitates, and of PFZ width tend to simultaneously vary with heat treatment. Control of one of these parameters is difficult and probably explains the disagreement which still exists. Alternative mechanisms have been proposed, involving: (i) hydrogen embrittlement and (ii) chemisorption of atom species at the surface of cracks, both of which will lead to a lowering of the cohesive strength of interatomic bonds in the region ahead of an advancing crack. Scamans[138] has shown that stress-corrosion cracking at grain boundaries occurs in a brittle and discontinuous manner with clear evidence of hydrogen diffusion to grain boundaries even in the absence of stress. It would appear that the presence of hydrogen does play an important role in SCC due to either hydrogen embrittlement or chemisorption, but the overall process of SCC is complex and probably one or more microstructural factors may be involved. The relative importance of each factor may depend also on the particular combination of alloy and environment.

1.9 Scope of the present investigation

There is considerable interest in replacing high-cost metal forgings with the cheaper cast components, although good quality castings with reliable properties are not, generally, easy to produce. This demand for a greater assurance in meeting a specified level of mechanical properties within actual castings has led to the concept of 'premium quality' castings and represents a major advance in foundry technology. Specifications for such castings require that guaranteed minimum property levels are met in any part of the casting and match more closely those obtained in test bars. Through strict control of factors such as melting and pouring practices, impurity levels, grain size and, in the case of sand castings, the use of metal chills to increase solidification rates mechanical properties previously thought unattainable have been achieved. Premium quality castings are more expensive to produce than normal castings but they may be cost-effective if wrought components can be replaced.

In this respect, considerable interest has been shown in the Al-Cu-Mg system (2000 series in the wrought condition) because of its age hardening response. A subsequent development has been the introduction of two cast alloys (201[112] and Avior[113]) with a nominal composition Al-4.7Cu - 0.3Mg - 0.7Ag (weight %). Both alloys show particularly high response to age-hardening and using 'premium quality' casting techniques, guaranteed properties of 345MPa proof stress and 415MPa tensile strength with a minimum elongation of 5% having been obtained from castings heat treated to a T6 temper. Values as high as 480MPa proof stress and 550MPa tensile strength with 10% elongation have been recorded. These properties are much higher than can be obtained with any other aluminium casting alloys and compare well with the high-strength wrought alloys.

However, these alloys have been reported[122] as being susceptible to SCC when heat treated to the T6 condition. Research at AUWE, Portland has been directed towards the development of strong, light-weight components with reasonable corrosion resistance and this has involved investigations of grain-refinement additions to Al-5%Cu alloys of similar composition to 201 and optimum precipitation-hardening heat treatments. Complimentary research at Bath University had focussed on the relationship between microstructure of the cast metal and its mechanical properties. Previous

research by Smith and Scott[139] had shown that the strength of sand-cast aluminium-copper alloys could be increased by additions of magnesium and silver provided that both elements were present, and that enhancement was related to the development of a different precipitate morphology in the alloy. Subsequent studies[140] were concerned with chill-cast alloys where it was shown that, despite the smaller grain size compared with sand-cast metal, a similar age-hardening response could be achieved for comparable alloy compositions. In addition, encouraging results were obtained by adding a small ($\sim$ 1 wt%) amount of zinc, whilst iron (even at levels below 0.3 wt%) was identified as being a detrimental impurity.

The present research involves a series of Al-Cu-Mg-Ag alloys, formulated on the basis of the above data and prepared by the sand casting route, and concerns particularly the relationship between microstructure of the cast alloys and their mechanical properties. The research can be considered as having three objectives:

(i) to study the effect on microstructure of varying the amount of magnesium, silver and zinc on the precipitation behaviour of an aluminium-copper alloy;

(ii) to relate the resulting microstructures with the mechanical behaviour of the alloys;

(iii) to carry out a preliminary study of stress-corrosion of the alloys in salt water.

CHAPTER 2

EXPERIMENTAL DETAILS

2.1 Materials

The sand-cast aluminium alloys used in this investigation were supplied by ARE, Portland in the form of plates measuring 345 mm x 205 mm x 14 mm thickness. These were fabricated using a bottom-fed CO_2 bonded silica sand mould, and after pouring were allowed to cool in air.

Chemical analysis of the alloys was carried out at ARE, Portand laboratories. The results are given in Table 2.1, nominal compositions being given in brackets.

2.2 Heat Treatment

Solution treatment of the cast alloys was carried out using a muffle furnace with a flowing atmosphere of argon. The argon was necessary to avoid preferential oxidation of magnesium and the consequent depletion of surface regions in this element. The solution treatment consisted of a preliminary treatment of 6 hours at 500°C ± 5°C, followed immediately by 42 hours at 525°C ± 5°C and then quenching into water at room temperature.

Precipitation ageing treatments were conducted in an oil bath which could be controlled to ± 2°C for temperatures up to 200°C. Ageing was carried out on all alloys at temperatures of 140°C and 170°C.

2.3 Optical Microscopy

Samples of each alloy in various heat-treated conditions were mounted in epoxy cold-curing resin. The specimen surfaces were prepared by abrading on emery paper down to 600 grade, followed by polishing on cloths impregnated with first "Brasso" and then "Silvo". The surfaces were finally finished using alumina down to 0.1 μm grade.

Surfaces were examined in the as-polished condition and also after etching in a solution of 5 ml nitric acid and 2 ml hydrofluoric acid in 100 ml distilled water. Etching for approximately 10 seconds was sufficient to reveal microstructural features such as grain boundaries and second phases.

Table 2.1

Compositions of Alloys Studied

All compositions in weight % . Nominal compositions in brackets.

Alloy	Element (wt%)								
	Cu	Mg	Ag	Zn	Mn	Ti	Fe	Si	Al
A3	4.66 (4.5)	0.74 (0.75)	0.57 (0.75)	0.03 (0)	0.31 (0.30)	0.18 (0.2)	0.02 (0)	0.029 (0)	Bal. (Bal)
A4	4.72 (4.5)	0.66 (0.75)	0.61 (0.75)	1.13 (1.2)	0.29 (0.3)	0.17 (0.2)	0.02 (0)	0.025 (0)	Bal. (Bal)
A5	4.8 (4.5)	0.23 (0.25)	0.50 (0.50)	1.24 (1.20	0.31 (0.30)	0.18 (0.2)	0.02 (0)	0.035 (0)	Bal (Bal)

2.4 Hardness Testing

Hardness measurements were made using a Vickers testing machine with a 2.5 kg load on metallographically prepared samples in the as-polished condition. Ten readings were averaged for each sample.

2.5 Electron Microscopy and Analysis

When an electron beam is directed at the specimen various interactions can occur, as shown schematically in Figure 2.1. If the specimen is suitably thin electrons can penetrate the specimen to give information on its crystal structure and morphology. Additionally, topographical information on surfaces can be obtained by imaging back-scattered and secondary electrons. To complement these data, elements present in the specimen can be identified by analysis of the X-rays produced by the electron bombardment.

Such techniques have been used extensively throughout the research and are detailed below.

2.5.1 Scanning electron microscopy (SEM)

The scanning electron microscope (SEM) has a greater resolving power ($\sim$ 10 nm) than the optical microscope, and also little sample preparation is necessary for the majority of applications. In the SEM an energetic electron beam, characterised by its accelerating voltage (typically 5 kV to 25 kV), is projected onto the specimen by a series of electromagnetic lenses. When the beam hits the specimen various interactions with the specimen occur. Firstly, some of the primary electrons are reflected back from the surface and are collected in a scintillator-light pipe-photomultiplier combination and an image of the surface is finally formed on a cathode-ray tube (CRT). These reflected (back scattered) primary electrons have sufficient energy (tens of kilovolts) to emerge from deep ($\sim$150nm) within the specimen and, although they are sensitive to the orientation of the specimen, they are relatively unaffected by the exact nature of the surface. On the other hand, some of the secondary electrons emitted from the surface have such low energies (<50eV) that they can only escape from within 10-20 nm of the specimen surface. These secondary electrons are, therefore, heavily influenced by the exact nature of the surface of the specimen and as such can reveal a greater wealth of information regarding the specimen surface.

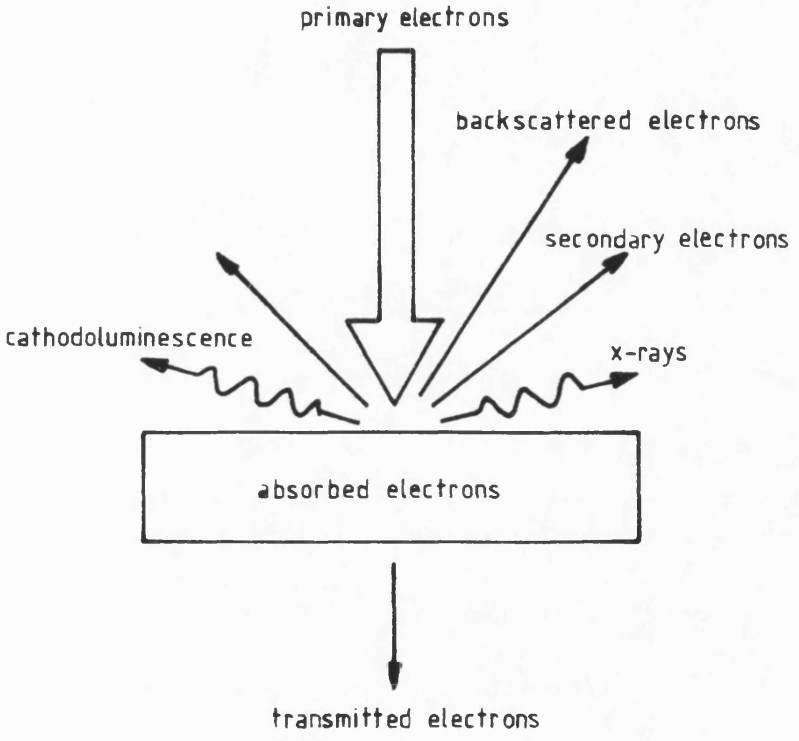

Figure 2.1 Phenomena associated with electron-specimen interaction

A JEOL 35C scanning electron microscope (SEM) operating at 25 kV was used to examine the fracture surfaces of both tensile and stress-corrosion test specimens. All specimens were first cleaned in de-ionised water and ethanol, and mounted on aluminium stubs with silver paint before insertion in the SEM.

2.5.2 Electron-probe microanalysis (EPMA)

As mentioned previously, when a specimen is bombarded with an electron beam X-rays may be produced in the following way. The incident electron collides with an electron in the core shells of an atom in the specimen causing it to be ejected. In order to stabilise the atom an electron from a higher energy orbit falls into this vacancy, the excess energy associated with this electron transition being emitted as an X-ray photon. Since each species of atom has its own characteristic electron energy levels, the X-ray photon will also be characteristic of the emitting atom. Measurement of the energy, or wavelength, thus provides a means of identifying the element, whilst recording its intensity gives a measure of the concentration of the element. Analysis of X-ray emission spectra from the specimen may be carried out using either a wavelength-dispersive spectrometer (WDS) or an energy-dispersive spectrometer (EDS).

A wavelength-dispersive X-ray spectrometer (WDS) uses a crystal of known interplanar spacing to diffract the X-rays emitted from a specimen. Measurement of the diffraction angle, θ, thus gives the X-ray wavelength according to the Bragg law, $n\lambda = 2d \sin \theta$. This diffracted beam of X-rays is detected and its intensity measured by a gas proportional counter. By setting the spectrometer to a particular Bragg angle so as to select a particular X-ray energy, the variation in concentration of each detected element in the specimen can be monitored by moving the electron beam relative to the specimen. Similarly, X-ray maps of selected elements can be produced using the electron beam scanning mode.

In energy-dispersive spectrometry (EDS) the X-rays enter the detector, an Si(Li) semi-conductor kept under high vacuum and at liquid nitrogen temperature, through a thin beryllium window. Electron-hole pairs are created by ionisation within the detector, the number of these pairs being proportional to the X-ray energy. In a Si(Li)

detector the energy required to create a pair is about 3.8eV. The total charge produced by the incident X-ray photon is collected at the electrodes, amplified and then fed to a multichannel analyser (MCA) in which the pulses are separated in terms of amplitude and stored in memory channels corresponding to these amplitudes, ie X-ray photon energies. The resulting spectrum can be displayed on a CRT, plotted on an X-Y recorder, or stored on magnetic tape. In addition, X-ray maps can be produced.

WDS and EDS are complementary rather than competitive. The EDS system has the advantage of speed of spectrum acquisition and it can give results at low beam currents (essential for fragile specimens), and from rough surfaces. On the other hand, the WDS has higher accuracy and energy resolution, giving lower detectability limits and better performance with light elements. Both analysis techniques were used during the course of this work.

The JEOL 35C was fitted with an EDS system and this was used to analyse the fracture surfaces of the stress-corrosion test pieces where corrosion products may have been present.

A JEOL JXA 733 electron-probe microanalyser fitted with three WDS systems was employed to measure elemental concentrations in aluminium alloys before and after solution treatment. Analysis here was carried out on specimens in the as-polished condition.

2.5.3 Transmission electron microscopy (TEM)

The operation of the TEM depends primarily upon the fact that fast electrons are deflected by magnetic fields and can be focussed by suitably constructed magnetic lenses. Thus, in principle, electrons can be used in the same way as light to form a magnified image of an object. However, since the wavelengths of the wave representing fast electrons are short (0.037 Å at 100 keV) the resolution of a microscope using electrons will be much higher than is possible with an optical microscope, current TEM's having a spatial resolution below $\sim$ 0.5 nm.

The maximum thickness of specimen usable in TEM depends upon the atomic number of the material, but is typically 500 nm for specimens composed of light elements, decreasing to less than half this value for materials of higher atomic number. Also, the greater the electron

energy the better the transmission through the specimen, so microscopes are generally constructed to run at the highest accelerating voltage that can conveniently be used, 100 kV to 200 kV in modern instruments.

As they pass through the thin specimen, the electron waves interact with its structure and may suffer consequent changes in amplitude and phase. The transmitted electrons (see Figure 2.1) can be projected onto a fluorescent screen by a further series of magnetic lenses below the specimen to form an image. A schematic ray diagram is shown in Figure 2.2a. If the specimen is crystalline then all the suitably oriented sets of lattice planes will scatter electrons into corresponding diffracted beams. If the second condenser lens current is sufficiently reduced, parallel illumination will fall on the specimen so that electrons in any given diffracted beam will be travelling parallel to each other. As they are brought to focus in the back focal plane of the objective lens (A in Figure 2.2), an electron diffraction pattern will be formed there. This plane can be focussed onto the projector lens object plane by reducing the intermediate lens current with the result that an enlarged image of the diffraction pattern appears on the viewing screen. This situation is shown schematically in Figure 2.2b.

It is possible to analyse small areas of the specimen by inserting an aperture in the object plane of the intermediate lens (eg at B in Figure 2.2). If the TEM is now adjusted to show the diffraction pattern, this pattern is formed only by those electrons passing through the aperture at point B and corresponds to the selected area visible on the screen with the aperture in position. By recording this selected area diffraction pattern (SADP) the crystal structure of a small area can be analysed.

TEM was used extensively throughout the project to analyse precipitates in the alloys and also to measure precipitate populations ("densities"). These techniques will be described in the following sections.

2.5.3.1 Precipitation studies

For TEM studies slices of alloy $\sim$ 3 mm thick were cut from the as-cast slabs. They were solution treated and aged to give the required

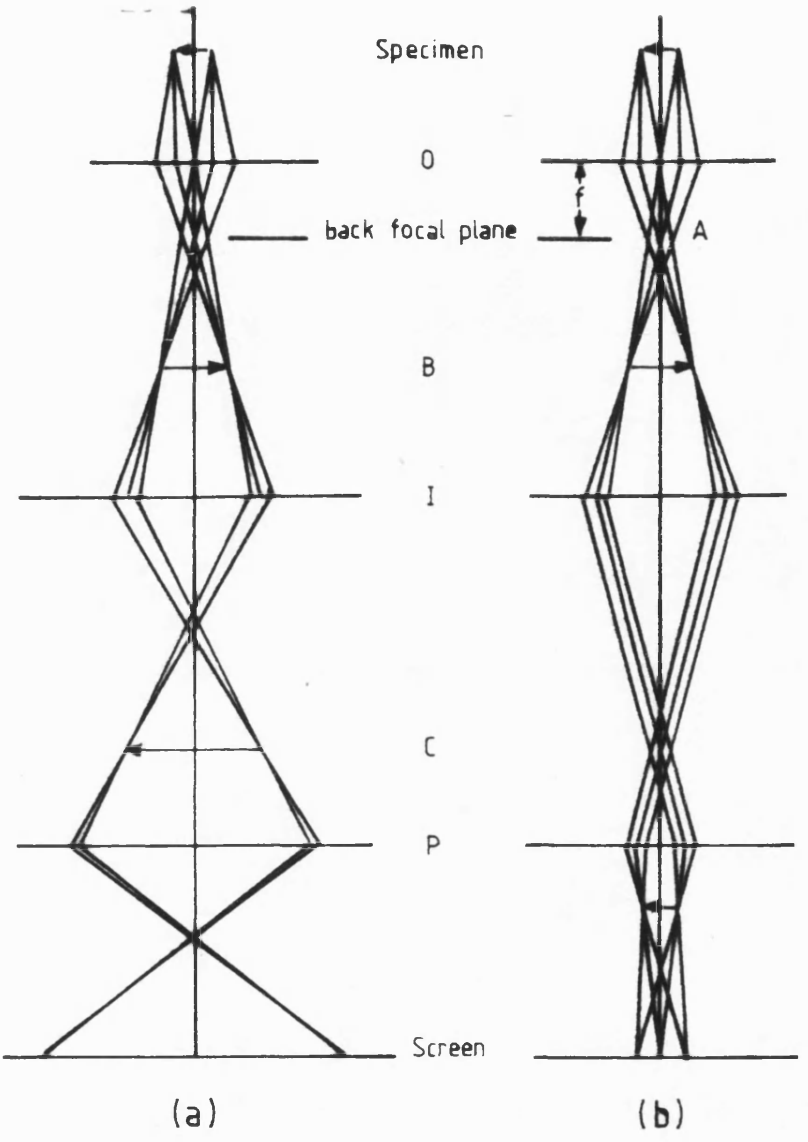

Figure 2.2 Schematic ray diagrams for (a) image and (b) diffraction pattern formation in the TEM.

metallurgical condition, as assessed previously from curves of hardness versus ageing time.

Next, the treated slices were ground on successively finer grades of emery paper to a thickness of $\sim$ 0.2 mm, from which discs 3 mm in diameter were stamped out. The discs were electropolished in a Tenupol electropolishing unit using a solution of 20% nitric acid and 80% methanol as electrolyte. The solution was maintained at -20°C using liquid nitrogen as coolant, and the applied voltage continually adjusted in order to maintain a constant current of 140 mA. A photo-electric cell device incorporated in the Tenupol apparatus indicated when the specimen was thinned to perforation, upon which the voltage to the cell switched off. Upon perforation, specimens were removed immediately, thoroughly washed in ethanol and transferred to the electron microscope, a JEOL 100CX instrument operating at 100 kV. Selected area diffraction patterns were taken, corresponding to each electron micrograph, for crystallographic analysis.

Interplanar (d) spacings were calculated as follows. Figure 2.3 is a ray diagram showing a diffraction spot produced on a photographic plate at position P by electrons of wavelength, λ, incident on the specimen S; O is the position where undiffracted electrons (the direct beam) strike the plate. From the diagram we may write:

$$\text{Tan } 2\theta = \frac{R}{L}$$

where R is the distance from O to P and L is the camera length. Now since diffraction angles are small, a few degrees or less, the equation approximates to:

$$2\theta = \frac{R}{L} \qquad (2.1)$$

And from the Bragg law,

$$n\lambda = 2d \sin \theta \qquad (2.2)$$

Eliminating θ then gives:

$$n\lambda = \frac{R}{L} \quad \text{ie} \quad d = n\frac{\lambda L}{R}$$

The term λL is known as the "camera constant" and since the operating conditions of the microscope can vary over a period of time, this had

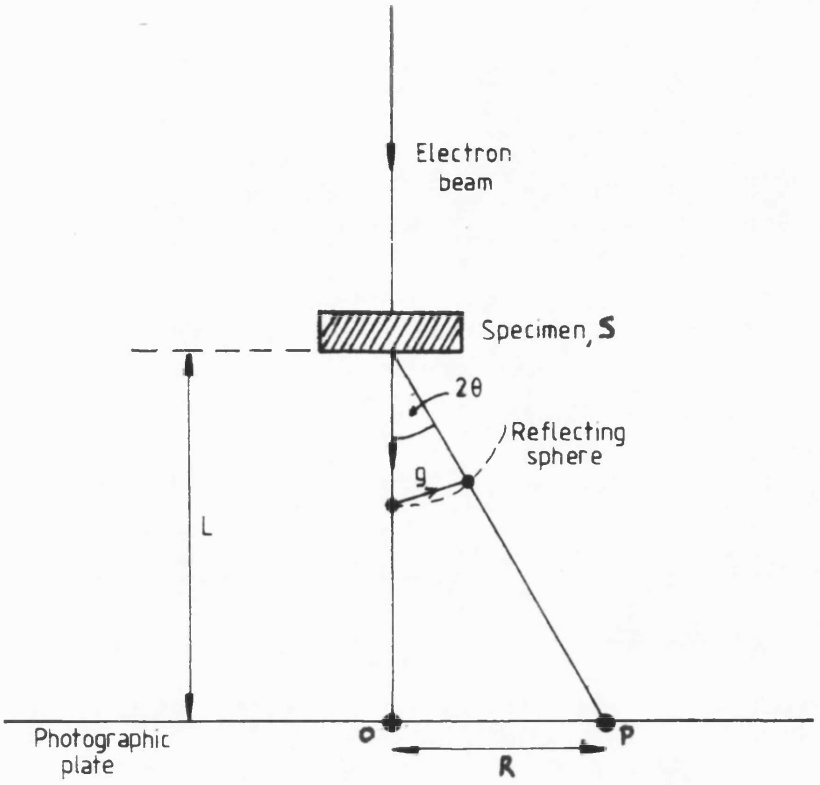

Figure 2.3 Schematic diagram showing the relationship between the camera length, L, and the diffraction spot on a S.A.D pattern.

to be determined from measurements on a known crystal structure; in the present work the matrix of pure aluminium was used. As well as analysing the crystal structure of precipitates from the diffraction patterns the orientation relationship of the precipitate with respect to the aluminium lattice was established.

The sizes of precipitates were measured from electron micrographs enlarged to the same scale. Measurements were made using a X4 magnification graticule with an accuracy of ± 0.2 mm. Values of actual precipitate sizes were then calculated using a computer program (see appendix 1) which also computed the mean and standard deviation of precipitate sizes. Where possible a minimum of five hundred precipitates were measured to improve statistical analysis.

2.5.3.2 Precipitate density determination

The image formed by a TEM is a magnified two-dimensional projection of the object and for determining precipitate densities the local foil thickness must be accurately measured. A variety of techniques have been adopted for measuring the thickness of a thin foil, some methods being more accurate and flexible in use than others.

Although this work will not be reviewed here, a short review of the various methods used previously by other workers is presented in appendix 2.

The method used in the present investigation involved the measurement of the continuum X-ray emission from the area of interest and reading the value of the foil thickness at this point from a previous constructed calibration curve of foil thickness as a function of the continuum X-ray emission. The construction of the calibration curve and the method of foil thickness determination are detailed below.

As well as conventional TEM, the JEOL 100CX was equipped with facilities for scanning transmission electron microscopy (STEM) and energy dispersive X-ray analysis (EDS) of small areas. These facilities were used to determined foil thickness. An aluminium-4 wt % copper alloy used in a previous investigation[139] was aged for 100h at 250°C in order to produce large precipitates, lying on {100} planes of the aluminium lattice, which intersected both top and bottom of the foil.

(A thin foil was produced by the method described in section 2.5.3.1). These precipitates were aligned so that they lay perpendicular to the tilt axis of the microscope and the projected width, w, of the precipitates was measured. They were then tilted until they were lying parallel to the electron beam and the angle of tilt, Θ, was noted. Thus, it was possible to determine the foil thickness, t, unambiguously at several points using the expression, $t = w/\tan\Theta$ (see Figure 2.4).

For each projected width measurement above, the continuum background level was recorded from two channels, 3.5 to 5.5 keV and 9.5 to 11.5 keV, for a period of 200 live seconds (after tilting 35° towards the x-ray detector). Typical x-ray spectra from thin and thick regions are shown in Figure 2.5. It must be noted that the beam current of a TEM will vary from session to session, and since, within the "thin film" limit, x-ray emission varies linearly with beam current it was necessary to correct the x-ray readings by recording the beam current after each session and using: the beam current after the first session as baseline.

Thus, a calibration curve of x-ray emission as a function of foil thickness was constructed. To obtain a value for the foil thickness at the area of interest, each foil was tilted 35° towards the x-ray detector and the x-ray emission in these two channels was recorded, again for a time of 200 live seconds. The value of foil thickness was then simply read from the calibration curve.

2.6 Mechanical Testing

2.6.1 Tensile testing

The dimensions of the tensile test pieces are illustrated in Figure 2.6. Tests were carried out on an Instron 1195 testing machine with an Instron 2620-601 extensometer attached to the specimen to record extension. All tests were carried out using a strain rate of $6.67 \times 10^{-4} S^{-1}$. A minimum of ten specimens were tested for each alloy in the various metallurgical conditions detailed below:

(i) As-solution treated.

(ii) Peak hardness at 140°C.

(iii) Peak hardness at 170°C.

From the load-extension curves provided, the 0.2% stress and tensile strength could be calculated.

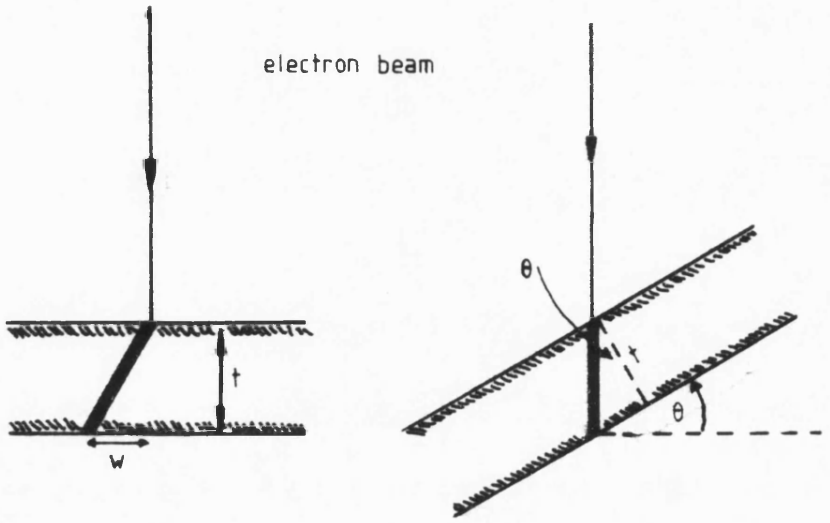

$$t = w / \tan \theta$$

Figure 2.4 Principle of the foil tilt method for foil thickness measurement.

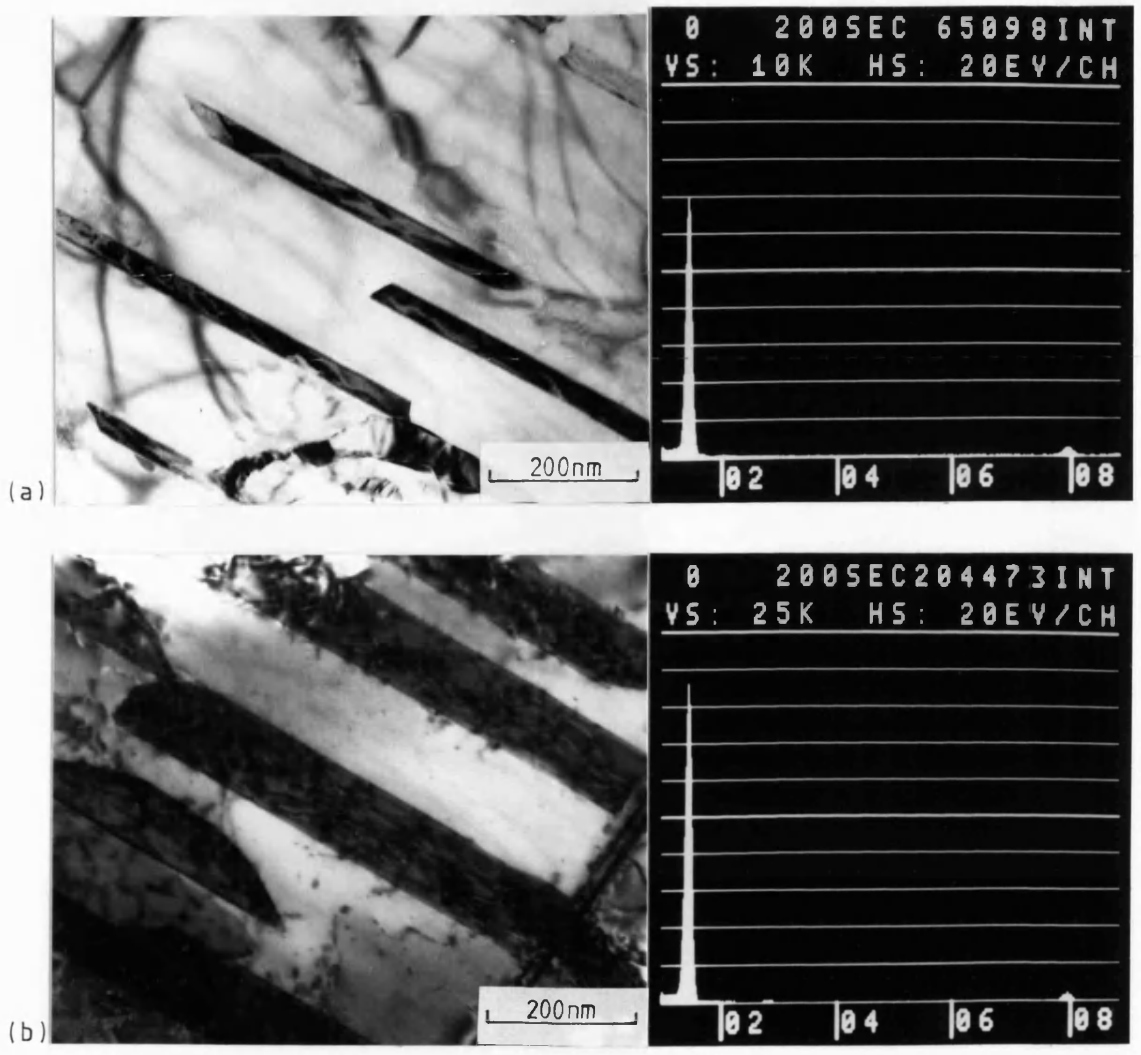

Figure 2.5 Electron micrographs and EDS spectra from a thin foil prepared from overaged Al-Cu alloy showing precipitates on 100 planes which intersect both top and bottom of the foil from (a) thin and (b) thick regions of the foil.

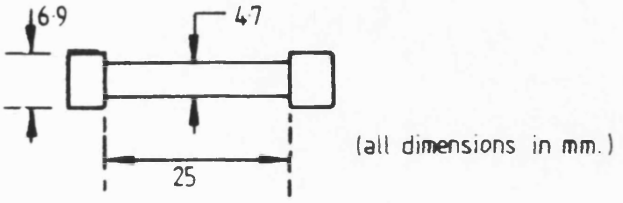

Figure 2.6 Tensile test piece.

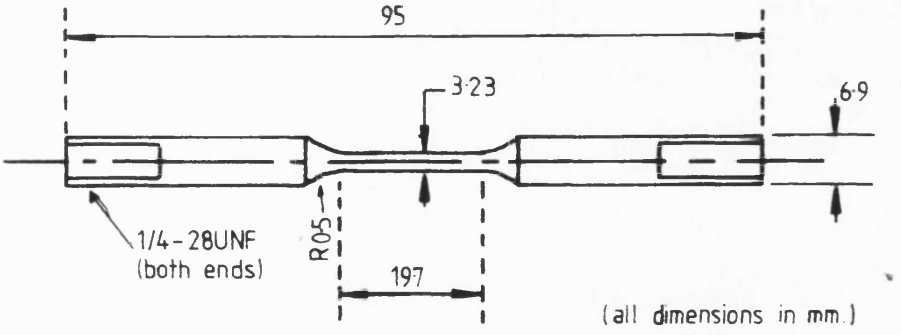

Figure 2.7 Environmental test piece.

2.6.2 Environmental testing

The dimensions of the test pieces used in the environmental test program are shown in Figure 2.7. They were heat-treated in this form and tested in the as-heat treated condition.

A photograph of the environmental testing apparatus, which was constructed at the University of Newcastle, is shown in Figure 2.8. It embodies two tensometers which operate electrically via worm reduction units. Using this apparatus a number of constant strain rates in the range 3×10^{-7} to $3 \times 10^{-5} S^{-1}$ could be employed by selection of the appropriate gear ratio. After preliminary trials on all alloys in the peak hardness condition, a strain rate of $1.13 \times 10^{-6} S^{-1}$ was selected as this strain rate revealed evidence of some stress-corrosion cracking (SCC) in all alloys and gave test times conveniently within the range 5 to 30h. For tests in synthetic sea water an enclosed perspex tube fed by a circulating pump was fitted around the sample. The synthetic sea water used was to Defence Standard DEF 1053 and British Standard BS3900 part F4, and its composition is given in Table 2.2

During the progress of a test the load was monitored continuously and displayed on a chart recorder as a function of time. The times to failure were noted as well as tensile strengths. At least five specimens from each alloy were tested, both in air and the synthetic sea water environment. The metallurgical conditions tested are listed below:

(i) As-solution treated.

(ii) Peak hardness at 170°C.

(iii) Overaged at 170°C.

Unfortunately it was impossible to time an experiment so that the specimen could be removed from the salt water environment immediately after fracture. Obviously, if the specimen were not removed immediately then some degree of post-fracture corrosion of both the stress-corroded region and the final "ductile" fracture might be expected. Therefore, in order that this possibility might be checked samples of each alloy were polished and immersed in the salt water environment, at room temperature, for several hours. The exposed samples were then examined using the SEM and EDX facilities.

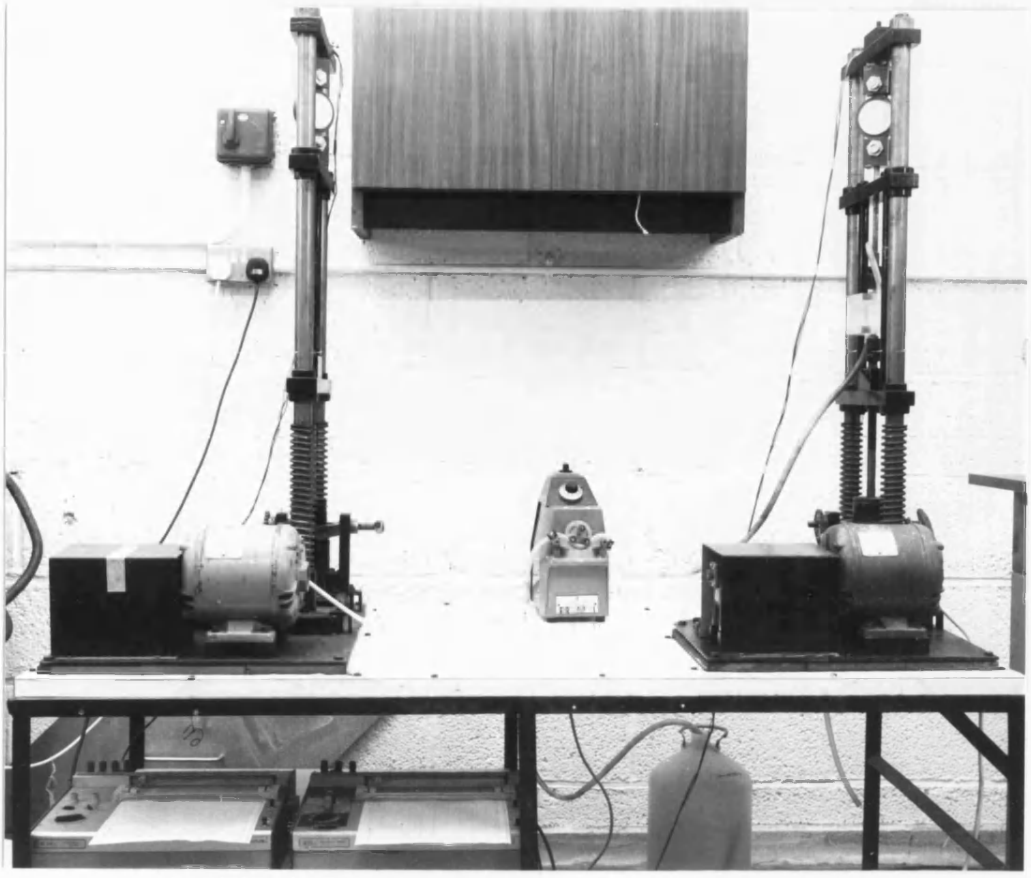

Figure 2.8 Environmental test apparatus.

Table 2.2

Composition of Synthetic Sea Water

(DEF1053 and BS3900 Part F4)

NaCl	26.50g
$MgCl_2$	2.40g
$MgSO_4$	3.30g
KCl	0.73g
$NaHCO_3$	0.20g
NaBr	0.28g
$CaCl_2$	1.10g

+ distilled water - made up to 1000 ml.

CHAPTER 3

RESULTS

3.1 As-cast materials

A typical optical micrograph of an as-cast microstructure is illustrated in Figure 3.1. This shows a coarse-grained structure with a second phase present at the grain boundaries, estimated at ∿5.0% by volume. Within the grains a progressive darkening is apparent in regions towards the grain boundaries which is indicative of coring. This coring is revealed more clearly in the scanning electron micrograph, Figure 3.2, taken from an unetched specimen.

Electron-probe microanalysis of the specimen showed that the centre of the grain contained ∿1.3wt% copper; the amount of copper dissolved in the aluminium increased towards the grain boundaries to give a maximum of ∿3.8wt%. This is illustrated in Figure 3.3. Other elements analysed were also associated with coring but to a lesser extent, Figure 3.4.

Only small differences in composition were found between the grain-boundary phases analysed. Phase A (see Figure 3.5) contained ∿50wt% copper while phase B contained ∿45wt% copper. The zinc level in the phases was less than within the grains, although little difference was observed between the two phases. There was also little difference in the magnesium content of the two phases. However, both silver and manganese were present in greater amounts in phase B, ∿0.5wt% silver and 1.5wt% manganese in phase B compared to ∿0.25wt% and ∿0.1wt% in phase A respectively.

3.2 Solution treated materials

The essential features of solution treatment were that, firstly, the coring effect has been substantially removed, as illustrated in Figure 3.6, an optical micrograph of alloy A3. The grains contained a uniform distribution of ∿4.6wt% copper (see Figure 3.3). Secondly, there was also a substantial reduction in the amount of grain boundary phases, <1% by volume being present after solution treatment.

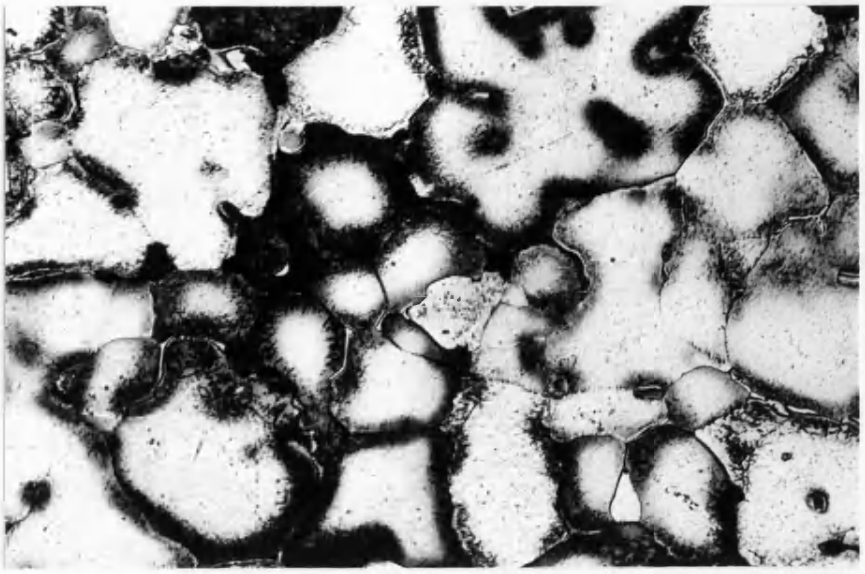

Figure 3.1 Typical as-cast microstructure,alloy A4. ×100

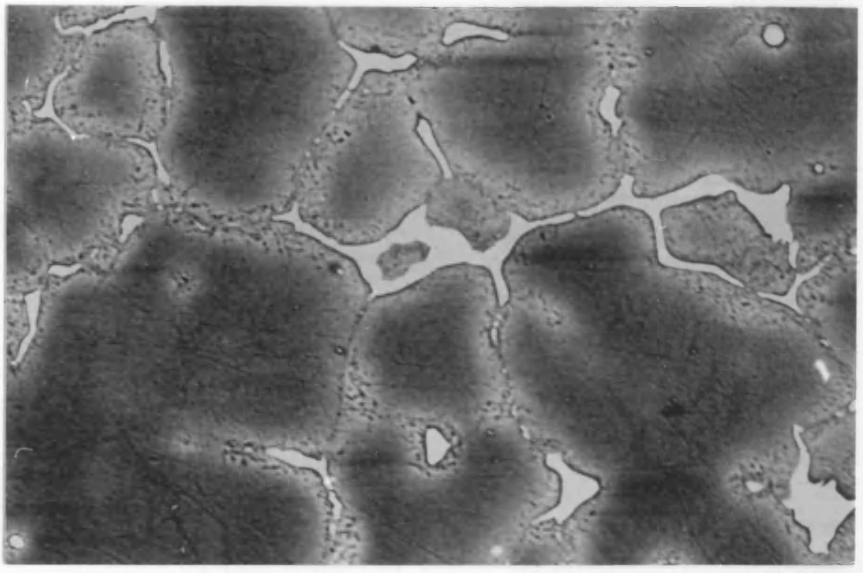

figure 3.2 As-cast microstructure,scanning electron micrograph of alloy A4. ×250

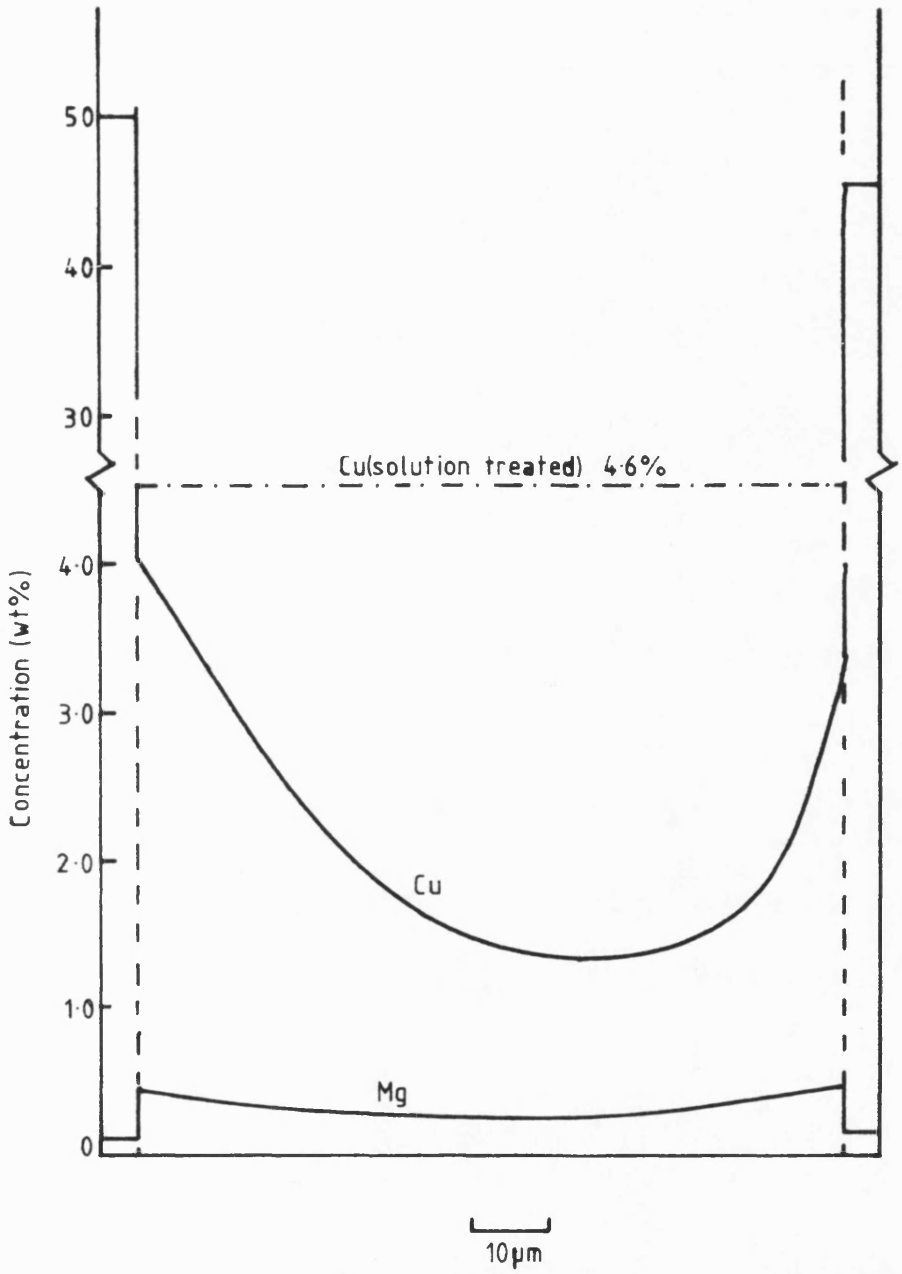

Figure 3.3 Concentration profiles of Cu and Mg across as-cast grain.

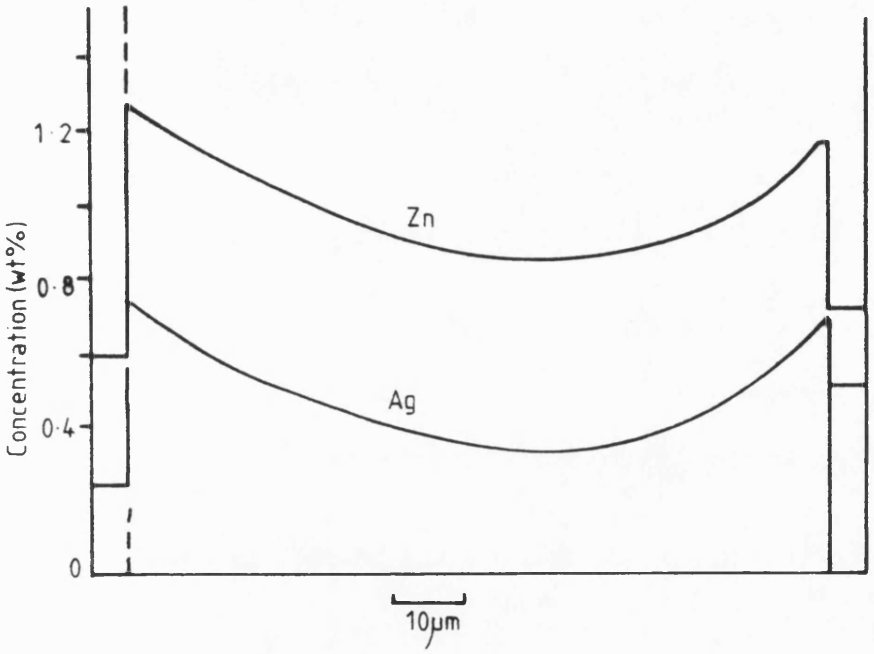

Figure 3.4 Concentration profiles of Zn and Ag across an as-cast grain.

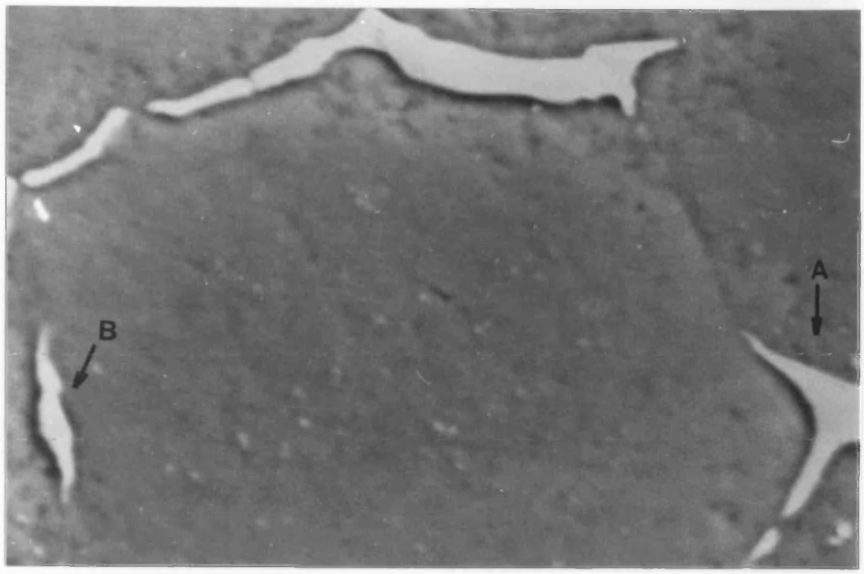

Figure 3.5 Grain boundary phases analysed.

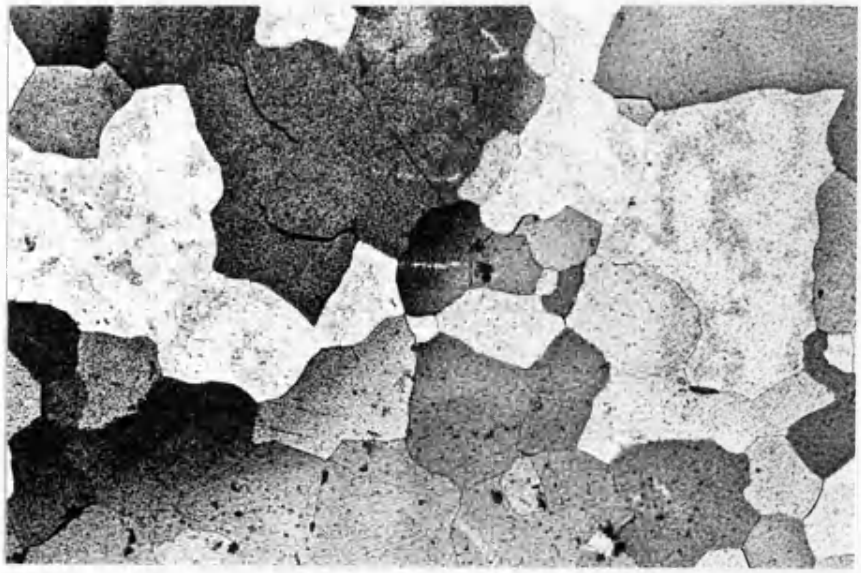

Figure 3.6 Solution treated microstructure,alloy A3. ×80

3.3 Ageing characteristics

In this section the studies on the precipitation hardening behaviour of all alloys will be presented, the results being presented in the following order. Firstly, the precipitation hardening response at both ageing temperatures will be presented. Secondly, the microstructure of all alloys in the peak hardness condition will be shown, with particular reference to the structure produced on ageing at 170°C. Next, the calibration curve for foil thickness determinations and the resultant error in any calculations based upon such curves will be described. Finally, studies on the nucleation and growth of precipitates will be presented.

3.3.1 Ageing response

3.3.1.1 Ageing at 140°C

Curves of hardness as a function of ageing time at 140°C are shown in Figure 3.7. The data show a single-stage hardening response with no evidence of a "plateau" - or two-stage hardening behaviour.

The maximum hardness value achieved by alloy A5 is $\sim 154H_V$ $\pm(4H_V)$ and is reached after ageing for 120 h. In contrast, both alloy A3 and A4 exhibit an increase in hardness of $\sim 30H_V$, over that achieved by alloy A5 and also a reduction in the time to reach "peak" hardness ($180H_V$ and $184H_V$ after 48 h and 48 h respectively for alloys A3 and A4).

3.3.1.2 Ageing at 170°C

Ageing at 170°C also produces single-stage hardness curves, and these are presented in Figure 3.8. Alloy A5 achieved a peak hardness of $151H_V$ ($\pm 4H_V$) after 25 h at 170°C. Again alloys A3 and A4 showed a marked increase in hardness at peak ($\sim 180H_V$ and $\sim 184H_V$ respectively) and also a reduction in the time to reach peak hardness (2h in each case).

3.3.2 Structure and orientation relationship of precipitates

Figure 3.9a, a thin foil electron micrograph of alloy A5 aged to peak hardness at 170°C, shows the presence of a high population of oriented plate-like precipitates. The electron diffraction pattern taken from this area, Figure 3.9b, identified the electron beam as {110} with respect to the aluminium lattice. Three sets of precipitates are clearly visible, situated edge-on to the beam; two

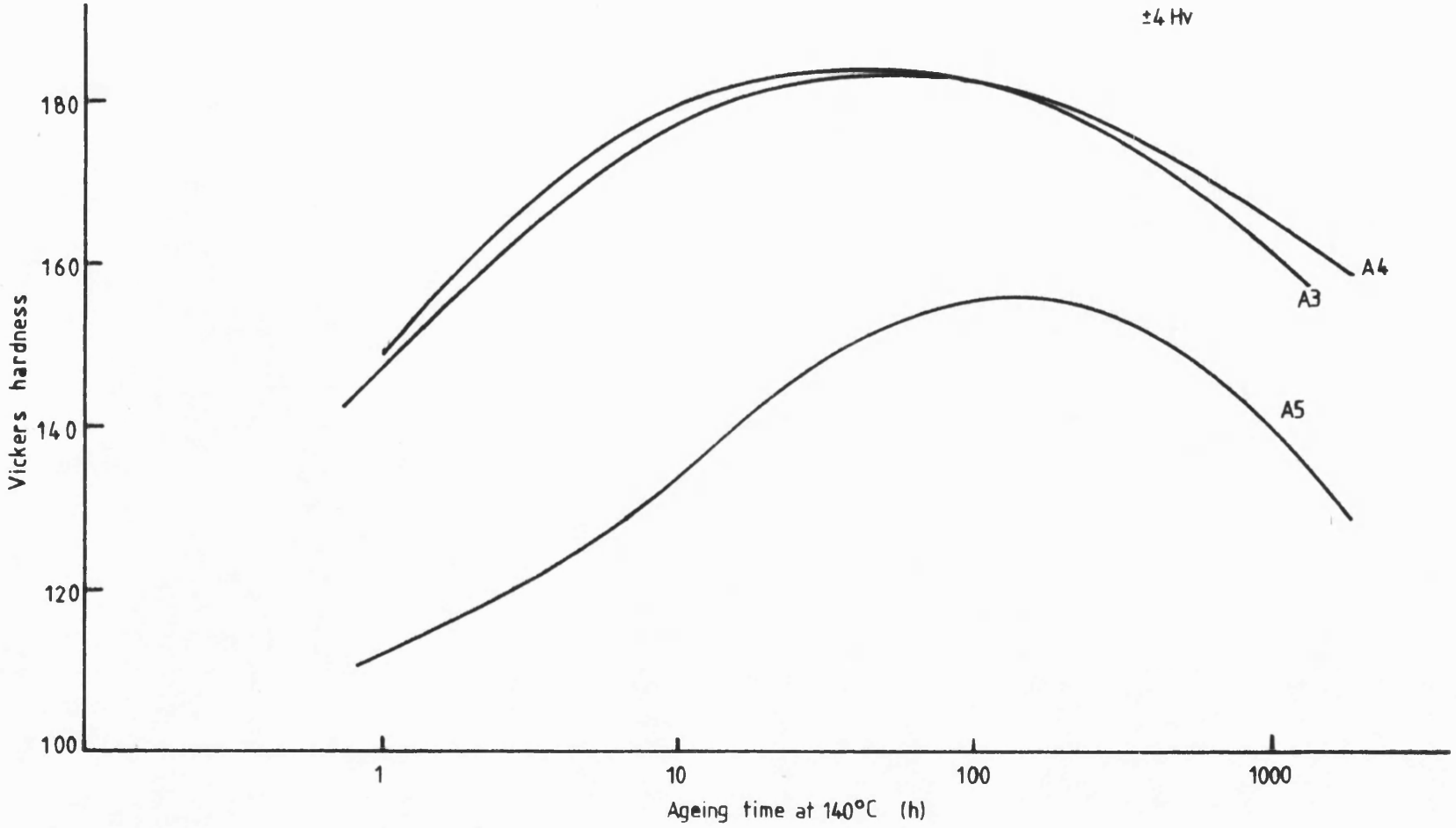

Figure 3.7 Hardness versus ageing time at 140°C

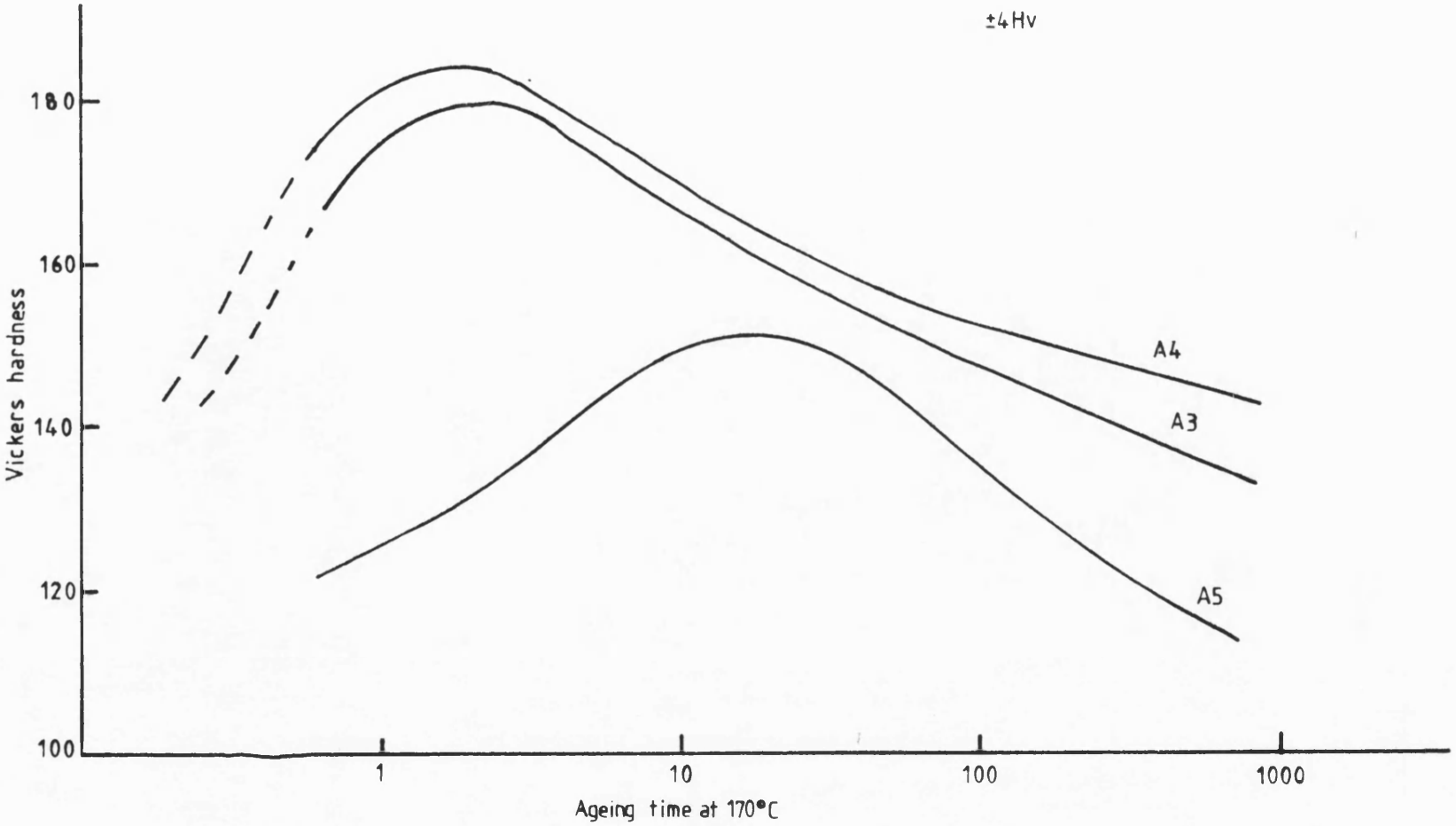

Figure 3.8 Hardness versus ageing time at 170°C

of these are consistent with the {111} habit plane, the third is {100}. Hence, the remaining precipitates, on planes inclined to the foil surface, make up the other {111} and {100} precipitate morphologies. The combined presence of two sets of precipitate morphologies makes unambiguous identification of their crystal structures more difficult. However, both alloys A3 and A4 showed a virtual absence of the {100} precipitate morphology when aged to peak hardness at 170°C. Thus, in order to determine the crystal structure of the {111} type precipitate, analysis was conducted on alloy A3.

The absence of {100} precipitation in alloy A3 at peak hardness is apparent in all following illustrations, but perhaps most obviously in Figure 3.11a, a $\{1\bar{1}0\}$ foil directly comparable with Figure 3.9a but in which only two edge-on orientations are present. However, Figure 3.10a will be considered first, where the correspond- electron diffraction pattern, Figure 3.10b, shows a hexagonal array of spots from aluminium indicating a beam direction of $\{\bar{1}11\}$. The plate like precipitates are very thin and this is evident from the low contrast of the micrograph, especially those precipitates lying perpendicular to the beam direction. Although there is little evidence of their having a hexagonal shape, they appear to show a tendency to grow along <110> directions of the matrix. The weaker spots seen in the diffraction pattern (Figure 3.10b) originate from the precipitates and also from a hexagonal array. Both sets of diffraction spots can be indexed, the aluminium spots using Miller indices and the spots from the precipitates using Miller-Bravais indices (Figure 3.10c) since a hexagonal rotation is chosen for the precipitate. Hence, the {0001} direction in the precipitate is parallel to the beam, and the orientation relationship between precipitate and aluminium lattice can be expressed as:

$$[0001]_{ppt} \parallel [\bar{1}11]_{A\ell}$$

and

$$[10\bar{1}0]_{ppt} \parallel [110]_{A\ell}$$

However, precipitation also occurs on three other {111} planes of the aluminium lattice and each orientation produces diffraction spots of its own. In the case of the $[\bar{1}11]$ orientation shown in Figure 3.10a, the construction given in Figure 3.10d show that these other precipitate orientations (B, C and D) have a $\{10\bar{1}0\}$ plane

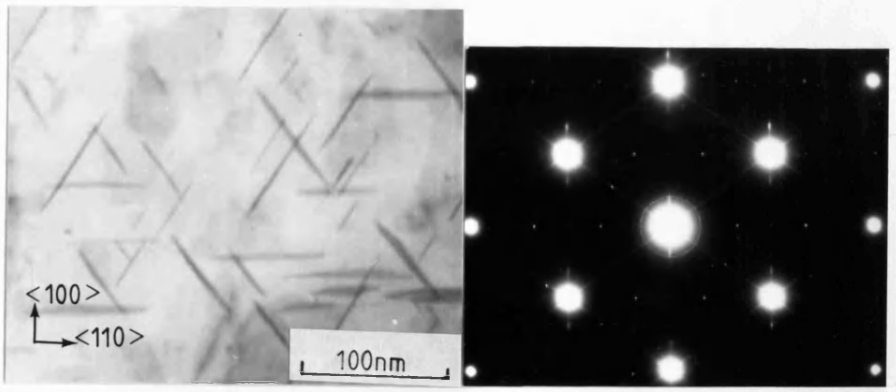

Figure 3.9 Alloy A5 aged to peak hardness at 170°C,<110> foil. (a) electron micrograph,(b) corresponding SADP.

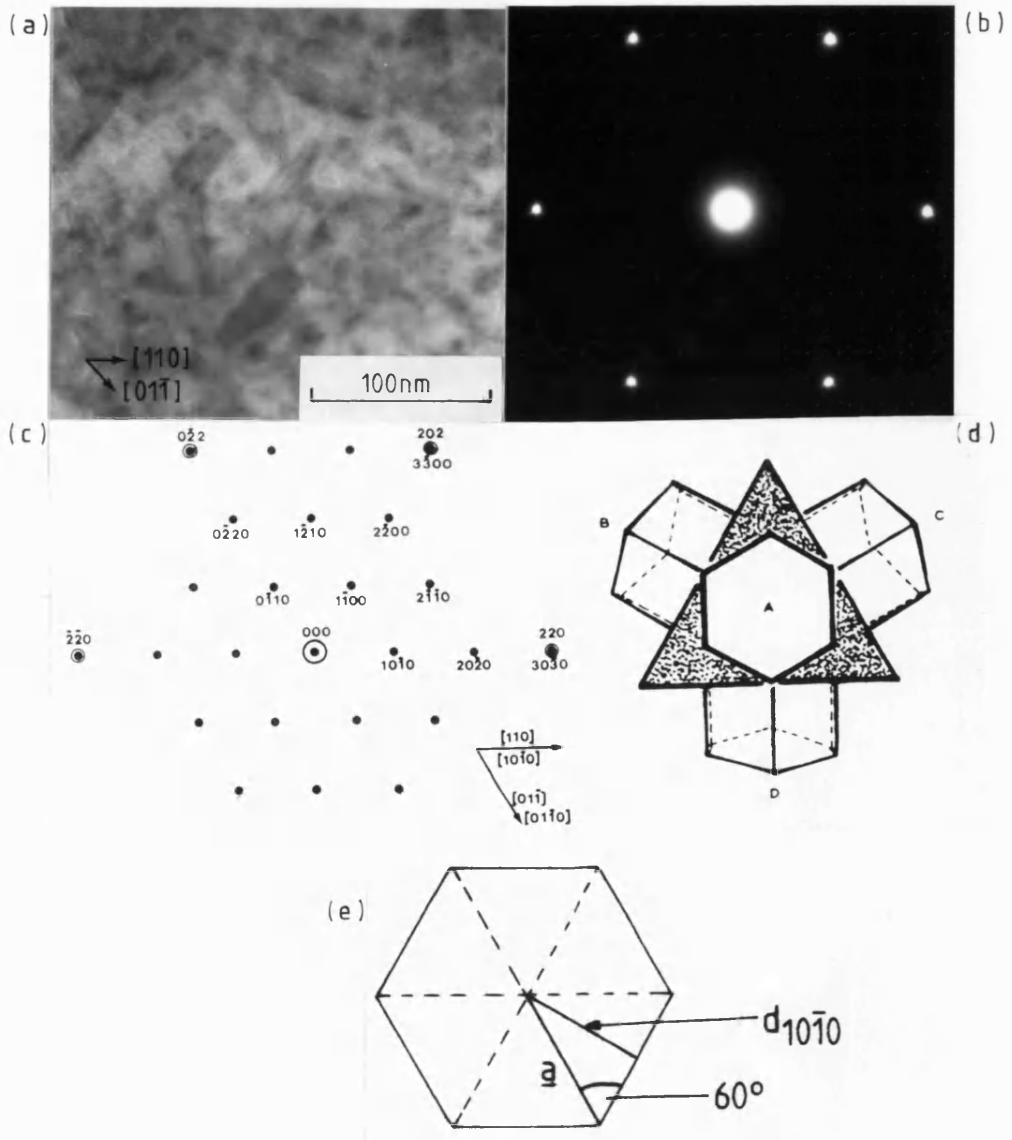

Figure 3.10 Alloy A3 aged to peak hardness at 170°C,[111] foil; (a) precipitates on {111} planes,(b)electron diffraction pattern,(c)indexed pattern,(d)precipitate orientations viewed along [111],(e) a parameter calculation.

parallel to the beam direction; the diffraction spots produced from these planes coincide with those from the first precipitate, orientation A. Such coincidences also occur for diffractions such as h1 $\overline{h+1}$ 0 etc. Thus, it is now possible to calculate the $\underline{a}$ parameter of the hexagonal unit cell. Referring to Figure 3.10e, a representation of the basal plane of the hexagonal unit cell, the $\underline{a}$ parameter is given by:

$$\underline{a} = d^{ppt}_{10\bar{1}0} \Big/ \cos 30°$$

$$\underline{a} = d^{ppt}_{10\bar{1}0} \times \frac{2}{\sqrt{3}}$$

Also, the $\{10\bar{1}0\}$ is equal to ×3 the {220} plane spacing of aluminium, ie:

$$\underline{a} = 3 \times d^{A\ell}_{220} \times \frac{2}{\sqrt{3}}$$

$$\rightarrow \qquad \underline{\underline{a \equiv 0.496 \text{ nm}}}$$

Returning to Figure 3.11a, where two sets of precipitates are seen edge-on the beam, the corresponding electron diffraction identifies this region of the foil as $[1\bar{1}0]$. The extensive streaking which produces the diamond shape pattern originate from these two sets of precipitates. The other two sets of precipitates, indexed in Figure 3.11c, give rise to the symmetrical pattern of sharp spots. These precipitates are oriented with $(10\bar{1}0)$ parallel to the beam to produce the horizontal row of $h0\bar{h}0$ diffractions. Hence:

$$[10\bar{1}0]_{ppt} \parallel [110]_{A\ell}$$

as deduced from the previous analysis. A drawing of the precipitates when viewed along the $[1\bar{1}0]$ direction is shown in Figure 3.11d; A and B are the edge-on precipitates seen in Figure 3.11a, and C produces the diffraction spots in Figure 3.11b. Orientation D is not shown but is symmetrically beneath C, and diffractions from D coincide with those produced by C. Indexing Figure 3.11.c reveals that, for orientations C and D, the plane giving a diffraction spot equal to

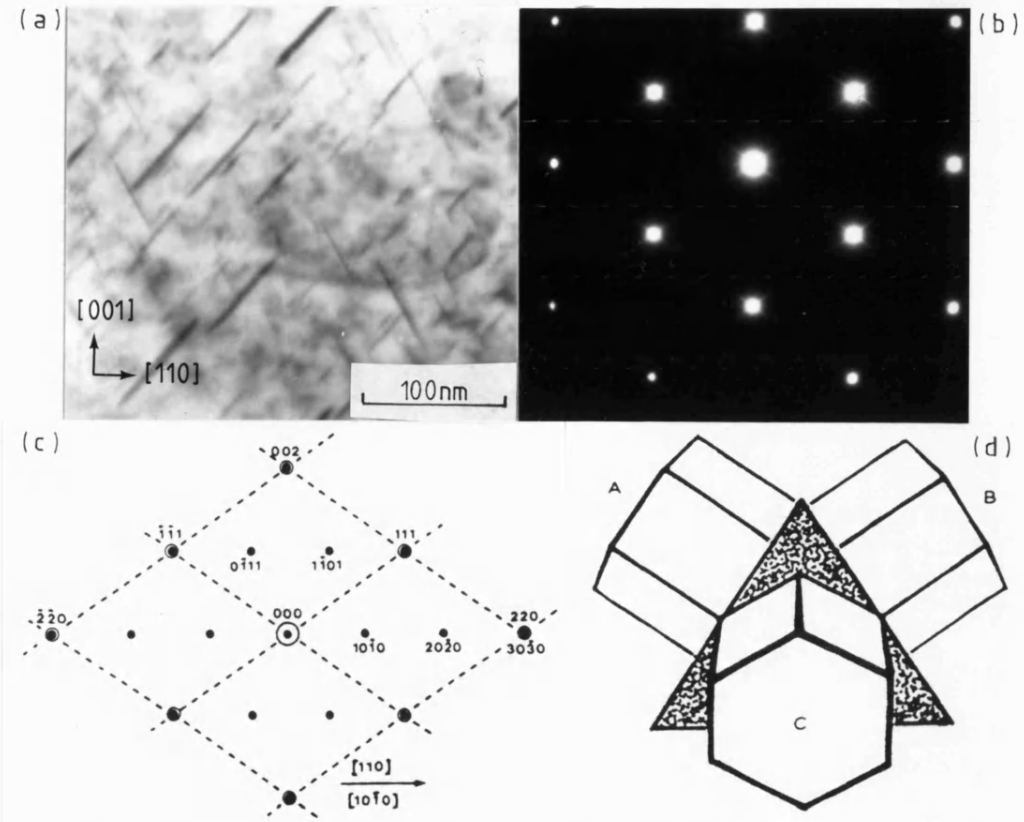

Figure 3.11 Alloy A3 aged to peak hardness at 170°C,[110] foil; (a)precipitates on {111} planes,(b)electron diffraction pattern,(c)indexed pattern,(d)precipitate orientations viewed along [110].

d^{Al}_{111} is $(2\bar{1}\bar{1}1)$. Therefore, the value of the c parameter of the hexagonal unit cell of the precipitate can be calculated using the expression:

$$\frac{1}{d^2} = \frac{4}{3a^2}(h^2 + hk + k^2) + \frac{\ell^2}{c^2}$$

$$c = 0.702$$

$$\rightarrow \quad \underline{c/a = 1.414}$$

Figure 3.12a shows a foil orientation where only one set of precipitates is seen parallel to the beam. The corresponding diffraction pattern, Figure 3.12b, indicates a foil orientation of $[\bar{1}12]$. It is this set of precipitates which produces the long vertical streaks seen in the diffraction pattern (see orientation A in Figure 3.12d), the distance between streaks being equal to a lattice vector of 0.429 nm, ie $3 \times d_{220}$ aluminium, plane spacing. Two systems of short streaks at different angles are also visible as well as a system of sharp spots lying along horizontal rows through the aluminium diffractions. The system of short streaks are produced by orientations B and C, whilst the sharp spots are produced by orientation D (see Figure 3.12d). In the accompanying indexed pattern, Figure 3.11c, different symbols are used to identify the various precipitate orientations; for example, open triangles represent the system of short diffraction streaks from orientation C, closed triangles the other set from orientation B, etc. The precipitate diffractions from orientation B are indexed on the basis of the proposed hexagonal unit cell ie with c/a = 1.414.

This orientation has $[4\bar{5}13]$ parallel to the beam direction $[\bar{1}12]$ and this is consistent with the orientation relationship previously described, ie

$$[0001]_{ppt} \parallel [\bar{1}11]_{Al} \text{ and } [10\bar{1}0]_{ppt} \parallel [101]_{Al}$$

The sys$[0001]_{ppt} \parallel [\bar{1}11]_{Al}$ and $[10\bar{1}0]_{ppt} \parallel [101]_{Al}$ a mirror image of the filled triangles about the vertical axis, and these can also be indexed. The sharp spots, represented by closed circles, are produced by orientation D and give a series of $h0\bar{h}0$ reflections, $d_{30\bar{3}0}$ coinciding with d_{220} from aluminium, as previously described.

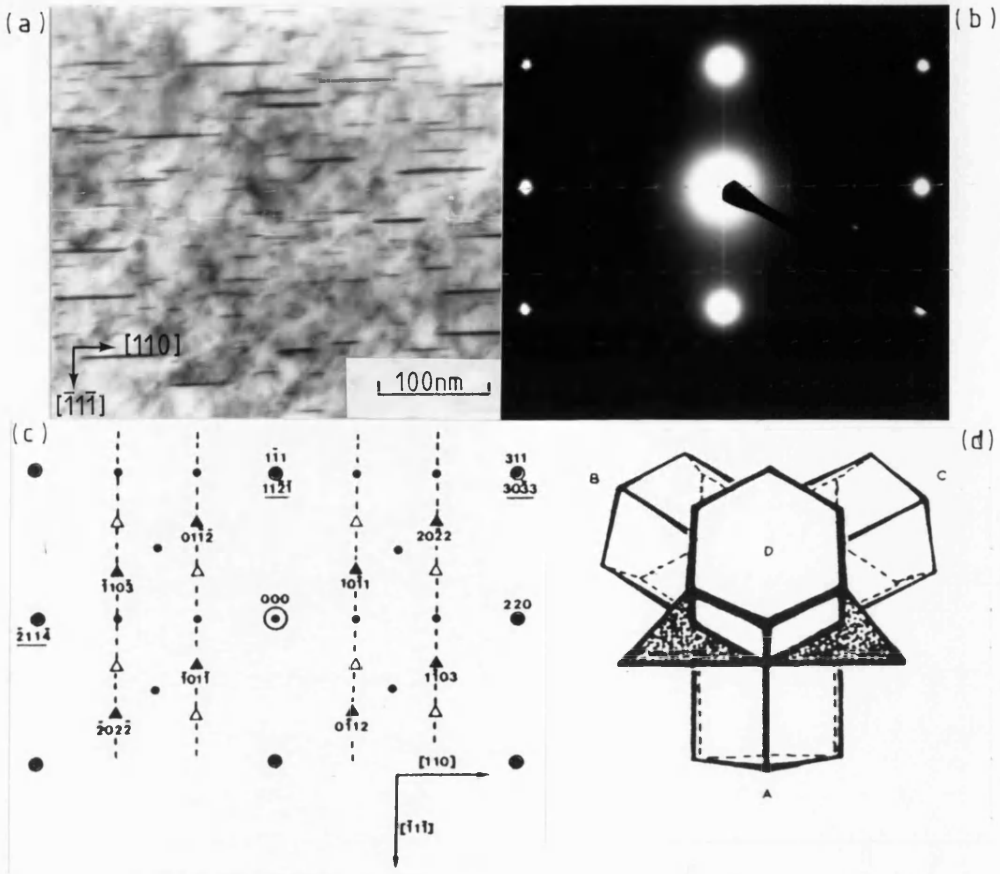

Figure 3.12 Alloy A3 aged at 170°C to peak hardness,[112] foil; (a) precipitates on {111} planes,(b)SADP,(c)indexed pattern,(d)precipitates orientations viewed along [112].

A [001] electron diffraction pattern is shown in Figure 3.13a. This, too, is a symmetrical pattern and the absence of any large scale streaking is consistent with the precipitates lying on the four [111] planes of the aluminium lattice. The indexed pattern, Figure 3.13b, indicates two single crystal orientations, identified by circles and triangles respectively. Both orientations have $\langle 22\bar{4}3 \rangle$ parallel to the electron beam, [001]. This direction is the lattice vector joining opposite sides of the hexagonal unit cell, and is again equivalent to the proposed orientation relationship. The four precipitates orientations as viewed along the cube axis of aluminium is shown in Figure 4.12c and clearly shows the symmetry of the composite structure, with each opposite pair of precipitate orientations (AB and CD) producing a single-crystal spot pattern at 90° to the other (see Figure 3.13c).

Alloy A4, which also showed an absence of [100] precipitation, was treated in the same manner as alloy A3. Figure 3.14a shows a <110> foil orientation and again there are two sets of precipitates lying parallel to the electron beam. The corresponding electron diffraction pattern, Figure 3.14b, shows the long streaking produced by these edge-on precipitates. The diffraction spots are produced by the other two precipitate orientations and is consistent with Figure 3.11b. This, therefore, is also indicative of precipitation on only the {111} planes of the aluminium lattice. Thus, by choosing those low index electron diffraction patterns analysed for alloy A3, it was possible to ascertain that, in alloy A4 at peak hardness at 170°C, the precipitates lying on {111} matrix planes of aluminium have a hexagonal structure with:

$$\left.\begin{aligned} \underline{a} &= 0.496 \text{ nm} \\ \underline{c} &= 0.701 \text{ nm} \end{aligned}\right\} \rightarrow c/a = 1.414$$

$$[0001]_{ppt} \parallel \langle 111 \rangle_{A\ell} \text{ and } \langle 10\bar{1}0 \rangle_{ppt} \parallel \langle 110 \rangle_{A\ell}$$

With the structure of this precipitate now established it is possible to return to alloy A5 aged to peak hardness at 170°C and analyse the precipitates lying on the {100} aluminium matrix planes. Figures 3.15a and 3.16a show the electron diffraction patterns from various foil orientations of alloy A5 when aged to peak hardness.

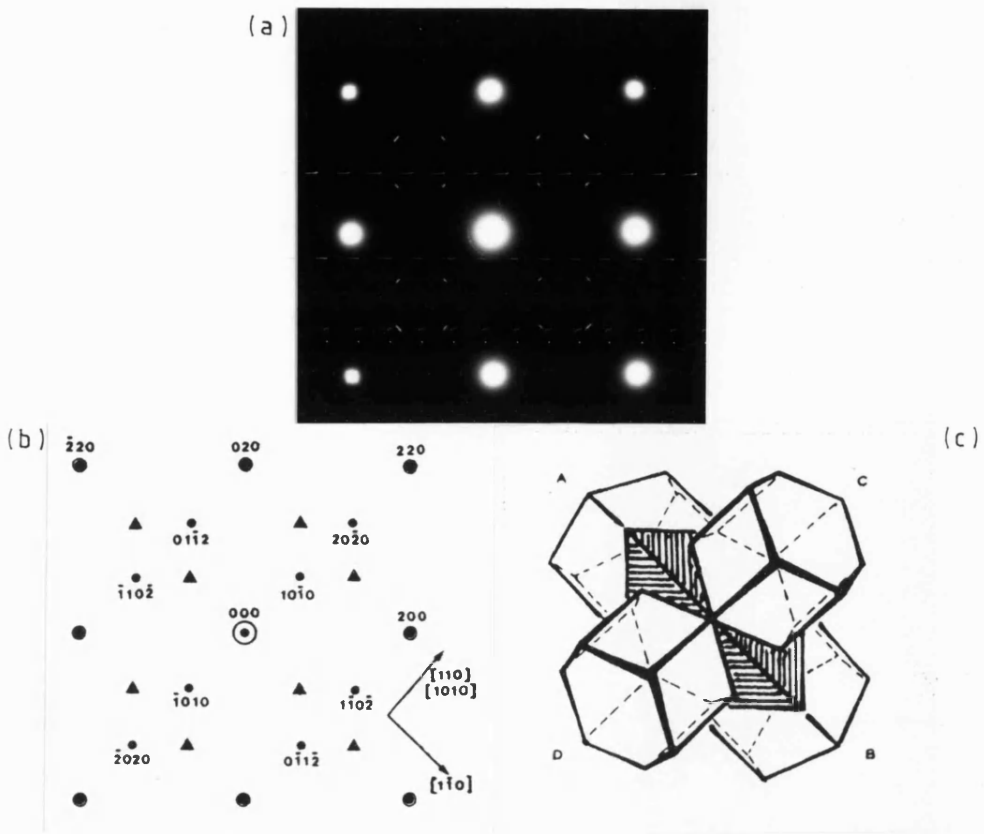

Figure 3.13 Alloy A3 aged at 170°C to peak hardness,[100] foil; (a)electron diffraction pattern,(b)indexed pattern,(c)precipitate orientations viewed along [100].

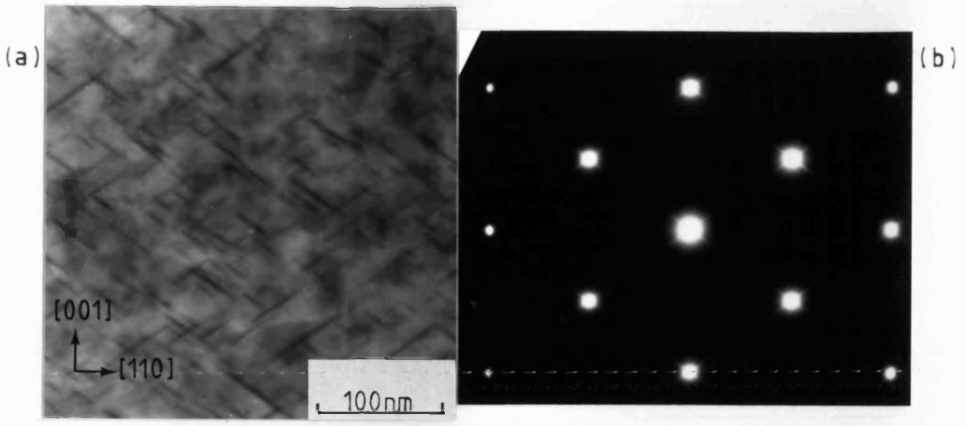

Figure 3.14 Alloy A4 aged to peak hardness at 170°C,<110> foil; (a)electron micrograph,(b)corresponding SADP.

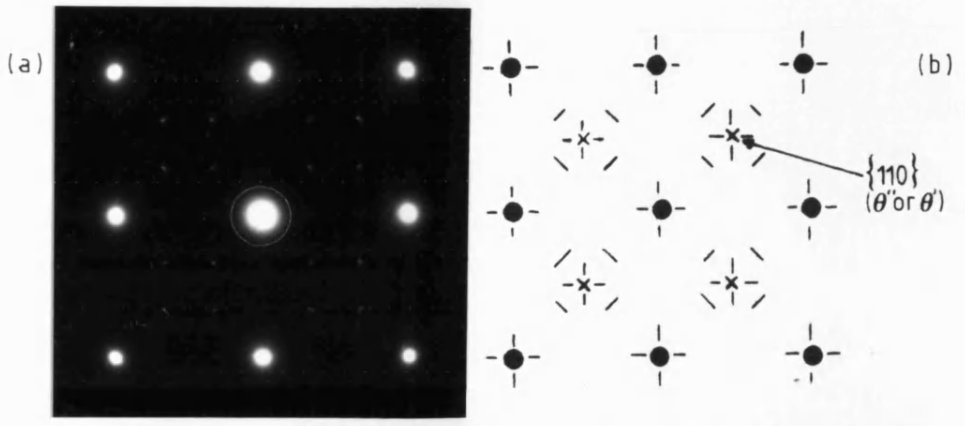

Figure 3.15 Alloy A5 aged at 170°C to peak hardness,<100> foil; (a) SADP,(b)indexed pattern.

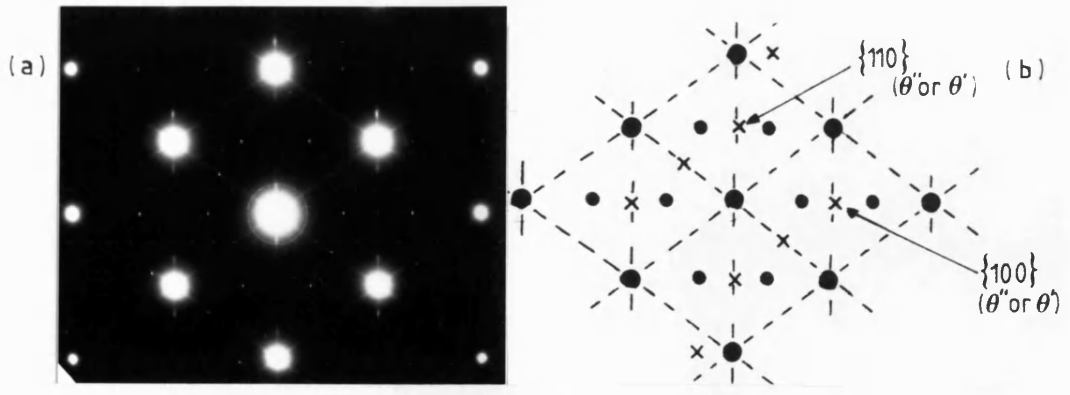

Figure 3.16 Alloy A5 aged to peak hardness at 170°C,<110> foil; (a) SADP,(b)indexed pattern.

Both diffraction patterns show evidence of streaking in the <100> directions, indicative of precipitation on {100} matrix planes. In the <100> zone SADP, Figure 3.15a, there are spots present at half the distance to a {220} aluminium reflection, ie reflections from a plane having a d spacing equal to twice the $d^{A\ell}_{220}$ plane spacing. This reflection, representing a plane with d_x = 0.286 nm, can be indexed on the basis of both the θ" and θ' unit cells which both have a {110} plane spacing of 0.286 nm. These were the only spots which could be indexed (see Figure 5.15b). However, there are many diffuse streaks apparent along <100> directions around the diffraction spots from aluminium and also around the {110} θ' (or θ") diffraction spots. These diffuse streaks are characteristic of the presence of θ" and θ' in binary aluminium-copper alloys. (For example, see Silcock[57]).

Figure 3.16a is a <110> zone SADP from alloy A5 in the peak hardness condition (at 170°C). As well as the large scale streaking in <111> directions there is also diffuse streaking in the <100> direction, indicative of precipitation on {100} aluminium matrix planes. This is also shown in the indexed pattern in Figure 3.16b. Spots from the {111} type precipitate are indicated by closed circles and have been indexed previously. Spots from precipitates on {100} matrix planes are marked with crosses. Again, there are diffraction spots at $\frac{1}{2} \times R_{220}$ aluminium, giving a plane spacing of 0.286 nm, and as indicated above these can arise from either θ" or θ' precipitates. Also there are distinct spots at $\frac{1}{2} \times R_{200}$ aluminium. This is equivalent to a plane with a spacing of $2 \times d_{200}$ aluminium ie these reflections originate from planes with a spacing of 0.404 nm. Again, these spots can be indexed on the basis of either the θ" or θ' unit cells which both have {100} planes at a spacing of 0.404 nm. The diffuse streaking in the {100} directions also appears to have produced "satellites" around each bright aluminium diffraction spot. Such "satellites" are a characteristic of θ" and θ' presence on {100} matrix planes (see Silcock[57]). These effects will be discussed in more detail later.

In summary, Alloys A3 and A4, when aged to peak hardness at 170°C, contain only precipitates which lie on {111} aluminium matrix planes. These have been identified as having a hexagonal unit cell

with c/a = 1.414 and having an orientation relationship with the aluminium matrix such that:-

$$[0001]_{ppt} \parallel \langle 111 \rangle_{A\ell} \quad \text{and} \quad \langle 10\bar{1}0 \rangle_{ppt} \parallel \langle 110 \rangle_{A\ell}$$

On the other hand, alloy A5 in the peak hardness condition contains precipitates on both {100} and {111} aluminium matrix planes. The precipitates on the {111} matrix planes are hexagonal, as described previously. The precipitates on {100} planes have been identified as either θ" or θ', ie in accord with data available on aluminium-copper binary alloys.

3.3.3 Calibration curve for foil thickness determination

In order that quantitative data concerning the nucleation and growth of precipitates could be obtained it was necessary for the foil thickness to be measured at specific points of interest. In this respect the measurement of X-ray intensity from such areas has been used. The x-ray intensities were converted into foil thickness using a calibration curve of continuum x-ray intensity versus foil thickness as determined by an independent method; ie the fault tilt method. The calibration curve used for all measurements of foil thickness for nucleation and growth data is shown in Figure 3.17. This indicates that for the two x-ray energy channels analysed, 3.5 to 5.5 keV and 9.5 and 11.5 keV, there is a linear relationship between x-ray emission and foil thickness, with correlation coefficients of 0.986 and 0.988 respectively. Thus, the foil thickness from all specimens at the point of interest was found by recording the x-ray emission from this region and simply reading the value of foil thickness from the calibration curves.

However, it must be noted that there are several possible errors in the construction of such a calibration curve. Firstly, measurements of the projected widths of the intersecting precipitates were made from TEM negatives, using accuracy of ±0.1 mm. All measurements were taken from negatives of magnification ×50,000 and this indicates an accuracy of ±2 nm in projected width measurement. In the thinnest region analysed this gives an expected error of ±3%.

Secondly, there will be an error in the x-ray counting statistics. For all measurements of x-ray intensity a spot size of

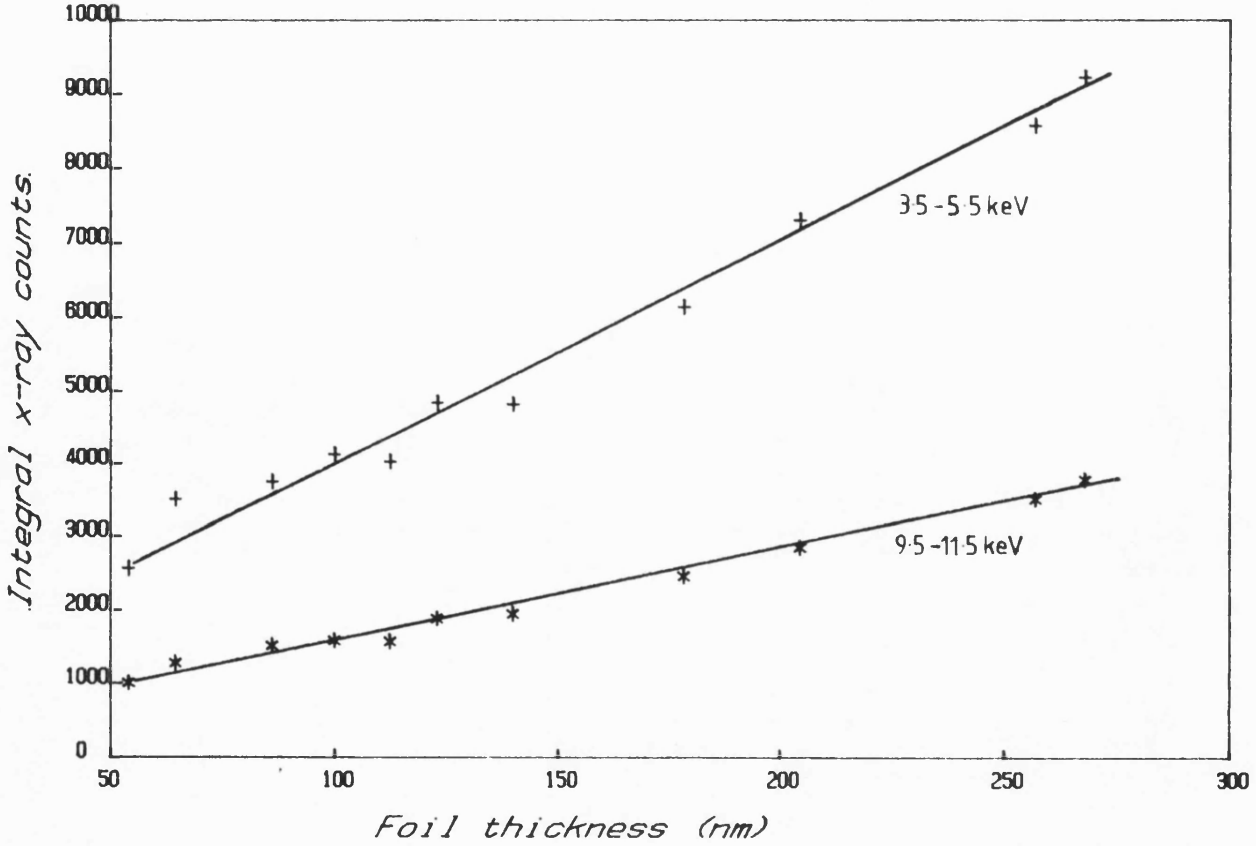

Figure 3.17 X-ray counts as a function of foil thickness

300 nm was used. However, it was noted that movement of the electron beam by approximately 600 nm (ie two spot diameters) could produce a change of up to 10% in the x-ray counts due to local differences in foil thickness. Therefore, every effort was made to minimise this error.

The standard deviation (S) for the measurement of x-ray photons is given by the square root of the total number of counts (N). The standard error of the count is given by:

$$\varepsilon = \frac{S}{N} = \frac{1}{\sqrt{N}}$$

Hence, a high counting time and a large window width were used in order to minimize, as far as possible, the error associated with the collection of x-ray photons. Generally, however, the error in x-ray intensity measurements associated with counting statistics was probably no more than 2%. Thus, the overall accuracy of the calibration curve was estimated to be ±5%.

3.3.4 Nucleation and Growth of precipitates

In this section data are presented on the nucleation and growth of precipitates as a function of ageing time at 140°C. As far as the examination of samples aged at 170°C was concerned, the faster reaction kinetics at this temperature made a quantitative study of the early stages of precipitate nucleation and growth difficult.

Precipitate data obtained from all three alloys after ageing at 140°C are summarised in Table 3.1.

3.3.4.1 Alloy A5

In alloy A5, which showed precipitates on both {100} and {111} planes of the aluminium lattice in the peak hardness condition, precipitates were first observed to form on {100} lattice planes after ageing for only 2 h at 140°C, with an average diameter of ≈6 nm, see Figure 3.18a taken from a [100] foil. The corresponding electron diffraction pattern, Figure 3.18b, shows streaks through 200-type aluminium diffractions extending from one diffraction spot to the next (000 to 200, 020 to 022, etc). These streaks are associated with the two sets of precipitates oriented edge-on to the electron beam, the length of streaking being consistent with a

Table 3.1

Precipitate data obtained by ageing at 140°C

Alloy	Time (h)	d (nm)	t (nm)	V (nm^3)	N $x10^{22}m^{-3}$	f
A3	2					
{100}	3	9.5	2.3	131	2.3	0.003
	4	16.3	1.5	313	2.5	0.008
	7	22.5	2.5	994	1.3	0.013
	16	18.2	2.2	572	0.7	0.004
	100	47.7	3.0	5360	0.1	<0.001
{111}	2	6.5	1.0	33	5.0	0.002
	3	7.9	1.5	74	10.0	0.007
	4	13.8	1.6	240	9.7	0.024
	7	17.6	1.8	438	7.6	0.033
	16	20.2	2.5	800	6.6	0.053
	48	27.0	3.0	1718	3.3	0.057
	100	35.5	3.0	2970	2.0	0.058
A4	2	11.2	1.6	158	0.7	0.001
{100}	3	10.9	1.6	150	1.3	0.002
	4	10.7	1.6	144	0.45	0.001
	7	12.1	1.8	207	0.8	0.002
	25	22.2	2.5	965	0.2	0.002
	48	32.8	3.2	2704	<0.01	<0.001
	72	46.8	3.8	6540	<0.01	<0.001
	100	51.5	4.2	8750	<0.01	<0.001
{111}	2	9.4	1.4	97	4.2	0.004
	3	10.1	1.5	120	4.8	0.006
	4	11.7	1.6	161	6.9	0.012
	7	13.7	1.8	265	7.2	0.019
	25	20.0	2.8	880	4.5	0.040
	48	23.3	3.0	1280	4.2	0.054
	72	29.6	3.0	2064	2.7	0.056
	100	32.0	3.0	2413	2.3	0.056
A5	2	6.9	0.4	15	82	0.012
{100}	7	14.9	1.4	244	12	0.029
	16	18.9	1.4	392	8.2	0.032
	24	20.5	1.5	495	3.4	0.017
	48	26.3	1.6	870	2.1	0.018
	120	37.4	2.8	3075	0.5	0.015
	400	39.3	2.8	3395	0.4	0.014
{111}	2					
	7	11.5	1.8	187	2.2	0.004
	16	13.3	1.9	264	5.5	0.015
	24	20.3	2.2	712	4.9	0.027
	48	22.6	2.7	1083	3.6	0.039
	120	30.0	2.8	1980	2.4	0.048
	400	45.4	3.2	5180	0.9	0.047

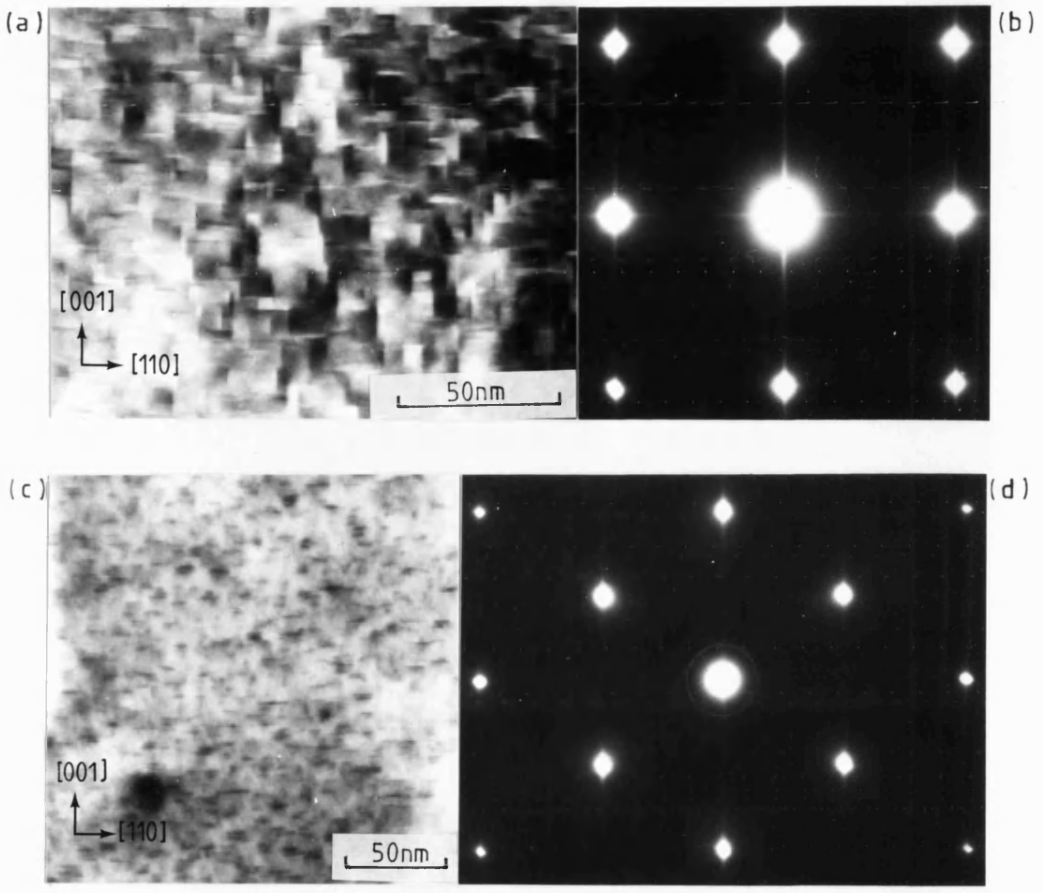

Figure 3.18 Alloy A5 aged for 2h at 140°C;
(a)<100> electron micrograph,(b)corresponding
SADP,(c)<110> foil electron micrograph,(d) corresponding
electron diffraction pattern.

platelet thickness of unit cell dimensions. Very faint spots positioned half-way between the centre spot and 220-type diffractions are seen on the negative, but are not visible on the print. These spots are produced by the set of precipitates lying perpendicular to the electron beam and correspond to a d-spacing of 0.28 nm, the [110] foil shown in Figures 3.18c and d confirm these findings. However, the data do not allow the {100}-type precipitates to be identified as either θ" or θ' phase.

As ageing time increased the microstructure changed progressively, with precipitate sizes increasing to a mean of ∿25 nm after 48 h at 140°C, Figure 3.19a. From the corresponding SADP, Figure 3.19b, it can be seen that the length of 200-type streaking is now one-third the inter-spot distance. This is in accord with the observed thickening of precipitate platelet to ≈2 nm. The indexed pattern is shown in Figure 3.19c, and spots corresponding to a d-spacing of 0.28 nm, labelled a, in Figure 3.19c, are stronger. Surrounding each of these spots are four short arcs, marked b_1 to b_4, which are produced by the precipitates on {111} planes. These have been identified as having a hexagonal structure (see section 3.3.2) and designated Ω phase, following Chester and Polmear[115]. In the [110] foil orientation, Figure 3.19d, three sets of edge-on precipitates are seen, two sets lying on {111} planes and the other on {100}. The corresponding electron diffraction pattern, Figure 3.19e, confirms the short streaking due to growth of the {100}-type precipitate but, in contrast, the streaks associated with the edge-on Ω platelets are very much longer. The diffraction patterns could be indexed on the basis that the phase formed on {100} planes at this stage of ageing was θ' (tetragonal with a = 0.404 nm, c/a = 1.436) . The Ω and θ' phases could not be distinguished as regards size and shape, although they form on different planes of the aluminium lattice.

On ageing to peak-hardness (ageing time ≈120 h) the mean precipitate diameters were ∿35 nm with a thickness of ≈3 nm. [100] and [110] foil orientations and their corresponding electron diffraction patterns are shown in Figures 3.20a to 3.20d. In Figures 3.20b and 3.20d streaking from θ' precipitate is virtually absent, although the long streaking from Ω remains (cf Figures 3.18d and 3.19d from <110> foils).

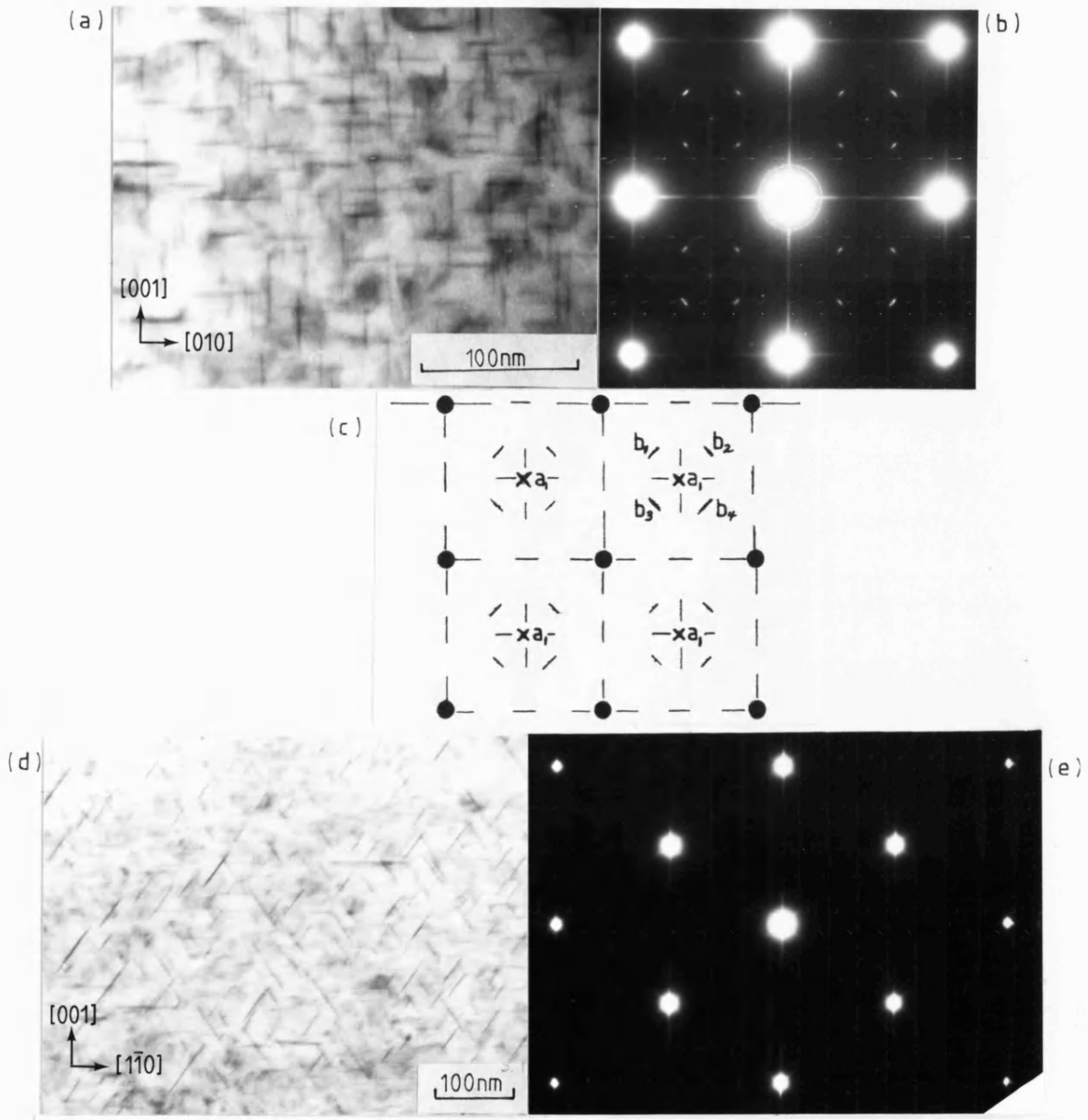

Figure 3.19 Alloy A5 aged 48h at 140°C;
(a)<100> foil electron micrograph,(b)corresponding SADP,(c)indexed pattern,(d)<110> electron micrograph,(e)corresponding <110> SADP.

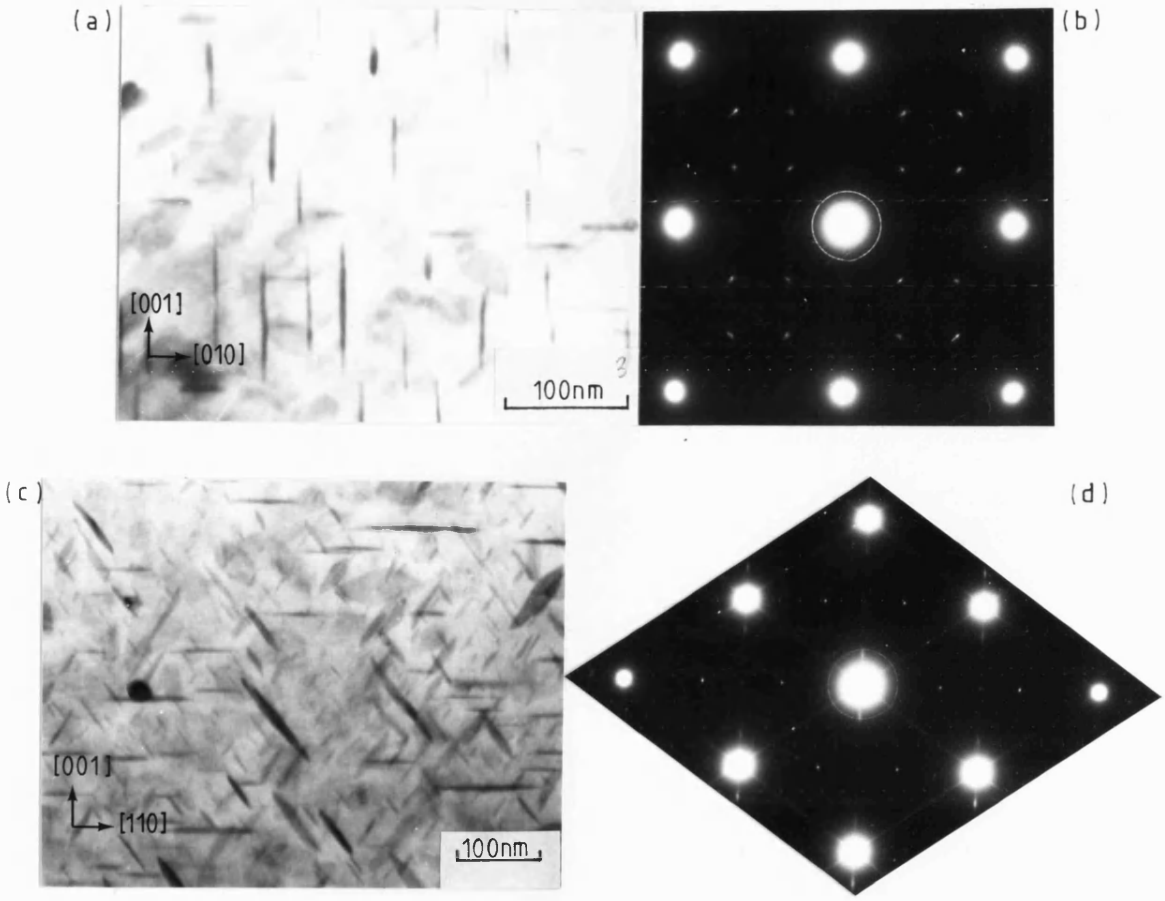

Figure 3.20 Alloy A5 aged for 120h at 140°C;
(a)[001] foil electron micrograph,(b)electron diffraction pattern,(c)[110] foil electron micrograph,(d)corresponding SADP.

In overaged material, the precipitates were larger but not measurably thicker, with proportionately more Ω phase than θ'. X-ray spectra were taken of individual Ω and θ' precipitates, but both showed only the presence of aluminium and copper.

Frequency distributions of precipitate diameters at various ageing times are illustrated in Figures 3.21a and 3.21b for θ' and Ω phases respectively. (It must be noted that the diagrams do not refer to the same measured volume of material.) The distributions can be seen to be asymmetrical with longer tails at larger diameters and a maximum particle size equal to twice the mean value. Mean precipitate diameters for θ' and Ω are plotted in Figure 3.22a as a function of ageing time. A plot of the corresponding precipitate thicknesses, Figure 3.22b shows that a limiting value of ∿3 nm is reached after 120 h at this temperature. The number of precipitates per unit volume ("precipitate density") and the volume fraction were calculated using measured foil thicknesses, as established by the continuum x-ray intensity method (see section 3.3.3). These results are illustrated in Figures 3.23a and 3.23b respectively, and clearly show a rapid decrease in the number of {100} precipitates (Figure 3.23a). However, although the number of precipitates is initially decreasing the {100} precipitate volume fraction increases, until it reaches a maximum value after ∿16 h. The {111} precipitate, on the other hand, shows an initial increase in precipitate density to a maximum after ∿24 h decreasing at longer ageing times but still remaining higher than the {100} precipitate. The volume fraction of {111} precipitate increases with time until a maximum is reached after ∿120 h.

3.3.4.2 Alloy A4

When aged for 2 h at 140°C this alloy contained precipitates on both {111} and {100} lattice planes, although there was much less of the latter phase present. A <110> diffraction pattern, Figure 3.24, shows the long 111-type streaks which characterised the Ω precipitates. Streaks of the 200-type are, however, relatively short when compared with Figure 3.18d taken from alloy A5 given the same ageing time; whether this phase was θ" or θ' could not be ascertained from the diffraction data.

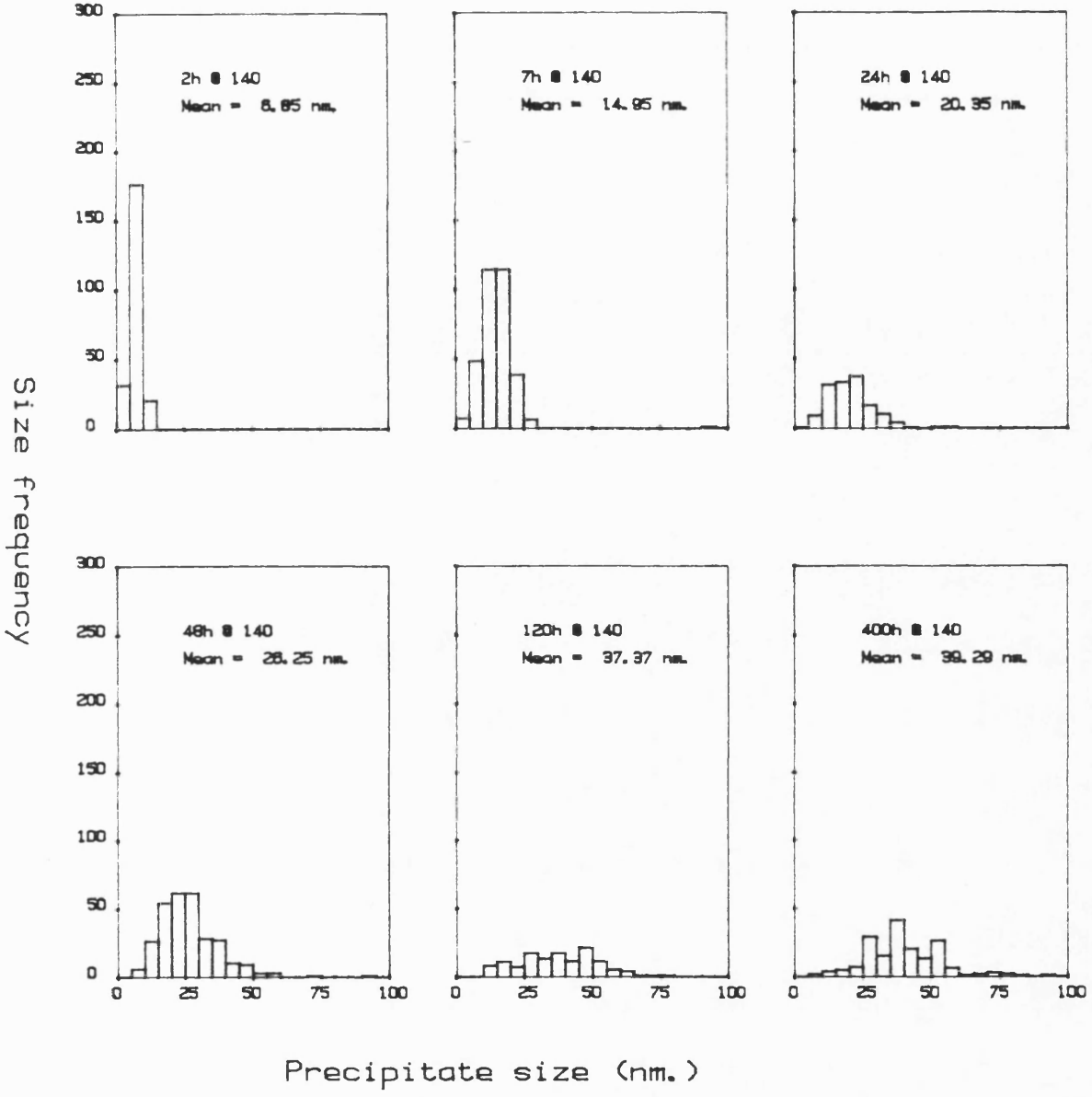

Figure 3.21.a Size distributions of θ' precipitate after various times at 140°C, alloy A5

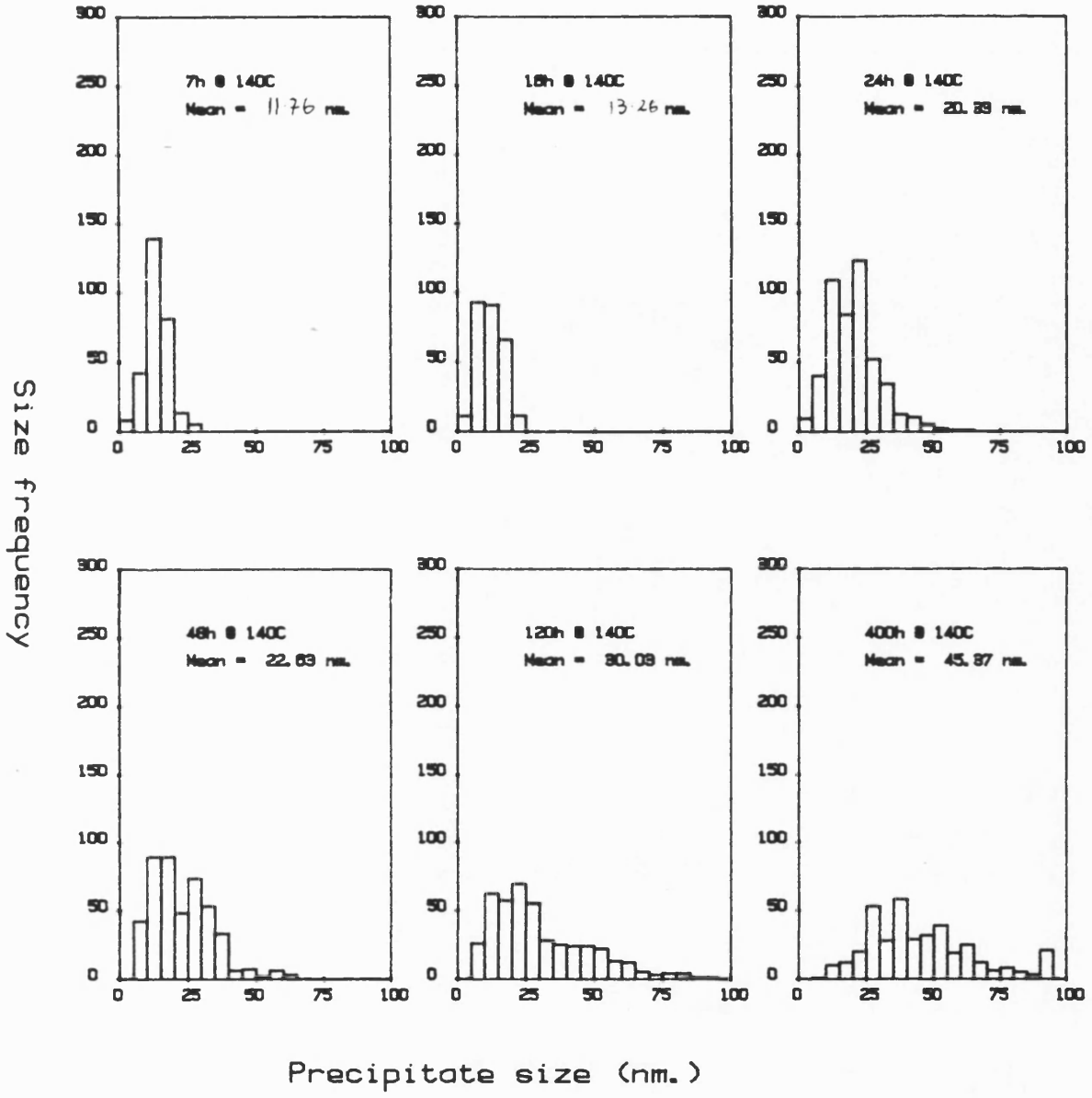

Figure 3.21.b Size distributions of Ω precipitate after various times at 140°C, alloy A5

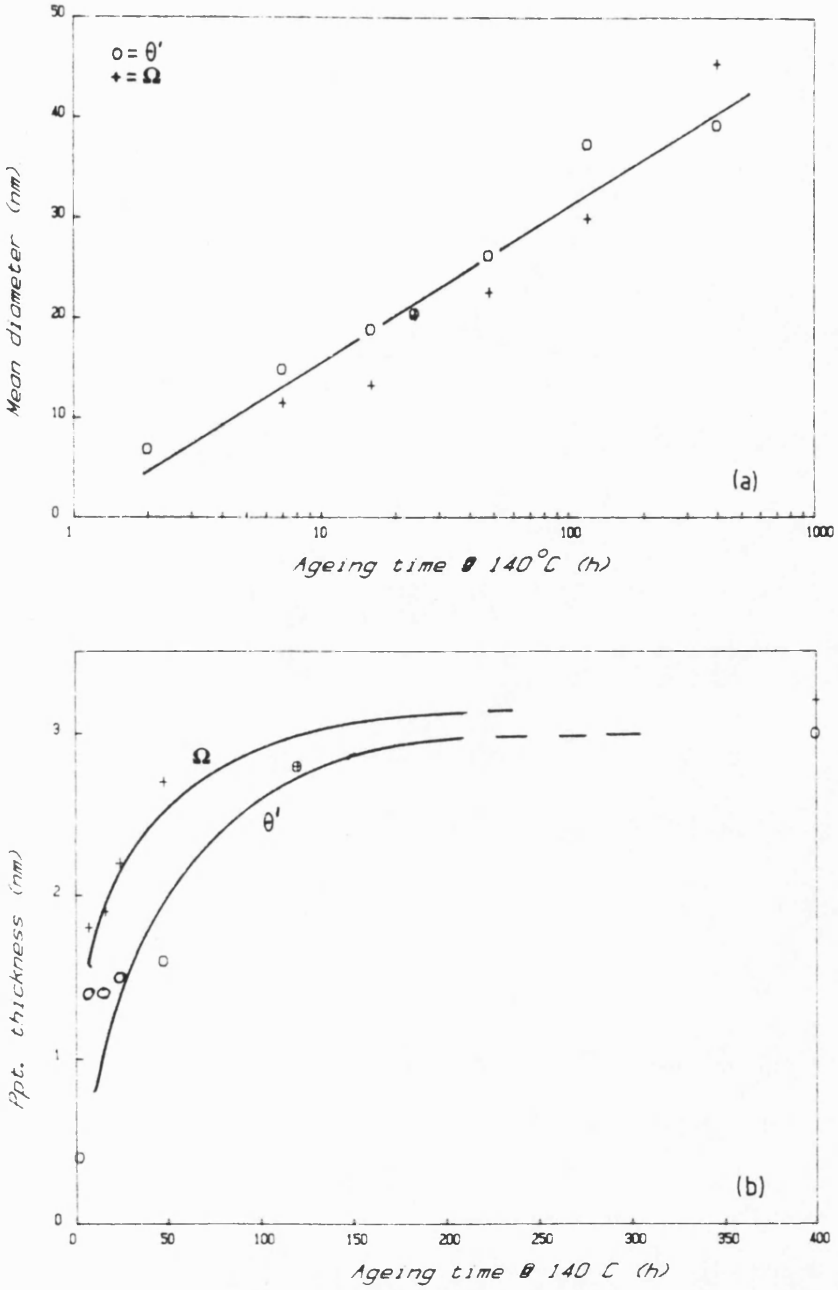

Figure 3.22 Precipitate parameters versus ageing time at 140°C for θ' and Ω precipitation in alloy A5;
(a) mean diameter , (b) mean thickness.

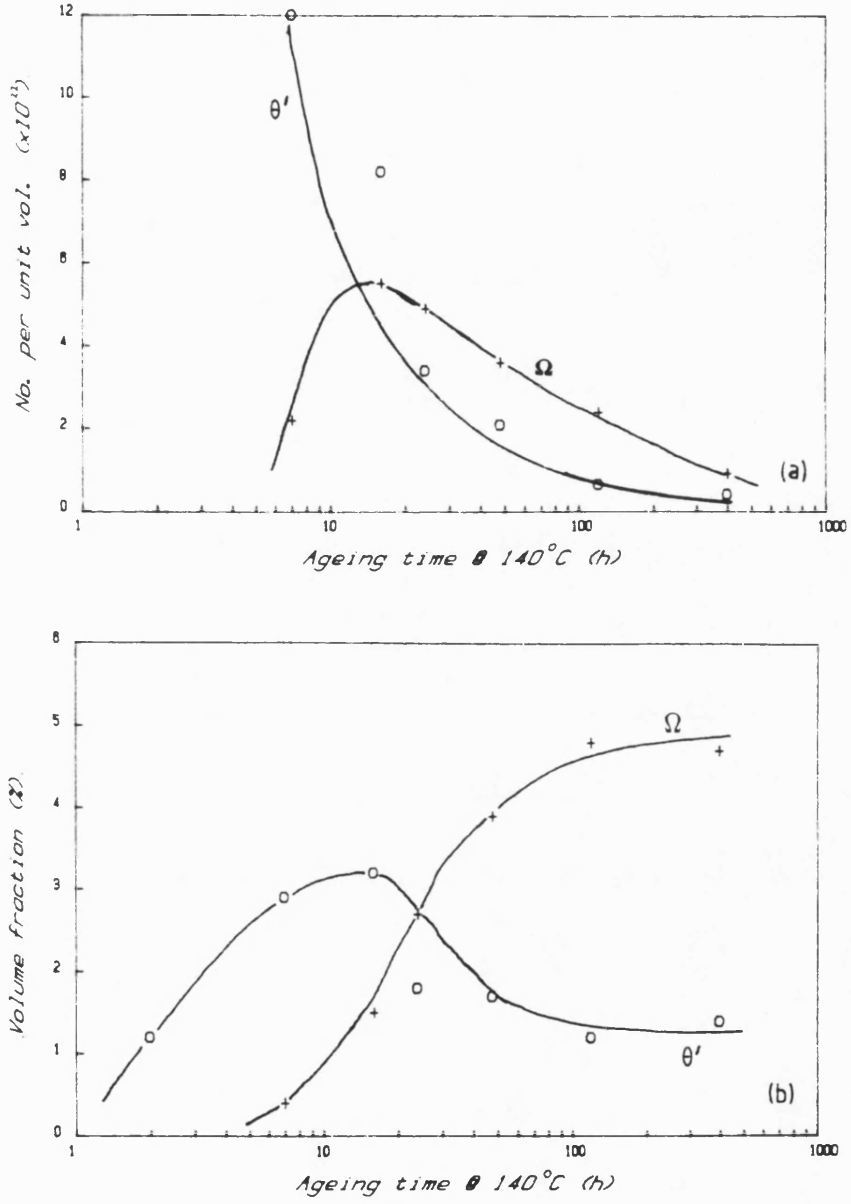

Figure 3.23 Precipitate parameters versus ageing time at 140°C for θ' and Ω precipitation in alloy A5;
(a) density , (b) volume fraction.

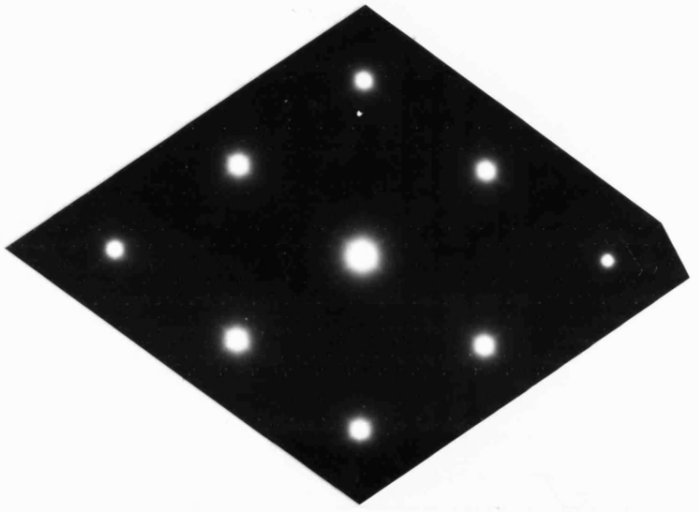

Figure 3.24 <110> selected area diffraction pattern from alloy A4 , aged 2h at 140°C

The mean precipitate diameters progressively increased with ageing time, Figure 3.25a, again reaching a limiting thickness of ≈3 nm by the time peak hardness (∿25 h) had been achieved, Figure 3.25b; this situation is similar to that shown for alloy A5 in Figure 3.22b. However, by the time peak had been reached the precipitates were essentially all Ω phase, Figure 3.26a, and no diffraction spots attributable to θ' were visible, Figure 3.26b.

The frequency distributions of precipitate diameters at various ageing times are illustrated in Figure 3.27 for the Ω precipitate. Again, the distributions can be seen to be asymmetrical with longer tails at large diameters. However, at long times the maximum particle size is roughly equal to three times the mean value. Precipitate densities and volume fractions of both types of precipitate (θ' and Ω) are shown in Figures 3.28a and 3.28b respectively. Clearly, it can be seen that the number of precipitates on {100} aluminium matrix planes remains at a low value throughout the ageing process, Figure 3.28a. The volume fraction of Ω phase increases with ageing tim at 140°C until a maximum value of ∿0.056, whilst the volume fraction of {100}-precipitate remains essentially constant, ∿0.002, throughout the ageing times investigated here, Figure 3.28b.

3.3.4.3 Alloy A3

TEM results obtained on this material were similar to those found for alloy A4. Frequency distributions of precipitate diameters at various ageing times are illustrated for the Ω precipitate in Figure 3.29. Asymmetric distributions are again apparent; the maximum size is roughly twice the mean diameter after short ageing times increasing to three times at long ageing times. The mean precipitate diameters again increased with ageing time at 140°C, Figure 3.30a, with a limiting thickness of ∿3 nm after ∿50 h, Figure 3.30b. Figures 3.31a and 3.31b show the variation in precipitate densities and volume fraction of precipitate respectively. In this alloy there appears to be slightly more θ' phase forming in the early stages of ageing, Figure 3.31a, but by the time the peak hardness had been reached (∿25 h) the precipitate was essentially all Ω phase, Figure 3.31b.

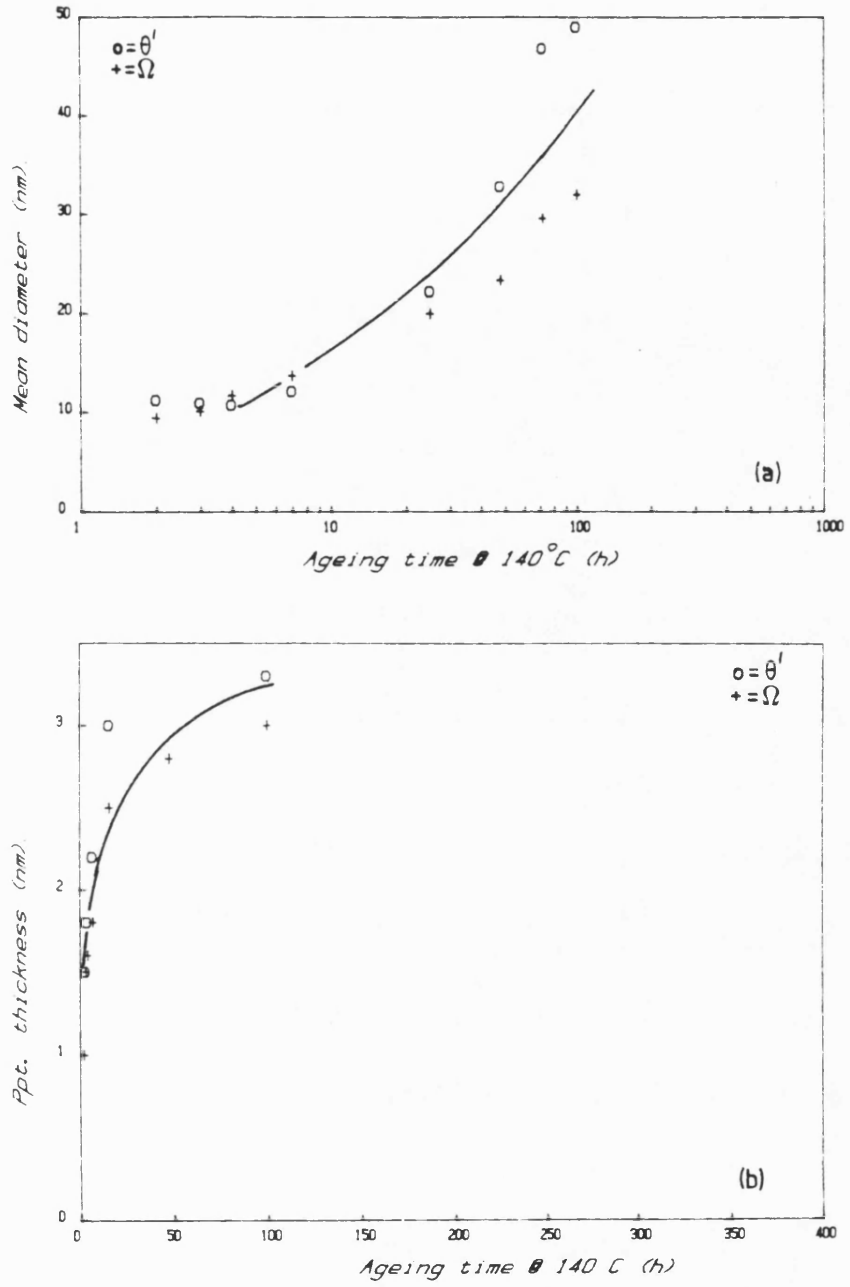

Figure 3.25 Precipitate parametrs as a function of ageing time at 140°C for θ'and Ω precipitation in alloy A4; (a) mean diameter , (b) mean thickness.

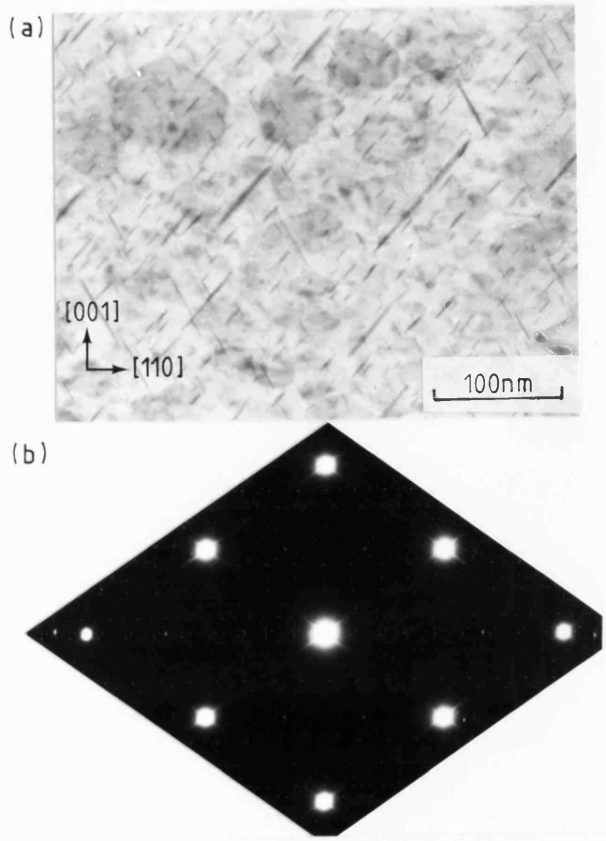

Figure 3.26 Alloy A4 aged for 30h at 140°C , <110> foil ;
(a) electron micrograph , (b) SADP .

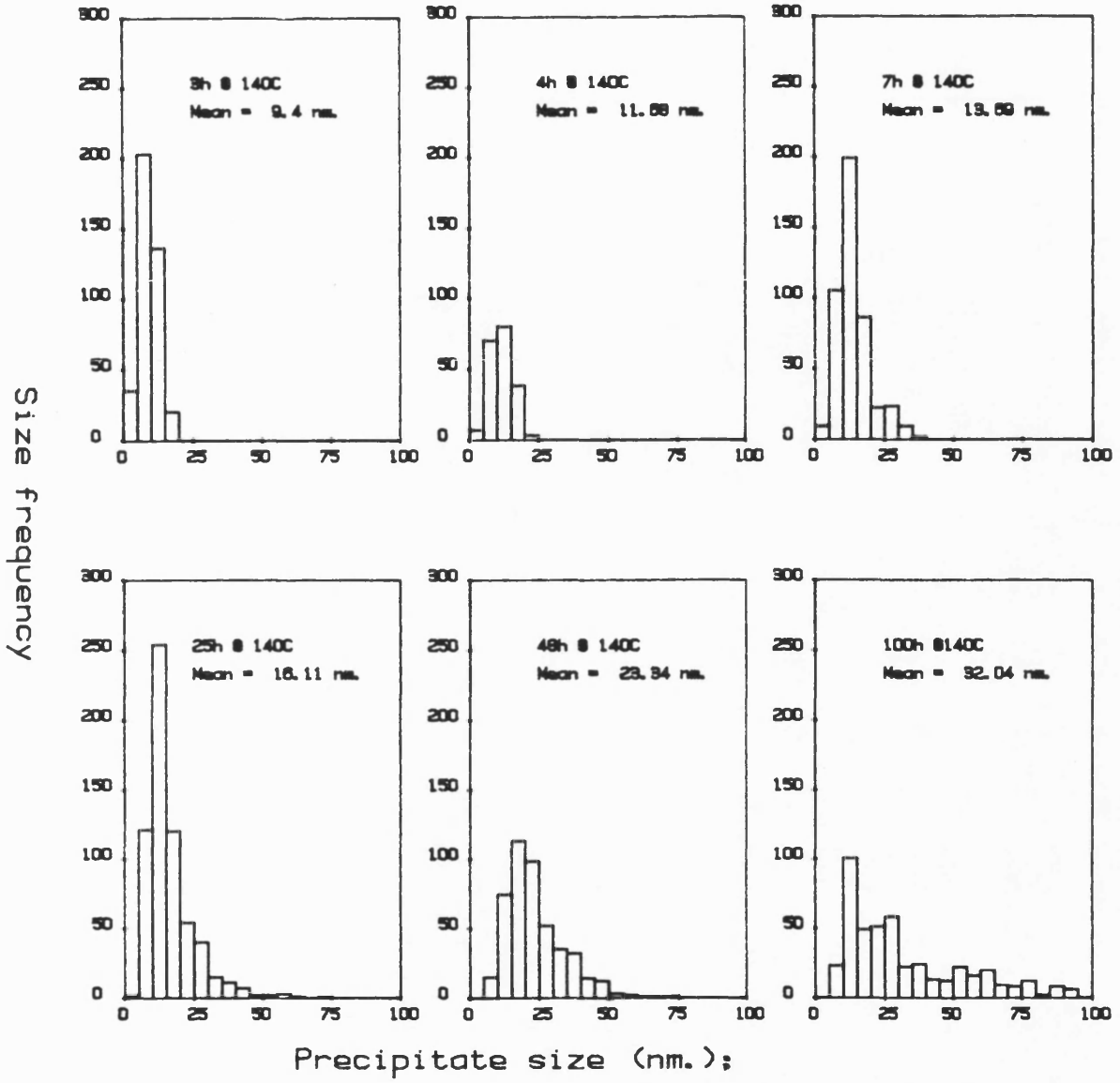

Figure 3.27 Size distributions of Ω precipitate after various times at 140°C, alloy A4

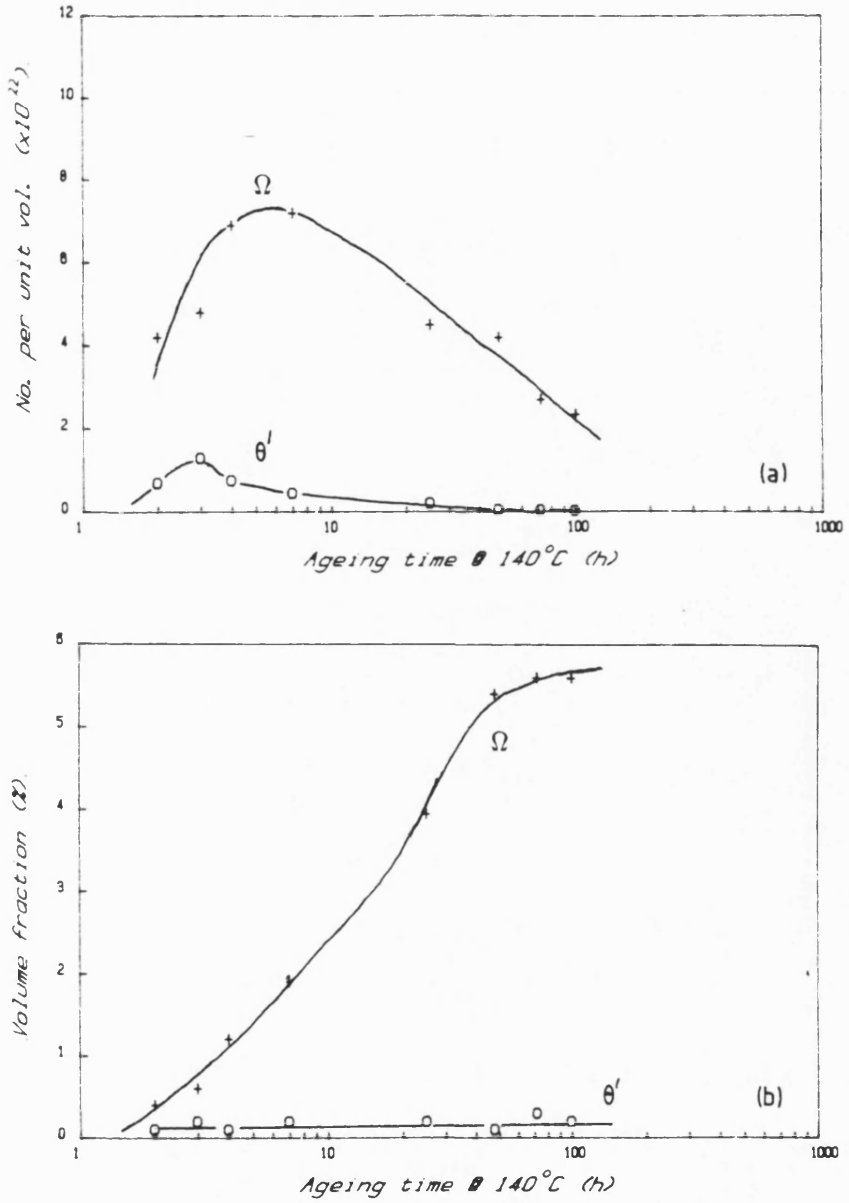

Figure 3.28 Precipitate parameters versus ageing time at 140°C for θ' and Ω precipitation in alloy A4;
(a) density , (b) volume fraction.

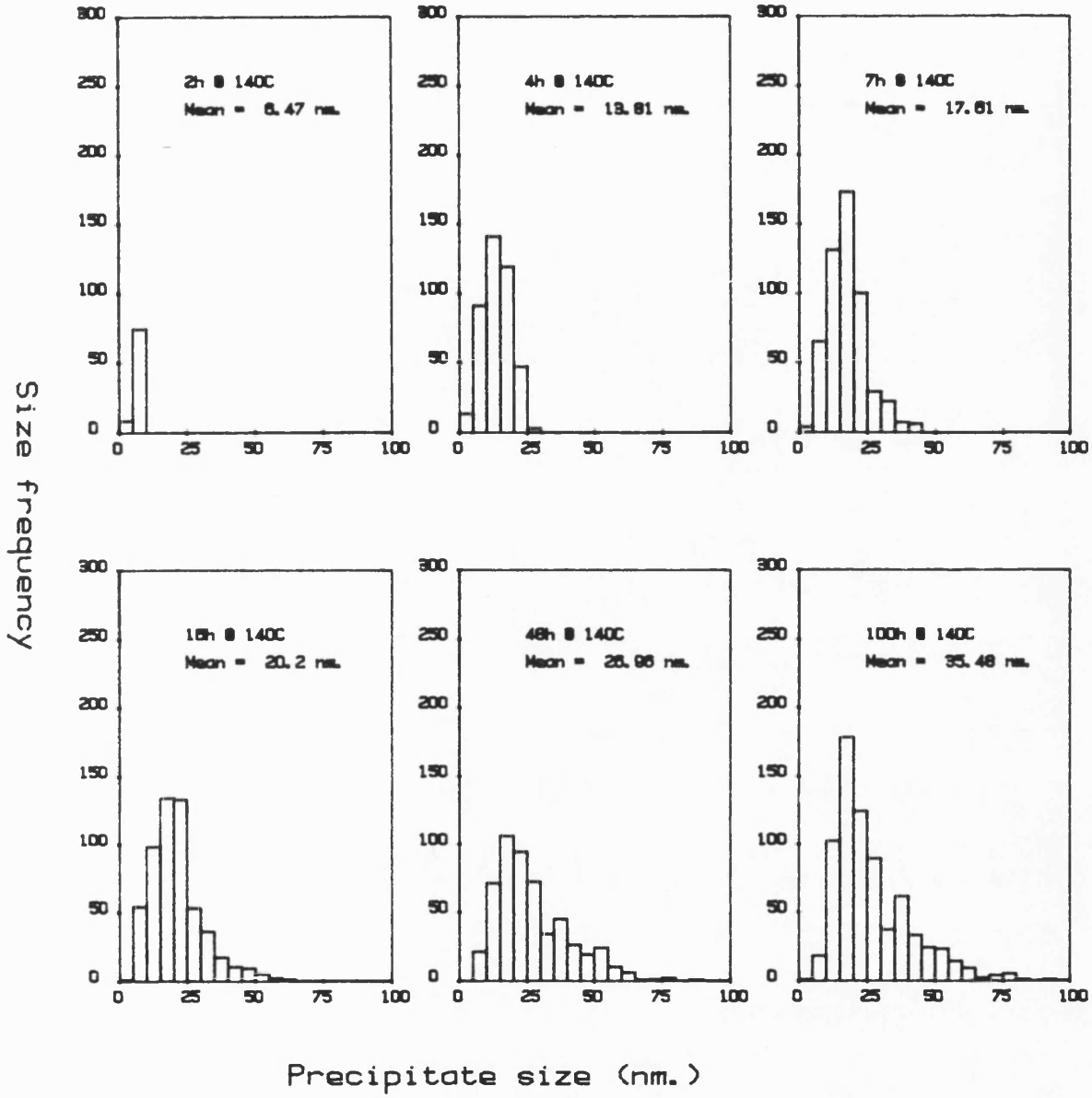

Figure 3.29 Size distributions of Ω precipitate after various times at 140°C, alloy A3

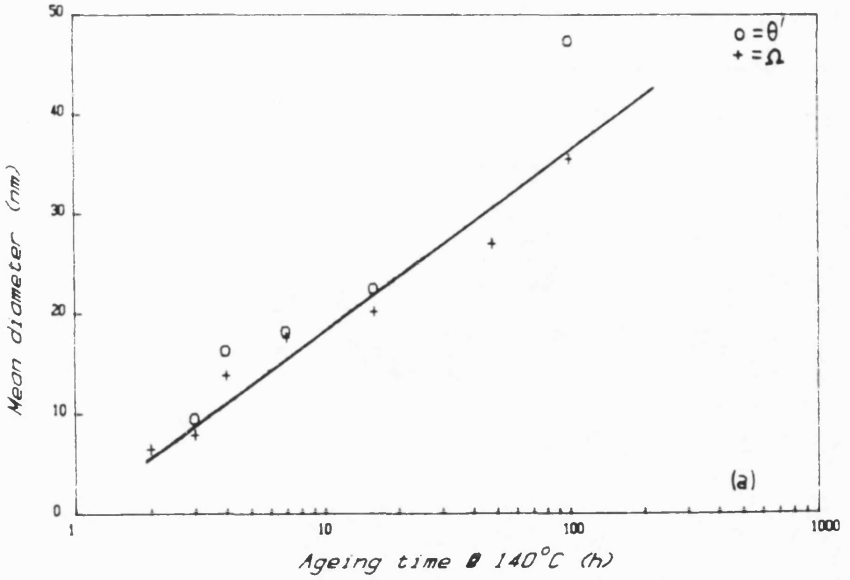

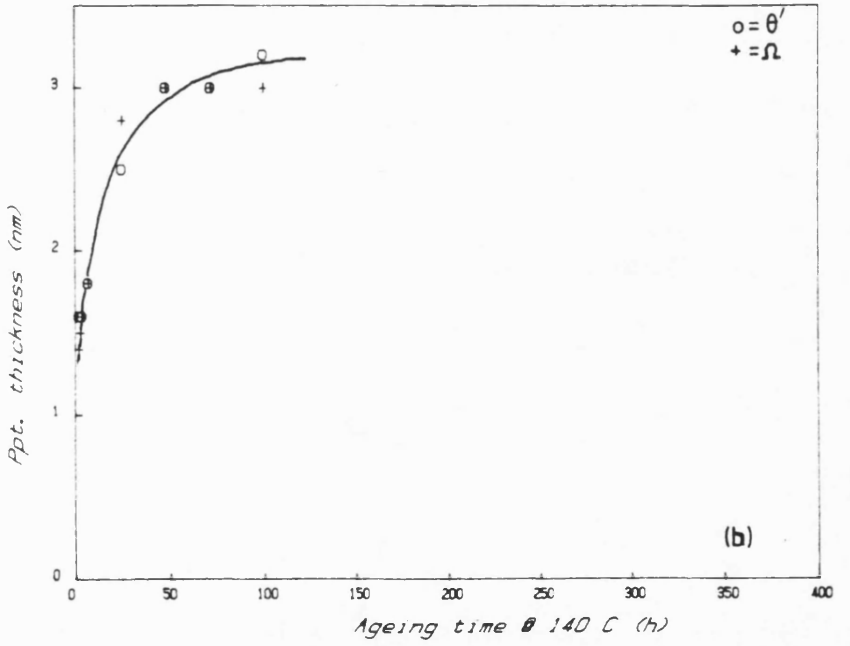

Figure 3.30 Precipitate parameters versus ageing time at 140 C for θ' Ω precipitation in alloy A3;
(a) mean diameter , (b) mean thickness.

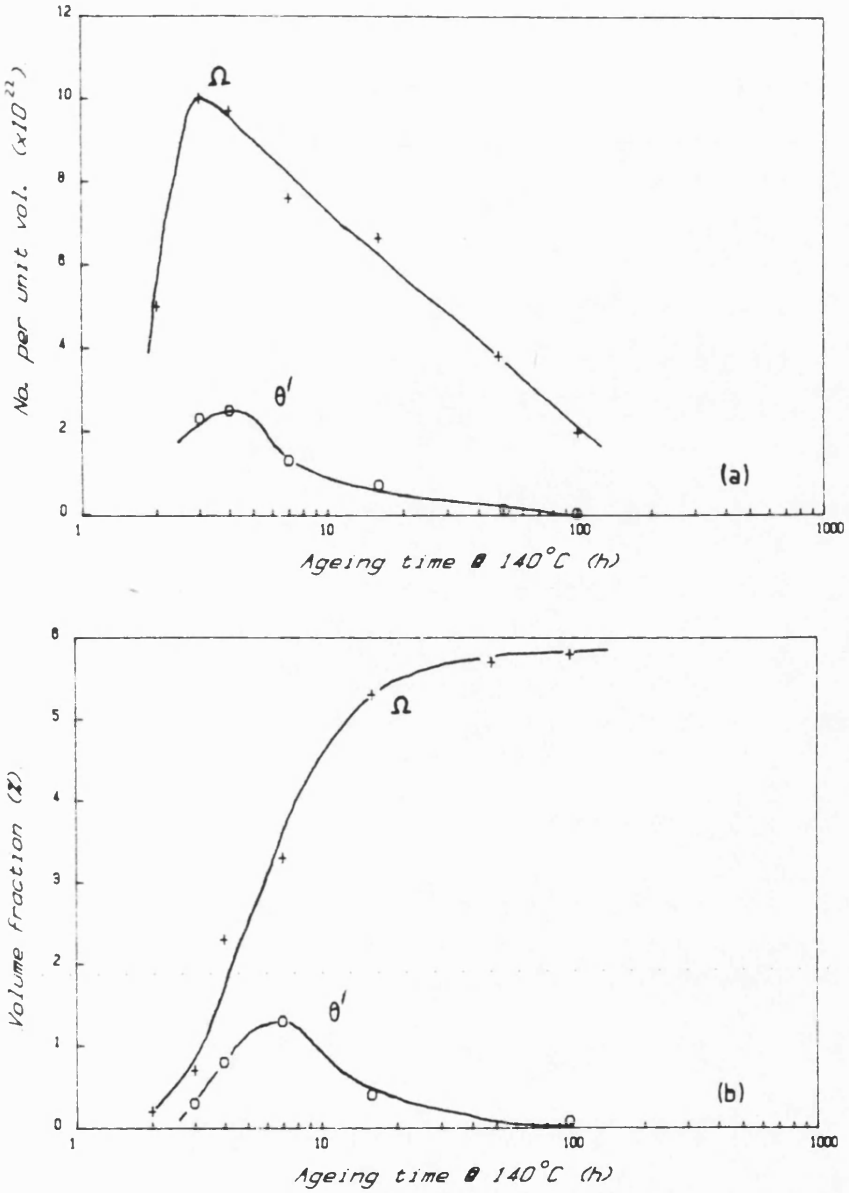

Figure 3.31 Precipitate parameters as a function of ageing time at 140°C for θ' and Ω precipitation in alloy A3; (a) density , (b) volume fraction .

3.4 Tensile Test data

Average values of proof stress (0.2%), tensile strength and elongation for alloys in the various metallurgical conditions tested are listed in Table 3.2, and typical stress/strain curves for all alloys are plotted in Figures 3.32, 3.34, and 3.35.

Figure 3.32 shows the stress/strain curves for all alloys in the as-solution treated condition. Alloy A5 exhibits a lower average 0.2% proof stress (≈110 MPa) than both alloys A3 and A4 (120 MPa and 132 MPa respectively). A similar trend is exhibited by the tensile strengths, with alloy A4 showing the highest average tensile strength (335 MPa). Alloy A5 showed the highest percentage elongation value, 16%. The relatively low elongation value for alloy A3, 7%, can be attributed to porosity which was more in evidence in these test pieces. Although in all cases the fracture mode was essentially ductile transgranular, Figure 3.33a, alloy A3 showed evidence of large regions of porosity surrounded by ductile transgranular type failure, as shown in the SEM fractograph in Figure 3.33b taken from alloy A3 in the as-solution treated condition.

Ageing to peak hardness at 140°C showed a marked increase in both 0.2% proof stress and tensile strength, Figure 3.34. However, elongations are markedly reduced to a few per cent or below. Alloys A3 and A4 again had higher 0.2% proof stresses and tensile strengths than alloy A5 with alloy A4 having the best performance, achieving an average tensile strength of 465 MPa in this condition.

Typical stress/strain curves for all alloys aged to peak hardness at 170°C are presented in Figure 3.35. Again, alloys A3 and A4 exhibited higher strengths than alloy A5 (Table 3.2), with elongations equivalent to those obtained on ageing to peak hardness at 140°C. However, when aged to peak hardness at 170°C the 0.2% proof stresses and tensile strengths of all alloys were slightly higher than those achieved after ageing at 140°C.

When aged to peak hardness at 140°C and 170°C all alloys showed ductile transgranular type failure, as shown in the SEM fractograph from alloy A4 aged to peak hardness at 170°C, Figure 3.36.

Table 3.2

Tensile Test Data

Alloy	Condition	0.2% Proof Stress (MPa)	Tensile Strength (MPa)	Elongation (%)
A3	Solution treated	128	305	7.0
	Peak Hardness (140 C)	427	435	1.5
	Peak Hardness (170 C)	425	455	1.5
A4	Solution Treated	132	335	12.1
	Peak Hardness (140 C)	445	465	3.2
	Peak Hardness (170 C)	475	485	1.5
A5	Solution Treated	110	290	16.0
	Peak Hardness (140 C)	365	400	0.9
	Peak Hardness (170 C)	382	415	2.0

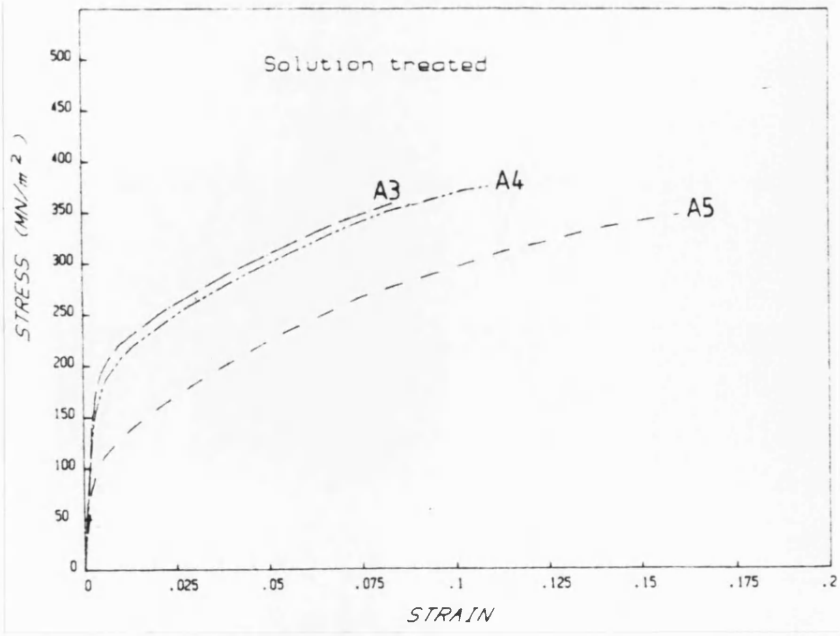

Figure 3.32 Typical stress/strain curves of all alloys in the solution treated condition.

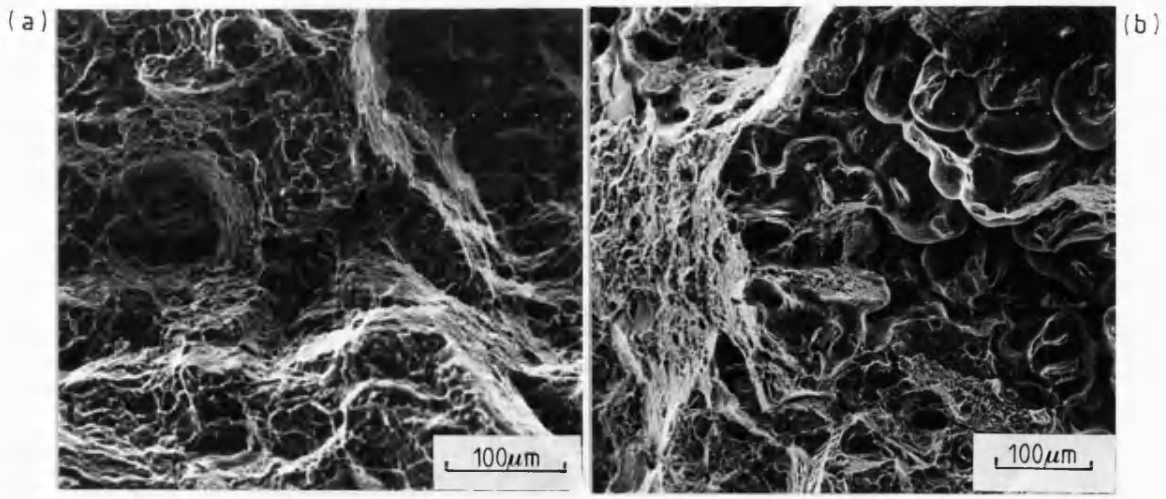

Figure 3.33 Scanning electron micrographs of as-solution treated fracture surfaces;
(a)alloy A5,showing ductile transgranular failure,
(b)alloy A3,showing porosity.

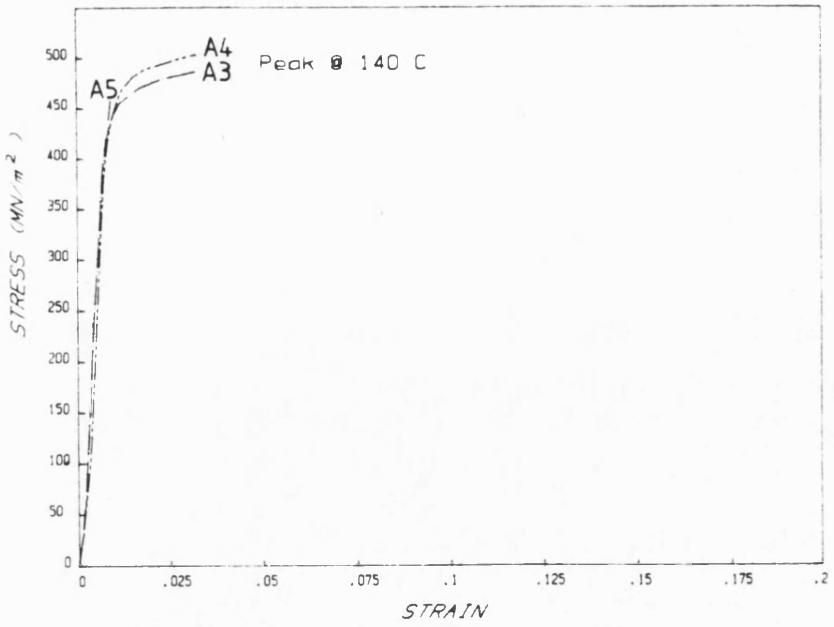

Figure 3.34 Typical stress/strain curves of all alloys aged to peak hardness at 140°C.

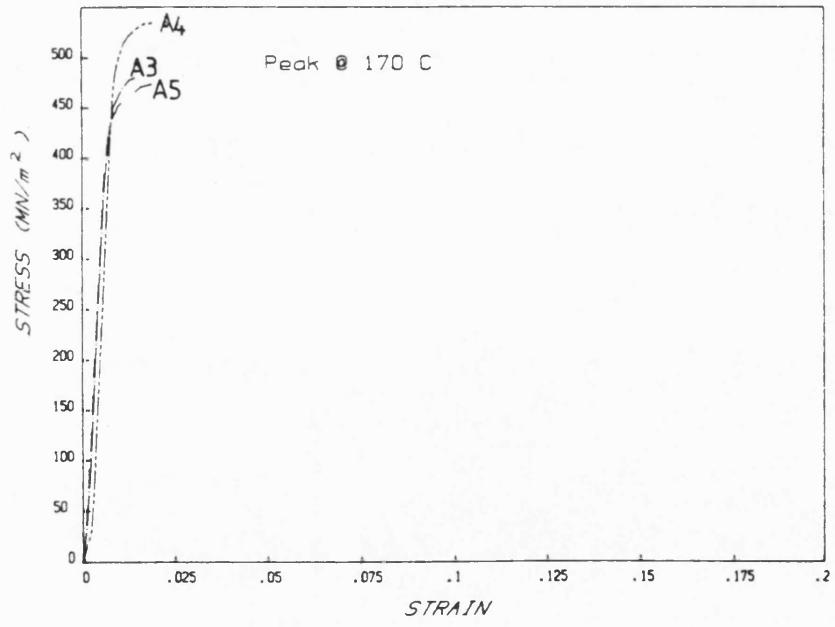

Figure 3.35 Typical stress/strain curves of all alloys aged to peak hardness at 170°C.

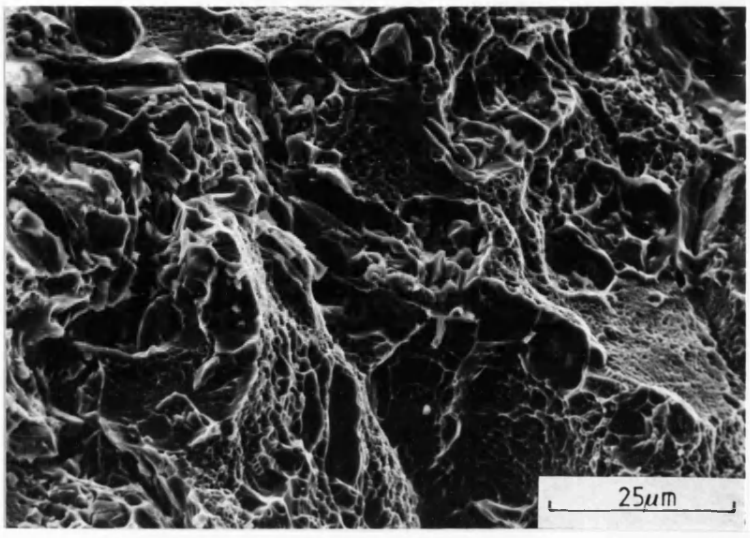

Figure 3.36 SEM fractograph of alloy A4 aged to peak hardness at 140°C.

3.5 Environmental Test data

3.5.1 Mechanical tests

Data obtained from the environmental test program is summarised in Table 3.3. Included in this table are the ratios of tensile strengths and ratios of times to failure as measured in sea water and in air. However, it must be emphasised that reproducibility between tests was not good, probably no better than ±20%.

Curves showing stress as a function of time (life) are presented in Figures 3.37a-c for alloys A3, A4 and A5 respectively in the solution treated condition and tested both in air and sea water. From these curves it is clear that testing in the sea water environment had significantly reduced the life in alloys A3 and A4 whilst alloy A5 (containing smaller amounts of magnesium and silver) had been unaffected.

However, when the alloys were aged to peak hardness at 170°C a different trend emerged (Figures 3.38a-c). Those alloys which contained appreciable amounts of zinc (A4 and A5) appeared to have been less affected by the sea water environment. The ratios of strengths and times to failure (Table 3.3) indicate that the strength and life of alloy A3 have been more than halved, whereas for alloys A4 and A5 the strength is decreased by only 20%-25% and the life by less than 5%.

Typical stress/life curves from alloys in the overaged condition are shown in Figure 3.39a-c. All alloys were given heat treatments at 170°C which were three times that required to produce peak hardness, ie alloy A5 was aged for 60 h at 170°C. The results, summarised in Table 3.3, indicate that alloy A5 appears to be affected by the salt water environment with a reduction in strength of ≈40% and a decrease in time to failure of ≈75%. Both alloy A3 and A4 appeared to be little affected by exposure to the sea water when in the overaged condition.

3.5.2 Fractography

3.5.2.1 Alloy A5

A typical view of the fracture surface of solution-treated alloy A5 after testing in air is shown in the scanning electron micrograph, Figure 3.40a. The fracture mode was essentially ductile

Table 3.3

Environmental Test Data

Alloy	Condition	In Air TS	In Air TTF	In Sea Water TS	In Sea Water TTF	A	B
A3	Solution Treated	325	15.5	298	11.0	0.92	0.71
	Peak Hardness	410	15.5	190	7.0	0.46	0.45
	Overaged	420	12.0	406	11.0	0.97	0.92
A4	Solution Treated	365	28.0	325	8.5	0.78	0.30
	Peak Hardness	465	15.5	460	12.0	0.99	0.77
	Overaged	407	11.0	402	9.5	0.99	0.86
A5	Solution Treated	340	28.0	330	24.0	0.97	0.86
	Peak Hardness	402	19.0	390	14.5	0.97	0.76
	Overaged	420	27.0	250	6.7	0.59	0.25

TS = Tensile Strength , +10 MPa
TTF = Time to Failure , h
A = ratio of tensile strengths, Sea Water/Air
B = ratio of times to failure, Sea Water/Air

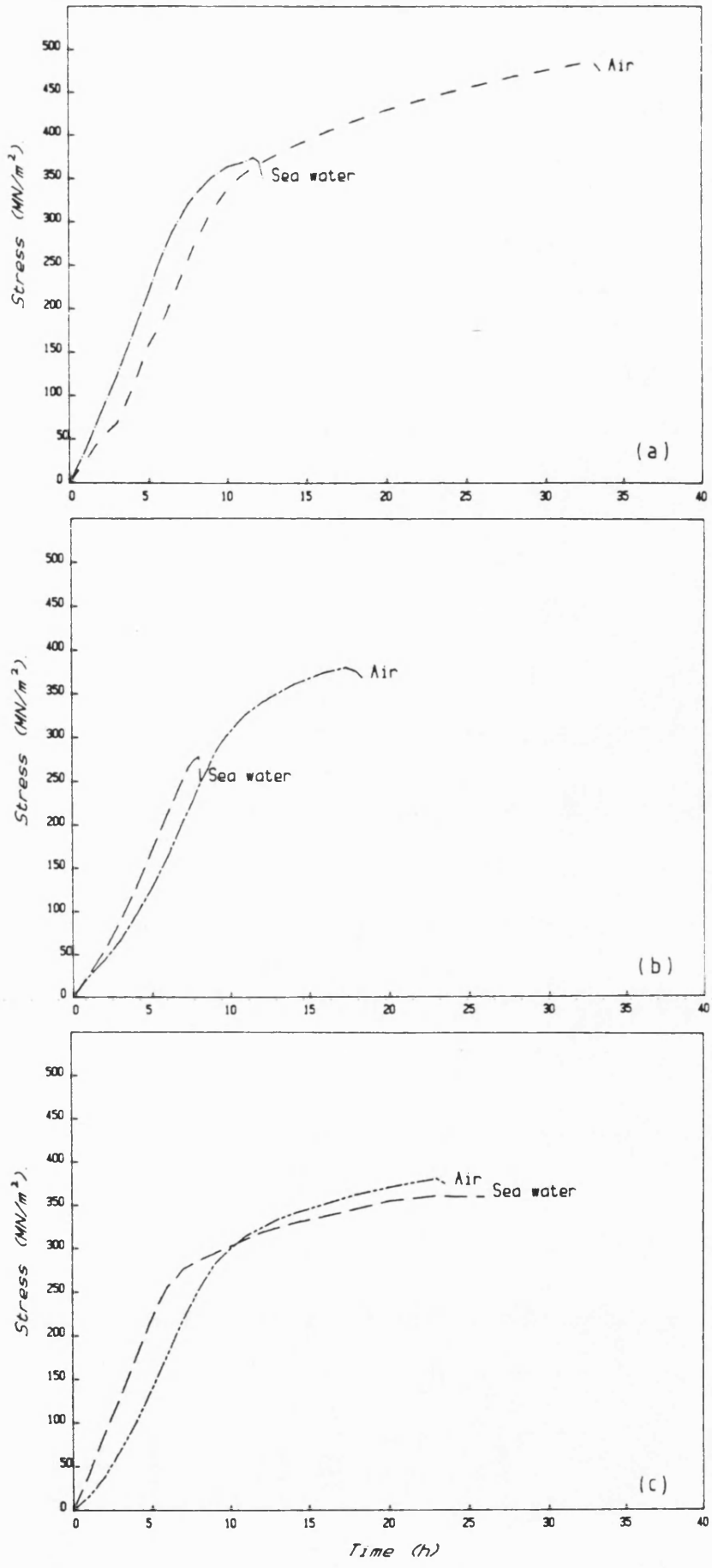

Figure 3.37 Stress versus life curves for solution treated alloys tested in air and salt water;
(a) alloy A3 , (b) alloy A4 , (c) alloy A5.

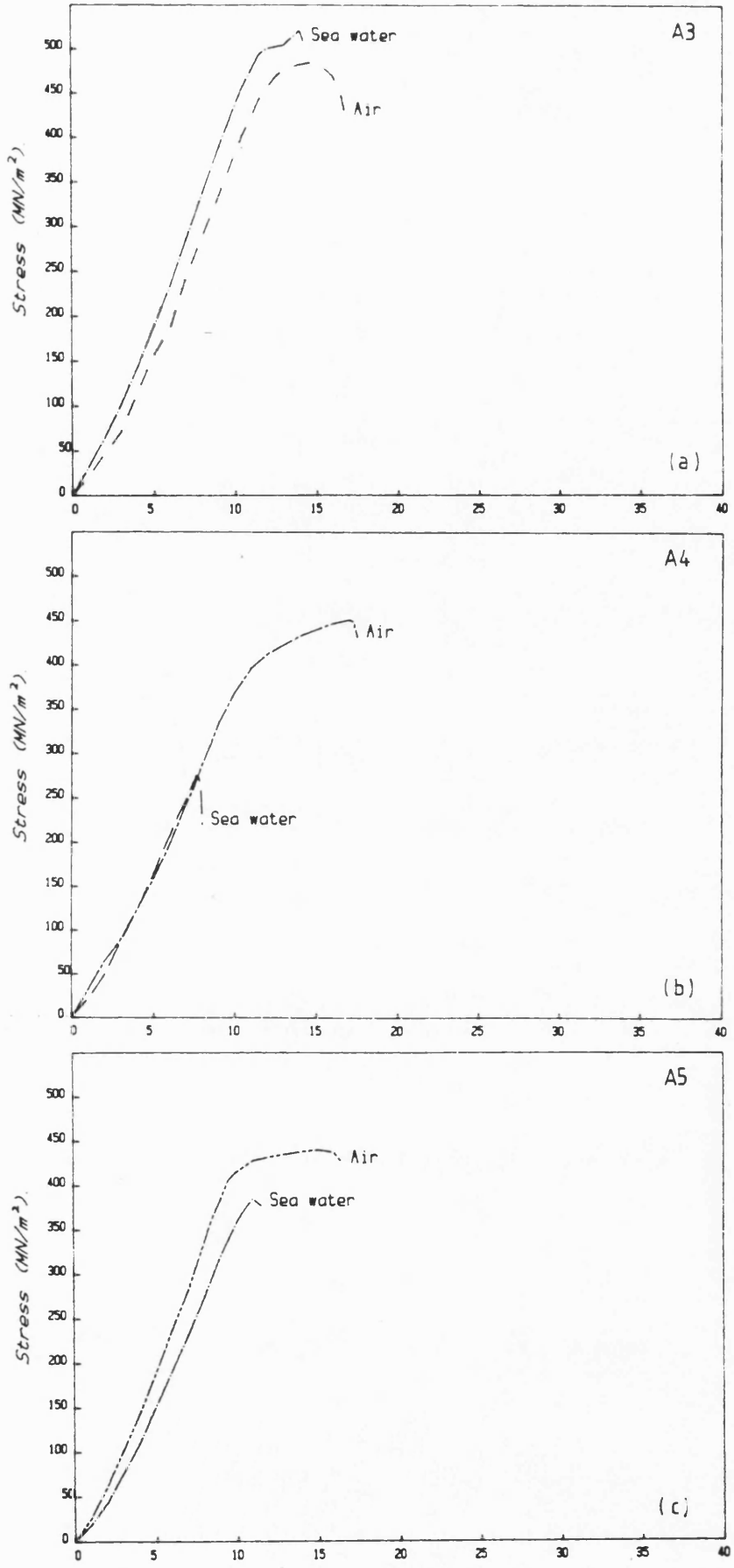

Figure 3.38 Stress versus life curves for alloys aged to peak hardness at 170°C and tested in air and salt water; (a) alloy A3 , (b) alloy A4 , (c) alloy A5.

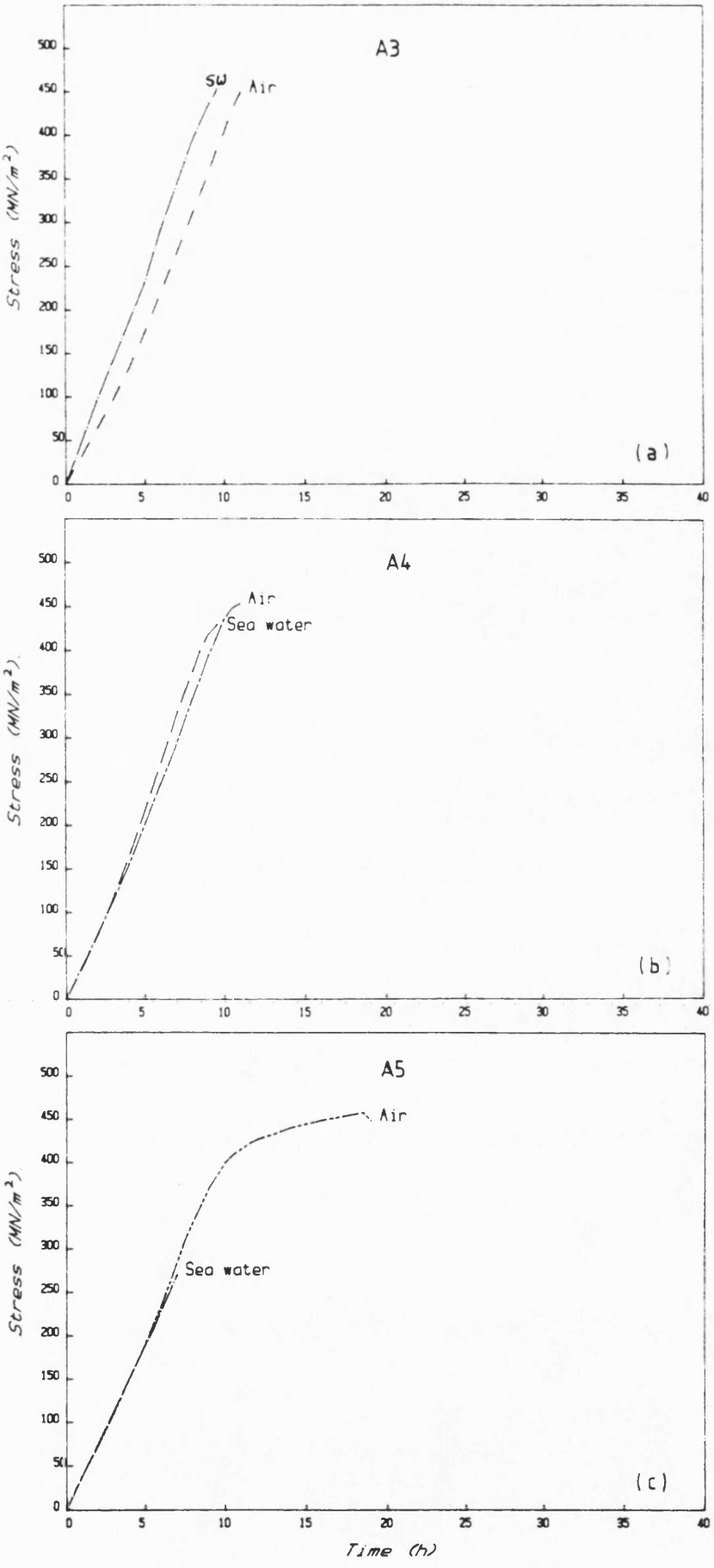

Figure 3.39 Stress versus life curves for alloys overaged at 170°C; (a) alloy A3 , (b) alloy A4 , (c) alloy A5.

transgranular, as in the case of faster strain-rate tensile testing (section 3.4). After testing in sea water, there was little difference in the appearance of the fracture surface apart from a few corrosion products. These products had undoubtedly formed post-fracture before the broken specimen could be removed from the saline solution.

When tested in air in the peak-hardness condition, alloy A5 again exhibited a ductile transgranular failure. However, when tested in sea water, the fracture mode was essentially intercrystalline with extensive corrosive attack, Figure 3.40b. Corrosion products were evident on the fracture surface, Figure 3.40c, as were "mud-crack" features, Figure 3.40d. Chemical analysis, using the ED attachment to the SEM, of the corrosion products and the "mud-crack" features is illustrated in Figures 3.41a and 3.41b respectively. The corrosion products, (Figure 3.41a), contained considerable amounts of oxygen, sulphur and chlorine, some sodium, as well as the alloy elements aluminium and copper. The "mud-crack" features, Figure 3.41b, also contained these elements, although their sulphur content appeared to be higher and chlorine generally lower. On the more ductile region of fracture, small amounts of chlorine and sulphur were found but these were the result of post-fracture immersion in the sea water. Confirmation of this was obtained from the tests carried out on polished alloy samples immersed in the saline environment for several hours; these showed localised attack with corrosion products containing the same elements identified in Figures 3.41a and 3.41b.

When overaged at 170°C, alloy A5 showed ductile transcrystalline failure when tested in air. However, the sea water test produced the largest degree of intercrystalline fracture observed for alloy A5. There was extensive corrosive attack with the products again containin oxygen, sulphur, chlorine and a trace of sodium, in addition to the alloy elements aluminium and copper.

3.5.2.3 Alloy A3

The A3 alloy series gave similar results to those of the A5 series. In the solution-treated condition the fracture mode was essentially ductile transgranular, with corrosion products on the surface, due to post-fracture immersion, when tested in salt water. In the peak hardness condition, testing in air again produced

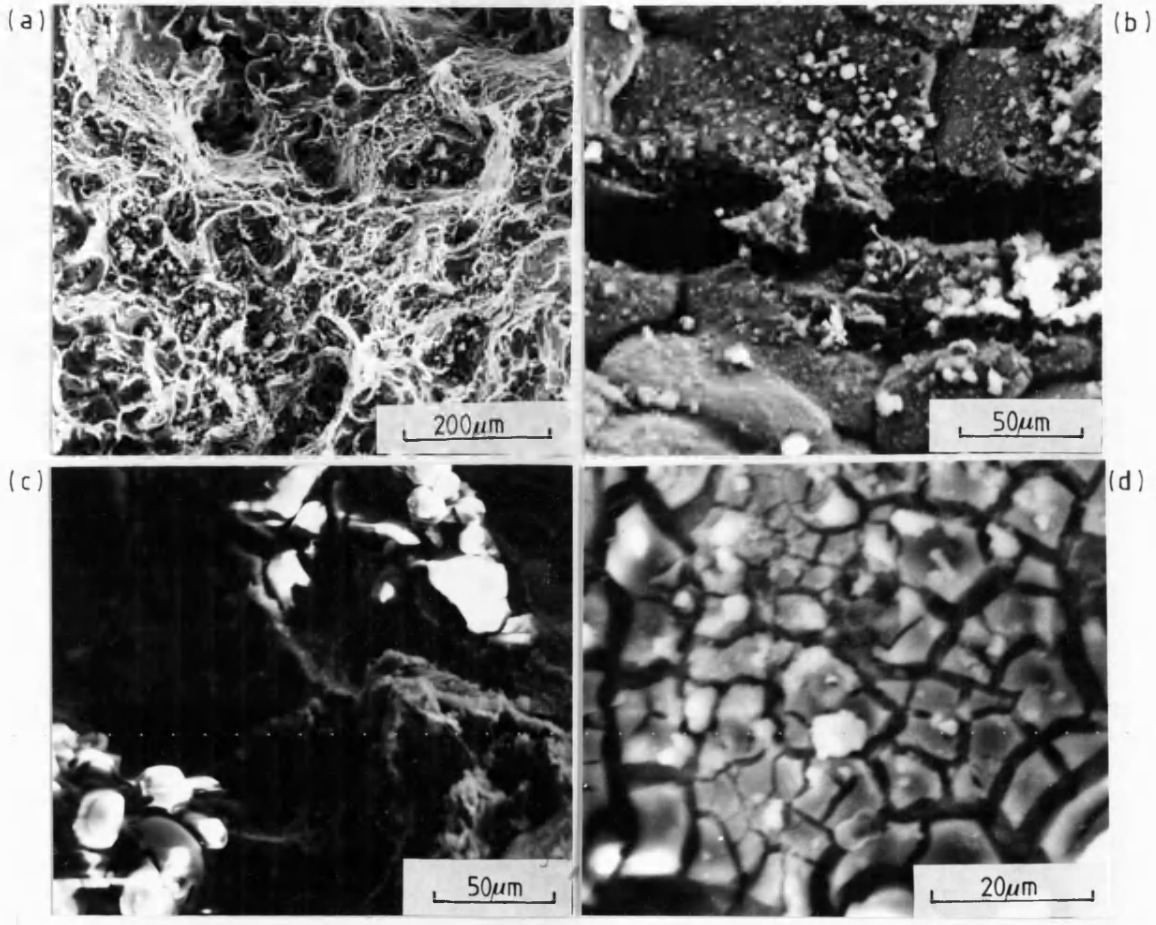

Figure 3.40 Scanning electron micrographs of fracture surfaces of environmentally tested specimens; (a) solution treated aloy A5 tested in air showing ductile transgranular failure , (b) A5 alloy in the peak hardness condition tested in salt water showing intercrystalline failure , (c) as (b) showing corrosion products , (d) as (b) showing "mud-crack" deposit.

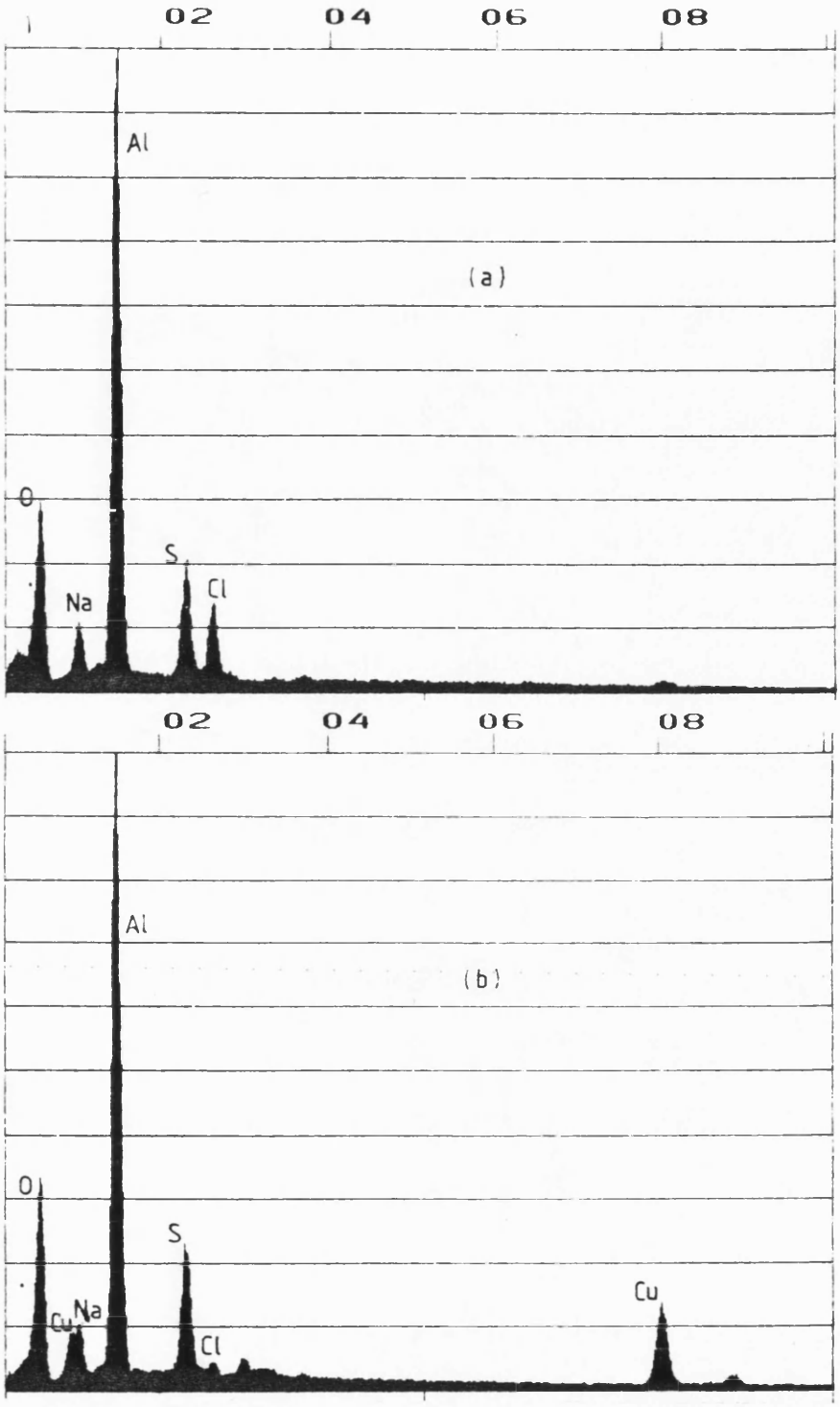

Figure 3.41 EDS spectra of:(a) corrosion products , (b) "mud-crack" deposit.

ductile failure, as illustrated in Figure 3.42a, but extensive intergranular failure when tested in the saline environment, Figure 3.42b. A feature of this fracture was the occurrence of extensive "mud-crack" corrosion products on the grain boundaries, Figure 3.42c. This is further illustrated in the higher magnification SEM micrograph of Figure 3.42d. In the overaged condition the failure mode reverted to the ductile transgranular behaviour observed in the solution-treated alloys. Analysis of the corrosion products, both post-fracture artefacts and "mud-crack" products, were similar to those obtained for alloy A5.

3.5.2.3 Alloy A4

Results on A4 alloy were similar to those obtained on the A5 alloy series. Isolated intergranular facets were observed on the fracture surface of alloy 221, solution-treated and tested in sea water, although very few were observed, Figure 3.43a. Again the "mud-crack" products are present. Ageing to peak hardness and testing in the salt water environment again produced some intergranular failure although this was much less than alloys A3 and A5, Figure 3.43b, and the fracture mode was a majority of ductile transgranular, Figure 3.43c. Again, in the overaged condition the failure was ductile transgranular, with corrosion products on the fracture surface after testing in sea water. Analytical data obtained on the corrosion products were similar to alloys A3 and A5, although sometimes a trace of magnesium and/or silver could be located in the "mud-crack" deposits.

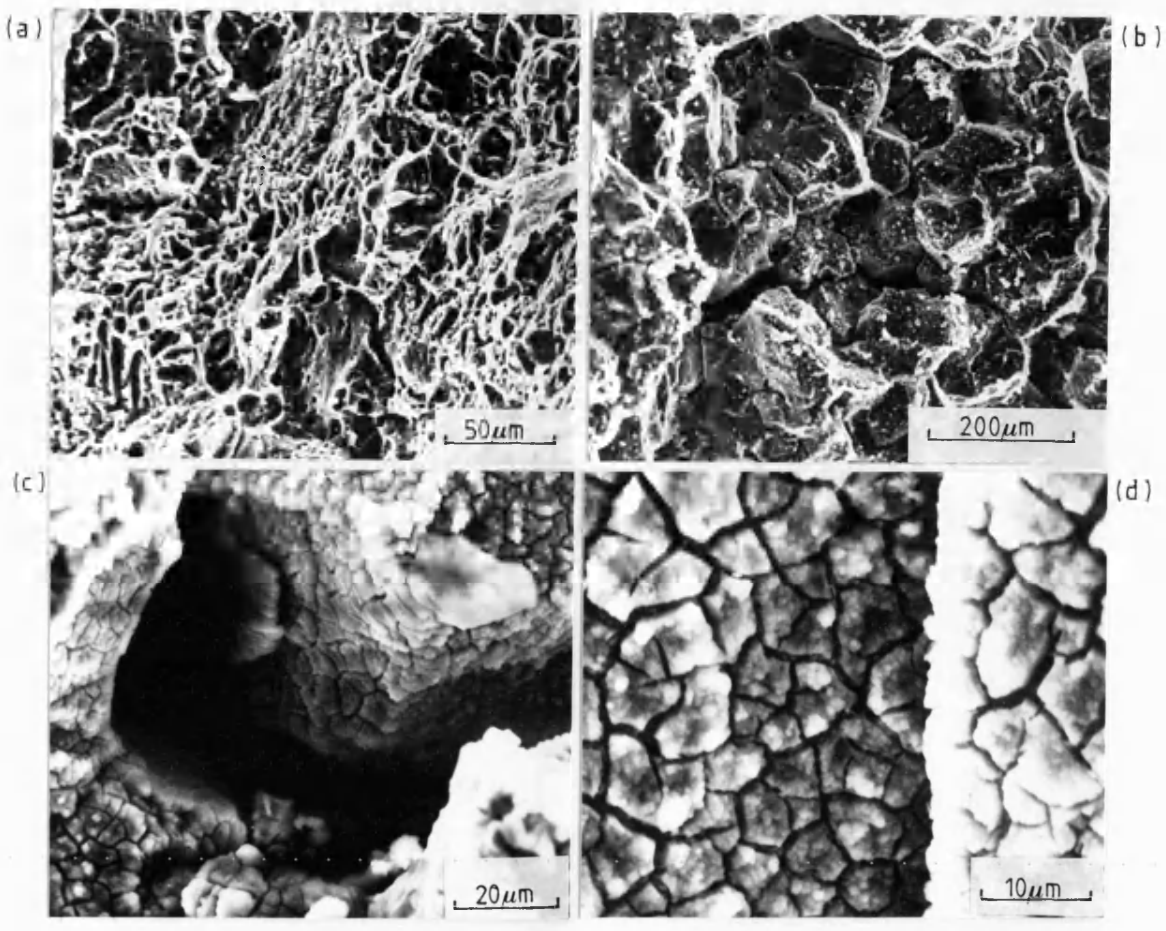

Figure 3.42 Scanning electron micrographs of fracture surfaces of environmentally tested specimens; (a) alloy A3 aged to peak hardness and tested in air , (b) alloy A3 aged to peak hardness and tested in salt water showing intercrystalline failure , (c) as (b) showing "mud-crack deposits on grain boundaries , (d) as (c).

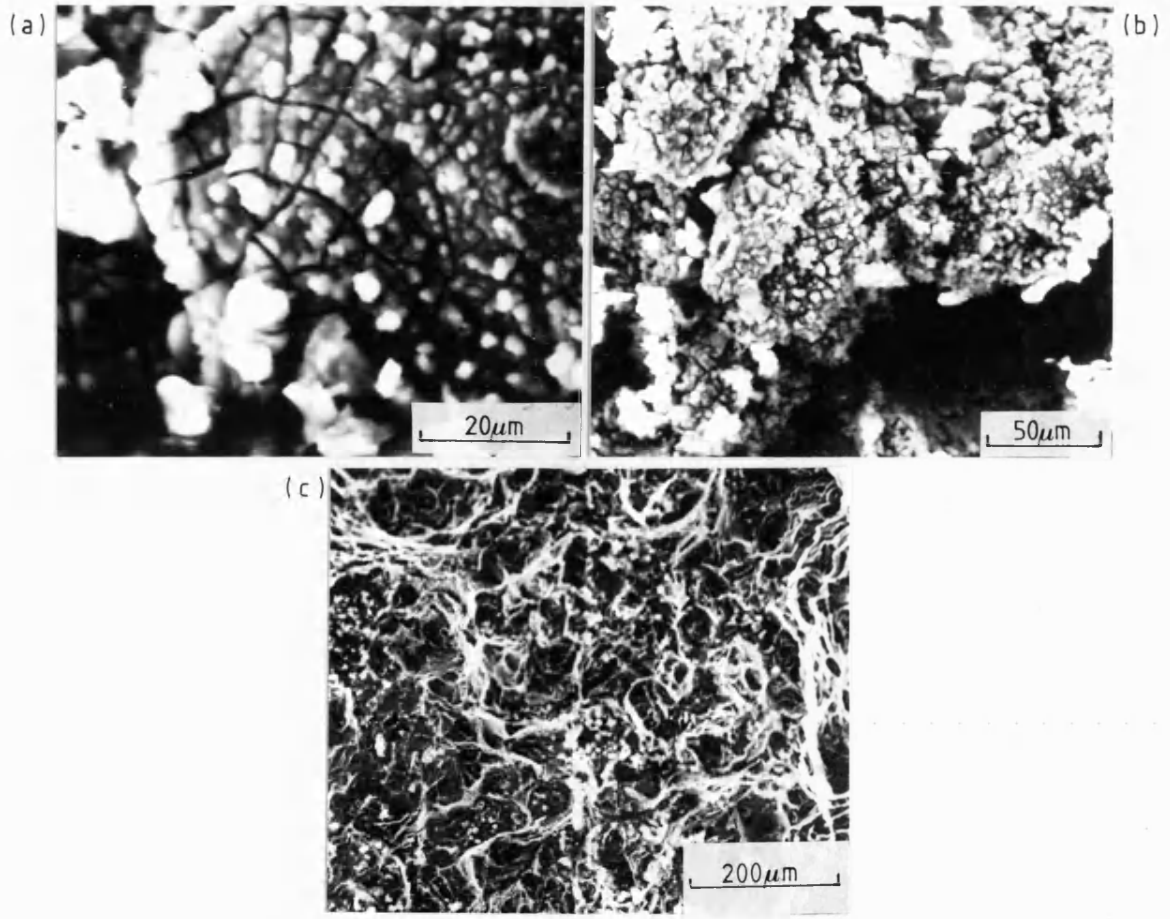

Figure 3.43 SEM fractographs of environmentally tested alloy A4; (a) solution treated and tested in salt water showing intergranular facets , (b) aged to peak hardness showing inter granular facets , (c) as (b) showing transgranular failure.

CHAPTER 4

DISCUSSION

This research, which concerns the relationship between the microstructure of several cast aluminium alloys and their mechanical properties, may be considered as having three objectives:

(i) to study the effects on microstructure of varying the amount of magnesium, silver, and zinc additions on the precipitation behaviour of an aluminium-copper alloy.

(ii) to relate the resulting microstructures with the mechanical behaviour of the alloys.

(iii) to carry out a preliminary study of the stress-corrosion behaviour of the alloys in a salt water environment.

We shall discuss the results in the above order but first we shall consider the as-cast structure and the efficiency of solution treatment.

4.1 As-Cast and Solution Treated Materials

A coarse-grained microstructure of the as-received materials is typical of cast aluminium alloys. In the initial stages of solidification, dendrites of almost pure aluminium have formed which have become progressively enriched in copper during growth, levels of copper increasing from ∿1.3wt% in the grain interior to ∿3.8wt% in the region of the grain boundaries. In the final stages of solidification when the dendrites impinge on one another, rejected solute has remained in the liquid phase until the eutectic composition is reached. The eutectic liquid trapped between grain boundaries and dendrites has solidified last, forming a network of particles containing ∿50wt% copper. This corresponds to the phase $CuAl_2$. Although other elements were observed in these grain boundary particles, the amounts were relatively small, less than a few per cent.

In previous work on similar alloy compositions[139, 140] iron was found to be detrimental with regard to the formation of grain boundary particles. Smith and Scott[139] observed some particles containing up to 12wt% iron and/or manganese, similar to the β phase found in Al-Cu alloys containing 0.05% iron as an impurity[141], Cu_2AlFe_7. The particles were insoluble at the solution treatment temperature (530°C), and

higher solution treatment temperatures were ruled out as it appeared that this grain-boundary phase reached its melting point before being completely dissolved and then migrated around the grain boundaries where it encouraged the formation of cracks during the quench.

One of the intentions in this work was, therefore, to keep iron impurity level as low as possible in order to restrict the formation of these insoluble grain boundary particles, thus allowing more copper for the precipitation processes. The two-stage solution treatment adopted in the present work was more effective than the single treatment used previously (ie 42 hours at 530°C) with the reduction in the level iron impurity in the castings contributing significantly to homogenisation of the alloys. This two-stage treatment also successfully eliminated the coring present in the as-cast alloys, and this is confirmed by the EPMA (See Figure 3.3) where a value of ∿4.6wt% copper was recorded across a grain. Similarly, the amount of grain-boundary phase was reduced to less than 1% by volume.

4.2 Response to Ageing

Whether aged at 140°C or 170°C, the tensile strength of all three alloys increased to maximum values in excess of 400 MPa. Alloy A4 was the stronger, giving an average tensile strength of 485 MPa after ageing at 170°C, with values as high as 525 MPa being acheived. Alloy A3 was the next strongest alloy (455 MPa) followed by A5 (415 MPa), both aged at 170°C. Tensile strengths were slightly lower when 140°C was adopted as the ageing temperature (465, 435) and 400 MPa respectively for alloys A4, A3 and A5). The hardness data indicated a single-stage ageing process at both 140°C and 170°C, although previous work[139] on alloys of similar composition had suggested the possibility, although not well defined, of a two-stage hardening process similar to that observed in binary Al-Cu alloys at lower ageing temperatures.

Precipitate morphologies present in alloy A5 at peak-hardness were similar to those reported previously by Taylor et al[114], by Smith and Scott[139], by Colbeck and Scott[140], and by Chester and Polmear[115], all of whom studied alloys of comparable composition. Two distinct precipitate types were observed - the θ' phase lying on the {100} matrix planes of the aluminium lattice, and a different precipitate forming on {111} aluminium matrix planes. However, in alloys A3 and A4, which contained greater amounts of magnesium (0.74wt% and 0.65wt% respectively compared with 0.23wt% in 219), the {100}-type precipitate

was virtually absent at peak hardness. Some {100} precipitate was observed in the early stages of ageing, in parallel with the {111} mode, but this tended to dissolve in favour of the {111}-type growth.

Comparison of alloys A3 and A4 reveals virtually similar behaviour at both ageing temperatures, with only minor differences. For example, in alloy A4, which contained a small addition of 1.13wt% zinc compared with A3, the size of precipitate was reduced slightly but the crystal structure was unaffected by the addition.

In the next section the crystal structure and orientation of the {111}-type precipitate is discussed.

4.3 Crystal Structure of the {111}-type Precipitate

The electron diffraction data from the Al-Cu-Mg-Ag alloys presented in the preceeding chapter have shown that the precipitate which forms on the {111} aluminium matrix planes has a hexagonal structure with:

$$\underline{a} = 0.496 \text{ nm}$$

and

$$c/a = 1.414$$

The precipitate has an orientation relationship with the aluminium lattice such that:

$$[0001]_{ppt} \parallel \langle 111 \rangle_{Al}$$

$$\langle 10\bar{1}0 \rangle_{ppt} \parallel \langle 110 \rangle_{Al}$$

Such an orientation relationship leads to close registry between the respective crystal lattices.

Based on the orientation relationship, the atom positions at the interface are shown in Figure 4.1. In this diagram shaded circles represent atoms in a (111) plane of the aluminium lattice. Atoms in the adjacent plane of the precipitate are indicated by open circles, with the base of the hexagonal unit cell superimposed on this layer. The close registry between the respective close packed planes is clearly evident, athough at this stage no distinction is made between copper and aluminium atom positions in the precipitate unit cell.

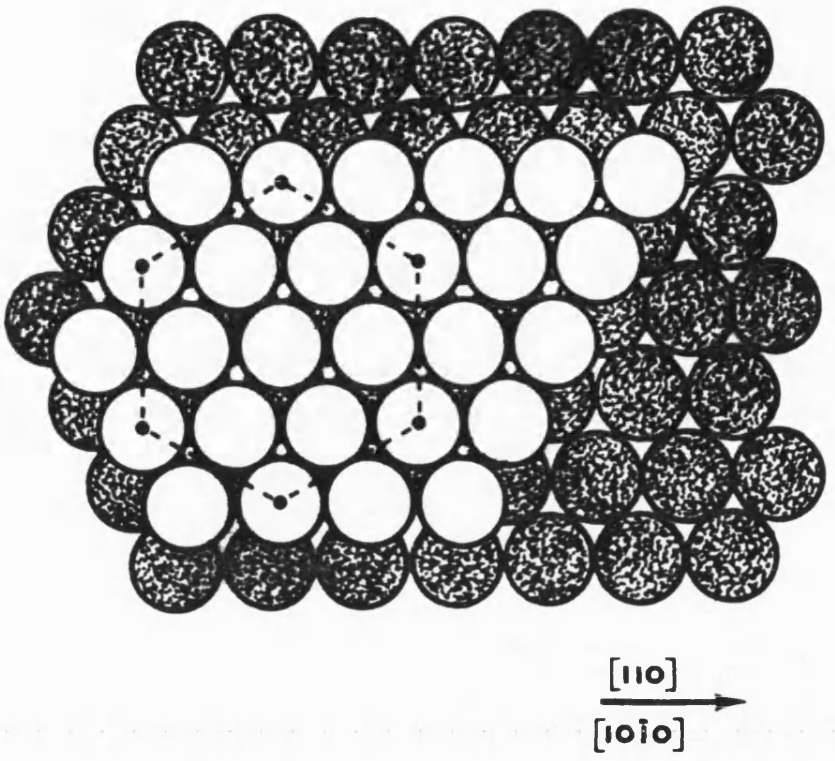

Figure 4.1 Atom positions at matrix/Ω precipitate interface; shaded circles represent atoms in a (111) plane of aluminium , open circles correspond to atoms in the precipitate , the base of the hexagon is shown as a broken line.

Attempts were made to obtain chemical compositions of the precipitates to complement the crystal structure data but these experiments were not entirely successful due to the small mass volume of the particles being analysed and the limited sensitivity of the EDS facility attached to the TEM. Thin foil specimens containing large overaged precipitates were examined and apart from a high aluminium signal only a small amount of copper was found in the particles. The results suggested that the precipitate was essentially the $CuAl_2$ phase. If any other elements, such as magnesium or silver, were present the particle could not have contained more than $\sim$1% of them.

Based on this premise, ie a precipitate composition of $CuAl_2$, one possible arrangement of atoms within the precipitate is illustrated in Figure 4.2. In this diagram hatched circles represent copper atoms in a (0001) plane of the hexagonal unit cell, one out of three aluminium atoms being replaced by a copper atom in accord with the formula $CuAl_2$. Although this is not the only configuration of atoms that could occur, it is a probable one, as the following analysis suggests.

The close-packed plane of atoms, designated an A layer, is represented by the upper triangle in Figure 4.2. This joins the copper atom positions. Triangle B indicates the adjacent close packed layer where the corners of the triangle again mark the copper atom positions. Triangle C marks the position of the third layer, and the next is represented by D. The corners of triangle D (representing copper atom positions only) are immediately above copper atoms in layer A. Thus, the stacking sequence may be expressed as ABCA ..... The $\underline{c}$ parameter of the hexagonal unit cell is then simply the distance between three close-packed planes, ie $\underline{c}$ equals x3 the aluminium d_{111} spacing - as deduced from the electron diffraction data. Also, the distance between a pair of copper atoms along $\langle 11\bar{2}0\rangle$ is equal to the $\underline{a}$ parameter of the unit cell, as illustrated in Figure 4.2, ie;

$$\text{Tan } 60° = \frac{\underline{a}}{\text{atomic spacing}}$$

$$\underline{a} = \sqrt{3} \times 0.286$$

$$\Rightarrow \underline{a} = 0.496 \text{ nm}$$

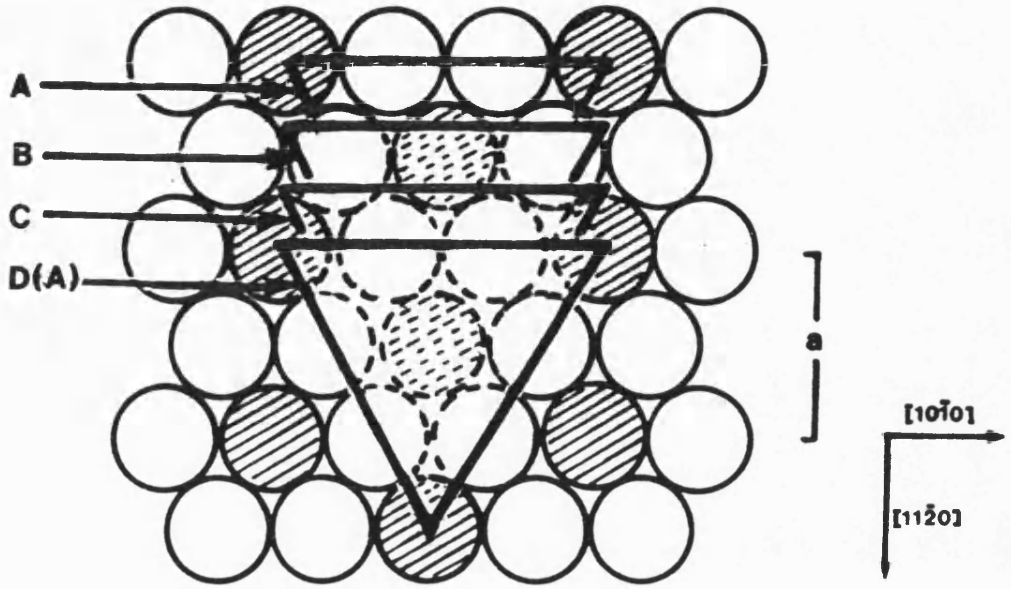

Figure 4.2 Atom positions in the basal planes of the Ω precipitate; open circles represent aluminium , hatched circles copper atoms; corners of triangles A,B,C, and D indicate positions of copper atoms in successive close-packed layers to give a stacking sequence ABCA....

Thus, the hexagonal unit cell may be envisaged as a continuation of the ABCA ..... stacking sequence of close packed planes of the aluminium lattice. However, when the precipitate forms copper atoms are added and consequently the close packed cubic unit cell is no longer an appropriate construction; the larger hexagonal space lattice must be adopted containing 27 atoms of which 9 are of copper. In addition, the introduction of copper atoms in place of some of the aluminium atoms as the precipitate grows would suggest that some measure of instability will be introduced into the structure. The very long streaking observed in the diffraction patterns, is however, greater than would be expected from the estimated thickness ($\sim$3nm) of the precipitate platelets seen, for example, in Figures 4.11b and 4.12b suggesting there is some faulting on a unit cell level between close-packed planes of the structure.

Streaking is a common occurrence in diffraction patterns, and all types of particle have been shown to produce streaking to some degree[141]. Thin coherent precipitates produce streaking in diffraction patterns due to two factors; the aggregation of solute atoms in the precipitate provides small centres of different scattering power for the matrix and, secondly, if the atom size of the solute and solvent are different then elastic distortion of the matrix may occur. The nature of such streaking depends on the shape of the particle, with, for example, streaks through each reciprocal lattice point occurring if the particle is disc shaped and a diffuse shell around each reciprocal lattice point if the particle is spherical. A simple example of this type of effect is seen in an Al-Cu alloy containing GP zones.

Semi- or partially-coherent precipitates have also been shown to produce streaking[141], with the precipitates diffracting according to its own crystal structure rather than by distortion of the matrix spots, as for coherent particles. A system where streaking is observed for semi-coherent precipitates is the aluminium-silver binary system, where precipitation of the γ' phase often gives rise to streaking in diffraction patterns depending on the zone axis of the pattern itself. This is simply because the γ' phase has a hexagonal close packed structure with a definite orientation relationship with the aluminium matrix[15].

Non-coherent particles mostly bear no simple orientation relationship to the matrix and have a completely different structure. Often, just imaging the diffraction pattern is difficult. Wheeler[142].

successfully obtained diffraction patterns from a number of coarse intermetallic phases in commercial aluminium alloys and thereby identified the particles. For one such phase, Mg_2Al_3, streaking was observed in the diffraction pattern which, on viewing the corresponding micrograph, was attributed to stacking faults within the precipitate itself.

Thus, streaking effects in electron diffraction patterns are widespread. In general, the length of the streaks is inversly proportional to the precipitate thickness. However, internal faulting of the precipitate may lead to streaking, and there is some danger in regarding streaks as indicative of very fine precipitates.

The very long streaking observed in Figures 3.11b and 3.12b would be indicative of very thin precipitates, much thinner than the estimated thickness of ∿3nm. This suggests that the precipitate develops a series of intercellular stacking faults rather than adopt a completely different structure. For example, a sequence such as ABC/BCA/CAB/ABC would give a distance of 2.8nm, which is similar to the observed precipitate thickness of ∿3nm. One such stacking fault is shown in Figure 4.3, where block spheres represent copper atoms and white spheres aluminium atoms.

The "a" parameter of the unit cell of the {111} precipitate is in close accord with that given by previous workers[111, 109], who concluded that the phase was monoclinic with a = b = 0.486 nm, c = 0.848 nm and γ = 120°, referring to it as "modified θ", $CuAl_2$. This unit cell could give close matching at the interfacial plane, similar to that illustrated in Figure 4.1, by making the 'a' and 'b' axes parallel to the hexagonal axes, ie their unit cell can be regarded as pseudohexagonal with the ab plane essentially one-third of the base of hexagon of the new interpretation. In order to properly index a diffraction pattern such as Figure 3.11b double-diffraction effects must be used, where the diffracted beams from the aluminium lattice act as primary beams. Thus, Figure 3.11b could be indexed on the basis that the row of spots labelled $\ell o \bar{\ell} 0$ produced by the direct beam and $\ell 1 \bar{\ell} \bar{1} 0$ by 111 and $\bar{1}\bar{1}1$ beams. Using double-diffraction principles is not an entirely adequate interpretation since double-diffraction spot intensity will be related to the intensity of the diffraction beam which produces them. Again referring to Figure 3.11b, the $h \theta \bar{h} 0$ row of spots produced by the primary beam should be stronger than

Figure 4.3 A pictorial representation of a stacking fault in the Ω precipitate .

double-diffraction spots produced by the much weaker 111 beams. As can be seen this is clearly not the case.

Considering now the $[11\bar{2}]$ zone axis diffraction pattern of Figure 3.12b, a problem arises as to how to arrive at a monoclinic indexing of diffractions such as $h0\bar{h}1$ when there is no diffracted beam from aluminium which might produce them by double diffraction. This would mean that the fine structure effects observed in the diffraction patterns would virtually have to be ignored. However, this is not to imply that double-diffraction does occur, but that when a monoclinic unit cell is assumed for the precipitate, double-diffraction does not provide a consistent means of accounting for all the spots in the diffraction patterns. Also, diffractions were not found in any of the diffraction patterns which would be attributed to 101 and 102 monoclinic cell reflections

4.4 Precipitate Morphologies

Nucleation of Ω precipitate in Al-Cu-Mg-Ag alloys occurs uniformly throughout the aluminium lattice as platelets on {111} planes. Since the crystal structure of Ω remains unchanged during ageing, from nucleation to a fully overaged state, it is contended that it is the equilibrium phase in these alloys. Further support for this is evidenced by the fact that platelets of Ω may attain diameters in excess of 100 nm, while reaching a limiting thickness of $\precsim$ 3 nm. If the faulting hypothesis (Section 4.3) is correct then this allows a perfect match with the aluminium lattice along the direction of the precipitate normal, further promoting the Ω as the equilibrium phase.

In addition, θ' platelets were formed on {100} aluminium matrix planes. However, the amount of θ' present was dependent upon the concentration of magnesium and silver in the alloy, as noted previously by Taylor et al[114]. For example, θ' precipitate was virtually absent in alloys A3 (0.74wt%Mg,0.57wt%Ag) and A4 (0.65wt%Mg,0.61wt%Ag) in the peak hardness condition; some was observed in the early stages of ageing in parallel with Ω but tended to dissolve in favour of Ω growth as ageing progressed. Even in alloy A5 (0.23wt%Mg,0.50wt%Ag), the volume fraction of θ' was found to decrease progressively on further ageing while Ω increased (See Figure 3.23b). Clearly, it would appear that Ω is the more stable phase in these alloys.

Auld and Vietz[109], working on alloys of similar composition to that of A5, have reported that the Ω phase is stable to at least 350°C, further supporting the fact that Ω is the stable equilibrium phase in alloys of this type.

4.5 Nucleation and Growth of Precipitates

4.5.1 Nucleation

Classical nucleation theory predicts that the change in free energy, ΔG, when a new phase (β) of volume V_β, and interfacial area, A_β, forms in a matrix (α), is given by:

$$\Delta G = V_\beta \Delta G_{\alpha\beta} + A_\beta . \gamma_{\alpha\beta}$$

where $\Delta G_{\alpha\beta}$ is the free energy change per unit volume, $\gamma_{\alpha\beta}$ is the specific energy of the α-β interface. With solid systems a strain energy term, ΔG_ε, must be introduced due to the formation of the new phase in an otherwise unstrained matrix, giving:

$$\Delta G = V_\beta . \Delta G_{\alpha\beta} + A_\beta . \gamma_{\alpha\beta} + V_\beta . \Delta G_\varepsilon \qquad (4.1)$$

In many precipitation-ageing alloys, metastable intermediate phases may develop during the ageing sequence; their occurrence is dependent upon the relative magnitude of the interfacial energy and strain energy contributions ($A_\beta \gamma_{\alpha\beta}$ and $V_\beta . \Delta G_\varepsilon$ respectively in equation (4.1)). It can be seen that a reduction in interfacial energy, $\gamma_{\alpha\beta}$, and/or elastic strain energy, ΔG_ε, will result in a reduction in the overall free energy of the system, leading to preferential precipitation of the β phase. For example, the θ'' and θ' phases which form on {100} planes in Al-4wt%Cu alloys have differing degrees of interface coherency and lattice strain[15]. Hence, the highly coherent θ'' phase, which has low interfacial energy and high strain, may develop first provided that GP zones are available to act as nucleation sites. On the other hand θ' is less coherent than θ'' and has a higher energy barrier for formation from supersaturated solid solution and tends to nucleate directly onto helical dislocations because these offer energetically more favourable lattice sites for θ'.

No real evidence for GP zones formation or θ'' precipitation could be found in the Al-Cu-Mg-Ag alloys studied here. Silcock[75] and Heal[143] have also observed the absence of GP zones in Al-Cu alloys containing additions of cadmium, indium or tin; this led them to suggest that such solute atoms may interact strongly with vacancies thereby reducing

vacancy mobility and inhibiting formation of vacancy-related nucleation sites. Both magnesium and silver have been reported as having a relatively high vacancy binding energy compared with copper atoms, indicating that a similar situation, ie GP zone suppression, may arise in the Al-Cu-Mg-Ag system. This hypothesis may also explain the lack of dislocation loops and helical dislocations in the solution-treated material, as well as accounting for the absence of GP zones.

The Ω phase forms on {111} planes of the aluminium lattice, in contrast to θ' precipitation. The close-packed {111} matrix planes would, however, appear to be crystallographically more favourable than other lattice planes. Indeed, several aluminium alloy systems show precipitation on {111} planes, eg Al-Ag (γ phase) and Al-Zn-Mg (η phase) and therefore such a habit plane in the Al-Cu-Mg-Ag alloys is, perhaps, not surprising. There is also a high degree of coherency between the matrix and Ω which implies a low interfacial energy contribution, $A_{\Omega} \cdot \gamma_{\alpha\Omega}$, to equation 4.1. This would promote nucleation of Ω in preference to θ' which has a higher interfacial energy. Coherency of Ω is maintained during particle growth by incorporating stacking faults within the precipitate structure and also by adopting a plate-like habit. Mabarro[144] suggests that the strain energy is a minimum when precipitation occurs in the form of a thin sheet. Therefore, it is reasonable to assume that since coherency is maintained then there will be little significant increase in the strain energy term, $V_{\Omega}\Delta G_{\varepsilon}$. Certainly, since Ω represents the equilibrium phase, the extent of the strain energy contribution during growth would appear never to reach a level sufficient to cause loss of coherency and the necessary change in crystal structure which would follow.

Precipitation of Ω phase in these alloys appears to be sensitive to small additions of silver and magnesium. Therefore, it is worth considering the effect that these and other alloy additions have on the stacking-fault energy of aluminium. Aluminium has a relatively high value, $0.15 Jm^{-2}$, for the stacking-fault energy when in the pure state. This value will be reduced by the addition of solute atoms, the most soluble elements producing the greatest effect. Solubility in aluminium is limited, at 200°C the most soluble elements are zinc (50at%), magnesium (4.4at%), lithium (3.2at%), silver (0.2at%) and germanium (∿0.2wt%), all other elements having solubilities less than ∿ 0.05at% at this temperature. Three of the most soluble elements

(magnesium, silver and zinc) are thus present in the alloys studied. Such additions will reduce the stacking fault energy of aluminium, and it is therefore suggested that the addition of magnesium, silver and zinc reduce the stacking-fault energy of aluminium in these alloys. This reduction is sufficient to allow stacking faults to form readily and thus give sites for nucleation of Ω.

Clearly, the amount needed for Ω phase precipitation is fairly critical. Too high a magnesium level could lead to the formation of the magnesium-containing intermetallic phases such as S' phase[93], Al_2CuMg, and the T-phase[99], as found in Al-Cu-Mg and Al-Cu-Mg-Ag alloys respectively when the magnesium content > 1wt%. On the other hand, if the magnesium content is too low then precipitation of θ' will predominate. Indeed, Smith and Scott[139], working on alloys of similar copper content to those studied here have shown that in alloys with a magnesium content of ∿ 0.25wt% and a silver content close to that of alloys studied here (0.5wt%) the predominant precipitation morphology is that of θ', with about 30% precipitation on {111} aluminium matrix planes. Alloy A5, containing ∿ 0.6wt% silver and ∿ 0.3 wt% magnesium, showed similar dual-mode precipitation behaviour but with much more Ω precipitate (∿ 80%) than θ' precipitate. Although alloy A5 also had an addition of ∿ 1.13% zinc, the increase in magnesium content appears to have been the most critical. This is further highlighted by a comparison of alloys A4 and A5 which have essentially the same silver and zinc contents, but where both Ω and θ precipitation occurs in alloy A5, θ' precipitation has been virtually surpressed, presumably by an increase in magnesium content.

An alternative proposal for the nucleation of Ω has been put forward by Taylor et al[114]. They proposed that small Mg_3Ag complexes were formed in the initial stages of ageing and that these acted as nucleation centres for the growth of Ω. It was agreed that since Mg_3Ag nucleated on {111} planes due to epitaxial constraints, then the copper rich phase then followed this pattern of growth. They suggested, also, that the formation of Ω rather than {100}-type precipitates was sensitive to presence together of silver and magnesium, preferably with an atomic ratio of at least 1:3. Whilst the results here would suggest a qualitative agreement with this hypothesis in that magnesium and silver should be present in amounts in excess of ∿ 0.6wt% if precipitation on {100} matrix planes is to be suppressed, the electron diffraction data do not show the presence of any zones/complexes on

{111} aluminium matrix planes prior to nucleation of Ω. Furthermore, the Mg_3Ag hypothesis does not explain why the copper-rich precipitate with a composition of, or close to, $CuAl_2$, should not revert to the {100} form characteristic of the binary Al-Cu system. Also, although the prior-formation of Mg_3Ag complexes is certainly an attractive hypothesis for Ω nucleation, it does not explain the secondary effects produced by an addition of zinc which appears to refine the Ω phase and promote its formation.

4.5.2 Growth of Precipitates

The growth of precipitates in the three alloys studied here follow the principles of Ostwald ripening, whereby the small precipitates dissolve in the matrix and the larger precipitates grow, as ageing proceeds. Such coarsening of precipitates derives its driving force from the consequential reduction in the total interfacial energy of the system. Although θ' precipitates initially form alongside the Ω phase, the fact that they dissolve in preference to Ω on ageing that is consistent with them having the higher specific surface energy. Since it is suggested θ' phase has a higher strain energy than Ω, then it is likely that some contribution to the driving force for coarsening may be provided by a reduction in the overall strain energy of the system, ie the dissolution of θ'.

In order to ascertain the rate-controlling process for growth in these alloys it is worth considering the various theoretical treatments of particle growth. Lifshitz and Slyozov[29], and Wagner[30] have established, independently, that diffusion controlled growth follows an R^3 versus t relationship. Expanding these theories Greenwood[28] has shown that the mean radius $\bar{r}$, of a spherical particle under such conditions can be expressed as:

$$\bar{r}^3 = \frac{8DS\gamma\Omega t}{9kT} \qquad (4.2)$$

where D is the diffusion coefficient, S is the solubility of a particle of infinite radius, Ω is the atomic volume of atoms in the particle, γ is the interfacial energy and t is time. Similarly, for interface-controlled growth Greenwood has shown that the mean radius can be expressed as:

$$\bar{r}^2 = \frac{64CS\gamma\Omega t}{8kT} \qquad (4.3)$$

where c is a constant.

Although the particles observed in the Al-Cu-Mg-Ag alloys studied here are not spherical, an indication of the rate-controlling process can be established if the logarithm of the mean precipitate diameter, $\bar{d}$, is plotted as a function of logarithmic time, t. This is shown in Figure 4.4, for Ω precipitation at 140°C in alloy alloys. (Points corresponding to the earliest stages of ageing have been ignored due to the fact that nucleation was still occurring). In Figure 4.4 the points are seen to lie on a series of straight lines, one for each composition and each with a slope close to $\frac{1}{3}$. The results, therefore, accord closely with a cube-law relationship, $\bar{d}^3 = \text{const} \times t$, and are consistent with diffusion-controlled growth. Alloy composition may be affecting the rate of growth as evidenced by the slightly displaced lines, one for each composition. Further, since silver contents do not differ appreciably and zinc is virtually absent in alloy A3 compared with more than 1wt% in A4 and A5, it is feasible that growth rates are most sensitively affected by the level of magnesium.

Since the Ω precipitates are not spherical another way to analyse the growth process is to look at the way the volume and surface area of the precipitates behave as a function of ageing time. Referring to equations 4.2 and 4.3, at constant temperature these equations may be written as $\frac{d\bar{V}}{dt}$ = constant and $\frac{d\bar{A}}{dt}$ = constant respectively for diffusion- and interface-controlled growth. Thus, by plotting both mean volume, $\bar{V}$, and mean surface area, $\bar{A}$, as a function of time it is possible to ascertain the rate-controlling process. Figure 4.5 a-c show the variation in mean precipitate volume, edge surface area, and total surface area respectively. For interface-controlled growth either Figure 4.5b or c should produce points lying on a series of straight lines, one for each alloy. Considering first the active growing edge of the precipitates, Figure 4.5b, the points can be seem to lie on a series of curves. This would tend to rule out interface-controlled growth a favour of diffusion control. Indeed, if the planar surfaces were included in the surface area plots, Figure 4.5c, the conclusion remains the same due to the fact that, although having a large area compared with the narrow cylindrical edge of a precipitate, their slow growth rate means that their rate is much less significant. Figure 4.5a, however, shows that by plotting mean precipitate volume as a function of time, the points lie on a series of straight lines, one for each alloy, confirming that diffusion of solute through the aluminium lattice is the rate-controlling process.

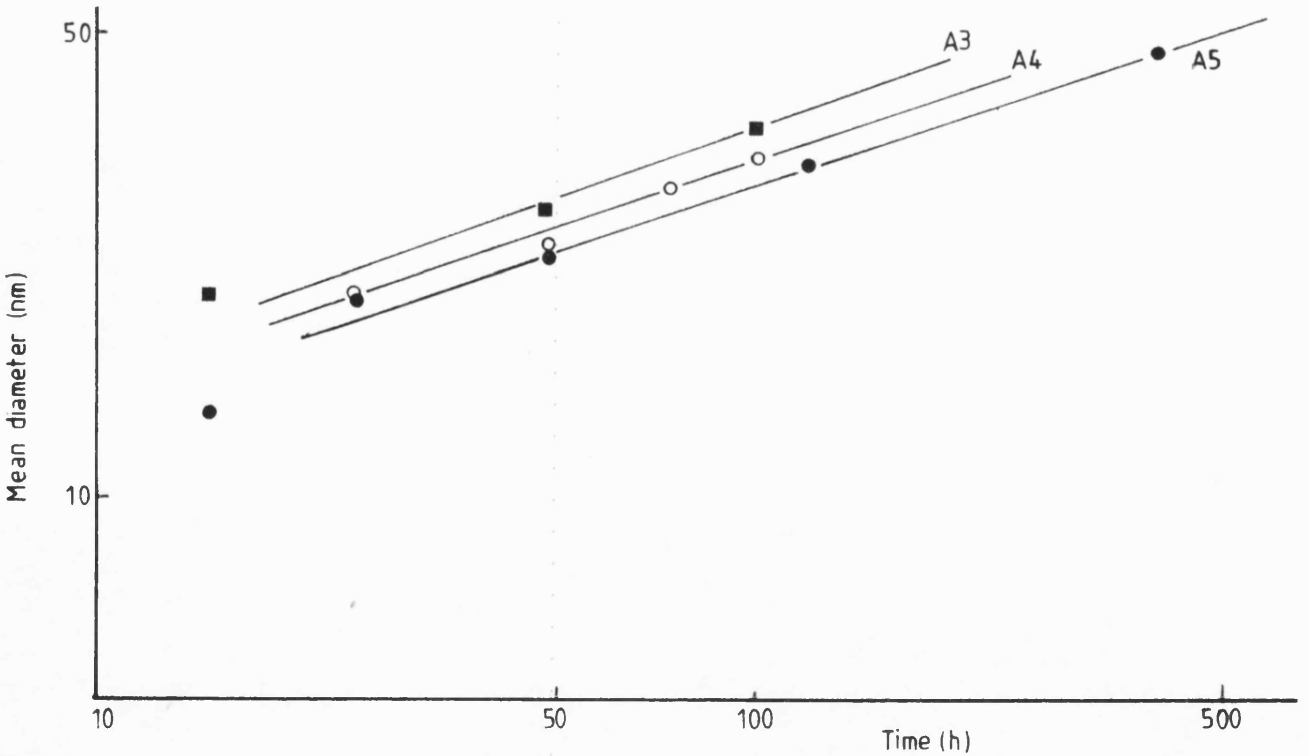

Figure 4.4 Log plot of mean diameter versus time for Ω precipitate.

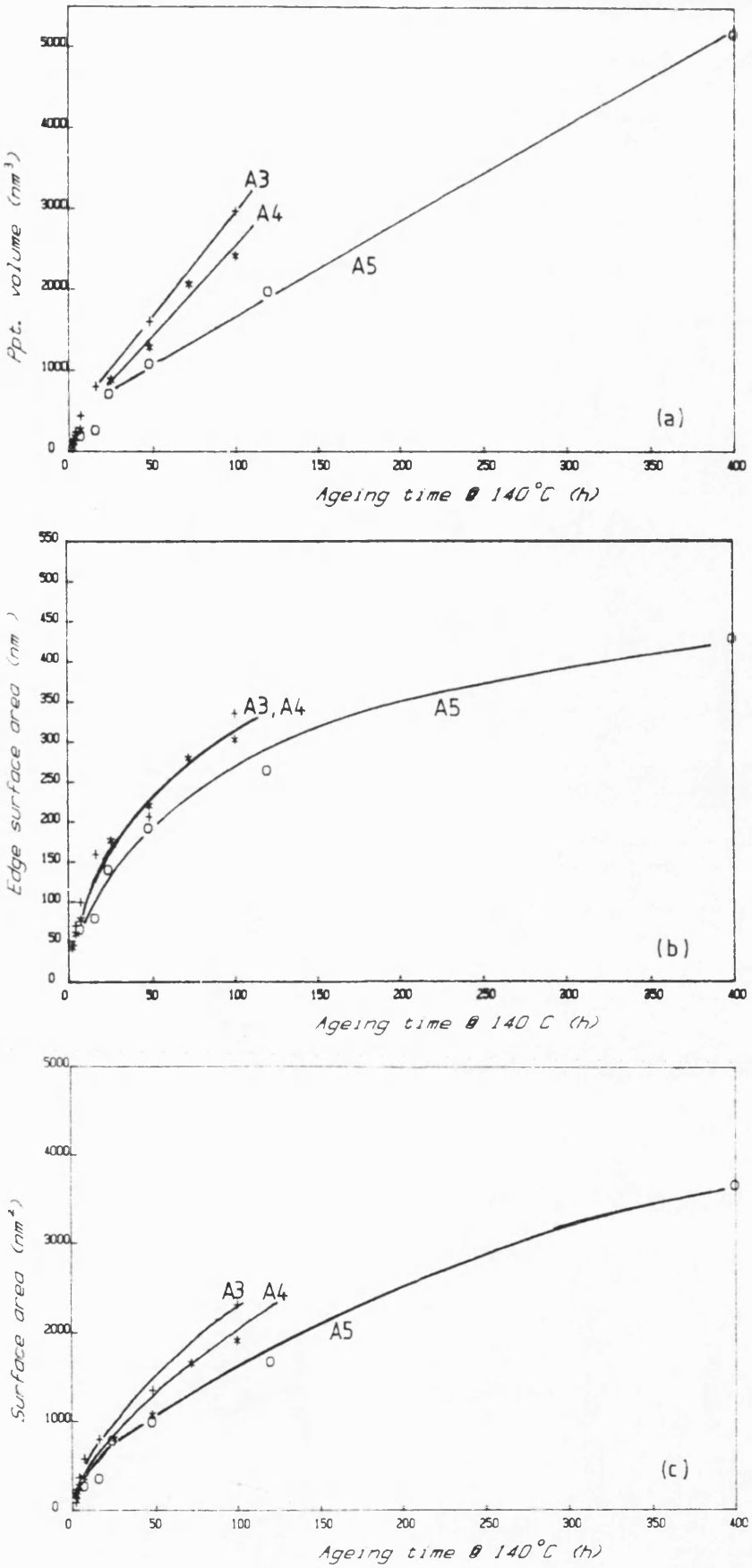

Figure 4.5 Precipitate parameters plotted as a function of ageing time at 140°C for the Ω precipitate;
(a) mean volume , (b) mean edge surface area , (c) mean total surface area.

Turning to the rate-controlling process for θ' precipitate, analysis is made rather more difficult due to their lower population and relative rapid dissolution in these alloys plots of mean precipitate volume and edge surface area are illustrated in Figures 4.6a and b respectively. There is little to choose between the graphs for deciding whether the growth of {100} precipitate is diffusion or interface controlled. However, there would appear to be no clear-cut evidence to suggest that it differs from the Ω growth mechanism.

The Lifshitz-Wagner theory of particle coarsening predicts a theoretical distribution of particle sizes. For diffusion-controlled growth the particle size distribution is asymmetrical, with a steeper slope on the side of larger-sized particles with a cut-off at one and a half times the mean precipitate size. The ideal spherically-shaped particle does not usually occur in practical systems and many experimental observations show departures from the theoretical distribution. Other factors such as volume fraction and particle impingement[145-7] have also been shown to affect the form of the distribution and the cut-off value. This has been demonstrated in Al-Cu alloys[148] where the particle shape, a thin platelet, is far from spherical and may account also for the oppositely-skewed distributions found in Al-Cu-Mg-Ag alloys as well as cut-off at approximately twice the mean particle size (See Figures 3.21, 3.27 and 3.29).

Growth data for alloy A5 at 140°C, 155°C and 170°C are plotted in Figure 4.7. (Data at 155°C was supplied by Mr R L Trumper at ARE, Portland). The slope of each line is plotted logarithmically against reciprocal temperature in Figure 4.8. The line drawn through the points indicates that the activation energy for diffusion is $136 kJmol^{-1}$, a value which compares favourably with a reported value of $\sim 128 kJmol^{-1}$ for the diffusion of copper through aluminium of somewhat higher temperatures.

4.6 Strengthening Mechanisms

The data for the hardness, yield stress and tensile strength of solution-treated materials are consistent with there being some degree of solid solution hardening upon quenching. Mott and Nabarro[43] have shown that the hardening due to solid solution alloying may be related to the atomic concentration of solute (c) and the atomic mismatch (ε) according to:

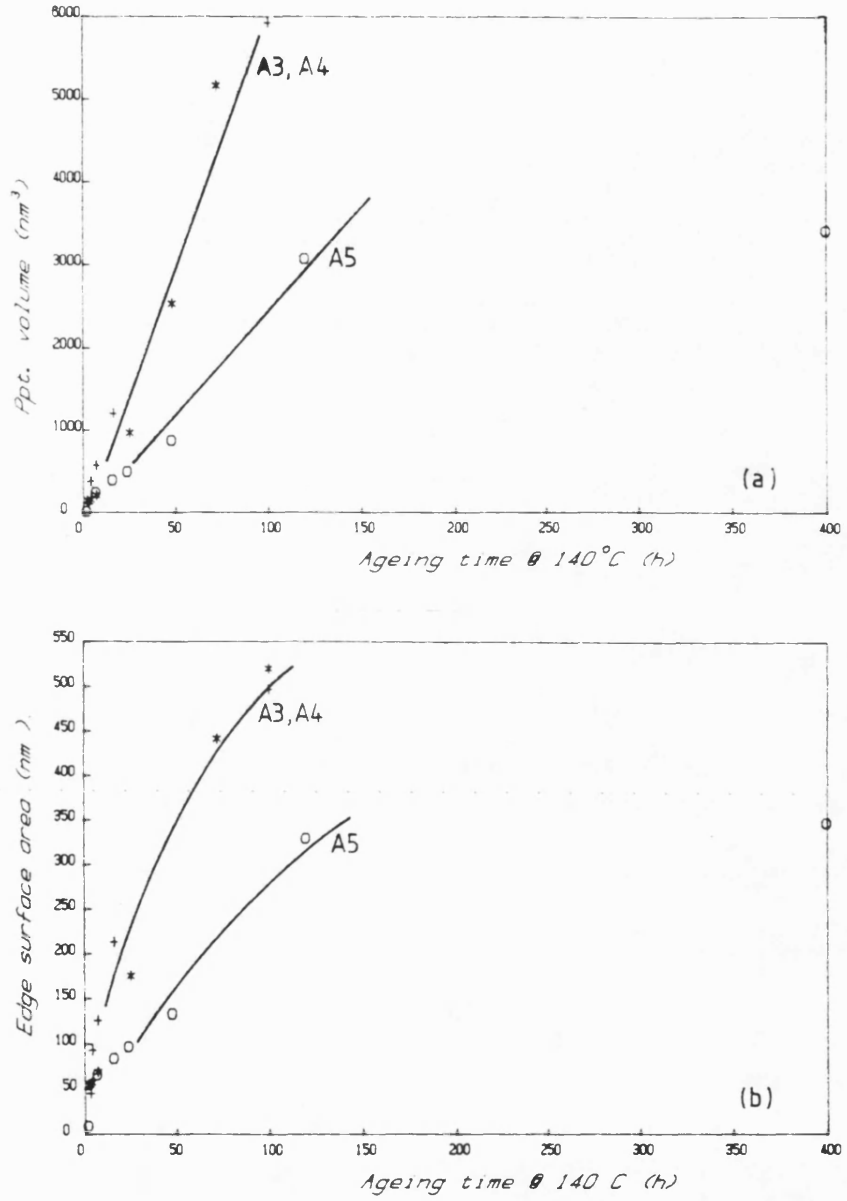

Figure 4.6 Precipitate parameters plotted as a function of ageing time at 140°C for the θ′ precipitate;
(a) mean volume , (b) mean edge surface area.

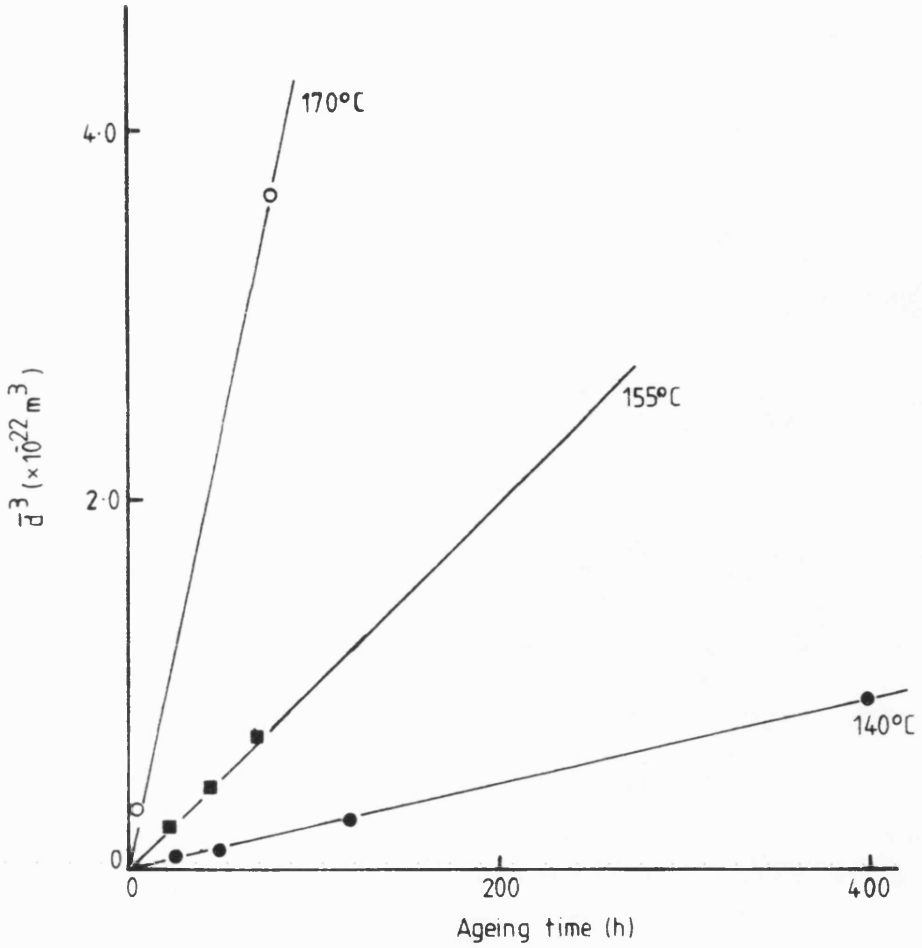

Figure 4.7 Growth data for alloy A5 at various temperatures.

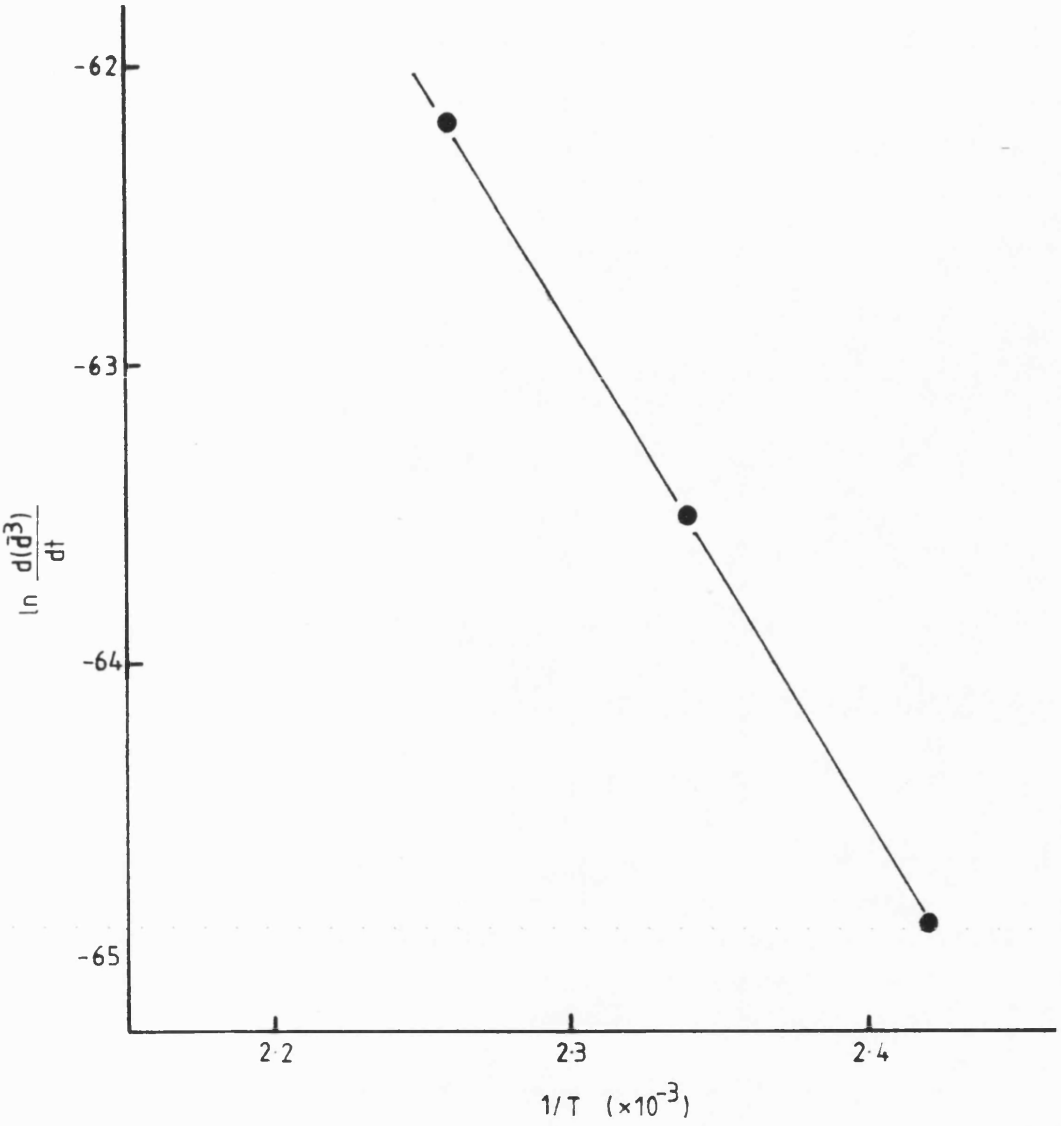

Figure 4.8 Arrhenius plot of precipitate growth data

$$\Delta\tau = 2G\varepsilon c \qquad (4.4)$$

where τ is the yield stress and G is the shear modulus of the matrix. Table 4.1 gives the predicted yield stress increments due to the alloying additions Cu, Mg, Ag and Zn for all alloys studied. As an example, Alloy A4 which has an addition of 4.72wt% copper (c = 0.021) is predicted to give a yield stress increment of $\sim$ 140 MPa due to solid solution hardening. Similarly, 1.13wt% zinc may give $\tau\sim$ 19 MPa whilst 0.65wt% magnesium may give $\tau\sim$ 40 MPa. Silver gives a negligible increase in yield strength due to its small atomic mismatch. However, the nett effect of such alloying additions is difficult to ascertain because the radius of a copper atom and a zinc atom are smaller (2.555Å and 2.66Å respectively) and magnesium larger (3.196Å) than an aluminium atom (2.862Å). Therefore, some compensation effect might be expected if larger atoms were to associate with smaller atoms. Still, the measured yield stresses of the solution-treated alloys (110-130 MPa) is close to what might be expected from the above examination.

The yield stresses of alloys aged to peak hardness were in the range $\sim$ 400-475 MPa, depending on alloy composition and ageing temperature, although the effect of temperature was less than for alloy composition. The results have been summarised in Table 3.2, but the general conclusion to be drawn from the data is that a structure containing virtually all Ω precipitate (alloys A3 and A4) gives higher strengths than that in which a significant amount of θ' is present (alloy A5). In a previous study[139] on the Al-4.8wt% copper system additions of 0.27wt% magnesium and 0.44wt% silver were found to give proof stresses of 360 and 375 MPa after ageing to peak hardness at 140°C and 170°C respectively and tensile strengths of 365 MPa and 380 MPa. This alloy (Al-4.92Cu-0.27Mg-0.31Ag) is similar in composition to alloy A5 studied here and also contained a mixture of Ω and θ' precipitation, with approximately 30% of the Ω precipitate. This earlier study also showed that alloys containing entirely θ' phase had lower strength, for example an alloy containing 0.24wt% magnesium and <0.01wt% silver had a proof stress of $\sim$ 300 MPa and a tensile strength of $\sim$ 350 MPa.

Taking these observations together, the indication is that Ω precipitates have a greater strengthening effect than that of θ' precipitates. However, before such differences can be explained it is necessary to establish the operative strengthening mechanism. In

Table 4.1

Increase in yield stress , $\Delta\tau$, due to solid solution hardening according to Mott and Nabarro.

Alloy	Element	c	ϵ	$\Delta\tau$(MPa)
A3	Cu	0.0204	0.12	135
	Mg	0.0085	-0.10	46
	Ag	0.0015	0.01	0.8
	Zn	0.0001	0.07	0.4
A4	Cu	0.0210	0.12	139
	Mg	0.0075	-0.10	41
	Ag	0.0016	0.01	0.9
	Zn	0.0048	0.07	19
A5	Cu	0.0212	0.12	140
	Mg	0.0027	-0.10	15
	Ag	0.0013	0.01	0.7
	Zn	0.0053	0.07	20

this respect, there are two important pieces of microstructural information recorded in this study which may be utilised. Firstly, the number of precipitates per unit volume (N_V) were found to be decreasing as the hardness peaks were approached. This is illustrated in Figure 5.9, where N_V is plotted as a function of time at 140°C for the Ω precipitate. It can be seen that maximum values of N_V occurred after ∿ 17h for alloy A5 and after ∿ 3-4h for alloy A3 and A4, whereas the respective peak hardnesses were not reached until times of ∿ 120h (A5) and ∿ 48h (A3 and A4). Secondly, the volume fraction of precipitate (f) progressively increased with ageing time to give total values ∿ 0.06 as illustrated in Figure 4.10 for the {111} precipitate morphology.

According to the Orowan[46] model of particle strenthening the yield stress, τ, is related to particle spacing, λ, such that:

$$\tau = \frac{Gb}{\lambda} \qquad (4.5)$$

where G is the shear modulus and b is the Burgers vector. Table 4.2 lists various parameters relating to interparticle spacing and volume fraction of precipitate. From this table it can be seen that the interparticle spacing $\lambda_1 = \frac{1}{N_V^{\frac{1}{3}}}$ is greater at the recorded peak hardness for each alloy at 140°C. This clearly demonstrates that the increase in strength of the alloy as the peak hardness is reached is not attributable to a mechanism based upon dislocations bowing around precipitates, ie the Orowan model of particle strengthening, since according to this theory the maximum strength should occur when N_V is at a maximum.

An alternative precipitate-hardening mechanism which involves shear of the precipitate by the dislocation leads to a relationship between the volume fraction of precipitate and the interfacial energy of the precipitate (Kelly and Fine[45]) leads to an increase in yield stress, $\Delta\tau$, of:

$$\Delta\tau = \frac{\gamma}{b}.f^{\frac{1}{2}} \qquad (4.6)$$

This equation predicts that yield stress should increase with volume fraction of precipitate. A more quantitative test of the precipitate shear mechanism is difficult to make because of uncertainties regarding an appropriate value to choose for γ, but assuming a typical value of $0.25 Jm^{-2}$ and taking b = 0.25 nm the

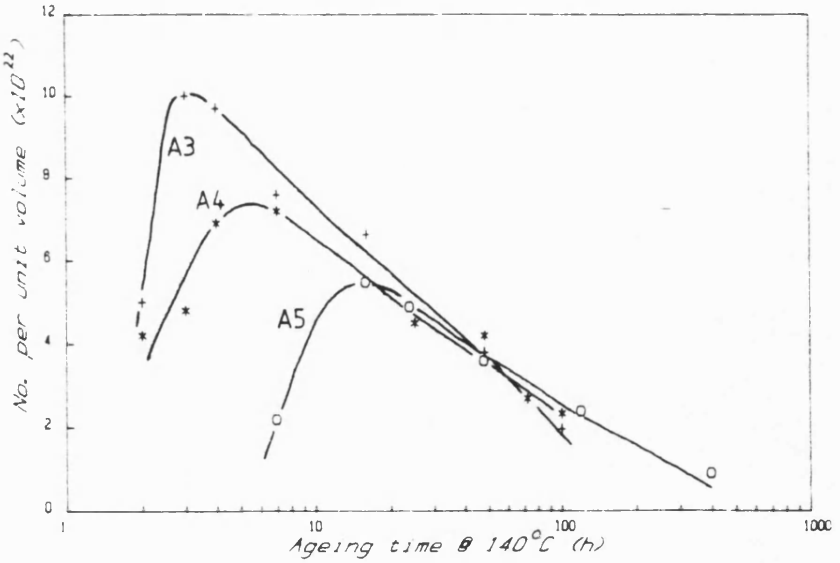

Figure 4.9 Density of Ω precipitate versus ageing time at 140°C for all alloys.

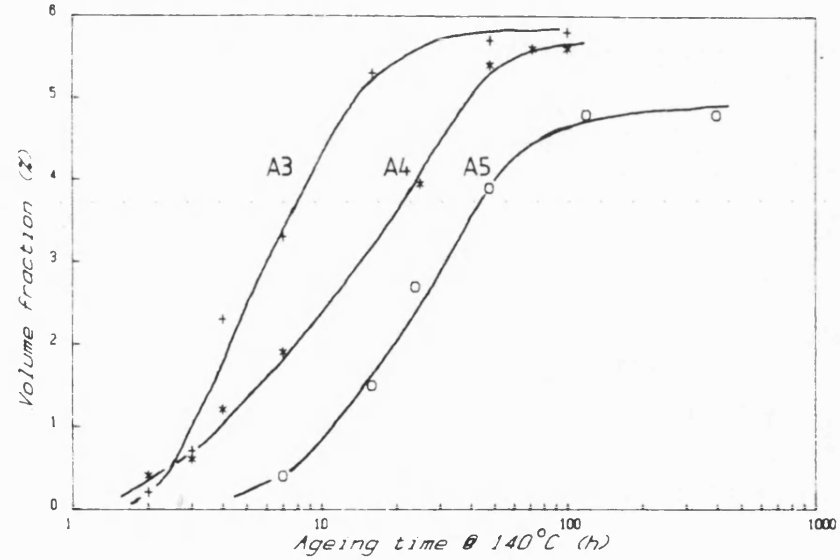

Figure 4.10 Volume fraction of Ω precipitate versus ageing time at 140°C for all alloys.

Table 4.2

Precipitate densities , Interparticle spacing and Volume fraction after various ageing times at 140°C.

Alloy	Ageing Time (h)	N_v ($\times 10^{22}$)	λ (nm)	f	$f^{\frac{1}{2}}$
A3	3	10.0	21.5	0.007	0.084
	48	3.3	31.2	0.057	0.238
A4	7	7.2	24.0	0.019	0.138
	48	4.2	28.8	0.054	0.224
A5	16 } Ω	5.5	26.3	0.015	0.122
	120 } Ω	2.4	34.7	0.048	0.219
	16 } θ′	8.2	23.0	0.032	0.179
	120 } θ′	0.5	58.5	0.015	0.122

experimental value of 0.057 for f (at peak hardness, alloy A4) gives $\Delta\tau\sim$240 MPa. This is of the same magnitude as the measured increase in strength caused by precipitation, although still $\sim$ 80 MPa short of the measured value. This extra increment could possibly be due to solid solution strengthening by the elements magnesium and zinc.

The subsequent drop in strength as ageing proceeded can be attributed to the fact that, although the volume fraction has remained the same, the precipitate density has decreased to a point where the interparticle spacing is now sufficiently large to allow the Orowan dislocation bowing mechanism to compete with the precipitate-cutting process. For example, taking the results of alloy A3 aged at 170°C, at peak hardness (2h) $N_V \sim 3.0\times10^{22} m^{-3}$. After 70 hours at 170°C (beyond peak hardness) this value decreased to $\sim 0.5 \times 10^{22} m^{-3}$ giving a value for $\lambda \sim$ 32nm. According to the Orowan model, an increase of $\Delta\tau\sim$ 214 MPa would be expected over the solution treated condition whereas according to the Kelly and Fine precipitate cutting mechanism the increase would be 240 MPa. Thus, the strength and hardness start to decrease as ageing time increases beyond peak hardness due to dislocations being able to bow between the precipitates.

Another factor which supports the precipitate cutting mechanism up to, and including peak hardness, is that alloy A4 (zinc addition) aged to peak hardness, had a similar strength to alloy A3 (no zinc) and possessed a similar volume fraction of precipitate, yet precipitate densities, and hence interparticle spacings, were significantly different.

Thus, it is possible to represent the ageing curve in terms of the operating strengthening mechanisms, and this is illustrated in Figure 4.11. Initially the strength of the alloy is that of the supersaturated solid solution. As precipitation takes place the yield stress is governed by the stress necessary to force dislocations through the precipitates. The work done in forcing the dislocations through the precipitates is governed by several factors, including internal order of the precipitates and interface effects. As peak hardness is reached the work done in cutting each particle increases and dislocations are eventually forced between the particles instead of through them. Further increase in particle size (and therefore spacing since volume fraction of precipitate remains the same) then leads to a decrease in strength, according to the Orowan criterion.

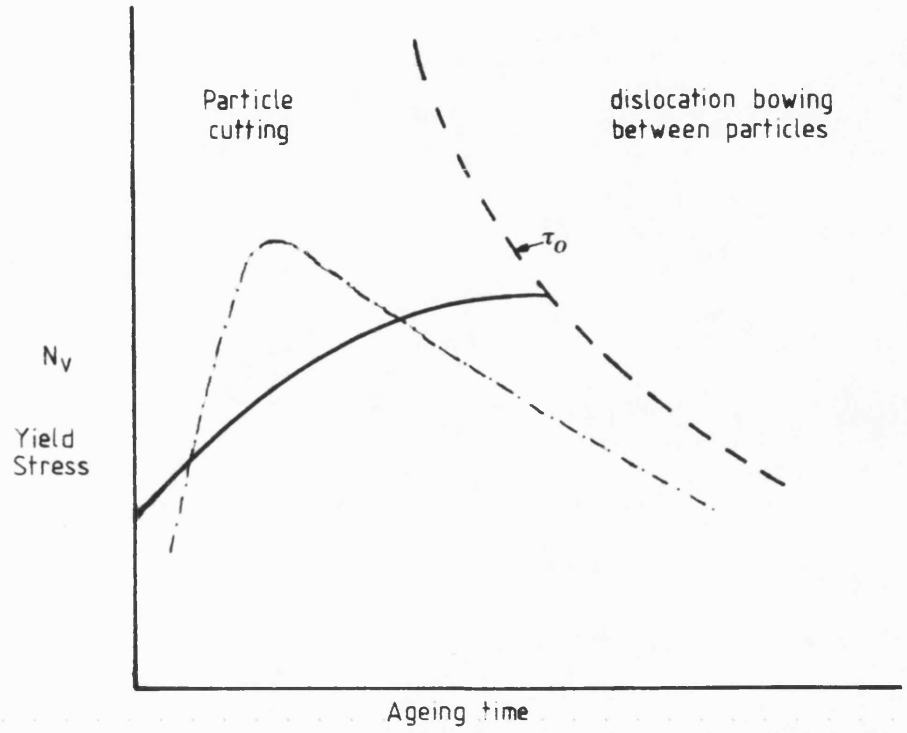

Figure 4.11 Schematic representation of the variation of yield stress and precipitate density (N_v) with ageing time

At short ageing times the applied stress (τ_o) necessary to force dislocations between particles is much larger than the measured yield stress[44]. The variation of τ_o with ageing time is denoted by the dotted curve in Figure 4.11, where the precipitate density as a function of ageing time is also represented.

Returning to the question of the higher strength developed in alloys containing Ω precipitate, equation 4.4 indicates that this may be achieved by increasing either the volume fraction of precipitate, f, or the interfacial energy, γ. Since present results show that f does not differ significantly from one alloy to another at peak hardness, the high strengths conferred by Ω precipitate might be attributable to a higher interfacial energy, ie the energetics involved in shearing an Ω precipitate may be greater than that for shearing a θ' precipitate. A problem with this hypothesis, however, is explaining why a precipitate of apparently higher interfacial energy would appear to be the more stable form in the nucleation and growth process.

It must be noted that the dislocation-bowing theory of Orowan and the precipitate-cutting mechanism of Kelly and Fine are both based on the assumption of spherical particles. Particle shape can play an inportant role in hardening primarily by changing the value of the particle spacing, λ. Kelly[149] has pointed out that at equal volume fraction, rods and plates strengthen about twice as much as spherical particles. Thus, it is tempting to suggest that the effect of particle shape plays a more important role than demonstrated; indeed, if the interfacial energy between Ω and the aluminium matrix is lowered (making Ω the more stable phase) then particle shape plays a crucial role in strengthening. For example, if the interfacial energy is reduced to, say, $0.15 Jm^{-2}$, then $\Delta\tau \sim 143$ MPa for spherical particles. The actual increase recorded was ~ 310 MPa and could indicate the way in which particle shape is influencing the degree of strengthening. However, without a value for γ the argument must be regarded as speculative at the present time.

4.7 Environmental Behaviour

Although the experimental accuracy in the environmental tests was generally poor, partly as a result of the relatively large effect that segregated porosity has upon the small diameter specimens, some clear trends emerged from the work.

Testing in sea water, compared with testing in air, resulted in a reduction in life and in load bearing capacity of all alloys. The extent of this degradation was, however, dependent on metallurgical condition. For example, after ageing to peak-hardness at 170°C, the alloys containing zinc (A4 and A5) showed relatively small reductions in strength (a few per cent) and in life (∿ 20%). On the other hand the properties were reduced by at least 50% in alloy A3 (See Table 3.3). In the peak-hardness condition corrosion cracks were present in all alloys, with reaction products containing oxygen, sulphur and chlorine being associated with intergranular attack (for example, see Figure 3.42b). The cracks grew under the combined effect of stress and corrosive environment until the load bearing area was reduced such that failure of the sound metal occurred to give a tensile fracture similar to that observed in the tests in air (eg Figure 3.31a). There were clear indications that samples which suffered the greater loss in properties were those in which intergranular corrosive attack was the more severe, although the growth of corrosion products on post-fracture surface before removal of the broken specimen from the sea water precluded any quantitative assessment of the extent of corrosive attack.

This type of accelerated cracking has, in some systems, been associated with electrochemical reactions where local anodic regions are set up in the metal which are preferentially attacked by the environment[150]. Clearly there would be preferential attack at grain boundaries by the salt water since all alloys tested possessed both grain boundary precipitation and adjacent precipitate-free zones, a structure which enhances the electro-chemical effects in these regions. However, it would be difficult to account for the differences observed between alloys aged to peak hardness solely on this basis, particularly since they contained the same type and quantity of grain-boundary precipitate.

A more likely explanation is that the zinc addition has modified the precipitate-free zone (PFZ) adjacent to the grain boundaries. Removal of the PFZ or a reduction in its width would be expected to suppress electrochemical effects and thereby reduce the extent of corrosive attack[127, 137] and this may well be one role of the zinc addition. However, the limited number of grain boundaries present in these coarse-grained structures meant that reliable data was difficult to obtain, although there was a suggestion from TEM work that PFZ's

were narrower in alloys containing zinc.

As regards the overaged alloys, the microstructures were different and any effect of zinc was hidden by some other mechanism since alloy A5 now has poor properties whereas alloys A3 and A4 give the better performance. This cannot be explained fully, although the fact that alloy A5 had a mixed mode of precipitation may be of some significance in this respect. Similarly, the poorer properties of solution-treated A4 compared with alloys A3 and A5 cannot be explained, since as-quenched supersaturated solid solutions of aluminium alloys are generally found to be relatively resistant to stress-corrosion cracking[122].

As an interesting comparison a French casting, alloy, Avior (Al-4.6Cu-0.4Mg-0.8Ag-1.4Zn) is reported[122] as belonging to the group of most stress-corrosion susceptible alloys when in the T6 heat treatment condition, ie solution-treated and aged to peak hardness. The composition of this alloy is similar to that of alloys A4 and A5 which in this work show greater resistance to SCC in the peak hardness condition. However, no direct comparison between the alloys has been made.

CHAPTER 5

CONCLUSIONS

1 Coring and much of the grain-boundary precipitate present in cast alloys based on the Al-Cu composition can be removed by treatment at 500°C for 6 h followed by 42 h at 525°C.

2 Ageing at both 140°C and 170°C gave tensile strengths >400 MPa, the stronger alloys (A3 and A4) being those in which magnesium and silver were present at $\sim$ 0.6 wt%.

3 Precipitation in alloys containing $\sim$ 0.6 wt% magnesium and silver (A3 and A4) was essentially homogeneous and occurred on {111} planes of the aluminium lattice. Precipitation in alloy A5 occurred on both {100} and {111} lattice planes.

4 The precipitate formed on {111} planes has been identified as having a hexagonal structure with $a = 0.496$ nm and $c/a = 1.414$. The orientation relationships are given by:

$$[0001]_{ppt} \,||\, \langle 111 \rangle_{Al}$$

and $$\langle 10\bar{1}0 \rangle_{ppt} \,||\, \langle 110 \rangle_{Al}$$

This epitaxy results in close registry between lattice vectors in the respective structures.

5 {111}-type precipitation is associated with a single ageing peak and the precipitate does not change its crystal structure with increased ageing time. It is considered to be an equilibrium phase.

6 Precipitation on {100} lattice planes in alloy A5 has been identified as being θ'. No evidence was found for the formation of G P zones and θ", usually associated with Al-Cu alloys. {100} precipitation occurs only in small amounts in alloys A3 and A4, and tends to dissolve during the {111} growth process.

7 Precipitate growth is a diffusion-controlled rather than an interface-controlled process.

8 A small addition ($\sim$ 1.1 wt%) of zinc reduces the size of the {111}-type precipitate but does not change its crystal structure.

9 Quantitative TEM measurements of precipitate populations show that the hardness peak occurs as the volume fraction of precipitate starts off at its maximum value ($\sim$ 6% for all alloys). The hardening

mechanism is associated with the shear of precipitates by dislocations. The higher strength of alloys containing all {111}-type precipitate may then be due to a higher value for its interfacial energy, compared with the {100} precipitate structure.

10 As precipitates coarsen during longer ageing times (Ostwald ripening), the dislocation bowing mechanism becomes operative, causing a decrease in the strength of the alloys.

11 Testing in a sea water environment generally degraded the alloy properties. Intergranular attack occurred together with the formation of corrosion products containing the elements oxygen, sulphur and chlorine.

12 Zinc has a beneficial effect on the stress-corrosion behaviour of alloys in the peak-hardness condition, but more work is needed before the mechanism of stress-corrosion attack is understood.

13 Of the systems investigated an aluminium - 4% copper alloy which contained approximately 0.6 wt% of the elements magnesium and silver and $\sim$1 wt% zinc (alloy A4) possessed the best combination of strength and stress-corrosion resistance.

SUGGESTIONS FOR FUTURE WORK

It is clear that more work is needed to fully characterise the precipitation behaviour of Al-Cu-Mg-Ag alloys of similar compositions to those studied here, particularly with regard to the contributions of variations in magnesium and zinc contents have on the overall precipitation behaviour. In this respect, suggestions for future work are outlined below:

1 A more detailed quantitative study of the alloys studied here, particularly with reference to the microstructures produced at different ageing temperatures. Of particular interest would be the effect of ageing at higher temperatures, up to say 350°C, to assess the stability of the Ω precipitate.

2 The study of a wider range of compositions; for example, an interesting study would be to define the "window" in which only Ω precipitation occurs. This has been qualitatively established as necessitating the presence of $\sim$0.6wt% of both magnesium and silver. However, variations in magnesium content from, say, 0.5 to 0.8wt% may prove instructive.

3 A study of low magnesium content alloys in order to fully characterise the GP zone $\rightarrow \theta'' \rightarrow \theta'$ precipitation sequence by electron diffraction, and therefore help in understanding the effect of two precipitation modes, as found in the lower Mg content alloys.

4 Tensile testing after different ageing times along the ageing curve in order to fully assess the strengthening mechanisms as a function of ageing time. This work could be complimented by TEM examination of the deformed alloys to look for particle cutting etc.

5 A more detailed study of the SCC behaviour of the alloys, using the fracture mechanics approach to assess the SCC susceptibility. Of equal importance in this respect is the study of grain boundary precipitation, and the effect that additions such as zinc may have on PFZ width and SCC susceptibility in general.

REFERENCES

1 I. J. Polmear; "Metallurgy of the light metals", Edward Arnold (Publishers) Ltd, London, (1981).

2 A. Wilm; Metallurgie, 8, (1911), p 225.

3 P. D. Merica, R. G. Waltenberg and H. Scott; Trans. AIME, 64, (1920), p 41.

4 D. A. Porter and K. E. Easterling; "Phase Transformation in Metals and alloys", Van Nostrand Reinhold Co Ltd, (1981).

5 A. Guinier; Nature, 142, (1938), p 699.

6 G. D. Preston; ibid, 142, (1938), p 570.

7 M. Volmer and A. Weber; Z. Phys. Chem., 119, (1925), p 277.

8 R. Becker and W. Döring; Ann. Phys., 24, (1935), p 719.

9 J. W. Martin and R. D. Doherty; "Stability of Microstructure in Metallic Systems", Cambridge University Press, Cambridge, (1976).

10 I. S. Servi and D. Turnbull; Acta Met., 14, (1966), p 161.

11 J. W. Cahn; ibid, 5, (1957), p 169.

12 U. Dehlinger; Z. Metallk, 51, (1960), p 353.

13 G. Thomas; 4th Int. Conf. on Electron Microscopy, Springer-Verlag, (1960), p 603.

14 G. Thomas and J. Nutting; "The Mechanism of Phase Transformations in Metals", Inst. of Metals, (1956), p 57, p 280.

15 A. Kelly and R. B. Nicholson; Progress in Materials Science, [3], 10, (1963).

16 H. Suzuki; Rep. Res. Inst. Tohoku Univ., A1, (1949), p 183.

17 R. D. Heidenreich; Acta Met., 3, (1955), p 79.

18 R. B. Nicholson and J. Nutting; ibid, 9, (1961), p 332.

19 J. W. Christian; "Phase Transformations" in Physical Metallurgy, Ed. R. W. Cahn, North-Holland Publ. Company, London, (1970), Chapter 10.

20 J. Burke; "Kinetics of Phase Transformations in Metals".

21 H. K. Aaronson; "The decomposition of Austenite by Diffusional Processes", Interscience, (1962), p 387.

22 H. I. Aaronson, C. I. Laird and K. R. Kinsman; "Phase Transformations", ASM, Metals Park, Ohio, (1970), p 313.

23 C. I. Laird and H. I. Aaronson; Acta Met., 17, (1969), p 505.

24 C. Zener and C. Wert; J. Appl. Phys., 21, (1950), p 5.

25 F. S. Ham; J. Chem. Phys. of Solids, 6, (1958), p 335.

26 C. Zener; J. Appl. Phys., 20, (1949), p 962.

27 J. Burke; Phil. Mag., 6, (1961), p 1439.

28 G. W. Greenwood; "The Mechanism of phase Transformations in Crystalline Solids", Inst. of Metals, London, (1969), p 103.

29 I. M. Lifshitz and V. V. Slyozov; J. Phys. Chem. Solids, 19, (1961), p 35.

30 C. Wagner; Z. Electrochem, 65, (1961), p 581.

31 A. J. Ardell and R. B. Nicholson; Acta Met., 14, (1966), p 1295.

32 A. J. Ardell and R. B. Nicholson; J. Phys. Chem. Solids, 27, (1966), p 1793.

33 J. W. Cahn; Acta Met., 10, (1962), p 907.

34 E. N. Bower and J. A. Whiteman; "The Mechanism of phase Transformations in Crystalline Solids", Inst. of Metals, London, (1969), p 119.

35 D. M. Schwarz and B. Ralph; Met. Sci. J., 3, (1969), p 216.

36 J. D. Boyd and R. B. Nicholson; Acta Met., 19, (1971), p 1379.

37 D. M. Schwarz and B. Ralph; Phil. Mag., 19, (1969), p 1069.

38 A. Youle, D. M. Schwarz and B. Ralph; Met. Sci. J., 5, (1971), p 131.

39 R. B. Nicholson; Interfaces Conference (Ed. R. C. Gifkins), Butterworths, London, (1969), p 139.

40 R. L. Fleischer; "Solid solution hardening" in "The strengthening of Metals" (Ed., D. Peckner), Reinhold Publishing Co, New York, (1964).

41 R. L. Fleischer; Acta Met., 11, (1963), p 203.

42 H. Suzuki; Sci. Rep. Res. Inst. Tohoku Univ., 4A, (1952), p 455.

43 N. F. Mott and F. R. N. Nabarro; "Report on Conference on the strength of solids", Phys. Soc., London, (1948), p 1.

44 G. E. Dieter; "Mechanical Metallurgy"; McGraw-Hill Kogakusha Ltd, Tokyo, (1961), p 215.

45 A. Kelly and M. E. Fine; Acta Met., 5, (1957), p 365.

46 E. Orowan; discussion in "Symposium on Internal Stresses", Inst. of Metals, London, (1947), p 451.

47 V. F. Kochs; Phil. Mag., 13, (1966), p 541.

48 M. F. Ashby; Acta Met., 14, (1966), p 679.

49 M. F. Ashby; in Proc. Second Bolton Landing Conf. on Oxide Dispersion Strengthening, Gordon and Breach, Science Publishers, Inc, New York, (1968).

50 N. F. Mott and F. R. N. Nabarro; Proc. Phys. Soc., 52, (1940), p 86.

51 V. Gerold and H. Haberkorn; Phys. Status. Solidi, 16, (1966), p 675.

52 P. B. Hirsch and A. Kelly; Phil. Mag., 12, (1965), p 881.

53 P. M. Kelly; Inst. Met. Rev, 18, (1973), p 31.

54 G. S. Ansell and F. V. Lenel; Acta Met., 8, (1960), p 612.

55 J. W. Martin; "Precipitation Hardening", Pergamon Press, London, (1968).

56 M. L. V. Gayler and R. Parkhouse; J. Inst. Metals, 66, (1940), p 67.

57 J. M. Silcock; T. J. Heal and H. K. Hardy; ibid, 82, (1953-4), p 239.

58 V. Gerold; Z. Metall K., 45, (1954), p 599.

59 R. B. Nicholson and J. Nutting; Phil. Mag., [8], 3, (1958), p 531.

60 A. Guinier; J. Phys. Radium, 8, (1942), p 122.

61 A. Guinier; Acta Cryst, 5, (1952), p 51.

62 H. K. Hardy; J. Inst. Metals, 79, (1951), p 321.

63 H. Yoshida, D. J. H. Cockayne and M. J. Whelan; Phil. Mag., 34, (1976), p 89.

64 G. W. Lorimer and R. B. Nicholson; "Mechanisms of Phase Transformations in Crystalline Solids", "Inst. of Metals, London, (1969), p 43.

65 G. Thomas and J. Nutting; Acta Met., 7, (1959), p 595.

66 R. B. Nicholson; Proc. Eur. Reg. Conf. on Electron Microscopy, De Nederlandse Vereniging voor Electronenmicroscopie, (1961), p 375.

67 R. B. Nicholson; "Electron Microscopy and the Strength of Crystals", Interscience, (1962).

68 H. Wilsdorf and D. Kuhlmann-Wilsdorf; "Defects in Crystalline Solids", Physical Society, (1955), p 175.

69 G. W. Lorimer; "Precipitation Processes in Solids", Ed. K. C. Russell and H. I. Aaronson, Met. Soc. AIME, (1978), p 87.

70 G. Thomas and J. Nutting; J. Inst. Metals, 82, (1953-4), p 610.

71 I. J. Polmear; J Australian Inst. Metals, 11, (1966), p 246.

72 H. K. Hardy and T. J. Heal; "Progress in Metal Physics", Pergamon Press, 5, (1954), p 143.

73 H. K. Hardy and T. J. Heal; "Mechanisms of phase transformations in Metals", Institute of Metals, (1956), p 1.

74 H. K. Hardy; J. Inst. Metals, 84, (1955-56), p 429.

75 J. M. Silcock; Phil. Mag., [8], 4, (1959), p 1187.

76 H. Kimura and R. R. Hasiguti; Acta Met., 9, (1961), p 1076.

77 J. M. Silcock, T. J. Heal and H. K. Hardy; J. Inst. Metals, 84, (1955-56), p 23.

78 I. J. Polmear and H. K. Hardy; ibid, 81, (1952-53), p 427.

79 G. B. Brook and B. A. Hatt; "The Mechanism of Phase Transformations in Crystalline Solids", Institute of Metals, (1969), p 82.

80 W. L. Fink, D. W. Smith and L. A. Willey; ASM Preprint No 36, (1936).

81 W. Fraenkel; Z. Metallkunde, 22, (1930), p 84.

82 M. L. V. Gayler; J. Inst. Metals, [1], 60, (1937), p 75.

83 H. W. L. Phillips; ibid, 82, (1953-54), p 197.

84 L. Mondolfo; "Aluminium alloys: structures and properties".

85 V. I. Arkharov and L. M. Magat; Fiz. Met. Metalloved, 5, (1958), p 804.

86 N. A. Khatarova and M. I. Zakharova; ibid, 22, (1966), p 55.

87 Y. Baba; Trans. JIM, 10, (1969), p 188.

88 R. S. Archer; Trans. ASST, 10, (1926), p 718.

89 D. A. Petrov; J. Inst. Metals, [1], 6, (1938), p 63 and 81.

90 M. L. V. Gayler; Proc. Roy. Soc, [A], 173, (1939), p 83.

91 K. M. Entwistle, J. H. Fell and K. I. Koo; J. Inst. Metals, 91, (1962-63), p 84.

92 H. Perlitz and A. Westgren; Arkiv. Kemi. Min. Geol., B16, (1943), p 13.

93 J. M. Silcock; J. Inst. Metals, 89, (1960-61), p 203.

94 V. Gerold and H. Haberkorn; Z. Metallk., 50, (1959), p 568.

95 Y. A. Bagaryatskii; Z. Tekhn. Eiziki Fulmer Res. Inst. Trans. Nos 11, 12, 55, 66, (1948).

96 R. N. Wilson and P. G. Partridge; Acta Met., 13, (1965), p 1321.

97 J. D. Embury and R. B. Nicholson; Fifth Int. Congress for Electron Microscopy, Philadelphia, Academic Press, New York, (1962), p J1.

98 H. K. Hardy; J. Inst. Metals, 83, (1954-55), p 17.

99 J. T. Vietz and I. J. Polmear; ibid, 94, (1966), p 410.

100 R. N. Wilson and P. J. E. Forsyth; ibid, 94, (1966), p 8.

101 I. J. Polmear; Trans. Met. Soc. AIME, 230, (1964), p 1331.

102 I. J. Polmear and K. R. Sargant; Nature, 200, (1963), p 669.

103 I. J. Polmear; J. Inst. Metals, 88, (1959-60), p 59.

104 I. J. Polmear; ibid, 89, (1960-61), p 193.

105 F. Laves, K. Löhberg and H. Witte; Metallwirtschaft, 14, (1935), p 793.

106 F. Laves and H. Witte; ibid, 15, (1936), p 15.

107 J. H. Auld; J. T. Vietz and I. J. Polmear; Nature, 209, (1966), p 703.

108 M. J. Wheeler, G. Blankenburgs and R. W. Staddon; ibid, 207, (1965), p 746.

109 J. H. Auld and J. T. Vietz; "The Mechanisms of phase transformations in Crystalline solids", Inst. of Metals, (1969), p 77.

110 N. Sen and D. R. F. West; J. Inst. Metals, 97, (1969), p 87.

111 J. H. Auld; Acta Cryst., 28A, (1972), p 598.

112 A. J. Iler; Met. Progr., Jan, (1969), p 57.

113 M. O. Spiedel; Proc. 6th Int. Conf. 'Light Metals', Leoben, Austria, (1975), p 67.

114 J. A. Taylor, B. A. Parker and I. J. Polmear; Met. Sci., 10, (1978), p 478.

115 R. J. Chester and I. J. Polmear; Micron, 11, (1980), p 311.

116 R. J. Chester and I. J. Polmear; Proc. 7th Int. Light Metals Congress, (1981), p 58.

117 R. J. Chester and I. J. Polmear; "The Metallurgy of Light Alloys", Proc. Conf., Loughborough Univ., March, (1983), p 75.

118 H. L. Logan; "The Stress Corrosion of Metals", John Wiley and Sons, Inc, New York, (1966).

119 M. O. Spiedel; "The Theory of Stress Corrosion Cracking in Alloys", Nato Scientific Affairs Division, Brussels, (1971), p 289.

120 M. O. Spiedel and M. V. Hyatt; "Advances in Corrosion Science and Technology", Plenum Press, New York, 2, (1972), p 115.

121 "Stress Corrosion Cracking in High Strength Steels and in Aluminium and Titanium Alloys", Ed. B. F. Brown, NRL. Washington DC, (1972).

122 M. O. Spiedel; Met. Trans. A., 6A, 1975, p 631.

123 T. H. Rogers; Corrosion 1961, Butterworths, London (1962), p 605.

124 D. O. Sprowls and R. H. Brown; in "Fundamental Aspects of Stress Corrosion Cracking" (Ed. R. W. Stachle, A Forty and D. van Rooyen), NACE, Houston, (1969), p 466.

125 H. J. Engell, W. Neth and A. Suchma; Z. Metallk., 61, (1970), p 261.

126 I. J. Polmear; J. Australian Inst. Met., 89, (1960), p 193.

127 A. J. Sedriks, P. W. Slattery and E. N. Pugh; Trans. ASM, 62, (1969), p 238.

128 A. J. De Ardo and R. D. Townsend; Met. Trans., 1, (1970), p 2573.

129 E. A. Starke; J. Metals, 22, [No 1], (1970), p 54.

130 T. Takahashi and Y. Kojima; J. Japan Inst. Light Metals, 20, (1970), p 498.

131 K. G. Kent; J. Australian Inst. Metals, 15, (1970), p 171.

132 W. J. Kovacs and J. R. Low; Met. Trans., 2, (1971), p 3385.

133 E. Hornbogen; Z. Metallk., 58, (1967), p 31.

134 H. A. Holl; Corrosion, 23, (1967), p 23.

135 M. O. Spiedel; Phys. Stat. Sol., 22, (1967), p 71.

136 M. O. Spiedel; "Fundamental Aspects of Stress Corrosion Cracking" (Ed. R. W. Staehle, A. Forty and D. van Rooyen), NACE, Houston, (1969), p 638.

137 P. T. Unwin and R. B. Nicholson; Acta Met., 17, (1969), p 1379.

138 G. M. Scamans; J. Mat. Sci., 13, (1978), p 27.

139 A. F. Smith and V. D. Scott; Report on MOD contract ER3/9/4/2112/029 AUWE, (1979).

140 R. A. Colbeck and V. D. Scott; Report on MOD contract ER1(a) 9/4/2112/040 AUWE, (1982).

141 P. B. Hirsch, A. Howie, R. B. Nicholson, D. W. Pashley and M. J. Wheelan; "Electron Microscopy of Thin Crystals", Butterworth, London, (1965), p 320.

142 M. J. Wheeler; Physics Conf. on Electron Microscopy, Cambridge, (1963).

143 M. K. Heal; J. Inst. Metals, 80, (1951-52), p 483.
83, (1954-55), p 337.
84, (1955-56), p 429.

144 F. R. N. Nabarro; Proc. Roy. Soc., 175A, (1940), p 519.

145 A. J. Ardell; Acta Met., 20, (1972), p 61.

146 A. D. Brailsford and P. Wynblatt; ibid, 27, (1979), p 489.

147 C. K. L. Davies, P. Nash and R. N. Steven; ibid, 28, (1980), p 179.

148 J. D. Cook and J. Nutting; "The Mechanisms of Phase Transformations in Crystalline Solids", London: Inst. of Metals, (1969), p 54.

149 P. M. Kelly; Scr. Metall., 6, (1972), p 647.

150 E. H. Dix; Trans. ASM, 42, (1950), p 1057.

APPENDIX I

Statistics Program for Precipitate Sizes

```
  TYPE STATS.BAS
10 REM STATISTICS PROGRAM FOR PRECIPITATE SIZES
20 DIM A(800),B(800),C(800),X(20),F(20)
30 I=1:N=0:S=0
40 INPUT "IDENTIFICATION";A$
50 PRINT A$:PRINT
60 INPUT A(I):IF A(I)=0 GOTO 80
70 N=N+1:I=I+1:GOTO 60
80 REM TO CONVERT READINGS INTO ACTUAL SIZES IN NM
90 INPUT "PRINT MAGNIFICATION";MA
100 FOR I=1 TO N
110 B(I)=(A(I)/MA)*1000
120 NEXT I
130 REM TO CALCULATE THE MEAN
140 FOR I=1 TO N
150 S=S+B(I)
160 NEXT I
170 ME=S/N
180 REM TO CALCULATE THE VARIANCE
190 FOR I=1 TO N
200 C(I)=(B(I)-ME)^2
210 NEXT I
220 VA=0:FOR I=1 TO N
230 VA=VA+C(I)
240 NEXT I
250 VA=VA/(N-1)
260 REM TOCALCULATE THE STANDARD DEVIATION
270 SD=SQR(VA):PRINT
280 PRINT A$
290 PRINT "PRINT MAGNIFICATION = ";MA:PRINT
300 PRINT "MEAN = ";ME;"NM":PRINT
310 PRINT "VARIANCE = ";VA:PRINT
320 PRINT "S.DEVIATION = ";SD:PRINT
330 PRINT "DO YOU WANT THE DATA SAVED ?          (Y OR N)"
340 B$=INPUT$(1)
350 IF B$="N" GOTO 450
360 IF B$="Y" GOTO 370
370 REM OPEN A DATAFILE
380 INPUT "FILENAME ?";F$
390 OPEN "O",£1,F$
400 WRITE £1,A$,MA,ME,VA,SD,G,L
410 FOR J=1 TO N
420 WRITE £1,B(J)
430 NEXT J
440 CLOSE £1 :GOTO 330
450 END
```

APPENDIX 2

FOIL THICKNESS DETERMINATION

The growth in TEM studies has been accompanied by an increasing need to provide fully quantitiative information about material structures and compositions. The image formed by a TEM is a magnified two-dimensional projection of the object and, for determining precipitate densities, the local foil thickness must be accurately measured. A variety of techniques have been developed for measuring foil thickness, some methods being more accurate and flexible in use than others.

Microstructural features present in a crystalline solid may be used to determine its specimen thickness provided that:

i they are visible,

ii they interesect top and bottom surfaces of the foil,

iii their precise crystallographic orientation can be determined.

Many different features have been used in foil thickness studies including slip-plane traces[A1], stacking faults[A2], dislocations[A3] and averaged precipitates[A4]. Figure A2.1 is a schematic representation of the ideal solution, where the thickness of the specimen is related to the crystallographic features by the equation:

$$t = w \cot \theta \qquad \text{A2.1}$$

The projected width of the feature can be obtained from an electron micrograph of the foil and thus, if the angle θ is known, the foil thickness can be determined. There are two general methods for determining the angle θ. The first requires prior knowledge of the defect habit plane; for example, stacking faults and slip traces are known to lie on {111} planes in face-centred cubic metals. A diffraction pattern of the relevant area will then allow the precise orientation of the defect to be determined. The second technique involves recording the projected width of a defect at various tilt angles. The relationship between these two parameters can then be used to determine the defect orientation.

Another approach, similar to the crystallographic technique, is to apply artefacts on top and bottom surfaces of the foil and relate the projected distance between these objects and foil thickness. For example, Von Heimendahl[A5] applied tiny latex spheres (diameter 234 ± 2.6 nm) to the foil surface by dipping the specimen into an

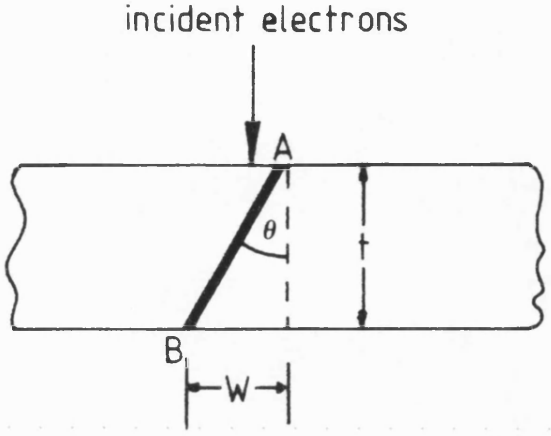

Figure A2.1 Ideal situation for measuring foil thickness using the fault tilt method

alcoholic suspension. For spheres on either side of the foil, a tilt in one direction caused them to converge apparently whilst tilting in the opposite sense resulted in further separation in the image plane. A novel method of producing artefacts within the microscope was devised by Lorimer et al[A6]. They found that a finely focussed electron probe produced a rapidly growing needle of contamination on the top and bottom surfaces in the immediate vicinity of the beam. Subsequent tilting of the specimen produced separation of the two "needles" on the viewing screen, as shown in Figure A2.2 and from the image of the separated spots a thickness value could be calculated. This method has an advantage over the latex sphere method in that it allows for in-situ measurement of foil thickness at any point of interest of the foil.

As well as crystallographic and surface artefact techniques, there are methods of foil thickness determination which utilise the interactions between the primary electron beam and specimen. They are non-absolute methods which mean they require calibration prior to use. Essentially a parameter is measured which varies proportionately with thickness, the constant of proportionality being determined experimentally. Such techniques include measuring (i) the absorption of electrons by the foil, (ii) the energy lost by an electron as it is transmitted through the specimen (iii) the number of electrons reflected back from the surface of the foil, and (iv) the intensity of X-ray emission from the specimen. In the present research the X-ray emission method has been used.

A typical X-ray spectrum is shown in Figure A2.3. It consists of a number of characteristic lines, which are a function of the elements present and in fixed positions on the energy spectrum, and these are superimposed on a background or continuum of X-rays. The distribution of X-rays generated in a sample is partly limited by the penetrating power of the incident electrons. Thus, in a bulk specimen, where no transmission of electrons is observed, the intensity of generated X-rays is insensitive to dimensional changes in the target, and the collected X-rays are a function of the composition of the target and the incident electron energy. However, if a thin target is irradiated with electrons a large proportion of them may be transmitted and no longer contribute to the excitation of X-rays. As the sample thickness increases so too does the number of

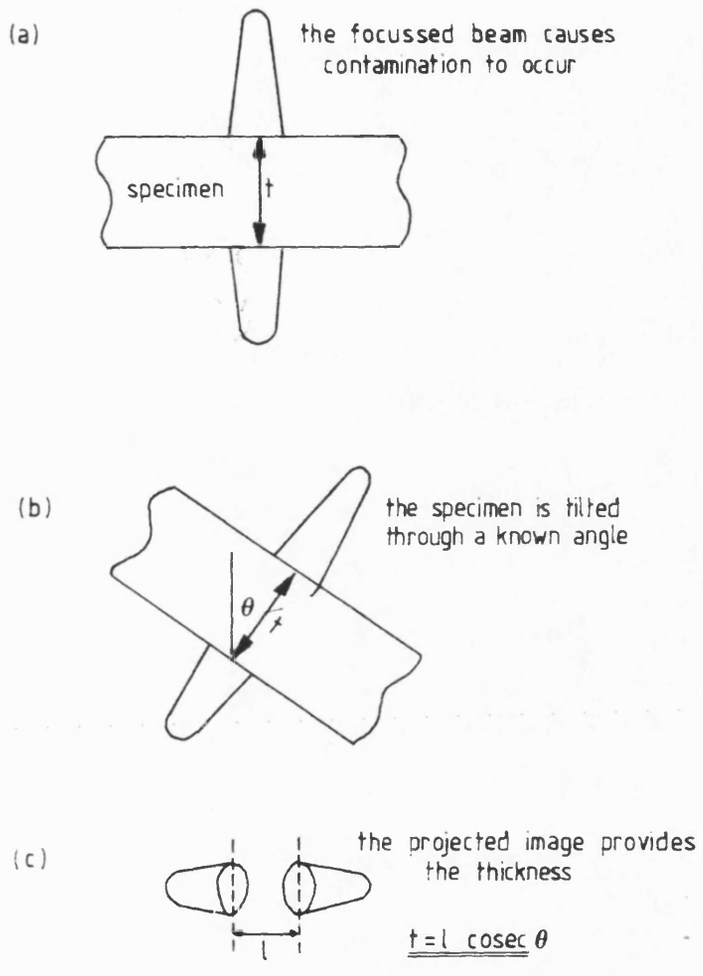

Figure A2.2 The contamination spot technique

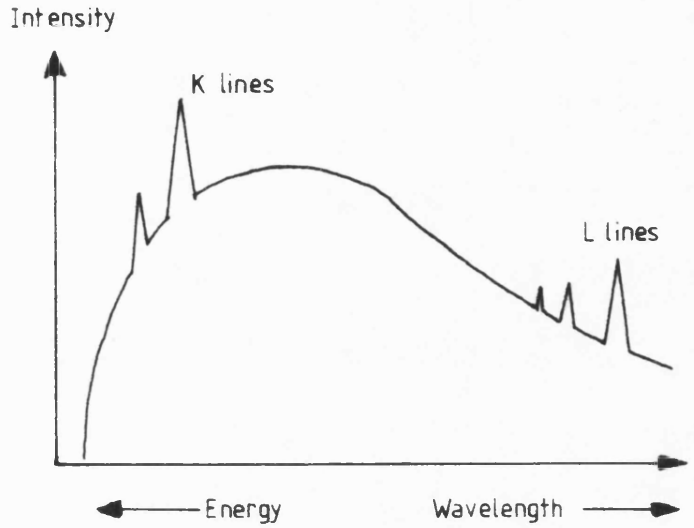

Figure A2.3 Typical x-ray spectrum (schematic)

X-rays generated until a constant level is reached corresponding to bulk dimensions. Thus, within the thin film region the X-radiation intensity will be a function of sample thickness.

As electrons and X-rays are scattered less in thin films, the 'spatial resolution' of the film X-ray analysis is higher than that for bulk specimens. This means that much finer particles can be analysed and much X-ray work on thin films has been done from the analytical standpoint. Since the intensity of characteristic X-ray lines is a function of the amount of each element present in a sample and of the beam current, Cliff and Lorimer[A7] introduced the concept of measuring the characteristic X-ray ratios in an attempt to eliminate current and thickness variables. For a thin film containing elements A and B, the relative concentrations could be found from:

$$C_A/C_B = K_{AB} \cdot I_A/I_B \qquad \text{A2.2}$$

The constant K_{AB} is independent of beam current, specimen thickness and composition and was experimentally determined from materials of similar known compositions. I_A and I_B are the simultaneously measured intensities of A and B. Nockolds et al[A8] have shown a linear dependence for film thickness as a function of the X-ray intensity.

Jacobs and Baborovska[A9] examined the variation of the Cu/Au ratio with thickness in foils of Cu - 75.5% Au. They used the continuum intensity, previously calibrated against twin-boundary traces, as their thickness measuring parameter. However, the low counts of the continuum gave rise to large statistical uncertainty in their measurements. Bentley and Kenik[A10] have also reported that characteristic X-radiation intensities varied in a linear fashion with foil thickness (measured using thickness fringes).

The ideal method for determining foil thicknesses must be capable of providing accurate and precise in-situ measurements over a wide range of thicknesses on a wide range of materials. The regions of interest to be measured should be determined by the operator and not be restricted to areas where a particular thickness related phenomenon occurs. The methods mentioned previously possess these qualities to varying degrees. Love et al[A11] have pointed out

some of the advantages and disadvantages of various methods for measuring foil thickness. Apparent inconsistencies were explained by the fact that each technique measures something different. The contamination spot method determines the total foil thickness including any surface layers of oxide and contamination, convergent beam diffraction gives the metal thickness, while X-ray methods will overestimate if radiation generated in any surface layer, eg oxide etc, is included in the measurement of X-ray intensity. An advantage of using X-ray intensity measurements is that the method is fast, virtually instantaneous once the calibration curve has been obtained. On the other hand, the contamination spot and convergent beam techniques require measurements to be made on film. However, it should be noted that, with all methods, the values derived refer to foil thickness in the beam direction and if the specimen is not accurately aligned perpendicular to the beam, a further error may be introduced when estimating the population density of fine structures. It may be concluded, therefore, that determining the local foil thickness of the specimen remains one of the more difficult measurements to carry out accurately in thin film analysis.

REFERENCES

A1 B. Vigeholm and J. Lindbo; Trans. Met. Soc. AIME., 245, (1969), p 883

A2 E. L. Hall and J. B. Vander Sande; Phil. Mag., 32, (1975), p 1289

A3 C. L. Formby; ibid, 13, (1966), p 621

A4 M. von Heimendahl; J. Appl. Phys., 35, No 2, (1965), p 457

A5 M. von Heimendahl, Micron, 4, (1973), p 111

A6 G W Lorimer, G. Cliff and J. N Clarke; "Developments in Electron Microscopy and Analysis", Ed. J. A. Venables, (1976), p 153

A7 G. Cliff and G. W. Lorimer; Proc. 5th Eur. Cong. Electron Microscopy, Manchester, (Inst. of Phys., London), (1972), p 140

A8 C. Nockolds, M. J. Nasir, G. W. Lorimer; "Electron Microscopy and Analysis 1979", Ed. T. Mulvey, (Bristol: Inst. Physics), (1980), p 417

A9 M. H. Jacobs and J. Baborovska; Proc. 5th Eur. Cong. Electron Microscopy, Manchester, (Inst. of Phys., London), (1972), p 136

A10 J. Bentley and E. A. Kenik; 34th Annual EMSA Meeting, (1976), p 426

A11 G. Love, M. G. C. Cox and V. D. Scott; "Developments in Electron Microscopy and Analysis 1977", Ed. D. L. Misell, (Bristol; Inst. Physics), (1979), p 347

ACKNOWLEDGEMENTS

The author would like to thank the following people for their help in the research:

Dr V D Scott, my supervisor, for his help, advice and encouragement throughout the period of research.

Mr R L Trumper, ARE, Portland, for his advice and many discussions which were conducted throughout.

To the Admiralty Research Laboratories, Portland for financial support during the research.

To Mr P Wakeford and the staff and technicians of the School of Materials Science for their assistance.

To Dr J E Restall for proof-reading this thesis, and finally

To Lisa, my fiancée, for her patience.